Interactions of weakly or non-magnetized bodies with solar system plasmas: Mars and the moons of Saturn

Von der Fakultät für Elektrotechnik, Informationstechnik, Physik
der Technischen Universität Carolo-Wilhelmina
zu Braunschweig
zur Erlangung des Grades eines
Doktors der Naturwissenschaften
(Dr.rer.nat.)
genehmigte
Dissertation

von Elias Roussos
aus Athen, Griechenland

Contents

List of Figures

List of Tables

Summary

The interaction of weakly or non-magnetized planets and moons with the solar wind as well as with a magnetospheric plasma have been studied at Mars and the moons of Saturn using plasma data from the ASPERA-3 instrument onboard Mars Express and energetic charged particle measurements at the moons of Saturn from the MIMI/LEMMS instrument aboard Cassini, respectively. The analysis of data recorded for Saturn's moons was complemented by hybrid plasma simulations. A series of results have been obtained from the study of each individual system:

(a) Using plasma data from the ASPERA-3 instrument onboard Mars Express, plasma fluid parameters (moments) have been extracted using two standard methods: by integration of the particle flux over the instruments energy range and by fitting the phase space density profiles to maxwellian distributions. The estimated moment values from two ASPERA-3 sensors were evaluated by comparing them with the expected values for the solar wind and the various interaction regions within the martian magnetospheric cavity. This comparison helped to identify the best calculation method and the limitations of each sensor. Following these steps, plasma moment maps that describe the interaction of Mars with the solar wind have been constructed for the first time and an estimation of the planet's atmospheric erosion rates has been performed.

(b) Using data on non-ionospheric electrons from the ELS sensor of ASPERA-3 onboard Mars Express, the influence of two different factors that can control the global configuration of the Martian magnetosphere has been investigated. These two factors are the direction that the solar wind convective electric field, E_{SW}, is pointing and the location and intensity of the crustal magnetic field sources of the planet. Information on the pointing of the solar wind convective electric field was extracted by the magnetometer observations of Mars Global Surveyor (MGS), which was operating in parallel with Mars Express in orbit around Mars. Crustal magnetic field data were retrieved from standardized maps that were originally constructed from MGS observations. The non-ionospheric electron data were organized in different coordinate systems based on the E_{SW} pointing and on the crustal field intensity. Interesting asymmetries were found for magnetosheath electrons, during extreme cases (high flux events). More specifically, it was found that high fluxes of magnetosheath electrons, measured at the terminator of the planet can intrude towards the wake under certain, combined geometries involving the planet's crustal field locations and the pointing of the E_{SW}. The influence of the crustal fields on the intrusion of magnetosheath electrons at low altitudes on the planet's dayside, has also been evaluated.

(c) Within $9\,R_s$ from the center of Saturn ($1\,R_s$=60268 km) seven moons with a diameter greater than 100 km are orbiting the planet in almost circular and equatorial orbits. These moons interact continuously with the trapped plasma of radiation belts. Many of

these moons are electromagnetically inert and absorb plasma effectively, resulting in very characteristic depletions in the energetic electron population. The kinematics of those electron "holes" (termed "microsignatures"), is similar to the one of the electrons before their depletion on the moon's surface. Therefore by studying the position of these signatures in the magnetosphere, with respect to the position of the moon that caused them, information can be extracted about the electron flow pattern in the radiation belts. In addition, the study of the refilling of these microsignatures, can give a direct estimate of the diffusion rates in the radiation belts. The detection and analysis of almost 80 microsignatures in energetic charged particle data collected from the MIMI/LEMMS experiment onboard the Cassini spacecraft provided the first derivation of the L-shell and energy dependence of radial diffusion coefficients in the planet's radiation belts. The large variability of the extracted coefficient values indicate a dynamic magnetosphere, with radiation belts being supplied with energetic electrons primarily through particle injections from the middle magnetosphere. The location where the electron microsignatures were detected also indicates disturbed electron trajectories, even deep in the inner Saturnian magnetosphere. The structure of the time independent depletion signatures in energetic ions (macrosignatures) at the orbits of Saturn's icy moons has also been studied in a similar way. Their presence and structure indicates that MeV ions in the radiation belts of the planet are not supplied by particle diffusive processes, but by an external, high energy plasma source that is most likely cosmic rays.

(d) A series of radially broad, energetic electron microsignatures have been identified at the orbits of two asteroid-sized moons of Saturn, Methone and Anthe. It is investigated whether these depletions did actually form by particle absorption on the surfaces of these two moons. For this study, basic theory on energetic particle absorption by small obstacles is considered, as well as relevant observations in the vicinity of two other small Saturnian moons: Telesto and Helene. It was found that the depletions at the orbits of Methone and Anthe originate from concentrations of large grains or dust clumps along the orbit of the two moons. This gives one of the first indications that rings or ring arcs are formed at these distances. Micrometeorid impacts on the two moon surfaces is releasing dust into orbit around Saturn, supplying material for a faint ring formation. A similar detection along the orbit of Saturn's G-ring was correlated with an arc-like structure superimposed on that ring, the complete physical characterization of which was made possible by combining energetic electron and imaging data by the Cassini spacecraft.

(e) The physics of a plasma absorbing interaction has been studied with a three dimensional hybrid plasma simulation code. Saturn's moon Rhea was selected for several simulation case studies. In the hybrid code ions are treated as individual particles and electrons as a massless, charge neutralizing fluid. The code used for the simulations has been originally developed for modeling the interaction of weak comets with the solar wind and has also been successfully applied for the simulation of the interaction of Mars and magnetized asteroids with the solar wind and of Titan with Saturn's magnetospheric plasma. For the simulation runs here a slightly modified version of the code was used. A resistivity term was added in the equations in order to achieve a more physically correct description of the electromagnetic fields in the interior of Rhea. Input parameters for the simulations were collected from a series of studies that used plasma and magnetic field data by Pioneer 11, Voyager 1 and 2 and Cassini missions. Simple, analytical solutions of the "plasma expansion into the vacuum" problem were also considered to support

the interpretation of the simulation results. Among the most important results was that the plasma wake has a different structure parallel and perpendicular to the magnetic field lines. Plasma expansion into the vacuum was found to be driven by different mechanisms, parallel and perpendicular to the magnetic field. A direct comparison was done with the physics of plasma absorbing interactions at objects immersed in the solar wind (eg. the Earth's Moon). Magnetic field measurements acquired by the Cassini spacecraft from a close flyby to Rhea in November 2005 were also well reproduced by the simulation results.

1 Introduction

It is estimated that the Sun's gravity dominates that of neighbouring stars in a sphere approximately 4 light years wide (or about 250000 AU/1 AU=149598000 km). This sphere probably defines the outermost boundary of our solar system, within which a variety of populations exists, with components ranging from the size of a planet, to that of a dust grain or a charged particle.

Under the latest definitions and catalogues by the International Astronomical Union (IAU), the solar system consists of the Sun, 8 planets and almost 170 moons that orbit them, 3 dwarf planets and hundreds of thousands of small bodies, in the form of asteroids, comets or Kuiper belt objects (with estimations bringing this number up to billions) (*IAU* 2006, *de Pater et al.* 2001). It also contains interplanetary dust particles, neutral gas clouds and magnetized plasmas, the latter confined within the boundaries of the heliosphere or that of planetary magnetospheres.

It is obvious that any attempt to study in detail each component of these populations is physically and technically impossible. However, the observational problems that such a large number of components create can be overcome by identifying common properties among them and then studying "representative" members of each "family". Computer simulations can also be used to complement the observations and improve our physical understanding.

One of the largest populations in our solar system is that of the weakly magnetized or unmagnetized bodies (WUBs). No specific definition exists for what "weakly magnetized" represents but the term commonly refers to celestial bodies with a magnetic field that is either generated by an external magnetization of the ionized gas that surrounds them (e.g. ionosphere of Mars and Venus, cometary comae), or by near-surface, permanently magnetized minerals (e.g. crustal field sources at Mars and the Earth's Moon). Celestial bodies with weak, intrinsic dipole fields are usually excluded from this category (e.g. Mercury, Ganymede, magnetized asteroids).

Most celestial bodies in the solar system have such "weakly magnetized" properties or no magnetization at all. Although six out of the eight planets have dipole fields (of various strengths), most moons of these planets show no signs of intrinsic magnetization. Magnetized asteroids have been discovered (*Kivelson et al.* 1993), but given that silicacious and metallic asteroids (asteroids with magnetic minerals) are about 20% of the asteroid family, the bulk of the population is probably unmagnetized. Most comets, Kuiper belt objects or other unexplored moons of giant planets are probably also unmagnetized due to the dominance of water ice in their composition (*Bockelée-Morvan et al.* 2004, *Cruikshank* 2005).

It is maybe not clear how this specific common property of all these bodies can be interesting. For instance, the Earth's Moon is vastly different in many aspects from an

unmagnetized asteroid. How exactly does the lack of magnetization couple these totally different bodies? The answer is that both bodies interact in the same way with an external, magnetized plasma flow. Both behave as plasma absorbing obstacles; both have their surfaces eroded by impinging plasma. Any observable difference in the interaction with the plasma flow could highlight the importance of the different interaction scales and the divergent characteristics of the plasma environments.

There are several examples where comparative approaches can be useful: Mars and Venus have both a CO_2 dominated atmosphere (and associated ionosphere), exposed to the solar wind. Mars also has crustal magnetic field sources, which Venus doesn't have, but the Earth's Moon has. In a way, the different elements that constitute the interaction of Mars with the solar wind can be individually found in two other solar system objects. Comparative studies could highlight the importance of each element in the global interaction (eg. *Lundin and Barabash* (2004a)).

Apart from the comparative approach, there are additional aspects that make the study of WUBs interesting.

First off all, all these bodies interact directly with the solar wind or the magnetospheric plasma that flows against them. Under these conditions the interaction can have a substantial impact in their geological evolution. For instance, the interaction of Mars with the solar wind is thought to be one of the primary channels for Mars loosing atmospheric material, and consequently, water from its surface (*Lundin and Barabash* 2004b). Such direct interactions can be interesting in another aspect: the magnetic field can "penetrate" into the interior of an obstacle and its deformation can provide insights on what the internal structure of that object is. The magnetic field induction signatures identified during several Europa flybys by Galileo provided substantial evidence that oceans are present below the surface of that moon (*Khurana et al.* 2001).

An additional interesting characteristic is that WUBs can have very simple physical interaction with certain plasma populations. For instance, many inert moons of the outer planets have a simple, geometrical and absorbing type interaction with energetic plasma (*Van Allen et al.* 1980a). The energetic plasma cavities that are formed evolve primarily due to diffusion processes in the magnetosphere, rather than due to processes associated with wake dynamics in the low energy plasma (*Samir et al.* 1983). As the disturbances that these moons cause in the energetic plasma can be accurately described, studying their evolution can help to quantify important parameters of a series of magnetospheric processes.

The present thesis contains results from the study of a series of WUBs and all the aforementioned aspects that make their study interesting are highlighted.

More specifically, Chapter 3 includes results from the study of the interaction of Mars with the solar wind, based on data collected by the ASPERA-3 plasma experiment aboard the Mars Express spacecraft. Results presented in this chapter can be directly compared with the forthcoming observations by the same experiment onboard Venus Express. The erosion of the planet's atmosphere by the solar wind is also briefly investigated, while a detailed study is also performed regarding the complications that the presence of crustal magnetic fields of Mars are introducing in the interaction.

Chapter 4 includes findings from the study of the interaction of Saturn's numerous icy moons with the planet's energetic particles. The study is based on data from Cassini's MIMI/LEMMS experiment. By studying the structure and the evolution of sev-

eral very characteristic, microscopic disturbances that the inert moons of Saturn cause to the trapped radiation particles, a series of macroscopic processes are evaluated in the Saturnian magnetosphere.

In Chapter 5 I present results on the extraction of the physical characteristics of obstacles in orbit around Saturn that interact with magnetospheric energetic particles. This study is again based on data from the Cassini MIMI/LEMMS experiment. Several specific events where energetic electrons were depleted by unknown absorbers are analyzed. It is shown how the understanding of the interaction of an inert obstacle with energetic particles can be used to extract results that are not only relevant for plasma and/or magnetospheric physics, but also for planetary dynamical system studies. Several findings towards this direction are also presented in Chapter 4.

The subject of Chapter 6 is the simulation of the interaction of an inert moon with Saturn's magnetospheric plasma. The Saturnian moon selected for this case study is Rhea. The topic is investigated by applying a three-dimensional plasma simulation code. The importance of comparative approaches is also highlighted in this chapter, as the simulation results are interpreted in the context of the Earth's Moon interaction with the solar wind and that of the other inert moons of Saturn with the magnetosphere. The outcome of the simulation is further interpreted in the view of Cassini data that have been acquired during a close flyby to Rhea.

Chapter 2 serves as a short introduction to the Mars Express and Cassini missions, and to the instruments from which data have been acquired for the research presented in Chapters 3-5.

In the following two sections basic facts and figures about Mars, Saturn, their moons and their space environment are collected. Additional details and references about each planet's (or moon's) space environment are given in the respective introductory sections of each chapter. Finally, as the research in this thesis is based on the analysis of both low energy and high energy plasma data, a brief section is included where the basic distinctions of these two populations are outlined.

1.1   Mars in the solar wind

Mars is the fourth planet from the Sun, orbiting at an average distance of 1.52 AU. With a radius of 3397 km (R_M), its size is almost half that of the Earth. The orbit of Mars is quite eccentric compared to that of the Earth, as its eccentricity is almost 0.1. On the other hand, there are several similarities between Mars and Earth: both planets have a 24 hour rotational period and an obliquity of their rotation axis with respect to their orbital plane of about 25°, the latter meaning that Mars also has seasons. A martian year lasts about 1.9 Earth years. Mars is orbited by two small asteroid-sized moons, Phobos and Deimos.

Mars has a relatively weak, CO_2 dominated atmosphere, with small concentrations of other gases like CO, H_2O, O_2, H_2 and Ar. The surface atmospheric pressure at Mars is about 100 times lower than at the Earth. It is the ionization of this atmosphere and the formation of an extended ionosphere and exosphere primarily controls the interaction with the solar wind. There are several review papers that summarize our current understanding of the planet's interaction with the solar wind (*Nagy et al.* 2004, *Dubinin et al.* 2006a, *Brain* 2006a). A simplified sketch of the resulting configuration is shown in Figure 1.1.
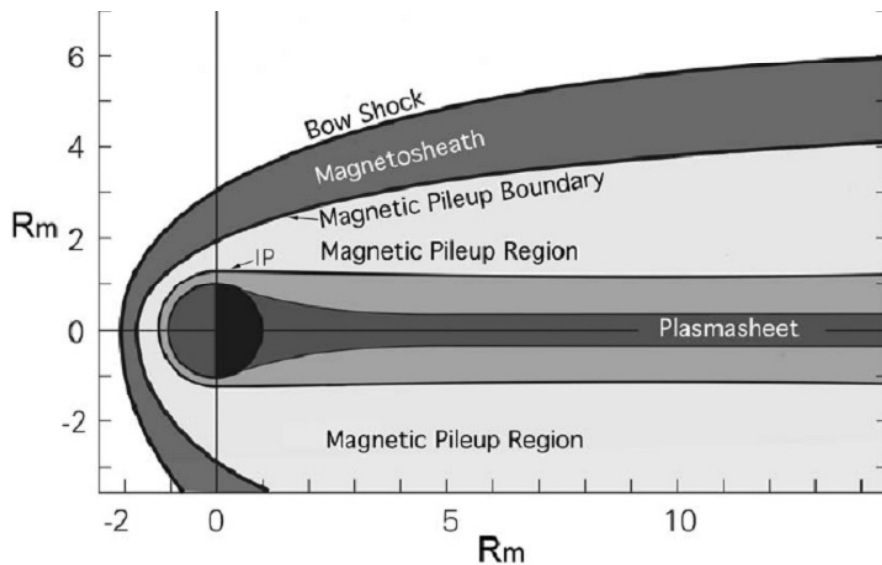
Figure 1.1: A sketch of the main interaction regions of Martian induced magnetospheric cavity (*Nagy et al.* 2004). The Sun is to the left and therefore the solar wind is parallel to the horizontal axis, flowing towards the right. The configuration peprendicular to the solar wind velocity axis is, to a first order, axisymmetric, but the sketch shows the magnetosphere to be slightly more expanded in the southern part. This illustrates the effects of the localized crustal fields that are thought to "push" the interaction boundaries outward (see text).

As for any obstacle with a conducting ionosphere in the supersonic solar wind, a bow shock forms upstream of the planet's dayside ionosphere, decelerating the solar wind to subsonic speeds. *Vignes et al.* (2000) found that the typical distance of the bow-shock at the subsolar region was at 1.67 ±0.03 R_M from the center of the planet and at 2.56 ±0.06 R_M at the terminator. This distance increases towards large solar zenith angles (the angle between the Sun-Mars and the Mars-observer lines). The observed variability shows a good correlation with the pointing of the solar wind convective electric field (*Vignes et al.* 2001). As the spatial distribution of the mass loading is also modulated by the convective electric field pointing (*Bößwetter et al.* 2004), it is then likely that this process affects the bow shock location. Recent results from Mars Express (*Dubinin et al.* 2006a) and older results from Phobos-2 (*Trotignon et al.* 1993) indicate no dependence of the average bow shock position from the solar cycle or the solar wind dynamic pressure.

The magnetic field and the plasma are compressed downstream of the bow shock. The magnetic field magnitude, the plasma density and temperature increase, forming the magnetosheath. The magnetosheath is dominated by solar wind plasma, however as the solar wind penetrates deeper, significant mass loading occurs from the extended exosphere of Mars. As solar wind and exospheric ions exchange energy and momentum due to collisions, the solar wind is effectively stopped at a location where a boundary is formed, termed as the Magnetic Pile-Up Boundary (MPB). The average subsolar distance of the MPB is at 1.29 ±0.04 R_M and at 1.47 ±0.08 R_M at the terminator (*Vignes et al.* 2000). This distance is controlled by the presence of crustal magnetic field sources in the southern

hemisphere of the planet (see text towards the end of this section) (*Vignes et al.* 2001, *Crider et al.* 2002).

Below the MPB solar wind ions are almost absent and planetary ions appear. The electron density does not show a substantial change, but the mean energy of electrons drops. It would be expected that at the MPB the ionospheric electron thermal pressure balances the solar wind dynamic pressure, but this is more the case for the interaction of Venus with the solar wind (*Elphic et al.* 1980). At Mars ionospheric pressures are found to be insufficient to stagnate the solar wind flow, which suggests that the balance at the MPB is achieved due to a magnetized ionosphere (*Nagy et al.* 2004).

Below the MPB the magnetic field piles-up and drapes around the planet. This region is called the Magnetic Pile-Up Region (MPR). What happens at even lower altitudes is not yet clear. According to Figure 1.1, an ionopause forms. This is based on several observations showing a boundary in the fluxes of suprathermal electrons (>10 eV) and a dropout in the magnetic field magnitude. However, whether this boundary is indeed an ionopause is still an open question. An alternative terminology used is that of the "photo-electron boundary" (PEB). Below the PEB CO_2 photoelectrons are commonly observed in the expected energy range of 21-24 eV and at 27 eV (*Frahm et al.* 2006).

Both the magnetosheath and the MPR extend towards the tail region. The MPR plasma properties are "interrupted" at the boundaries of the geometrical shadow of Mars, while the draped magnetic field lines form two magnetic lobes of opposite polarity. Several observations with the Phobos-2 spacecraft have shown that between the tail lobes a plasma sheet of hot solar wind plasma originating from the dayside, could be present (*Nagy et al.* 2004).

Such a global configuration is usually termed as "induced magnetosphere", and it is found (with several variations) in most unmagnetized bodies that have a substantial ionosphere or exosphere, such as Venus, active comets and Titan. Titan's induced magnetosphere, however, forms without a bow-shock (and a magnetosheath) as it is usually immersed in a subsonic plasma flow (*Simon et al.* 2007a).

At low altitudes or within the MPR and the tail regions planetary ions are detected. These ions can be accelerated above the gravitational escape velocity, primarily due to the effect of the convective electric field of the solar wind (*Bößwetter et al.* 2004). In this way the planet losses atmospheric mass. Estimates of the ion escape rates using Phobos-2 data vary over 3 orders of magnitude (*Lundin and Barabash* 2004b). This large difference in the various estimates reflects the limitations of the Phobos-2 instrumentation and its statistically insignificant observations.

A surprising discovery of the Mars Global Surveyor mission was that Mars has many strong, localized crustal magnetic field sources, most of which form an extended network of complex, mini-magnetospheres in the planet's southern hemisphere, as shown in the map in Figure 1.2 (*Acuña et al.* 1998). It is not yet clear whether the presence of magnetic anomalies introduces only localized complexities or if it affects globally the induced magnetosphere.

As mentioned earlier, magnetic anomalies tend to push outward the location of the dayside MPB (*Vignes et al.* 2001, *Crider et al.* 2002). Several authors have also argued that the crustal magnetic anomalies can be termed responsible for auroral-type events (*Brain et al.* 2006b) that have been reported by ultraviolet spectrometer observations (*Bertaux et al.* 2005). The study of *Verigin et al.* (2001) is the only one so far based
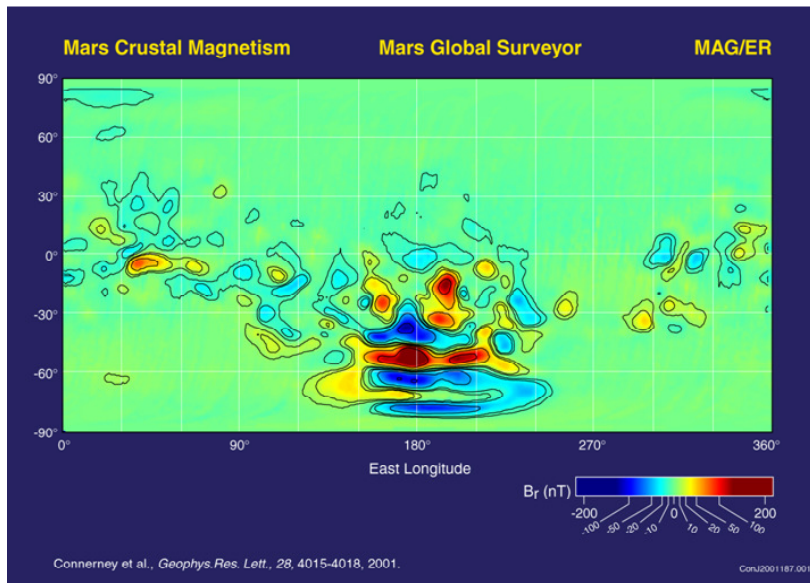
Figure 1.2: A map of the radial component of the crustal magnetic field, in planetocentric longitude and latitude coordinates (from *Connerney et al.* (2001)).

on spacecraft data that reports possible global changes in the induced magnetosphere (and more specifically in the diameter of the magnetotail), as a function of crustal field orientation. Computer simulation studies supporting this finding have been performed by *Harnett and Winglee* (2005).

A series of unresolved and interesting issues of the Mars-solar wind interaction still remain open for further research. Some of these, listed below, are discussed and are investigated in Chapter 3.

- What are the properties of the different interaction regions, in terms of plasma fluid parameters (moments)? Do the interaction regions and boundaries in electrons and ions coincide with those identified primarily with the magnetic field data from MGS?

- How does the weak Martian ionosphere balance the solar wind flow? Do the crustal magnetic anomalies have any contribution?

- What are the planetary ion escape rates and how do they compare with the various estimates from Phobos-2 and from computer simulations? How does this depend from upstream solar wind parameters and from the orientation of the crustal fields?

- Does the presence of magnetic anomalies have global effects in the configuration of the induced magnetospheric cavity? Is there a rotational or seasonal modulation associated with their continuously changing orientation with respect to the solar wind flow?

1.2   The Saturnian magnetosphere

Saturn is the sixth planet from the Sun. Its orbit is circular and close to the ecliptic plane, at a mean distance of 9.54 AU from the Sun. The planet's radius is about ten times that of the Earth, approximately 60268 km (R_S). Saturn is a gas giant, meaning most of its volume is filled with dense gases (mainly hydrogen and helium) that are gravitationally confined by a massive, metallic core in the planet's center. Saturn rotates relatively fast: a Saturnian day lasts about 10 hours and 40-50 minutes.

One of the most prominent and spectacular features of Saturn is its main ring system that extends up to 2.3 R_S from the center of the planet. Saturn is also orbited by more than sixty moons, many of which show unique geophysical characteristics (e.g. Enceladus, Titan and Iapetus). What is interesting is that the planet's rings and most of its large moons orbit Saturn inside its magnetosphere. These can act both as plasma sources and plasma sinks.

Saturn's magnetosphere is formed by the interaction of the planet's dipolar field with the solar wind. The planet's fast rotation probably has an important role, as the resulting corotational electric field can dominate that of the solar wind that penetrates in the magnetospheric cavity. A sketch of the magnetosphere, based on data acquired from the first missions that flew-by the planet (Voyager 1,2 and Pioneer 11) is shown in Figure 1.3. More facts and details about Saturn's magnetosphere can be found in several review papers (eg. *Blanc et al.* (2002) and references therein).

As at the distance of Saturn the solar wind density and the interplanetary magnetic field magnitude have dropped substantially, the magnetopause is on average between 20-25 R_S in the subsolar region, despite the fact that the surface magnetic field of the planet (0.21 G at the equator) is lower than that of the Earth (0.3 G). The bow shock is located at about 30-35 R_S. Unlike any other planet, Saturn's measured magnetic field is perfectly axisymmetric. This is also a mystery, given that fluid flows (e.g. at Saturn's interior) cannot generate axisymmetric magnetic fields (*Hide and Palmer* 1982).

In the middle and outer magnetosphere (from about 9 R_S to magnetopause), the magnetic field lines have magnetodisk like configuration. This means that the magnetic field lines are stretched outwards in a region close to the planet's magnetic equator, deviating from the dipolar field configuration. This is primarily due to the planet's fast rotation which "induces" strong centrifugal forces on hot plasma flux tubes. As these flux tubes have higher plasma than magnetic pressure (plasma beta higher than unity), the magnetic field is "carried" outwards with the centrifugally expanding plasma, forming the magnetodisk. A similar, and even more intense magnetodisk structure exists at Jupiter (*Khurana and Schwarzl* 2005, *Birmingham* 1982).

The outer magnetosphere is also the region where Titan is expected to load the magnetosphere with heavy ions, but such evidence has yet to be found. At the nightside magnetosphere, an extended magnetotail is formed with two north and south plasma depleted lobes and a central, intense plasma sheet, with hot, solar wind plasma (*Krimigis et al.* 2007).

The middle and inner magnetosphere (1-9 R_S) is uniquely structured: it coexists with the planet's ring system, more than 10 icy satellites, the neutral gas released due to sputtering from their surfaces forming a torus (3-8 R_S) and finally two diffuse dust rings (E- and G- rings). More specifically, the E-ring is formed by cryovolcanic activity of one of
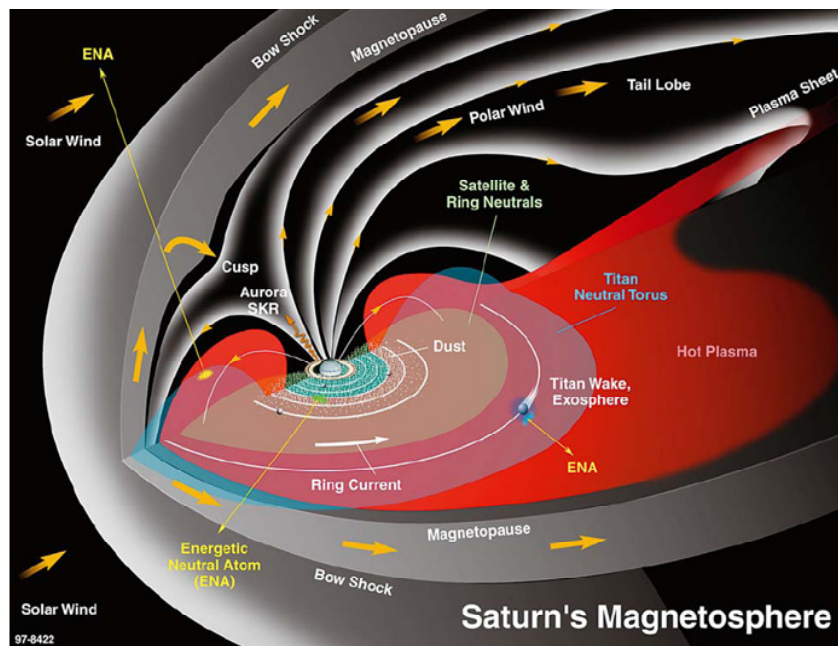
Figure 1.3: A sketch of the Saturnian magnetosphere, with its various regions indicated (from *Krimigis et al.* (2004)).

the satellites (Enceladus), which also further enhances the neutral gas torus (*Dougherty et al.* 2006). Absorption signatures in energetic electrons and ions originating at the moon surfaces are commonly detected by the respective detectors (*Van Allen et al.* 1980a,b, *Carbary et al.* 1983, *Chenette and Stone* 1983, *Paranicas et al.* 2005).

Particles with intense energies (hundreds of keV to tens of MeV) can be found mainly inside 6 R_S. This region constitutes the planet's radiation belts, that are to some extent transient, given the continuous depletion of energetic particles by the icy moons, the rings and the neutral gas. Inside 2.3 R_S and in the regions magnetically connected to the main rings, energetic particles are completely absent.

This typical picture of the middle and inner magnetosphere is shown in Figure 1.4. The top panel shows energetic ions and the bottom panel energetic electrons measured by two sensors of the MIMI experiment (see Section 2.2). Energetic ions are abundant in the middle magnetosphere (L>7-8) but between 3.5-7 R_S they are absent, probably because they charge-exchange with the neutral gas and they are lost as energetic neutral atoms. Energetic electron fluxes also drop inside 7 R_S with respect to the values in the middle magnetosphere, but in the region where energetic ions are not present, electrons are much more abundant. Inside, 3.5 R_S energetic particles in the range of 100 - 200 keV appear (typical for radiation belts), while also MeV particles are present (not shown in this plot). In the center of each panel, a plasma void region is seen, where energetic particles have been depleted by Saturn's main rings.

In both panels, ion and electron fluxes show dispersed features as a function of energy. These are called "injections" and are thought to be the result of instabilities occurring between the middle and outer magnetosphere (where hot plasma is present) and the inner magnetosphere (where energetic ions are absent and electrons are less abundant) (*Mauk et*
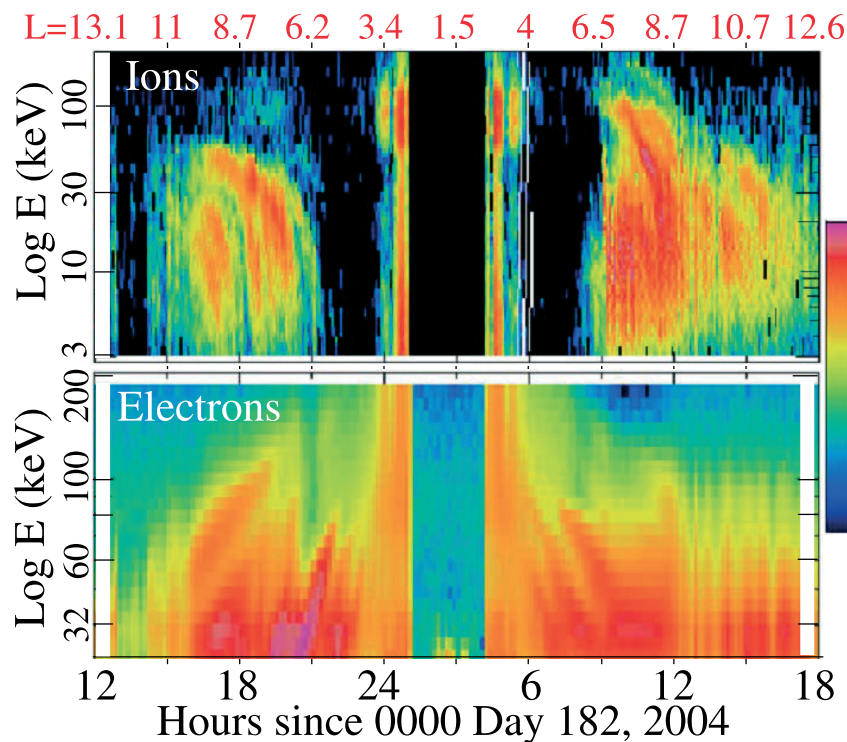
Figure 1.4: Energetic ions (top) and electrons (bottom) measured during the first orbit of Cassini in the inner magnetosphere of Saturn, by MIMI/LEMMS and MIMI/CHEMS sensors. The horizontal axis at the bottom shows the time while the same axis at the top (red letters) indicates the spacecraft position in terms of dipole L-shell, L (equatorial distance of a dipole field line in R_S). The vertical axis indicates the particle energy in keV. Color coded in each plot is each sensor's fluxes (red for high fluxes, black for low fluxes). Plot taken from *Mauk et al.* (2005).

al. 2005). Their shape is due to energetic particles of different energy and charge having different drift velocities at Saturn (see Section 1.3).

Given the existence of many plasma sinks it is peculiar how the radiation belts are sustained. One of the subjects investigated in Chapter 4 through the study of the absorption effects from satellites, neutral gas and rings is exactly that: what are the sources or the mechanisms that feed the inner magnetosphere with energetic plasma? How do these sources counter the effects of so many plasma sinks? Are injections important for transporting plasma in the radiation belts?

Furthermore, what is the relative importance of the large icy moons, dust and the neutral gas as energetic plasma sinks? Are there additional dust populations that can make their presence known by the absorption effects, as the planet's neutral gas torus and its main rings? Why are such depletions more pronounced in the energetic plasma? Is the formation and evolution of plasma cavities at different energy ranges different and why? These questions are investigated in Chapters 4-6.

1.3   Cold plasma and energetic particles

As it is obvious from the two previous sections, the plasma environments of Mars and Saturn have distinct differences. Both the induced magnetosphere of Mars and the magnetosphere of Saturn have external and internal plasma sources, however the energy range where charged particles are found is much broader at Saturn.

For both planets the solar wind is a particle source, while each planet's bow shock is a source of energization (*Dubinin et al.* 2006b, *Orlowski et al.* 1995, *Krimigis* 1992). However, due to the much larger scales and the higher complexity of the saturnian magnetosphere, particles there can be accelerated to much higher energies (tens of MeV) than at Mars (tens of keV). Furthermore, Saturn, due to its dipole field, can also trap particles of hundreds of MeV that originate from galactic cosmic rays (eg. secondary products from impacts of cosmic rays on Saturn's rings (*Randall* 1994)).

For example, thermalized particles downstream of Saturn's bow-shock at Saturn that leak through the magnetopause can be further accelerated through an inward radial diffusive transport. During such a process their magnetic moment remains constant. The magnetic moment ($\mu = \frac{1}{2}\frac{m\,u_\perp^2}{B}$) is proportional to E/B (where E is the particle's energy due to motion perpendicular to the field lines and B the magnetic field magnitude). In a dipole field and along the magnetic equator, $B \propto R^{-3}$, with R the distance from the dipole source (or in our case the planet's center). Therefore, conservation of μ means that a radially diffusing particle from 20 R_S to 4 R_S for example, can increase its energy 125 times.

Such a process is not possible for Mars, where the length scales for particle acceleration are about 1000 times smaller than at Saturn. Furthermore, due to the spatially restricted interaction region at Mars and the absence of an undisturbed dipole field, charged particles cannot be trapped for long time scales and be further accelerated by other processes, such as wave particle interactions (*Horne et al.* 2005). Therefore processes involving energetic particles can be better studied at Saturn than at Mars.

There is no real "energy boundary" above which a particle is classified as energetic. Both particle populations are governed by the same physical laws, however the energy of each particle can amplify or "hide" several effects which could be employed in order to illustrate some basic differences between energetic and low energy particles:

- Particle velocity (or energy) distributions in the solar wind or in planetary magnetospheres are usually described by a "kappa-distribution", where the effect of a maxwellian distribution at low energies and an inverse power law dependence at high energies ($f = f_o E^{-\kappa}$) are combined. Such a distribution is shown in Figure 1.5. Theoretically, a maxwellian distribution is valid for a plasma population in thermal equilibrium. The partial applicability of the maxwellian distribution in solar system plasmas results from the low frequency of collisions between charged particles, which means that non-equilibrium distributions are also present. These can be described by the power law component of the kappa distribution for energies much higher than κkT, where k is Boltzmann's constant and T is the temperature of the Maxwellian component of the distribution. The $E = \kappa kT$ limit can be used to distinguish low energy (cold) and energetic particles (or the "thermal" and the "suprathermal" component of the distribution).

- As it can be easily realized from Figure 1.5, energetic particles usually have a small
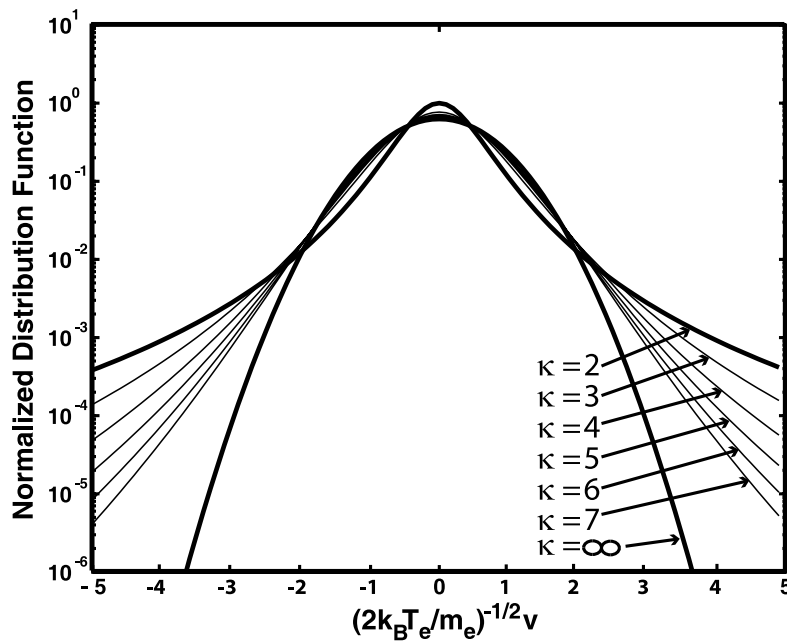
Figure 1.5: A kappa distribution for different values of the index κ. Note that for $\kappa \to \infty$ the distribution retains a purely Maxwellian form (from *Watt and Rankin* (2006)).

contribution to the total plasma density. By simply integrating the maxwellian component of the kappa-distribution over energy, the plasma density can be derived with only a small error. On the other hand, for a hot plasma (broad distribution/ low κ), energetic particles can have very high contribution to the total plasma pressure (see for example *Sergis et al.* (2007)).

- In a magnetized plasma and under the effect of an electric field, the bulk velocity of the thermal particles is dominated by the $\mathbf{E} \times \mathbf{B}$ force, while for energetic particles magnetic drifts can be very important. An example of a magnetic drift is that of the "gradient-drift", which results from a gradient in the magnetic field magnitude (Figure 1.6). As charged particles spiral around the magnetic field lines with a gyroradius that is different for a region of strong magnetic field than for a region of a weak magnetic field, the resulting trajectory is not closed and the particle's center of gyration (called the guiding center) drifts. This drift is different for particles of opposite charge and it is usually important only for high energies, as shown in Figure 1.7. The limit above which magnetic drifts dominate is different for each space environment, but can also be used to separate cold and energetic particles.

- For energies at which magnetic drifts are important, charged particle populations cannot be assigned to a single value and direction for the bulk velocity (eg. as in a fluid description). On the other hand, lower energy particle distributions can be assigned a single bulk velocity value.

While the discussion about the differences between cold plasma and energetic particles can be much more extensive, the most basic points relevant to the subjects discussed
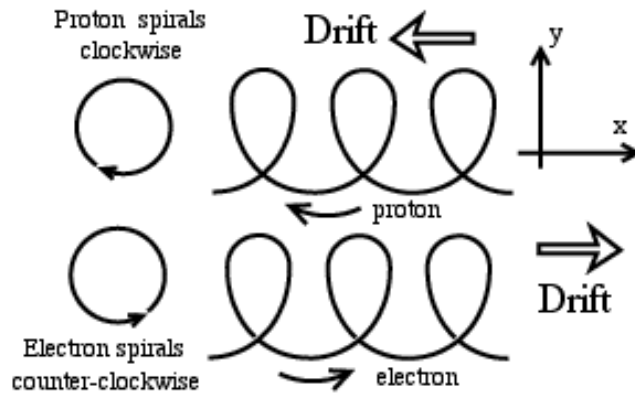
Figure 1.6: Illustration of the gradient drift. The magnetic field points out of the page and increases along the y-axis.
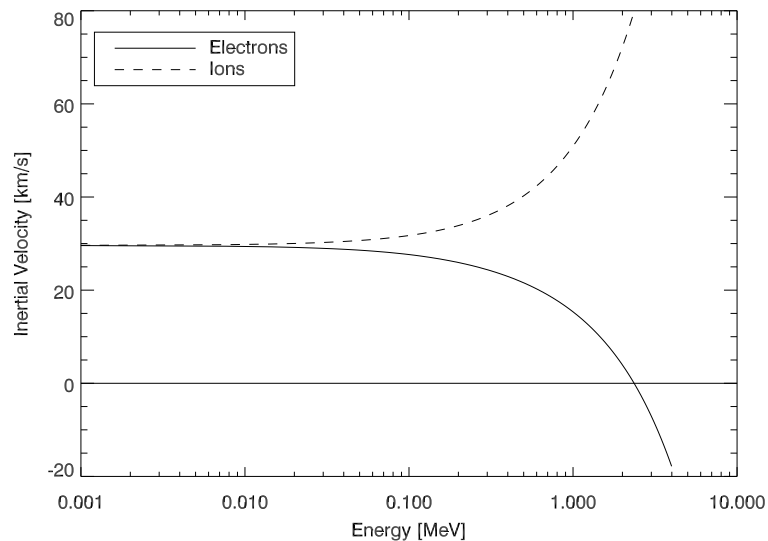
Figure 1.7: The effect of gradient drift at Saturn at a distance of 3 R_S from the center of the planet and for equatorial electrons and ions, as a function of particle energy. For energies lower than 1 keV the electric field drift, $\mathbf{E} \times \mathbf{B}$, controls the bulk motion of the particles. For higher energies the gradient drift results in velocities strongly dependent on energy and charge. The velocity is given in an inertial coordinate system centered at Saturn and the velocity calculation is based on formulas given in Appendix A.

in this thesis have been described in the aforementioned points.

2 Particles and fields instrumentation

In this chapter I summarize some basic facts about the different types of particle and fields instruments that are used in the space missions from which data has been obtained for this thesis. Rather than going into details, descriptions will mainly include the measurement principles and techniques of the various instruments. More emphasis will be given to the description of the charged particle detectors on Mars Express and Cassini from which most of the data has been acquired. These are the ASPERA-3/ELS and ASPERA-3/IMA electron and ion sensors, respectively, on Mars Express and the MIMI/LEMMS energetic charged particle detector of Cassini.

2.1 Particles and fields instrumentation on Mars Express

Mars Express is the first mission of the European Space Agency to a planet of our solar system other than the Earth. It was launched on the 2nd of June of 2003 and entered in orbit around Mars few days before the end of 2003. Despite being a low cost mission, Mars Express carries a set of advanced instruments for remote and in-situ observations of the plasma environment, the atmosphere, the ionosphere, the surface and the subsurface of the planet. Mars Express was also carrying a small lander (Beagle 2), which unfortunately failed to send a signal from the surface.

For studies of the planet's plasma environment the most important instrument on Mars Express is ASPERA-3 (Analyzer of Space Plasma and Energetic Atoms). ASPERA-3 combines electron, ion and energetic neutral atom (ENA) sensors. Only electron and ion data are used for this thesis. Data from the ENA sensors were not considered because these sensors turned out to be more sensitive to the UV light than expected. Taking advantage of the elliptical orbit of Mars Express, which covers sufficiently all interaction regions of the martian magnetospheric cavity, studies of the global magnetospheric dynamics are possible (Figure 2.1).

The ASPERA-3 instrument is also the first experiment capable of determining large scale statistics of plasma moments (density, velocity, temperature, pressure) in the environment of Mars. The plasma moments calculation was essential for a more detailed analysis of the ASPERA-3 data, as well as for the estimation of the erosion rates of the Martian atmosphere.

In the following sections, several additional details are provided for the ASPERA-3 instrument, as well for the additional data sources and tools that support the ASPERA-3 data analysis. The conversion of ASPERA-3 data to plasma moments is also briefly discussed in Section 2.1.3.
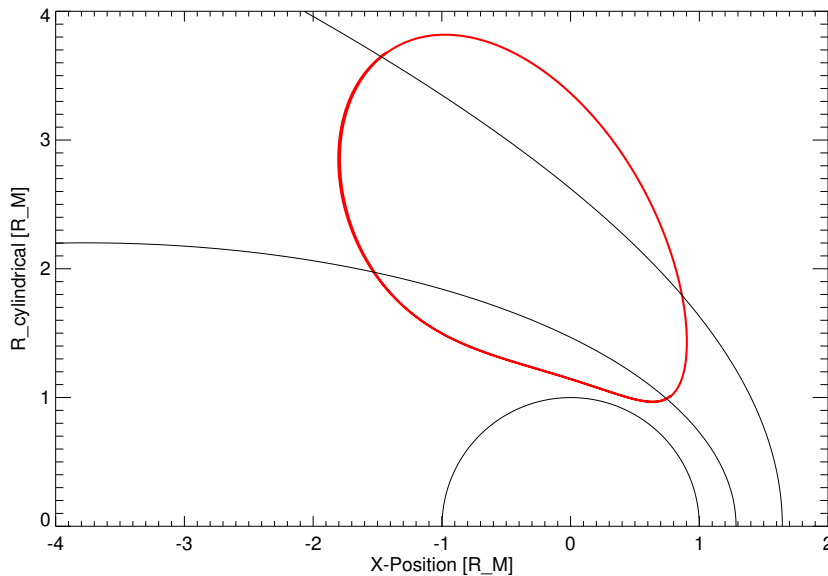
Figure 2.1: A typical orbit of Mars Express that crosses all interaction regions of Mars with the solar wind. The orbit is plotted in a coordinate system where the positive x-axis points opposite to the solar wind direction from the center of the planet and the y-axis is the cylindrical axis of symmetry (see Section 3.1 for more information on the coordinate systems). The locations of the bow shock and the magnetic pile-up boundary (MPB) are also drawn. The orbit shown is from August 2005. Under the effect of gravitational fields of Mars and the Sun the orbital plane gradually rotates, and in this way additional regions are accessed within the mission time.

2.1.1   The ASPERA-3 instrument

The ASPERA-3 instrument consists of the Main Unit (MU) and the Ion Mass Analyzer (IMA) (Figure 2.2). The MU houses three sensors: the Neutral Particle Imager (NPI), the Neutral Particle Detector (NPD) and the Electron Spectrometer (ELS). It also includes a scanner that is used to achieve a 3D coverage with these three sensors. The MU also houses the electronics for operations and data handling. IMA has its own electronics package. As data are used only from ELS and IMA, in the short descriptions that follow no details will be given for NPI and NPD. More detailed information on ASPERA-3 can be found in (*Barabash et al.* 2007a).

2.1.1.1   Electron Spectrometer - ELS

The ELS spectrometer is a top hat electrostatic analyzer that can measure electrons between 0.4 eV and 20 keV, with an energy resolution of 8% in a $4° \times 360°$ field of view. A cut-sectional view of ELS is shown in Figure 2.3.

As shown in the schematic, particles are entering from the top hat and are then deflected within the hemispherical structure by an electric field. The electrons that go through are detected and recorded through a Microchannel Plate (MCP), in a total of 16 anodes (each anode for a different direction). The deflection electric field is generated by applying a positive voltage in the inner hemispherical structure. The voltage is usually

Figure 2.2: The IMA sensor (left) and the Main Unit with the ELS in view (right)
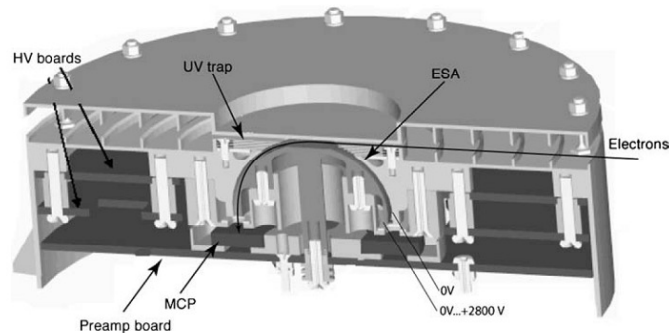
Figure 2.3: A cut-sectional view of the ELS sensor.

divided into 128 steps, up to 2800 Volts (equivalent to ~ 20 keV electron energy). This determines the energy channels of ELS. A full voltage scan lasts about 4 seconds. The cylindrical symmetry of the sensor ensures that during these 4 seconds a full 360°, 2D scan is achieved. If the MU scanner is operated then 3D coverage becomes possible. A full 3D scan takes between 32 and 128 seconds to complete, but has not been applied for the first two years of the mission.

ELS is not UV sensitive and can be operated even when the electron entrances are directly exposed to the sunlight. ELS is more sensitive to spacecraft photoelectrons. To avoid saturation of the sensor by spacecraft photoelectrons a negative voltage is applied to the top-hat entrance. This usually prevents the detection of less than 5 eV electrons.

2.1.1.2   Ion Mass Analyzer - IMA

IMA is the ion sensor of ASPERA-3 that is mounted on the side of the Mars Express spacecraft opposite the MU (and ELS) is. The IMA sensor can perform simultaneously both ion energy spectroscopy and ion composition analysis. More specifically, IMA determines the mass per charge (M/q) and energy per charge (E/q) of ions with 1-30 amu/e and 10 eV/e - 30 keV/e. A sketch of IMA is shown in Figure 2.4.

The IMA design ensures a full angular coverage in azimuth with 16 anodes oriented
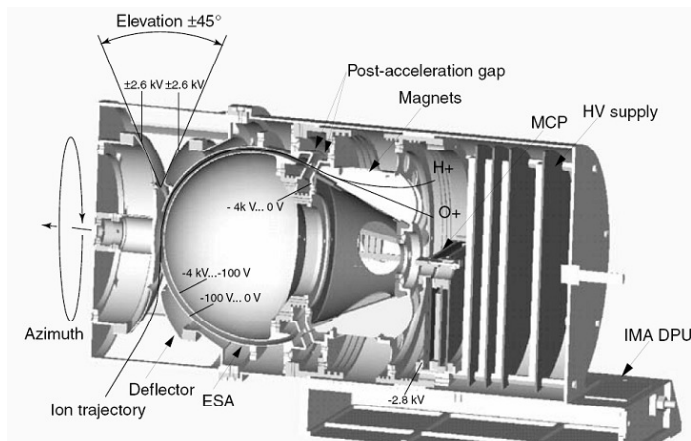
Figure 2.4: A cut-sectional view of the IMA sensor.

perpendicular to the instrument's primary axis of symmetry. 3D coverage is achieved by electrostatic scanning (or elevation scanning) perpendicular to the azimuthal plane. The opening angle for the elevation scanning is 90° and is divided into 16 sectors. A full elevation scanning lasts 192 s and it is achieved with the use of a deflector that applies changing voltages at the ion entrance.

Particles that pass the deflector continue their trajectory in a spherical electrostatic analyzer (ESA). By applying different voltages on the ESA surfaces, particles are filtered in energy per charge. The surviving particles are then distinguished according to their M/q, first by acquiring an acceleration by a negative voltage lower than 4 kV (Post acceleration - PAC), and then by deflection from permanent magnets, which form a total field of 1200 G. Three PAC levels exist, each selected to achieve different mass resolution.

The ions impact a MCP, and the electron cloud produced is detected by a system of 32 concentric anode rings (each corresponding to a different ion mass) and 16 anodes (corresponding to the particle's azimuth). Therefore, the output of IMA includes information of the particles M/q, E/q and direction in 3D-space. Full angular coverage is only limited by the opening angle for the elevation scan (180° would have been required for 4π coverage) and by the fact that the spacecraft body is shading several directions.

2.1.2   Additional data sources

One of the drawbacks of the Mars Express mission is that the ASPERA-3 experiment is not complemented by a magnetometer. A partial solution to this problem was possible by using the magnetic field data by the magnetometer of the Mars Global Surveyor spacecraft (MGS), which was operating until November 2006, covering 2.5 years of MEX operations. MGS was orbiting Mars at a 400 km, circular and sun-synchronous orbit. At this altitude and at the dayside of the planet MGS could sample information about the interplanetary magnetic field (IMF). At 400 km altitude the resulting magnetic field is strongly enhanced by the interaction with the planet's ionosphere, however its clock angle is not significantly altered with respect to the IMF.

Therefore, by using the MGS magnetometer data it was at least possible to infer the

approximate orientation of the IMF. One complication is that at the 400 km of MGS's orbit, the martian crustal fields are quite strong and could of course "shadow" the IMF. By using crustal field models and maps, MGS magnetometer data from regions where the crustal fields where stronger than 5 nT were not considered for the calculation of the IMF orientation (*Connerney et al.* 2001).

Several studies have shown that approximating the IMF orientation in this way reproduces the well understood asymmetry in the escape of planetary ions (*Bößwetter et al.* 2004), which is modulated by the direction of the IMF (*Barabash et al.* 2007b). This suggests that the method gives valid results. MGS orbits Mars every two hours, meaning that dayside data exist for at least twelve times per day for the determination of the IMF direction. Using this input from MGS a new coordinate system can be defined, with its primary axis associated with the IMF orientation (see Section 3.1).

2.1.3 Plasma moments: calculation methods

As mentioned earlier, the conversion of IMA and ELS fluxes to plasma moments (or plasma fluid parameters) is essential for a better physical description of the global configuration of the Martian magnetosphere, for a more detailed analysis of the ASPERA-3 data, and for the estimation of the erosion rates of the Martian atmosphere.

A simple definition for plasma moments exists for a homogenous and time independent population of single particle species:

$$\mathbf{M}^k = \int f(\mathbf{v})(\mathbf{v})^k d^3\mathbf{v}. \tag{2.1}$$

Here $\mathbf{M}$ is a tensor of order k and $f(\mathbf{v})$ is the distribution function, dependent on the velocity, $\mathbf{v}$. According to the order of the tensor, several normalization values exist.

For $k=0$ we get the particle number density n, $k=1$ gives the velocity vector, normalized by n, while $k=2$ gives the pressure tensor. The measurable quantity for particle counters is the differential flux $J(E,\Omega,\mathbf{r})$ for particles of energy E, at a position r, within a solid angle $d\Omega$. If m is the particle mass, the relation between the distribution function and the differential flux is:

$$J(E, \Omega, r) = \frac{v^2}{m} f(\mathbf{r},\mathbf{v}) = \frac{2E}{m^2} f(\mathbf{r},\mathbf{v}) \tag{2.2}$$

Two main methods exist for estimating moments from the differential flux. One is integrating over a given range in the phase space, and the second by assuming a Boltzmann distribution for the phase space density. These methods are briefly described below. Both methods require first the data to be cleaned from the various noise sources that affect IMA and ELS. More details can be found in *Fränz et al.* (2007).

2.1.3.1 Integration method

In this method analytical expressions are used to integrate the measurable quantities in the phase space. The advantage of this method is that it can provide plasma moments for distributions that cannot be easily described by distributions (e.g. Boltzmann). The disadvantage is that this integration is limited only within the phase-space range that the

instrument covers. Low energy (<5 eV) distributions, which for example could contain a large fraction of electron fluxes in Mars's ionosphere, cannot be accessed by ELS or IMA and the respective moments cannot be estimated.

Using equations 2.1 and 2.2, the formulas for moment calculation can be derived. For the calculation of electron moments, a spherically symmetric distribution is assumed.

For k=0 in Equation 2.1, the expression for the number density is:

$$n = \int_{\mathbf{V}} f(\mathbf{v}) d^3\mathbf{v} = \int d\varphi \int d\vartheta \sin\vartheta \int dv v^2 f(v, \vartheta, \varphi) \qquad (2.3)$$

In the case of spherical symmetry:

$$n = 4\pi \int_{\mathbf{V}} f(\mathbf{v}) v^2 dv \qquad (2.4)$$

Using equation 2.2, and because $dE = mudu$:

$$n = \int d\varphi \int d\vartheta \sin\vartheta \int dv f(\mathbf{v}) v^2 \Rightarrow n = \int d\varphi \int d\vartheta \sin\vartheta \int dE \frac{J}{v} \qquad (2.5)$$

If $c(E, \varphi, \vartheta)$ are the detector counts, $G(E, \varphi, \vartheta)$ the geometric factor of the detector, τ the acquisition time and $\Delta E = E_{n+1} - E_n$ the energy width of the n-th electron channel, then:

$$J = \frac{c(E, \varphi, \vartheta)}{G(E, \varphi, \vartheta)\tau\Delta E} \qquad (2.6)$$

Substituting integrals with sums and for dE≡ ΔE:

$$n = \sum_{\varphi} \Delta\varphi \sum_{\vartheta} \Delta\vartheta \sin\vartheta \sum_{E} \frac{c(E, \varphi, \vartheta)}{G(E, \varphi, \vartheta)\tau v(E)}, \qquad (2.7)$$

where $v(E) = \sqrt{\frac{2E}{m}}$.

The general expression for the velocity ($k = 1$)is:

$$n\mathbf{v} = \int_{\mathbf{V}} \mathbf{v} f(\mathbf{v}) d^3\mathbf{v} \qquad (2.8)$$

or explicitly:

$$nv_x = \int d\varphi \cos\varphi \int d\vartheta \sin^2\vartheta \int dE J(E, \vartheta, \varphi) \qquad (2.9)$$

$$nv_y = \int d\varphi \sin\varphi \int d\vartheta \sin^2\vartheta \int dE J(E, \vartheta, \varphi)$$

$$nv_z = \int d\varphi \int d\vartheta \sin\vartheta \cos\vartheta \int dE J(E, \vartheta, \varphi)$$

For $k=2$ the expression for the pressure tensor is:

$$\mathbf{P} = m \int_{\mathbf{V}} (v_i - v_k)(v_i - v_k) d^3\mathbf{v} = m[\mathbf{M}^2 - nv_iv_k], \qquad (2.10)$$

where:

$$\mathbf{M}^2 = \int_\Omega \int_\mathbf{v} v_i v_k f(\mathbf{v}) d\Omega d\mathbf{v}, \tag{2.11}$$

and i,k: (0,1,2) or (x,y,z) respectively.

P is a symmetric tensor with 9 directional elements. However, due to spatial coverage limitations of the sensor, only the three diagonal terms are resolved in the ASPERA-3 coordinate system. Assuming that these are the most important:

$$P_{xx} = m \int d\varphi \cos^2 \varphi \int d\vartheta \sin^3 \vartheta \int dEvJ(v, \vartheta, \varphi) - mv_x^2 n \tag{2.12}$$

$$P_{yy} = m \int d\varphi \sin^2 \varphi \int d\vartheta \sin^3 \vartheta \int dEvJ(v, \vartheta, \varphi) - mv_y^2 n$$

$$P_{zz} = m \int d\varphi \int d\vartheta \sin \vartheta \cos^2 \vartheta \int dEvJ(v, \vartheta, \varphi) - mv_z^2 n$$

and

$$P = \frac{P_{xx} + P_{yy} + P_{zz}}{3}, \tag{2.13}$$

$$T = \frac{P}{2nK} \Rightarrow T[eV] = 3122 \frac{P[nPa]}{n[cm^{-3}]}, \tag{2.14}$$

where K is the Boltzmann constant and 1 nPa$=10^{-8}$dyn/cm^2.

2.1.3.2   Fitting method

With the fitting method plasma moments are estimated by assuming that the phase space density has a Maxwellian distribution in the velocity space. The characteristic parameters of the extracted distribution can then be converted to plasma moments. The location of the distribution's peak defines the bulk plasma velocity, the width is characteristic for the plasma temperature and the area is indicative of the plasma density.

The advantage of this method is that the calculated distributions can be extrapolated to ranges in phase-space that are not covered by the instrument's sensors. Furthermore, it can be used to distinguish the characteristics of different plasma populations (by using more than one maxwellian). A disadvantage is that it can give erroneous results for distributions that deviate from that of a maxwellian or for data samples with low signal to noise ratio.

The velocity space distribution can be expressed as

$$f(v) = C \cdot e^{-\frac{(v-\bar{v})^2}{v_t^2}}, \tag{2.15}$$

where $\bar{v}$ is the bulk velocity which may be determined by integration or by identifying the energy where the distribution peaks. The constant C is determined by Equation 2.4:

$$C = \frac{n}{(\sqrt{\pi}v_t)^3}. \tag{2.16}$$

Replacing the thermal velocity v_t by the thermal energy using $v_t = \sqrt{\frac{2E_t}{m}}$ allows to express the phase space density as
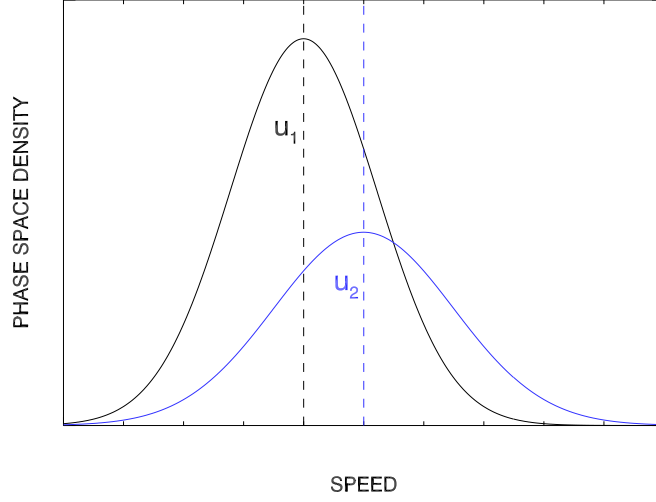
Figure 2.5: Illustration of two maxwellian distributions with different characteristics (in arbitrary units). Each distribution's area, width and peak location provide the plasma moments.

$$f(E) = n \cdot \left(\frac{m}{\pi 2 E_t}\right)^{3/2} \cdot e^{-\frac{E - 2\sqrt{E\bar{E}} + \bar{E}}{E_t}}, \tag{2.17}$$

where the mean energy is: $\bar{E} = \frac{\int_E E \cdot f(E)}{\int_E f(E)}$.

Expressing E in eV, n in 1/cm^3 and m in electron masses, m_e, the result is:

$$\bar{f}(E)[\text{s}^3/\text{km}^6] = 0.86 \cdot 10^6 n \cdot \left(\frac{m}{E_t}\right)^{3/2} \cdot e^{-\frac{E - 2\sqrt{E\bar{E}} + \bar{E}}{E_t}}. \tag{2.18}$$

On the other hand the phase space density for each energy channel can be expressed by the omni-directional differential flux $J(E)$ as:

$$f(E) = \frac{J(E)m^3}{p^2} = \frac{J(E)m^2}{2E}. \tag{2.19}$$

Using Equation 2.6, f(E) becomes

$$f(E) = \frac{m^2}{2G\tau} \frac{c(E)}{\Delta E \cdot E}. \tag{2.20}$$

Again expressing E in eV and m in electron masses m_e gives

$$\bar{f}(E)[\text{s}^3/\text{km}^6] = \frac{0.161 m^2}{G\tau} \frac{\bar{c}(E)}{\Delta E \cdot E}. \tag{2.21}$$

Demanding equality between Equations 2.18 and 2.21 allows to determine density n and thermal energy E_t by fitting to the measured spectrum of $f(E)$.

For a positive spacecraft potential, E_p, the energy for each step has to be replaced by $E - E_p$. Since spacecraft potentials are less than 20 eV, this correction is only important for electrons or low energy ion distributions (eg. in the ionosphere). In addition, for plasma bulk speeds below 400km/s, $\bar{E} < 1$eV for electrons such that $\bar{E} = 0$ can be used for fitting electron distributions.

2.2   Particles and fields instrumentation on Cassini

Cassini is part of the Cassini/Huygens mission which was launched in October 1997 and arrived at Saturn in July 2004. It is the fourth mission that visits the ringed planet after Pioneer 11 and the two Voyager probes, but just the first that enters in orbit around it. Cassini carries maybe the most advanced set of instruments ever flown on a planetary probe, including cameras and radio remote-sensing detectors for multi-wavelength observations, an advanced particles and fields package, a neutral mass spectrometer and a dust detector.

The orbit of Cassini is optimized for a series of scientific observations, both for the planet, its rings, moons and space environment. Regarding magnetospheric studies, the orbit covers most regions of Saturn's magnetosphere at both equatorial and high latitudes (Figure 2.6). Most of the data shown in the following chapter come from the first 22 orbits of Cassini (up to the end of 2005), but some cover also periods in 2006 and 2007.
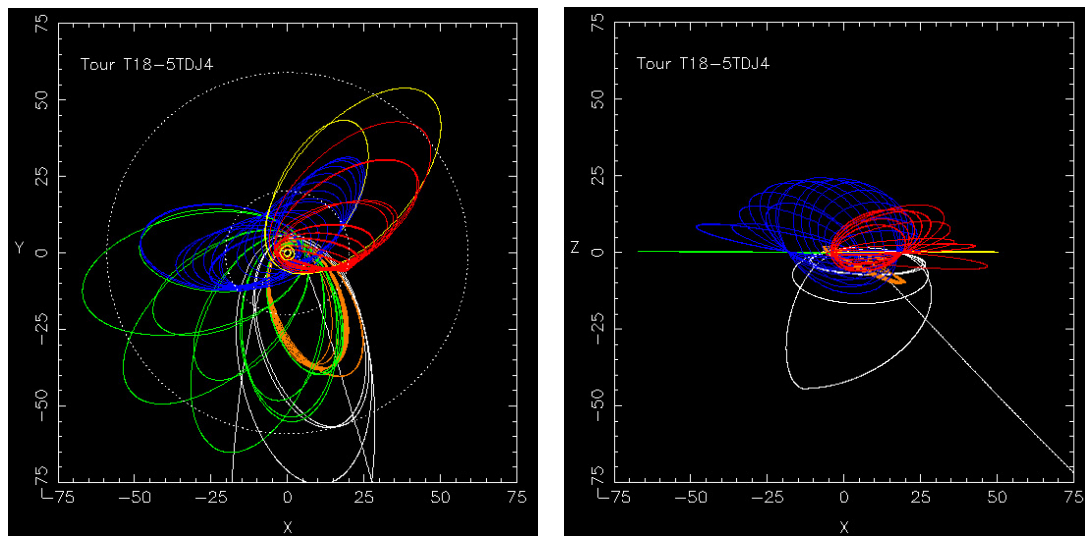
Figure 2.6: Cassini's orbital tour in two projection planes: on the equatorial plane viewed from the north of Saturn (left), and on a north-south plane (right), as viewed from an equatorial position. The Sun is towards the right, in both panels. The different parts of Cassini's orbital tour are indicated with different color, with the correct sequence being white (up to Feb. 2005), orange (up to Sept. 2005), green (up to July 2006), blue (up to July 2007), yellow (up to September 2007) and red (up to July 2008).

The research performed for the planet's magnetosphere and its interaction with the Saturnian moons is primarily based on energetic electron data from the MIMI/LEMMS

sensor of Cassini. MIMI stands for "Magnetospheric Imaging Instrument" and LEMMS for "Low Energy Magnetospheric Measurement System". LEMMS is one of the three sensors that comprise MIMI, the other being INCA (Ion and Neutral Camera) and CHEMS (Charge-Energy Mass Spectrometer). A detailed description of MIMI is given in *Krimigis et al.* (2004). As electron data were mainly used in this thesis, here I describe the capabilities of LEMMS as an electron sensor. In addition, few basic facts are outlined about several other Cassini experiments that their data has been used to complement energetic particle measurements by LEMMS.

2.2.1   The MIMI/LEMMS instrument

LEMMS is designed to make three dimensional energy spectroscopy of energetic electrons and ions in the energy range between ~10 keV and a few MeV. A picture of LEMMS is shown in Figure 2.7. As it can be seen, LEMMS consists of two telescopes, each one intended for "low-energy" particles (<1-2 MeV/nucleon) and one for higher energy particles. LEMMS is mounted on a turntable, the rotation of which establishes a full 2D coverage on a "disk". Combined with spacecraft rotations, LEMMS can measure 3D distributions. Few more details on the LEMMS instrument are given below.

Figure 2.7: A flight test model of the LEMMS sensor, with its main parts indicated.

2.2.1.1   Measurement principle and characteristics

Due to their very high energies most energetic particles cannot be deflected by electric or magnetic fields like those applied in electrostatic analyzers (e.g.. IMA and ELS of ASPERA-3). Under such fields the trajectories of energetic particles within the limited volume of a detector have negligible differences.

Therefore a different technique is used for their measurement, based primarily on the energy deposition of energetic particles in semiconductors. In principle, several thin solid-state detectors are arranged in line (telescope configuration). When charged particles impact one of these detectors, under the effect of Coulomb collisions they either deposit all their energy and are absorbed or they penetrate through the detector and are absorbed

by a subsequent one. Each impact on a detector is identified as an electronic pulse, the characteristics of which contain information on the particle's mass, atomic number and incident energy.

In the first case, an upper limit can be given for the energy of the particle, based on the thickness and the material of the detector. Particles that are absorbed in the first element of the detector are below a given energy threshold. This threshold depends on the thickness and the material of the detector, but can be also controlled manually (eg. to avoid saturation by many "low energy" particles). If particles cross the first detector, the energy deposition in that detector of thickness X_i ($\delta E \sim (dE/dx)X_i$), and the final absorption by a subsequent detector, provide the upper and lower limits of the particle's energy. These combinations are usually called "coincidences". Different coincidences can be used to distinguish not only the particle's energy, but also its mass or its nature (electron or ion). Various coincidences can also help to distinguish foreground from background.

This basic technique is used also by LEMMS, with several modifications. A cut-sectional view of LEMMS is shown in the left panel of Figure 2.8, where the different arrangement of detectors is shown for the low energy telescope (E1, F1, E2, F2, A and B) and the high energy telescope (D1, D2, D3a, D3b, D4). Coincidences of these detectors "form" the various channels of LEMMS (usually termed as "rate channels").
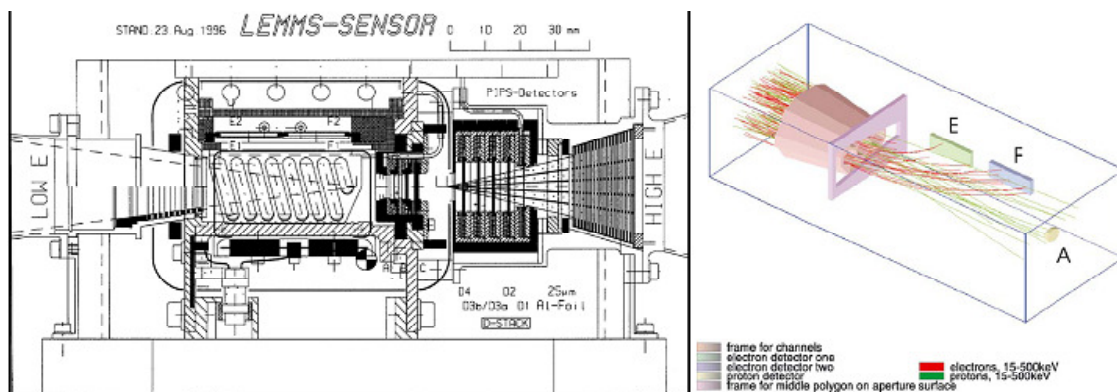
Figure 2.8: A cut-sectional view of LEMMS (left) and illustration of electron and ion separation and detection in the low-energy telescope.

In the right panel of Figure 2.8, the particle detection through the low energy telescope is also illustrated more clearly. Electrons in the range of 20-750 keV can still be deflected by permanent magnets placed in the entrance of the telescope. This deflection can be used as an additional "energy filter" for electrons. On the other hand, ions follow almost straight trajectories due to their large mass and impact the A-detector.

In this thesis mainly energetic electron data are used from LEMMS. The electron measurements of LEMMS that are analyzed cover the energy range between 20 keV and few MeV. 16 rate channels with coarse energy resolution are defined: C0-C7, that measure electrons between 18 and 750 keV, and the E0-E7 channels for electrons of 95 keV up to a few tens of MeV. The typical time resolution for the 16 rate channels is 5.375 s per data point although this can be varied during the mission. Three electron priority rate channels,

ELECTRON CHANNELS			
Channel	**Energies (keV)**	**Channel**	**Energies (MeV)**
C0	18-35.9	E0	0.095-1.8
C1	27.1-49.5	E1	0.237-2.5
C2	41-63.9	E2	0.21-3.51
C3	58.5-102.5	E3	0.665-~4
C4	94.1-204	E4	0.665-~3
C5	181.9-319.5	E5	>0.665
C6	300-496.3	E6	1.045-~11
C7	499-745.3	E7	~10.0-~100.0
ION CHANNELS	**Telescope**	**Energy range**	
A-channels	Low energy (A0-A8)	20 keV - 3 MeV	
P-channels	High energy (P2-P8)	2 MeV - 60 MeV	

Table 2.1: List of LEMMS electron channels and their energy ranges (passbands), considered for the thesis. Note that the values have been updated compared to the ones given in *Krimigis et al.* (2004). The E4 and E5 channels could possibly have a slightly higher threshold than 665 keV.

C1, C5 and E4, can also provide eight times higher time resolution.

A list of the characteristics of the 16 electron channels is given in Table 2.1. Several basic facts about the ion channels are also included in the same Table.

It is noted that although fairly accurate energy passbands exist for the E channels, there is still some uncertainty in the exact numbers, especially for the highest energy channels (E4-E7). For this reason, several results based on the E channel recordings are treated carefully, especially if it is possible that a change in the instrumental parameters can significantly affect the conclusions of the present work.

In order to achieve higher energy resolution, LEMMS uses a Pulse Height Analyzer (PHA) that can divide an electron spectrogram into 128 energy steps for energies between 20 keV and 2 MeV. The PHA channels have the typical time resolution of LEMMS. PHA analysis is also possible for ions, with 64 energy steps in this case. The technique is based on the fact that particles impinging on the solid state detectors produce pulses, the amplitudes of which are proportional to each particle's energy. Measuring the pulse height distribution on a given detector, a much higher resolution energy spectroscopy is achieved.

LEMMS also gives information on the particle's pitch angles, by taking into account the orientation of the magnetic field obtained by the magnetometer experiment (*Dougherty et al.* 2004a). The pitch angle is defined as the angle of the particle's velocity with respect to the magnetic field vector. As the sensor rotates on a platform with a period of 86 s, pitch angle coverage is achieved with an angular extent that depends on the spacecraft orientation. Therefore, when LEMMS rotates, the priority channels are actually of high angular resolution, rather than high time resolution. In this case, the time resolution for any one direction is 86 s.

When the sensor does not rotate (which is true for all orbits after 2nd of February, 2005), LEMMS is monitoring a very narrow pitch angle range with a high time resolution in that fixed direction. Pitch angle coverage is then achieved only during spacecraft attitude changes. This is a definite advantage for the detection and observation of the fine structure of satellite absorption signatures, which is the subject of study in Chapters 4 and 5.

LEMMS has two primary noise sources: the first is UV radiation, which primarily affects the lowest energy channels of the low energy telescope. Solar UV effects are easily identified as a sharp and unrealistic jump in the channel's count rates. Data from such intervals cannot be corrected and therefore were not considered for analysis. The high energy telescope is protected from UV radiation by a thin foil. This telescope cannot be used for keV particles, as the foil would have absorbed them.

The second source of noise are the MeV particles, which can penetrate the LEMMS structure and reach the detectors, giving a false signal. Penetrating radiation effects can be approximated, either by using a calibration shield on LEMMS, or by using data from close moon flybys, as discussed in Section 4.2.1.1.

2.2.2 Additional data sources

As with the analysis of ASPERA-3 data of Mars Express, several additional datasets have been considered in this thesis to complement the analysis of the Cassini/LEMMS data. In many cases, magnetic field data from the magnetometer of Cassini were used in order to calculate particle pitch angles (Chapters 4 and 5). Analysis of magnetic field data was also performed, in conjunction with theoretical modelling, in Chapter 6. The Cassini magnetometer from which data have been retrieved for the present study is a triaxial, fluxgate magnetometer, placed halfway along a 11 m long boom (*Dougherty et al.* 2004a).

For Chapter 5 images from Cassini's ISS camera (*Porco et al.* 2004) are also used to provide constraints to the LEMMS data analysis. The analysis of ISS camera images was not performed by me, but by researchers of the respective scientific group during collaborative studies.

2.3 Summary

In this chapter, the operating principles, the characteristics and the limitations of two different particle detectors have been outlined (Mars Express ASPERA-3 and Cassini MIMI/LEMMS). Results shown in the three following chapters are primarily based on data from these two instruments. Techniques to convert the ASPERA-3 IMA and ELS data to fluid parameters (plasma moments) have also been described and several secondary data sources important for scientific analysis have been also listed. In the following chapters the analysis techniques, each instrument's capabilities and the various problems or limitations of the two different datasets are discussed and illustrated through several scientific applications.

3 The interaction of Mars with the solar wind: Mars Express ASPERA-3 observations

The interaction of Mars with the solar wind has been under almost continuous research over the last two decades, through the particles and fields experiments of the Phobos-2, the Mars Global Surveyor (MGS) and the Mars Express (MEX) missions. While it is understood that the nature of the interaction is primarily determined by the presence of the planet's dayside ionosphere (*Nagy et al.* 2004, *Dubinin et al.* 2006a, *Brain* 2006a), it is difficult to establish the individual influence of all the different factors which control the configuration of the Martian induced magnetospheric cavity.

As briefly described in the Introduction (Chapter 1), complications come from the presence of the crustal fields (*Acuña et al.* 1998, *Connerney et al.* 2001), their rotation with the planet and their changing orientation with Martian season and with respect to the interplanetary magnetic field (IMF) direction. Their presence is known to be the source of localized asymmetries in the dayside magnetosphere, but the existence of global effects (*Verigin et al.* 2001) has not yet been verified.

The study of the global configuration is the primary subject of study in this chapter. As a first step, global moment maps are constructed to indicate the macroscopic structures of the interaction in terms of plasma fluid parameters and to provide a more statistically significant description of the overall configuration than the Phobos-2 and MGS missions did. The heavy ion escape fluxes are also calculated, as a direct application of this moment extraction.

Another aspect of the global configuration is then studied, using only a subset of the ASPERA-3/ELS data, in an attempt to distinguish possible asymmetries in the spatial distribution of non-ionospheric electron fluxes as function of the solar wind convective electric field orientation (E_{sw}) and of the crustal magnetic fields. The study of non-ionospheric (energetic) electrons can provide hints to the origin of the energetic electron high flux events that have been observed in the wake of Mars (*Lundin et al.* 2005, *Brain et al.* 2006b).

3.1 Coordinate systems

Before ASPERA-3 data are discussed, it is important to introduce the different coordinate systems where these data can be mapped to. Each coordinate system can be employed for different purposes. In this chapter, two coordinate systems are primarily used:

- **The Mars-Solar-Orbital coordinate system (MSO)**: This system has its primary axis oriented along the direction of the solar wind bulk velocity,**v**. More specifically, MSO has the positive X-axis pointing from the center of Mars to the Sun (opposite to **v**), the positive y-axis defines the direction opposite to the heliocentric orbital velocity of Mars, and the Z-axis (pointing towards the ecliptic north) completes the system.

- **The Mars-Solar-Electric coordinate system (MSE)**: This system has its z-axis oriented along the direction of the interplanetary electric field, **E** ($\sim$ **v** $\times$ **B**) (*Fedorov et al.* 2005). Here, **v** is the bulk velocity vector of the solar wind and **B** defines the IMF vector, estimated from the MGS magnetometer data. MSE has the positive X-axis pointing from Mars to Sun (opposite to **v**), the positive Z-axis defines the direction of **E**, and the Y-axis defines the transverse IMF component direction.
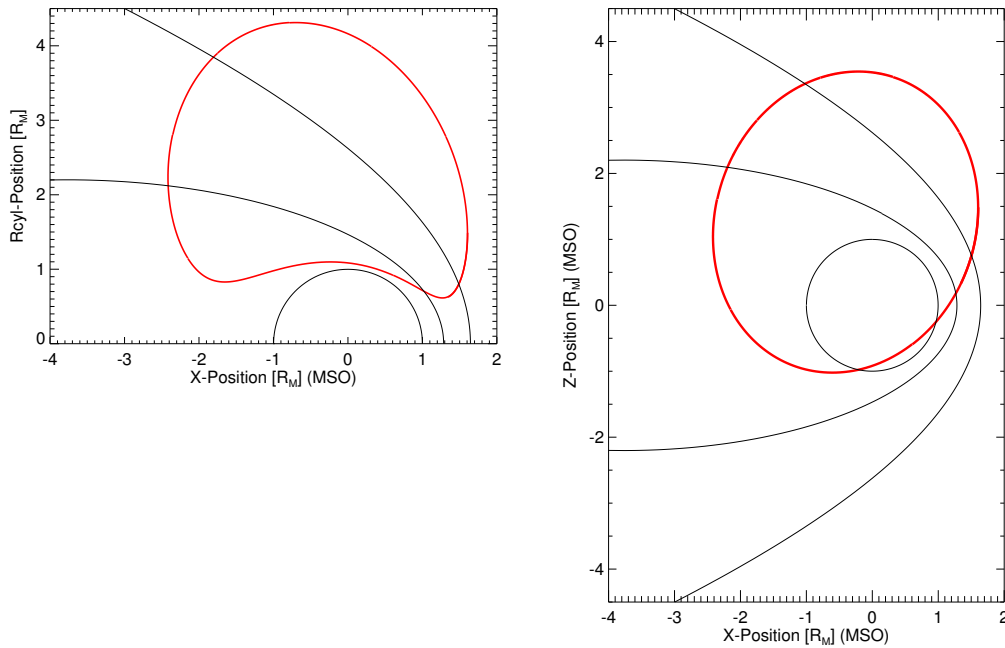
Figure 3.1: The same MEX orbit is shown in two different displays in order to illustrate the function of the R_{cyl} product. On the left panel, the x-axis corresponds to the X_{MSO}, and the y-axis to R_{cyl}. The right panel shows the same orbit, but with the y-axis this time being the Z_{MSO} direction. In both panels, the outer boundary is the bow shock and the inner boundary is the MPB, based on formulas for their average position and shape by *Vignes et al.* (2000).

A typical, common product for both coordinate systems is the cylindrical distance, defined as $R_{cyl} = \sqrt{Y_{MSO}^2 + Z_{MSO}^2} \equiv \sqrt{Y_{MSE}^2 + Z_{MSE}^2}$. This product is derived from the fact that the plasma distribution around the X-axis (of any of the two systems) is, to a first order, cylindrically symmetric. Plasma distribution maps are usually constructed in

an X-R_{cyl} plane. Although with such a display, equatorial and polar regions are mixed, statistics improve and macroscopic features of the interaction can be easily identified. Furthermore, as $R_{cyl} \geq 1$, the projected location of MEX does not "intersect" the Martian surface, which makes such plots easy to read and interpret (Figure 3.1).
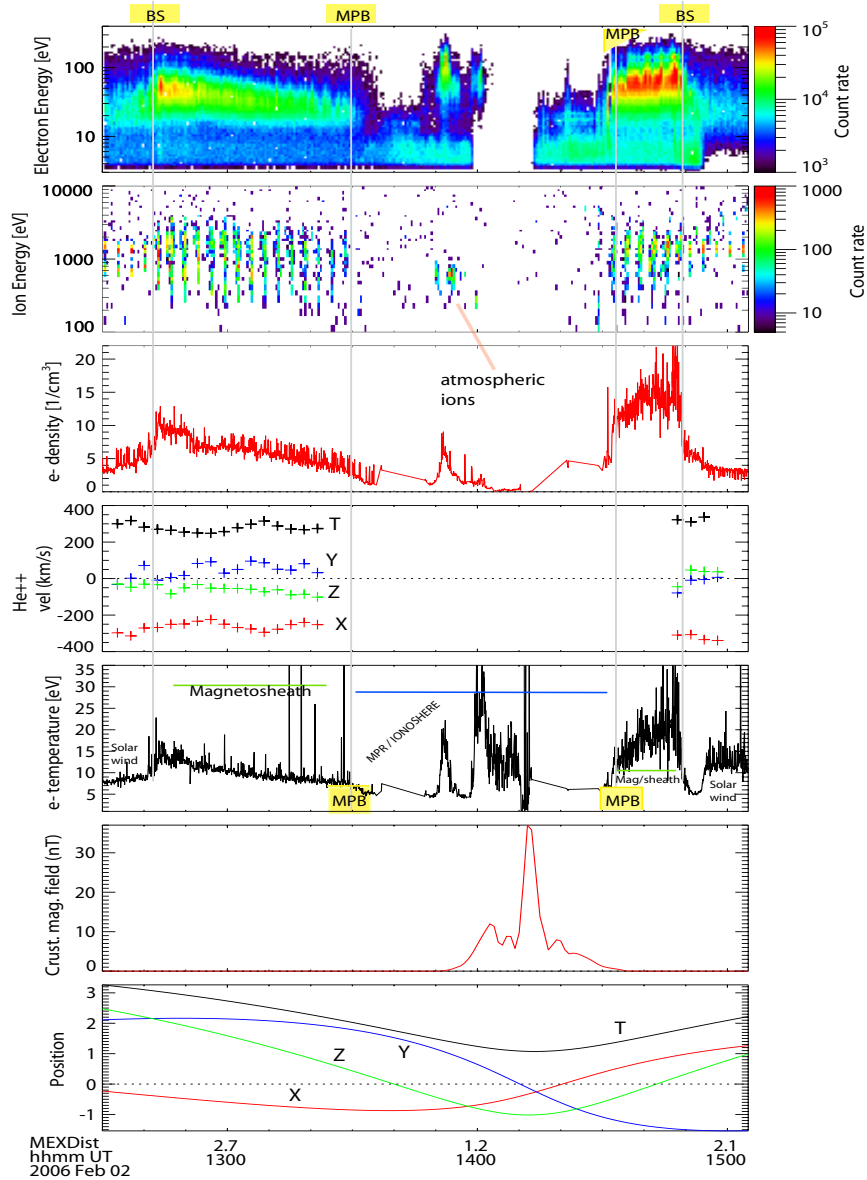
Figure 3.2: A typical ASPERA-3 dataset from an orbit in the 2nd of February, 2006. See text for detailed explanation. The following list of panels is shown (from top to bottom): ELS count rate energy spectrogram, IMA count rate energy spectrogram, fitted electron number density for non-ionospheric electrons, He^{++} bulk velocity components, non-ionospheric fitted electron temperature, modelled crustal magnetic field magnitude along the orbit of MEX, and MEX position components in the MSO coordinate system in units of R_M. The locations of the bow shock (BS), the MPB, the solar wind, the magnetosheath, the MPR/ionosphere and the detection of planetary ions are indicated.

43

3.2   ASPERA-3 data

As of March 2007, Mars Express has completed more than 3800 orbits around Mars and has achieved a very good coverage of most of the interaction regions of the planet with the solar wind. With such a large number of orbits, there is a huge variety of ASPERA-3 recordings. A representative dataset is shown in Figure 3.2.

The top two panels show an electron and an ion energy spectrogram retrieved along the trajectory of MEX. The altitude and the x,y,z positions of MEX in the MSO system are given in R_M in the bottom panel.

Starting from the electron spectrogram a sharp increase is observed in the electrons of 30-100 eV, at around 12:45. This is when Mars Express crosses the bow shock and enters the magnetosheath. The electron distribution becomes broader, indicating an increase in electron temperature.

Count rates then gradually drop and the distribution becomes narrower. At 13:35 there is a change in the electron spectrum, with magnetosheath electrons disappearing. This boundary is know to approximately coincide with the Magnetic Pile-up Boundary (MPB) (*Nagy et al.* 2004), although the exact association of the "magnetic" and the "particle" MPB is not yet clear. The region below the MPB is termed "Magnetic Pile-up Region (MPR)" or "ionosphere" (*Nagy et al.* 2004) (see also Section 1.1).

Within the MPR noticeable structures are commonly identified, such as intense increases in the fluxes of >30 eV electrons (e.g. between 13:50 and 14:05) or electron voids (e.g. between 14:05 and 14:15). While electron voids show a spatial correlation with crustal fields (*Soobiah et al.* 2005), the origin of the electron enhancements is not completely clear. This is investigated in Section 3.4. For reference, simulated crustal magnetic field strength is shown in the second panel from the bottom.

Between 14:20 and 14:30 two enhancements with narrow energy width appear at energies between 20 and 30 eV. These are the CO_2 ionospheric photoelectrons that can be identified thanks to the high energy resolution of ELS. The outermost boundary of these photoelectrons is sometimes termed as the photoelectron boundary (PEB). The PEB sometimes coincides with the MPB, although this is not always the case. Excluding the cases where there is a coincidence with the MPB, no other large scale change is identified in the particle populations when the PEB is crossed, suggesting that these photoelectrons most likely mix with the MPR plasma (*Frahm et al.* 2006), rather than separating different magnetospheric regions.

As MEX then moves on its orbit, it crosses again the MPB (14:33), the magnetosheath and the bow shock (14:50). These regions are easily identified in the electron spectrogram at, or between the given times.

Between 3 and 10 eV an almost isotropic population is identified, that reacts in most cases weakly to changes of the plasma environment. These are the spacecraft photoelectrons which, at high energies, still access the sensor. The effects of the deflection voltage are evident by the fact than no electrons are measured below about 3 eV.

The second panel shows IMA recordings. The periodic modulation of the signal is due to the electrostatic elevation scanning. As solar wind and magnetosheath ions are highly directional populations, they are only visible in certain elevation ranges. Electrons, due to their high thermal velocity, are more isotropic.

Most of the interaction boundaries and regions are also seen in this plot. Solar wind

electrons seem to reach to lower altitudes, although this could be an artifact of the different time resolution of IMA and ELS and the differences in the angular scanning methods of the two sensors. In the solar wind and the magnetosheath, are H^+ or He^{++} ions measured. Within the MPR, ions of atmospheric origin, mainly O^+ or O_2^+, are measured (e.g. the "blob" of 500 eV at 14:53 -see also Figure 3.3). IMA therefore observes the "expected" change in ion composition at the MPB (*Bößwetter et al.* 2004). Due to a low energy cut-off of IMA, for the data analyzed in this thesis, no ions below 100 eV could be resolved, as the technical problem causing this cut-off was corrected on May 2007.

The third panel shows electron densities derived from ELS. The numbers are realistic for the solar wind. The "density jump" across the bow shock and a gradual density decrease in the magnetosheath are clearly visible. Photoelectrons have been excluded from the calculation here, otherwise calculated densities would reach values an order of magnitude higher.

Proton densities (not shown) are much lower, mainly because IMA in certain configurations cannot resolve low energy protons, where the bulk of protons are present. The low energy protons appear usually as contamination of the high mass channels of IMA, in the solar wind and the magnetosheath (see indication of "reflected protons" in Figure 3.3). If this contamination is taken as a foreground signal, then ELS and IMA densities become comparable in the solar wind and the magnetosheath. Still, ELS measurements are a better and more reliable source for the plasma number density. Under the assumption of charge quasi-neutrality they can also provide a proxy for the ion number density in all interaction regions.

In the fourth panel, He^{++} velocity components and the total velocity are plotted. Velocities are close to the expected value of 300-400 km s^{-1} for the quiet solar wind. The velocity drop behind the bow shock is also seen, however, an increase is also visible in the inbound part of the trajectory (13:00-13:20) revealing that processes in the magnetosheath can be quite complex. Most of the velocity is "contained" in the x-component (along the Mars-Sun line), as expected. Non-zero v_y and v_z components indicate deflection of the flow within the magnetosheath. Below the MPB He^{++} velocities are not calculated, as solar wind ions are not present in this region.

Protons can also be used to estimate velocities, but these are usually biased towards high values (>400 km s^{-1}) as low energy protons cannot always be resolved. Electron velocities cannot be estimated, since ELS cannot measure electrons below 1 eV, the energy range where the electron kinetic energy lies.

The fifth panel includes the estimates of the electron temperature retrieved from the standard plasma moment code. Electron temperature series show solar wind electrons with typical temperature of about 10 eV. There is a clear signature of the heating behind the bow shock, both inbound and outbound, as well as a gradual temperature decrease from the bow shock towards the MPB. Within the MPR temperatures are not calculated in locations where spacecraft photoelectrons are mainly detected. During the high energy, electron flux enhancements, the temperature peaks at magnetosheath levels, while within the electron voids the temperature drops below 1 eV.

Proton temperatures (not shown) are about a factor of 2 higher than electron temperatures, contrary to expectations, as it is known that the electron temperature is higher in the solar wind. This could be a result of high background levels, as it can easily be realized from the noisy IMA spectrogram (second panel from the top). Automatic algorithms
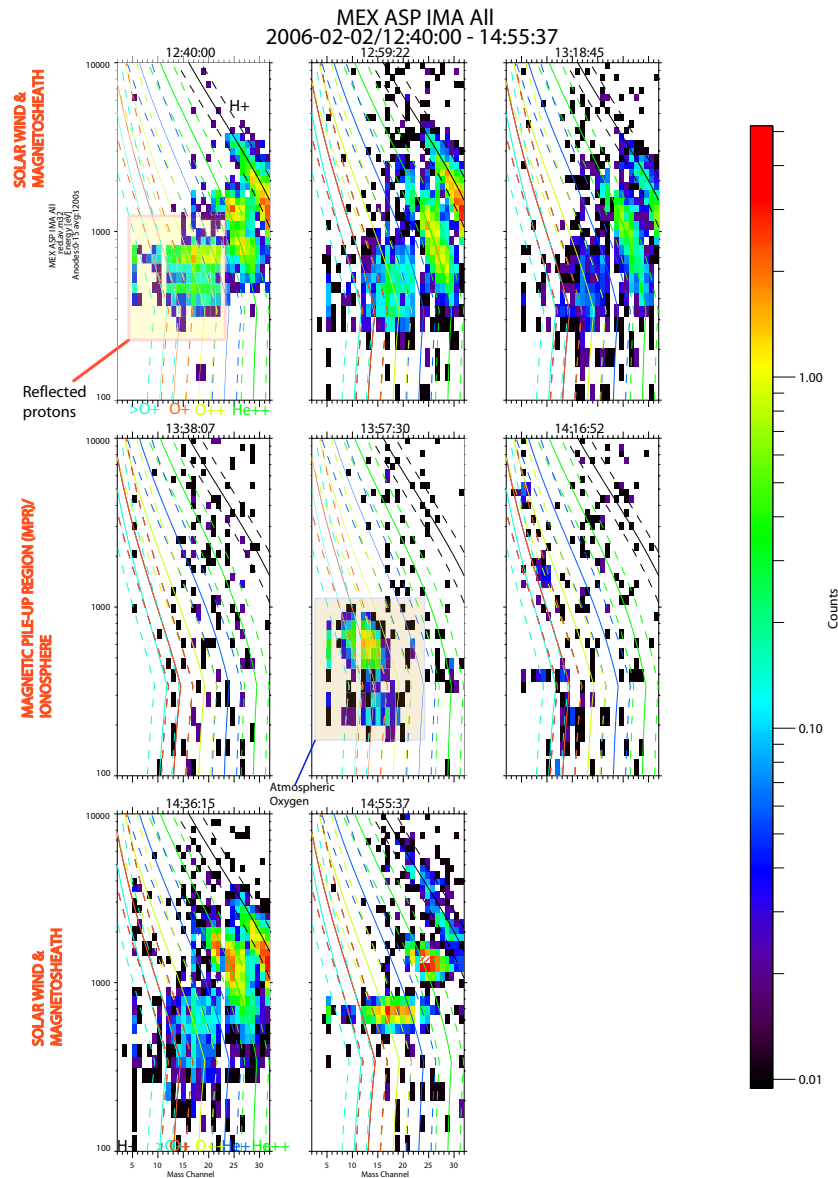
Figure 3.3: M/q vs E/q matrices from the IMA sensor for the orbit shown in Figure 3.2. Each matrix has been constructed by averaging IMA data for 1200 sec. Figure 3.2 should be used as a reference in order to identify from which location each matrix has been constructed. For each row, the region from which each matrix was constructed is indicated. Several characteristic features of the matrices are marked with yellow boxes. Notice the appearance of oxygen ions in the middle panels, when MEX is at low altitudes. Notice also how the proton trace line at low energies is beyond the "right boundary" of each matrix, indicating that low energy protons cannot be resolved with the IMA set-up for this specific MEX orbit.

cannot easily clean the noise sources of IMA.

This overview of the ASPERA-3 time series has shown several typical features measured during a single orbit of MEX. Several instrumental problems and limitations have

also been outlined. Overall, electrons can be used as tracers of plasma density and ions as tracers of plasma velocity. Temperature estimations are currently only reliable for electrons.

3.3   Moment maps and heavy ion escape

In this section plasma moments are organized in maps and the main interaction regions are identified. An estimation of the atmospheric erosion rates is also done. All moment maps shown are calculated from data acquired between February 2004 and March 2007. Electron and ion moments are calculated in the respective time resolution of ELS and IMA, respectively. Moment maps are shown for the plasma density, velocity and temperature. Respective maps for the thermal or the kinetic pressure can be constructed by combining the aforementioned parameters, accordingly. All maps are constructed by first dividing the data sampling region in bins of different size. Three methods are then used to display the sampling results in each bin.

In the first method, which is frequently used here, the value in each bin is defined by using the median average value of the data samples. The median average divides the distribution such that the same number of samples is equal above and below it. The method is useful to exclude single events with extreme values, with respect to the most frequent one, or to estimate a more frequently observed value for parameters that vary logarithmically.

In the second method, each bin's value is estimated by calculating the mean of the data samples (by dividing the summed value of the measured quantity by the number of samples). This method amplifies the effect of single event and can be misleading for parameters that vary logarithmically (in the latter case a logarithmic mean can be used). On the other hand, for several structures that are identified as short-lived and spatially constrained events (eg. "blobs" of escaping atmospheric ions), this method gives a better estimation of the average value per bin.

Finally, to explore extreme configurations, each bin can be assigned to the maximum or minimum measured value. However, as the maximum and the minimum can depend on the number of data samples, an alternative way to study extreme configurations is to assign a value indicative of the percentage of samples above (or below) a pre-defined, extreme data value.

3.3.1   Electrons

As discussed earlier, electrons are suitable for estimating the electron and ion number density, under the assumption of charge neutrality. The main issue for this calculation is how the signal at low energies should be treated. In the energy range between 1-5 eV, the signal can be dominated by spacecraft photoelectrons. Furthermore, spacecraft charging can shift ELS's energy levels even up to 10 eV. Under these conditions, the best method for calculating electron number density is the fitting method (Section 2.1.3). By integrating very low energies (<5 eV) can be excluded from the calculation. Still, spacecraft photoelectrons can be present in a relatively broad energy range which tends to lead to an overestimation of the number density. This is shown in Figure 3.4, where two

electron number density maps are shown, each one constructed with a different calculation method.
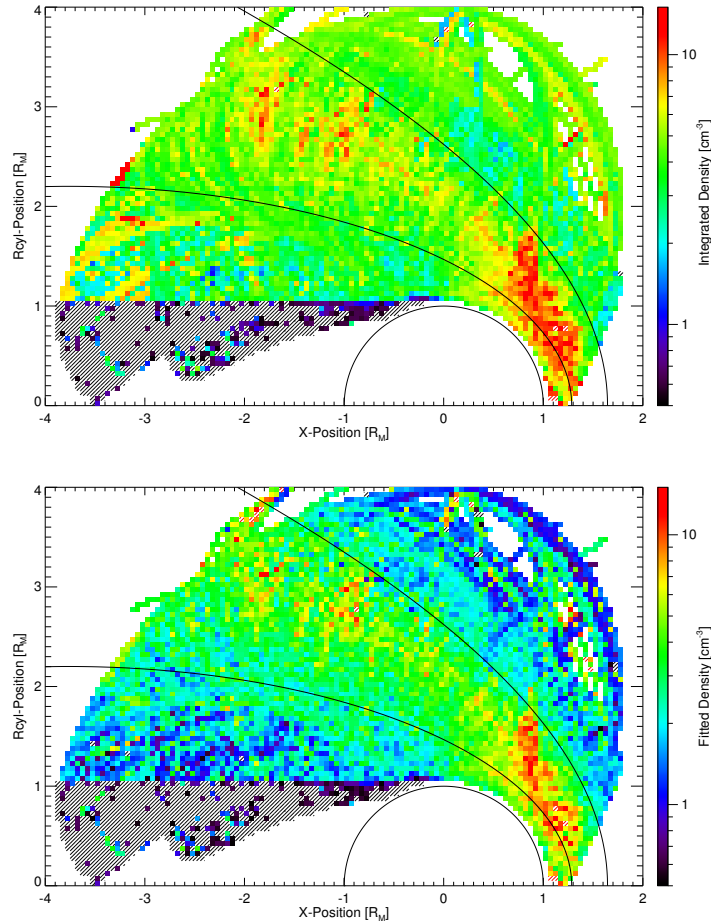
Figure 3.4: Median averaged electron number density maps calculated with the integration method (top) and with the fitting method (bottom). Both maps show number densities of non-ionospheric electrons. The fitting method gives more realistic results. Binsize is 0.05 R_M for both maps. In all color maps red-shaded bins correspond a value equal or higher than the maximum value in the color bar (and the opposite for grey shaded bins).

In the top panel (map of electron densities derived from integration) the transition region from the solar wind to the magnetosheath is only clear in the subsolar region, where a density increase of a factor of 1.5 is seen. Solar wind densities (4-5 cm^{-3}) are slightly higher compared to what one would expect for the average case. Furthermore, the spatial distribution of number density appears almost isotropic between the magnetosheath and the MPR, which is not realistic.

In the bottom panel (map of electron densities from fitting), solar wind number densities values are lower (1-3 cm^{-3}) and closer to what is expected. Both the solar wind, and the magnetosheath are clearly identified. Electron number densities drop below the MPB but a background value is present. This indicates that part of the solar wind electrons can access the MPR or that the MPB location is fluctuating and the averaging results in the

appearance of this "transition region". In the geometrical shadow of Mars, median electron densities drop to zero, as expected, although several bins with non-zero values can be identified. What is also interesting is that in the subsolar region, magnetosheath electrons are frequently present at altitudes 200-300 km lower than the *Vignes et al.* (2000) MPB location indicates. In the same region, the density enhancement is also shifted inwards compared to the *Vignes et al.* (2000) bow-shock position. At highest solar zenith angles, the *Vignes et al.* (2000) bow shock and MPB describe well the boundaries within which the magnetosheath is contained.

The fitting method provides better results as energies where photoelectrons can be present are excluded. The maxwellian fitted to the non-ionospheric electron distribution can be extrapolated to the "excluded" energy range and thus gives a more reliable estimate of the contributions to the total density. Furthermore, the location of the CO_2 photoelectron peaks with respect to the expected energy of 21-27 eV, can also give an estimate of the spacecraft potential, U_{sc}. A correction to the density calculation can be done by shifting the maxwellian distribution in energy, by an amount equal to U_{sc}.

While Figure 3.4 shows the average configuration (in terms of density) of the Martian induced magnetosphere, the picture looks quite different under extreme conditions. This can be realized if for each bin in the map, a value is assigned equal to the maximum density measured by ELS at the respective location during the 3-year interval . The result is shown in Figure 3.5.
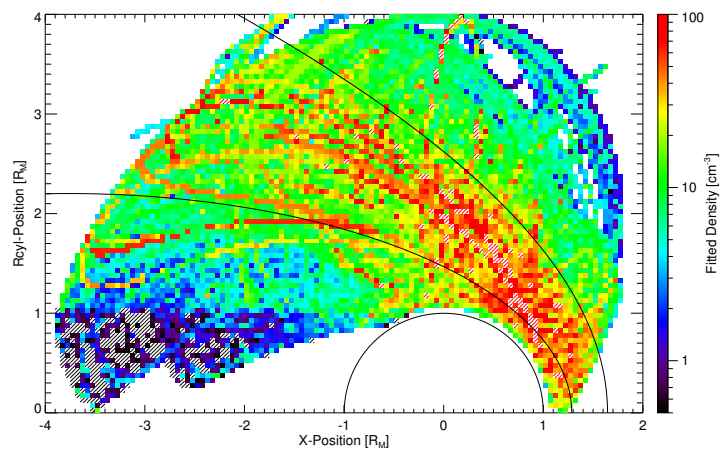
Figure 3.5: Maximum electron number density map calculated with the fitting method (bottom). The map shows number densities of non-ionospheric electrons under extreme conditions. Binsize is 0.05 R_M.

The density enhancement in the magnetosheath is shifted inward by about 300-500 km at all zenith angles, with respect to the *Vignes et al.* (2000) bow shock. Densities in the magnetosheath can even reach 100 cm^{-3}. Electrons penetrate the MPB at almost all zenith angles and electron densities of about 10 cm^{-3} can be found at low altitudes, and even within the geometrical wake of Mars. The mechanism under which high energy electrons can penetrate to low altitudes and intrude towards the tail is investigated in Section 3.5. What is also important is that high densities of non-ionospheric electrons at

low altitudes could enhance electron impact ionization, and even further the atmospheric erosion.

Creating the same map for the electron temperature (calculated with the fitting method), several additional structures can be identified. Figure 3.6 shows that on average, temperatures in the solar wind are about 10-15 eV, as expected. Electron heating occurs mainly in the subsolar region, where temperatures in the magnetosheath can reach values between 30-50 eV. The strong heating region shows a very good correlation with the electron density enhancement (Figure 3.4). At higher solar zenith angles, electron heating is not so pronounced, with temperatures rarely exceeding 25 eV.
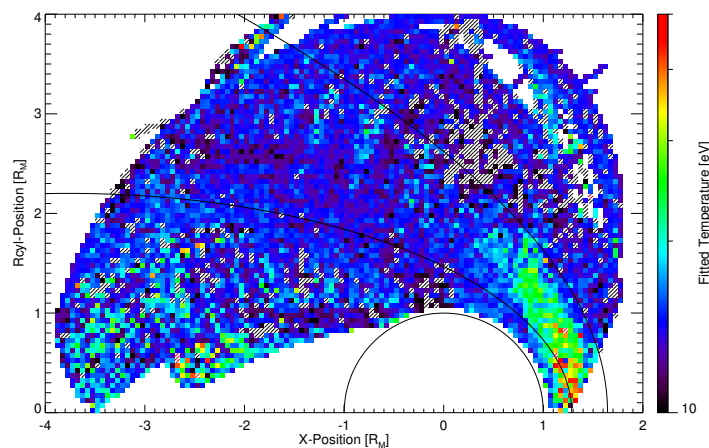
Figure 3.6: Median averaged electron temperature map, calculated with the fitting method. The map shows estimations only for non-ionospheric electrons. Binsize is 0.05 R_M.

The MPB is only visible for low solar zenith angles, while the temperature distribution seems to be almost isotropic for the rest of the induced magnetosphere. Several interesting features are identified within the boundaries of the martian shadow. These are electron populations with temperatures around 30 eV. Several bins show temperatures that exceed 50 eV (on average). Plotting the maximum of the temperature distribution per bin, several single events with temperatures up to 200 eV can also be identified. Such events are actually correlated to the high energy flux enhancements like the one illustrated in Figure 3.2 (top panel, between 13:50 and 14:05). They correspond to the map of the induced magnetosphere under extreme conditions (Figure 3.5).

Electrons of such energies only exist in the Martian magnetosheath. Lower energy electrons would need to be accelerated to reach these energy levels. Such acceleration mechanisms could be related to the presence of crustal fields. This is further investigated in Section 3.5.

3.3.2 Ions

As explained in Section 3.2, IMA cannot effectively measure low-energy protons. This results in very low number densities estimated in the solar wind and the magnetosheath.

Still, the effects of the low energy proton population tend to appear as instrument background in high mass channels of IMA. By considering this signal, a number density map combining protons and He^{++} can be constructed.
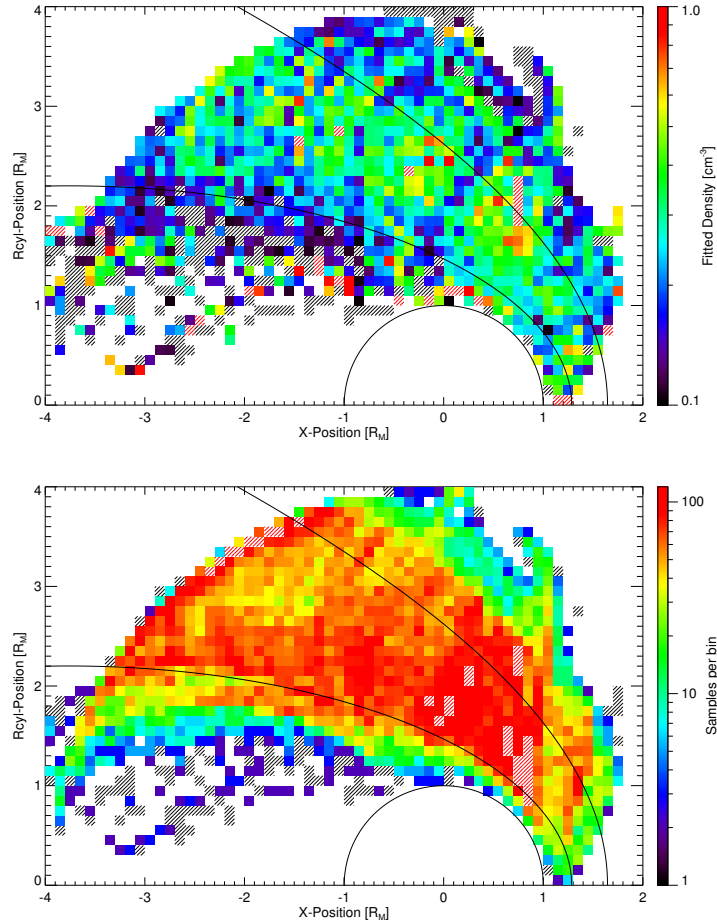
Figure 3.7: Median averaged solar wind ion density map, combining protons and He^{++}. The bottom panel shows the number of samples per bin. The number of samples below the MPB is very small. Given that samples are only selected if the estimated number density for protons is greater than $0.01 \mathrm{cm}^{-3}$, this indicates that solar wind ions access this region rarely. Binsize is $0.1\ R_M$ in both panels.

As solar wind and magnetosheath ions are highly directional distributions (unlike electrons), density estimations are performed only when the ion flow is within $45°$ of IMA's field of view, otherwise the density can be underestimated even more. As for the density estimation the proton "background" signal from the high mass channels of IMA is considered, a criterion is set in order to avoid mixing heavy ions with the solar wind. More specifically, when proton densities (without the background signal taken into account) are below the threshold value of $0.01 \mathrm{cm}^{-3}$, it is assumed that IMA is not measuring solar wind and the density estimation is not performed. The resulting solar wind density map is shown in Figure 3.7.

Extracted number density values are usually lower than $1\ \mathrm{cm}^{-3}$, meaning that even

when the low energy proton signal is considered, IMA density in the solar wind is not retrieved correctly. Still, the transition from the bow shock to the magnetosheath is qualitatively clearly identified. The depletion of solar wind ions below the MPB is also well displayed. What is interesting is that this boundary seems to be gradual and not sharp, but this can be the effect of the MPB fluctuation, as explained earlier.
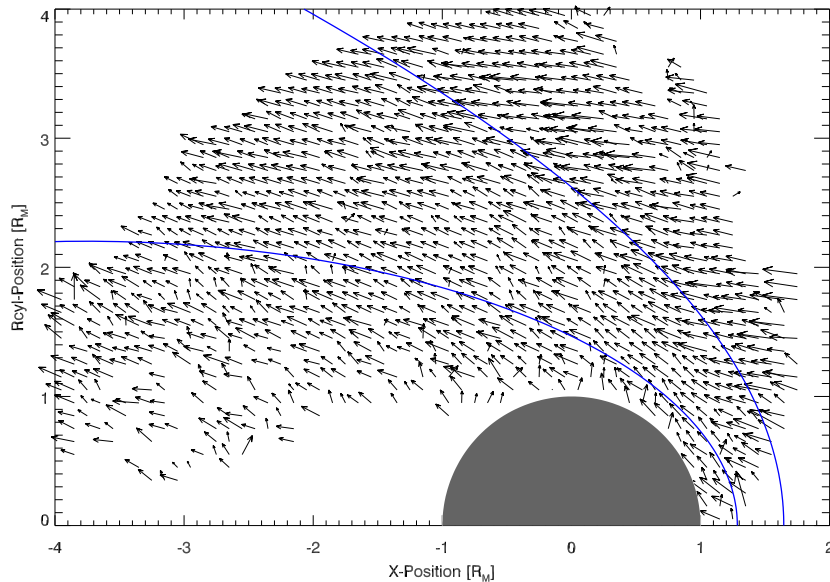
Figure 3.8: Vector velocity map of He^{++} ions. As it has been discussed for the Figure 3.7, velocity samples below the MPB correspond to statistically uncommon or extreme cases. Binsize is 0.1 R_M.

These non-zero solar wind ion densities can be found below the MPB should be carefully interpreted. As a 0.01 cm^{-3} proton number density threshold was set for the overall density calculation, bins in this region show only the average of few extreme cases where solar wind was present deep below the MPR. The second panel of Figure 3.7 shows the samples per bin for the map in the top panel. As it is seen, for most of the cases within the MPR, solar wind was detected for only few cases (1-10 times, depending on the bin), compared to the frequent sampling within the magnetosheath. Taking into account the global coverage achieved with IMA, the detection of solar wind much below the MPB occurs in less than 10% of the total sampling time.

IMA is the appropriate instrument for constructing plasma velocity maps, since the mean kinetic energy of solar wind ions is around 1 keV, well within the energy range of IMA. As explained in Section 3.2, He^{++} ions are better tracers of the velocity than protons, since their full energy distribution can be monitored. A vector velocity map is shown in Figure 3.8.

The vector direction illustrates well the behaviour of plasma in the solar wind and the magnetosheath. Plasma velocity in the solar wind is almost parallel to the x-axis, as expected for a radially expanding plasma population from the Sun. Within the magnetosheath, the solar wind is deflected in trajectories almost parallel to the shape of the

MPB. Plasma velocities are about 350 km s^{-1} in the solar wind and 250-300 km s^{-1} in the magnetosheath.

Nagy et al. (2004) gives that for the magnetic field the average dayside value in the magnetosheath is 20.7±14.0 nT, with the highest values (30-35 nT) corresponding to the subsolar region. Using this range of values and the estimated plasma moments it is actually found that in the subsolar region the flow behind the bow shock has a Magnetosonic Mach number (M_{MS}) with values between 0.9 and 1.0.

3.3.3   Heavy ion escape

A direct application of the moment calculation is also the estimation of the erosion rates of the martian atmosphere. The magnetized solar wind flow can access altitudes where substantial densities of atmospheric ions are present. The electric field of the solar wind can accelerate them to energies greater than the gravitational bounding energy of Mars (∼2-3 eV), and these ions can then escape from the planet. As this acceleration process involves the convective electric field from the solar wind (E_{SW}), escaping ions are expected to be seen in the direction where this electric field is pointing to (E^+ hemisphere). This asymmetry is visible when organizing heavy ion fluxes in the MSE coordinate system (Section 3.1). Fluxes can be calculated by multiplying heavy ion number densities with their respective velocities. A plot of the total heavy ion flux, organized in the yz-plane of the MSE system, is shown in Figure 3.9. The asymmetry with respect to the direction of the E_{SW} (positive z-axis) is clear.
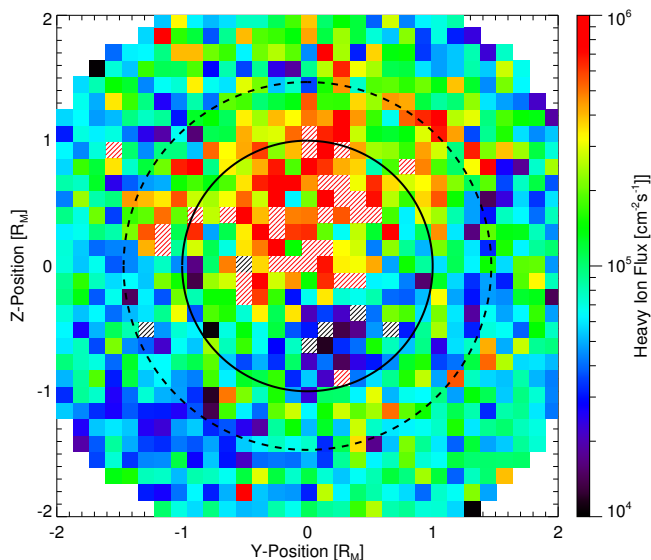
Figure 3.9: Mean heavy ion flux in the yz-plane of the MSE coordinate system. Bins are integrated along the x-direction, between x=-4 R_M and x=-1 R_M, the dashed line shows the MPB location at the terminator (*Vignes et al.* 2000). The E_{SW} is oriented along the positive z-axis. The binsize is 0.12 R_M.

Several additional processes have also been suggested as important sources of plan-

etary ion escape, such us the Kelvin-Helmholtz instability (*Bößwetter et al.* 2004). Escaping heavy ions practically remove mass from the atmosphere. Over geological time scales, the atmospheric mass loss can be so large that surface conditions (e.g. atmospheric surface pressure) can change significantly. Such a process could explain why water is absent from the surface of Mars, despite many indications of it being present 4.5 billion years ago.

In order to estimate the total escape rate, independently of the mechanism that leads to this escape, mean heavy ion fluxes can be determined within a circular cross-section that is perpendicular to the X-axis and limited by the MPB location. To take into account possible variability of the MPB location with respect to that given by (*Vignes et al.* 2000), a dropout in proton density below a threshold value of 0.01 cm^{-3} is used, as before, to identify it.

To calculate the total flow the result is then multiplied with the cross-section's area. This should normally give a constant escape rate along the x-axis, as there is no mechanism that adds or removes energy from these ions, along their escape trajectories. The result is shown in Figure 3.10.
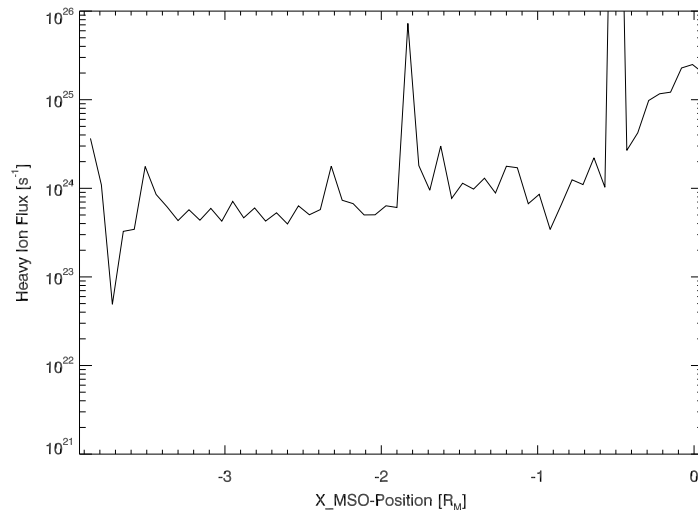
Figure 3.10: Total escape rate as a function of X-distance.

The plot shows the expected constant escape rate along the x-axis. This rate is estimated to be between $5\text{-}10\times10^{23}\text{s}^{-1}$, a result very close to that of *Barabash et al.* (2007b), the slight difference in the number resulting probably because here a larger cross-section is estimated here than the $2R_M \times 2R_M$ used by *Barabash et al.* (2007b).Several spikes in the plot signify extreme single events (probably instrumental problems) that dominate in the averaging process.

For x>-1 R_M, escape fluxes are most likely unrealistic. At this region IMA shows signs of saturation and intense contamination of its high mass channels (*Fränz et al.* (2007) assume that this is due to UV light). For this reason, this region has not been considered when constructing the plot of Figure 3.9.

On the other hand, there is a possibility that the observed increase of the total escape

54

rate found for x>-1 R_M is real. Several authors suggest that significant fluxes escape along a region called "plasma mantle", which is practically the location just above the MPB, where solar wind and atmospheric ions are significantly mixed (*Dubinin et al.* 1996, *Szego et al.* 1992). If high fluxes seen at the terminator escape along the mantle region, they cannot be identified through the present analysis for x<-1 R_M, as only data samples with depleted solar wind ions have been selected. Analysis of samples from the mantle is difficult, as low energy protons contaminate the high mass channels of IMA (see Figure 3.3) and the extraction of the heavy ion signal is very difficult.

The estimated escape rate is rather low and does not support the possibility that atmospheric erosion was the primary channel under which Mars lost its atmospheric mass, based on calculations by *Barabash et al.* (2007b). This calculation takes into consideration that this escape rate changes as a function of the total atmospheric content and solar wind conditions at Mars during the whole planet's geologic history (eg. *Wood* (2006)). The orbital evolution of Mars could further complicate the process (*Patharea and Paigeb* 2005).

It should also be noted that this number reveals only the escape rate for ions above 100 eV, as due to some technical problems IMA was not capable of monitoring lower energies. If when atmospheric ions are observed, ion densities are assumed to be equal with the electron densities, under the assumption of charge neutrality, then densities are found to be higher by about two orders of magnitude, meaning that significant part of the ion distribution is not detected. As this problem has been solved as of May 2007, the new data gathered by IMA could be used to evaluate the total escape rate, including the contribution by the low energy ions. A brief inspection of the new dataset revealed many low energy, atmospheric ion events (see Figure 3.11 for example).

As these ions have atmospheric origin, most of their energy is kinetic rather than thermal. Assuming a mean kinetic energy of about 10 eV and a mean mass of 12 amu (average between O^+ and O_2^+), a corresponding velocity of about 5-10 km s^{-1} is found. This is about half to one order of magnitude less than the typical velocity of the escaping ions above 100 eV. Assuming that these low energy ion populations have a density equal to that of electrons, the total flux for a low energy escaping population can be more than one order of magnitude higher than what is found for ions above 100 eV. Of course, more definite results will only be gained from a more direct analysis of the low energy ion data that ASPERA-3 can detect after May 2007.

3.4   Martian crustal magnetic field effects

Since the discovery of the Martian crustal magnetization (*Acuña et al.* 1998, *Connerney et al.* 2001) there have been numerous studies to investigate the effects of the crustal fields on the plasma environment of Mars. Using magnetometer observations only it could be qualitatively shown that the crustal fields move the MPB outward on the dayside (*Crider et al.* 2002). Most studies provided results on how crustal fields affect the overall magnetic topology at Mars, however the effects on the solar wind particle distributions have not been thoroughly investigated. If particle distributions "follow" the magnetic field, then a physical expectation is that the "particle MPB" will also be pushed outward by strong crustal sources. Still, crustal fields could focus electron precipitation in local
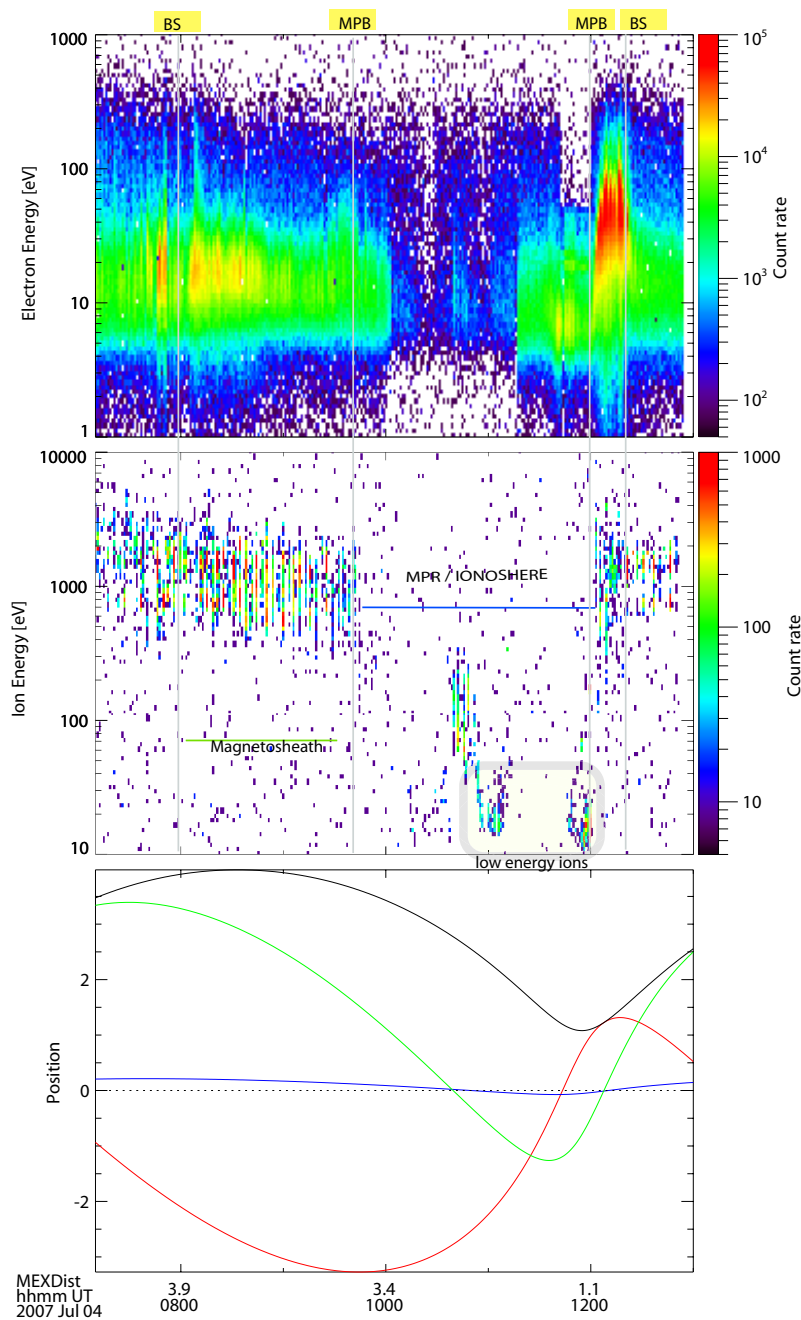
Figure 3.11: A typical ASPERA-3 dataset from an orbit in the 4th of July, 2007. The following list of panels is shown (from top to bottom): ELS count rate energy spectrogram, IMA count rate energy spectrogram and MEX position components in the MSO coordinate system in units of R_M. The locations of the bow shock (BS), the MPB, the solar wind, the magnetosheath, the MPR/ionosphere and the detection of planetary ions are indicated. Notice the detection of ion at energies lower than 100 eV, made possible only after May 2007.

cusps (*Brain et al.* 2006b). This can lead to auroral effects as they have been observed by the Mars Express ultraviolet spectrometer. Through the analysis presented in the next

sections such local effects are identified and analyzed.

The analysis is also then extended to global scales. Several results in the previous section indicate the occurrence of intense, high energy electron events within the geometrical shadow of Mars (Section 3.3.1). As it was realized, these events show high electron temperatures that are only found in the Martian magnetosheath. If indeed these electrons have magnetosheath origin, it is interesting to investigate under what conditions they can penetrate to the tail region. If, on the other hand, these are accelerated, low energy electrons, it would be interesting to investigate the acceleration mechanism. In both cases, the role of the crustal fields could be important.

Data analysis presented in the following sections, makes use of the omnidirectional flux of electrons in a given energy range, rather than plasma moments. The reason for doing that is that statistics are improved, as plasma moments cannot be extracted in every case. The selected energy range is that of 80-100 eV, which is typical for magnetosheath electrons or for the electrons observed in the induced magnetotail of Mars. Using a different energy interval in the range of ~40-200 eV, does not change the results significantly. Plasma moments are used in several cases in order to automatically distinguish populations from different interaction regions.

3.4.1   Non-ionospheric electron fluxes and crustal field spatial correlations

Fig.3.12(top) shows the median flux of 80-100 eV electrons measured by ELS below 800 km altitude on the nightside for all orbits between 2/2/2004 and 10/3/2007 as a function of Mars planetocentric eastern longitude and latitude for the southern hemisphere. The bottom panel shows the inverse of the total crustal field strength at 400 km altitude for the regions covered by the MEX orbit. The use of the inverse of the field strength is chosen in order to have similar color ranges in both panels. All data are binned at 2° resolution.

The observations show that on global scales magnetosheath electron fluxes are much lower above regions of strong crustal fields, while regions of weak crustal sources show more intense fluxes. However, on scales of a few degrees localized peaks can be observed in electron flux which may be associated with cusp-like structures above crustal field sources. Statistics are not sufficient to map data limited to smaller altitude ranges in this way.

3.4.2   Plasma Intrusion Altitude

The spatial correlation of electron fluxes and crustal fields shown before, is an indication that crustal sources have strong effects on electron distributions. However, such a correlation does not reveal any altitude dependence of these effects. In order to do this, electrons are classified in two different populations according to their characteristic flux. The behaviour of these populations is investigated as function of altitude, solar zenith angle and crustal field strength.

Fig.3.13 shows the distribution of 80-100 ELS data samples for the dayside (left) and nightside (right) of the magnetosphere, for altitudes below 1500 km, as a function of the logarithm of the omnidirectional flux in $cm^{-2}s^{-1}$
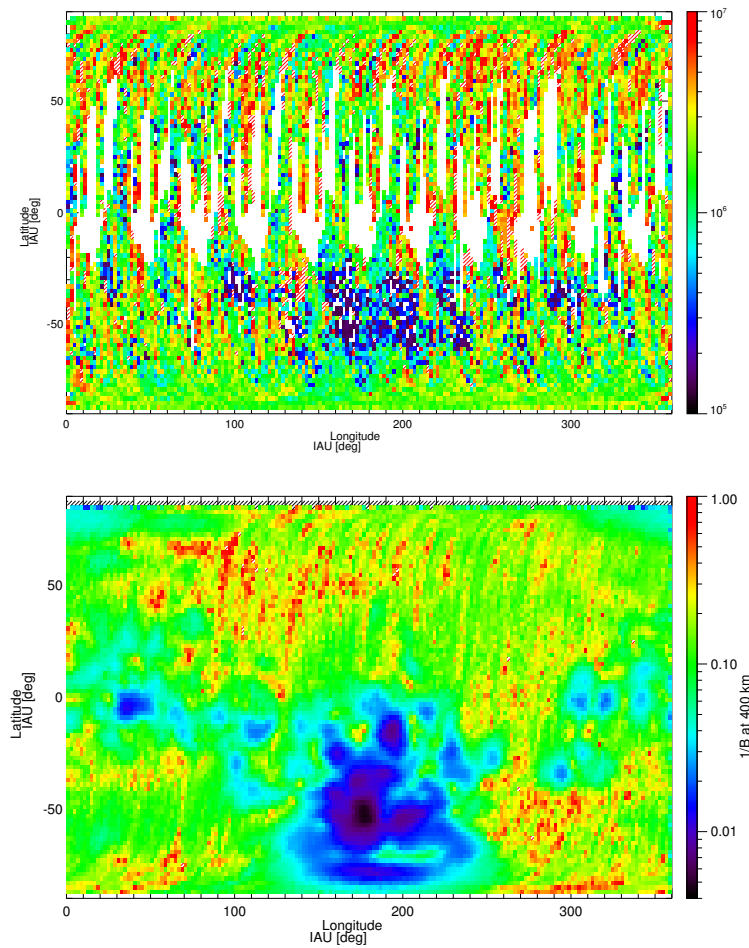
Figure 3.12: (Top) Median energy flux of 80-100 eV electrons measured below 800km altitude for all orbits between the 2/2/2004 and 10/3/2007 as a function of Mars planetocentric longitude and latitude. Bottom: Inverse of the total crustal field strength (nT^{-1}) at 400 km altitude.

On the dayside (left) the distribution can be separated into two distinct populations: one with a fitted median flux of about $10^{6.5}$ cm^{-2}s^{-1}, the other with a fitted median flux of about $10^{8.15}$ cm^{-2}s^{-1} . This bimodality is due to the two electron populations that the MPB separates: above the MPB (magnetosheath) the energy flux has a high median flux value and below a low median flux value.

If the flux across the MPB would happen on large spatial scales the distribution would not be bimodal but would show more samples of medium flux levels (a third distribution). This agrees with the observation that the MPB is a sharp boundary.

The interpretation of two separate distributions is further confirmed by the nightside distribution (Fig.3.13,right): here the MPB is on average located above 2000 km altitude such that even for times of strong solar wind pressure it is not observed below 1500 km altitude. This justifies the presence of just one Gaussian. The high flux tail of the distribution on the nightside may be explained by intrusion events along the crustal magnetic field lines.
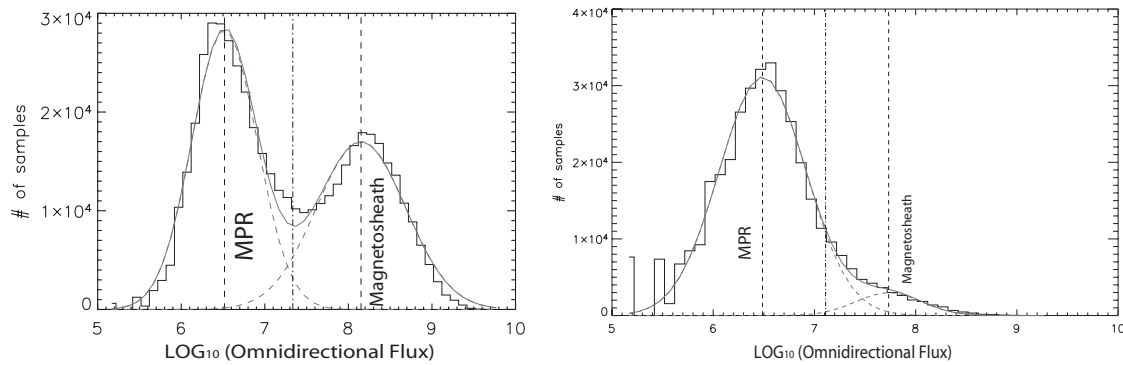
Figure 3.13: Number of ELS data samples below 1500km altitude and for the dayside (left) and the nightside (right). The dashed vertical lines mark the gaussian-fitted means, while the dash-dotted lines show the intersection point of the distributions. The two distributions in the left panel indicate the two different electron populations that can be found below 1500 km altitude, on the dayside: the MPR electrons (low mean flux value) and the magnetosheath electrons (high mean flux value). From the nightside distribution for the same altitude range (right), mainly MPR samples can be found, as expected. Binsize is 0.1 in units of logarithm of the omnidirectional flux.

If the middle point of the two Gaussians is taken as a separator ($\sim 10^{7.8}$ cm^{-2}s^{-1}), it can be estimated for any region in the magnetosphere how often fluxes higher than the separation flux are observed, or equally, how often magnetosheath fluxes are observed in that given region. Using the percentage of flux above this separator value as an index of the magnetosheath plasma, the two maps of Figure 3.14 are constructed.

The maps show the percentage of magnetosheath electrons (color-coded bins), as a function of the crustal magnetic field strength at 400 km altitude. Physically, the use of the crustal field value at a fixed altitude is indicative of whether MEX is above a region of strong or weak crustal magnetization. The two panels separate cases in the dayside (top) and the nightside of Mars (bottom).

The dayside percentages (top) describe how often at a specific altitude and above a region of weak or strong anomalies the spacecraft is inside the magnetosheath or below the MPB. Thus it characterizes how dependent the MPB location is from crustal field strength.

The average MPB location can be determined by the 50% level. Above regions of low fields (<20 nT) the MPB is on average at 600km altitude, while above high-field regions (>50 nT) it is observed at 800 km altitude. The dependence of the average MPB altitude on the field strength seems to be almost linear. This linear relation seems to break down for field strengths greater than > 100 nT and for altitudes greater than $\sim 1100 - 1200$km. Above strong crustal fields, several bins contain almost 100% of magnetosheath samples, even at low altitudes. This is evidence for electron intrusion along cusps under certain solar wind conditions. Still, statistics are poor for field strengths greater than 100 nT and no clear picture can be drawn for the frequency of such intrusion events (Figure 3.15).

The nightside map shows a much more complex distribution of the magnetosheath electron intrusion. Here, the MPB is routinely located above 1500 km altitude which ex-
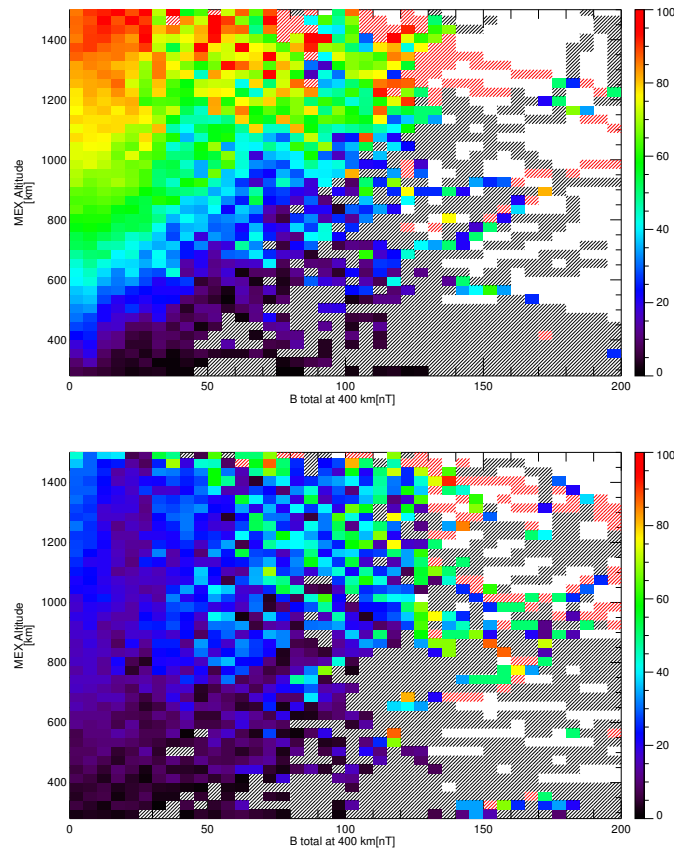
Figure 3.14: Color coded magnetosheath electron intrusion percentage, as a function of altitude and crustal magnetic field strength at 400 km altitude. The left panel is for the dayside and the right panel for the nightside of Mars. Binsizes are 5 nT for the x-axis and 30 km for the y-axis.

plains why low percentages of sheath electrons are seen. At altitudes below 700 km and crustal field strengths of 80 nT about 20% of sheath electrons constitute the electron distribution. For stronger crustal field regions magnetosheath samples are almost completely absent. This shows that for very low altitudes in the nightside, the crustal fields prevent the precipitation of sheath electrons and their expansion into the wake. This is consistent with the observation of electron void regions, reported by *Soobiah et al.* (2005).

For altitudes greater than 700 km the picture is different. For crustal field strengths up to 80 nT, almost 35-40% of sheath electrons are present, independent of the magnetic anomaly strength. Above 80 nT, the percentage of sheath fluxes gradually increases, suggesting again that strong crustal fields are accessible to higher altitudes and are therefore more likely to connect to the magnetic field of the sheath and accelerate electrons. For the region of the strongest anomalies, the scattering of the sheath electron percentage among different bins is significant, as statistics in this region are poor.

The increase of magnetosheath electron fluxes at high altitudes in the nightside is particularly interesting with respect to the intense energetic electron events observed in the wake of Mars. This is further investigated in the following section.
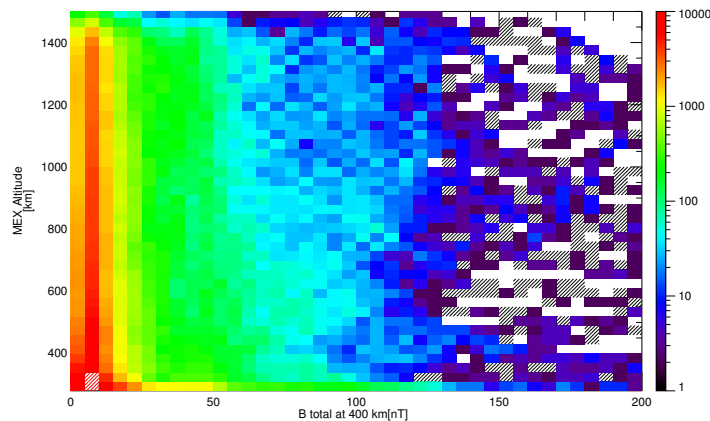
Figure 3.15: Statistics of observations above regions of different crustal field strength in the dayside magnetosphere, as a function of altitude. Color coded bins show the number of samples at each location. The low sampling of the strong crustal field region is mainly due to the small fraction of the martian surface that these crustal sources cover.

3.5   Energetic electron asymmetries behind the terminator plane

In the previous section it was established that the magnetic anomalies on the dayside generally prevent the intrusion of magnetosheath electron to low altitudes, with few exceptions above very strong crustal sources. On the nightside, very low altitudes are shielded by the crustal fields, but at intermediate altitudes, sheath fluxes are more intense above magnetic anomalies.

The latter indicates that magnetic anomalies could be related to the magnetosheath fluxes. On the other hand, several simulations indicate that magnetosheath electrons could find channels towards the tail region from locations where the MPB is not effectively formed. For instance, *Simon et al.* (2007a) suggest that the strength of the MPB can be modulated as a function of the orientation of the convective electric field from the solar wind (E_{SW}). Such an asymmetry could be further enhanced by the necessity for charge neutralization of high fluxes of escaping planetary ions.

In this Section, the combined influence of the crustal fields and the E_{SW} orientation is investigated with respect to the origin of high flux, energetic electron events in the martian tail. This is done by organizing electron 80-100 eV fluxes from the magnetosheath, the MPR and the tail, in different coordinate systems.

As in some of the plots that will be shown, the magnetosheath and the MPR overlap, a practical approach is used to separate them in order avoid mixing electron populations from different magnetospheric regions. This approach considers also that the MPB location can vary, compared to the average position defined by *Vignes et al.* (2000). If the normal distance of MEX from the Vignes et al. MPB is within 0.5 R_M, the identification of the proton depletion and/or the electron pressure dropout is required to locate the actual MPB and classify a region as MPR or magnetosheath. It is noted that this separation is primarily done for practical purposes and can only give a rough idea on how the MPB

position varies. The following results are not affected if the separation is not done, but are more difficult to illustrate.

Data are first organized in the MSE coordinate system. From this point on, the sector along the direction of E_{sw} will be called the "E^+ sector" ($Z_{MSE} > 0$), while the opposite sector will be referred as the "E^- sector". The E^+ and E^- sectors are almost equally covered in the region behind the Mars terminator plane ($X < 0$ - Figure 3.16, top panel). The crustal field contributions are averaged out in the MSE due to the continuously changing orientation of the IMF, during the 2 years of observations (IMF orientation data were only available until March 2006).
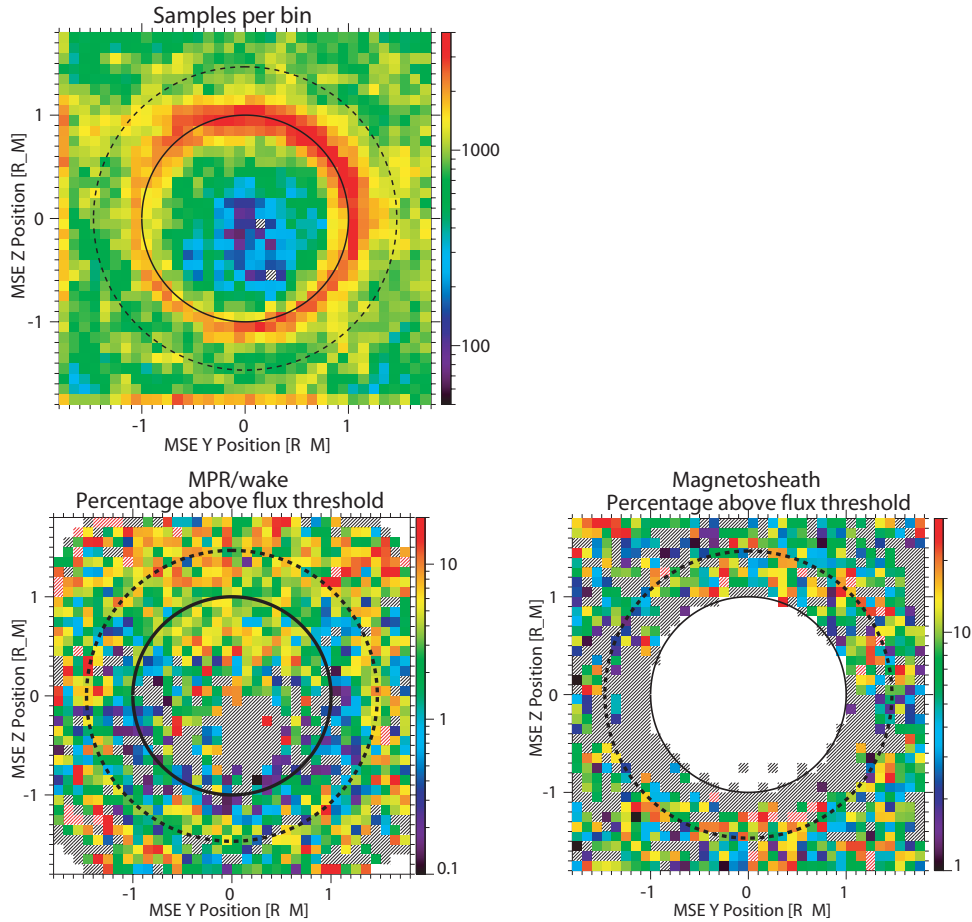
Figure 3.16: (Top): Number of samples per bin in the yz-plane of the MSE coordinate system. The sampling is equally homogenous if the magnetosheath and MPR/wake regions are separated. (Bottom): Percentage of bins with electron fluxes above $10^{7.1}$ cm^{-2}s^{-1} in the MPR and wake regiond (left panel) and above $10^{8.1}$ cm^{-2}s^{-1} in the magnetosheath (right panel). Clear asymmetries exist between the E^+ ($z > 0$) and E^- ($z < 0$) sectors. In all plots, bins are integrated along the X-direction, between X=-4 R_M and X=0, the dashed line shows the MPB location at the terminator (*Vignes et al.* 2000). The binsize is 0.1 R_M. Red shaded bins are for values greater or equal to the maximum in the color bar. The opposite is valid for the grey shaded bins.

Starting with the MPR and wake regions, 80-100 eV electron flux data are binned.

Using a median average filter on the data does not reveal any significant asymmetry in the flux distribution in the MSE system. Interesting asymmetries appear when the high flux end of the distribution is studied. For this reason the percentage of cases per bin with fluxes above $10^{7.1}$ cm^{-2}s^{-1} are instead plotted (Fig. 3.16, bottom left). The flux thresholds are selected to be the high-flux, 2σ value of the flux distribution.

The middle panel of Figure 3.16 shows that high electron fluxes are more frequent in the E^+ hemisphere of the MPR and wake regions. These events occur in less than 10% of MEX orbits. This explains why no such asymmetry is visible in the median plot, where statistics over all the flux distribution are considered.

The same analysis is done for the 80-100 eV electrons in the magnetosheath. Results are shown in Figure 3.16 (bottom right panel). Fluxes above the threshold flux in the E^+ sector are again higher than in the E^- sector. The low altitude, high-flux bins in the right panel of Fig. 3.16 can only come from the terminator as the MPB altitude increases significantly for $X < 0$.

These observations establish that the convective electric field pointing direction has an important role in the formation of the high-flux events in the nightside. An additional important observation is that these events seem to be connected to a similar asymmetry identified in the magnetosheath at the terminator region. If this connection is interpreted as intrusion of sheath electrons towards the tail, then the terminator region of the E^+ sector is the intrusion location. Therefore a key to the origin of these high-flux tail events should be hidden in processes at the terminator.

We therefore study the terminator region in more detail: for cases where MEX was at an altitude of less than 1500 km (average MPB location at the terminator) and at solar zenith angles between 90° and 120°, E^+ and E^- hemisphere data are separated and 80-100 eV electron fluxes are organized as a function of crustal field strength at 400 km altitude, as in Section 3.4.2.

The bottom panels of Figure 3.17 show the percentage of 80-100 eV electron fluxes above a threshold of $10^{7.7}$ cm^{-2}s^{-1}. As expected from the analysis for E_{SW} related asymmetries, more high flux events are seen in the E^+ hemisphere (bottom left) than in the E^- hemisphere (bottom right). But most importantly, the contribution to the asymmetry increases with increasing crustal field strength. Below ~ 10 nT high flux percentages are similar in the two hemispheres. For field strengths between 10 and 60 nT, where statistics are still good (top panel), high flux percentages are greater than $\sim 20\%$ for the E^+ sector and $\sim 0\%$ for the E^- sector.

It is therefore found that the mechanism that generates the high flux, energetic electron tail events requires the combination of different conditions to be satisfied. The first condition that has to be met is that a moderate or strong crustal field region should be located close to the terminator. In the same time this region should "belong" to the E^+ hemisphere. Observations supporting this have also been reported by *Dubinin et al.* (2006a).

The fact that these high flux events constitute less than ~10% of the total ASPERA-3 observations, is consistent with the necessity of having the E_{sw} and the crustal fields in certain configurations: these are only a small fraction of the possible orientation combinations. This small percentage also implies that these high-flux events are transient and not a steady state situation.

The role of the E_{sw} is discussed in several hybrid plasma simulation approaches. For example, *Simon et al.* (2007a) and *Bößwetter et al.* (2004) argue that the MPB does not
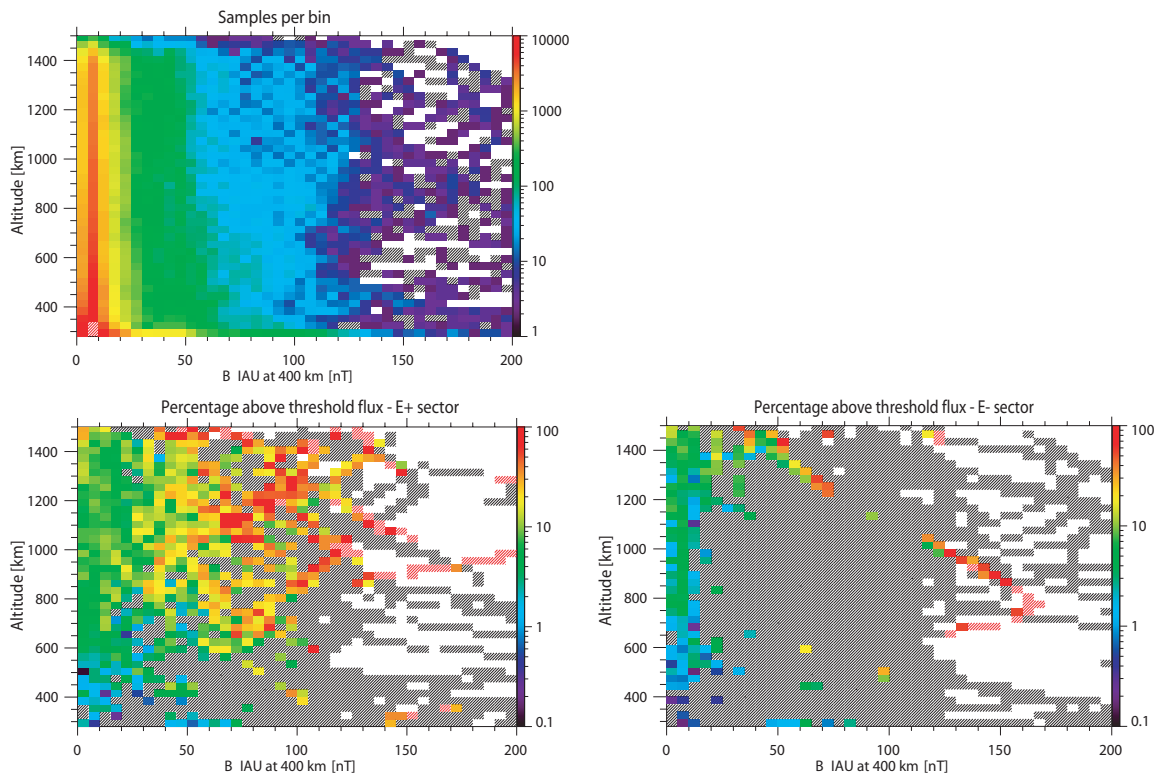
Figure 3.17: (Top): Number of samples per bin as a function of altitude and crustal field strength at 400 km altitude. The sampling profile is similar for the E^+ and E^- hemispheres. (Bottom, left and right): Percentage of bins with fluxes above $10^{7.7}$ cm^{-2}s^{-1} in the terminator region. The middle panel shows E^+ hemisphere samples and the right panel shows the E^- samples. In all panels, binsize is 30 km for the altitude and 5 nT for the crustal field magnitude. The magnetosheath and MPR and wake regions are not separated here.

form effectively at the E^+ sector, despite the stronger field pile-up there compared to the E^- sector. This statement is consistent with the more frequent occurrence of electron intrusion events in the E^+ hemisphere. In these simulations no crustal sources were used. Alternatively, a relation between the asymmetry observed in the escape of planetary ions might exist, with electrons acting as a charge-neutralizing fluid. Investigation of individual energetic electron events show that these populations in the tail are indeed associated with low or high energy, escaping atmospheric ions (see eg. Figures 3.2 and 3.11 at about 13:50 and 10:45 respectively). Unfortunately, as low energy ion data was made possible only after May 2007, a comprehensive study was not possible to be completed for this thesis.

One explanation for the additional contribution of the magnetic anomalies, is that intruding plasma in the E^+ sector can carry the frozen-in field to altitudes where the crustal fields dominate. As the anomaly fields have complex structures, opposite polarity field lines with that of the IMF lines will be present and reconnection can occur.

A previous study on the crustal field influence has been done with non-ideal MHD, 3D simulations (*Harnett and Winglee* 2005). The authors suggest that the presence of

magnetic anomalies at the terminator can lead to reconnection with the IMF and to large scale asymmetries in the plasma distribution at the magnetotail. However, the effects of the E_{sw} direction were not realized. The simulation of the combined action of E_{sw} and the magnetic anomalies should be investigated in future modelling attempts.

3.6   Summary and outlook

In this chapter, electron and ion data from the ASPERA-3 instrument of Mars Express have been analyzed and a series of new results have been obtained:

- For the first time, plasma moment maps have been created for Mars. Despite a series of limitations by the IMA and ELS sensors, it was possible to construct reliable maps of plasma density, electron temperature and ion velocity. All macroscopic interaction regions have been identified in the moment maps, still the observed spatial distributions show slightly different shapes and locations for the various interaction boundaries (bow shock, MPB). This could suggest that plasma boundaries can differ from boundaries identified with magnetic field data. It is also worth noting that recently, the estimated plasma moments have been compared with hybrid plasma simulation results, and a good quantitative agreement was achieved (*Bößwetter et al.* 2007).

- An estimation of the atmospheric erosion rates was done using the calculated plasma moments. The estimated number is $5\text{-}10 \times 10^{23} \text{s}^{-1}$, which is about a factor of 2 higher than the value given by *Barabash et al.* (2007b), but covers only ions above 100 eV.

- In both the electron density and temperature maps, several distinct regions with relatively dense and hot plasma have been identified in the wake of Mars

- Detailed analysis of high energy, electron flux data revealed that these electron density and temperature enhancements in the wake are of magnetosheath origin. The conditions under which electrons from the magnetosheath can intrude towards the wake requires the combination of two different conditions to be satisfied: a moderate or strong crustal field region should be located close to the terminator and in the same time "belong" to the E^+ hemisphere. This is the first time that combined effects of crustal field and solar wind conditions are identified.

- The crustal field influence on the dayside, magnetosheath electron population have been assessed: it was found that on average, magnetic anomalies "push" magnetosheath electrons to high altitudes. However in few cases, very strong magnetic anomalies can accelerate electrons to low altitudes and result in auroral type events.

Apart from resolving several issues, these results point towards new research topics and applications. The continuous collection of plasma moments could eventually be used to construct a global Mars-solar wind interaction reference model, which could be used not only for scientific applications (e.g. calculation of electron impact ionization or

charge exchange rates), but also for a better planning of future space missions to study the interaction of the planet with the solar wind.

The discovery that magnetosheath electrons intrude towards the magnetotail under certain conditions, could also be further investigated, not only in a statistical sense, but also with single event studies, where a detailed analysis of electron spectra can be done, in conjunction with ion data from IMA.

The fact that IMA can after May 2007 resolve ions below 100 eV might be also important, not only for searching possible correlation with energetic electron tail events, but also for updating the total escape rate estimations. As we are also in the ascending face of the solar cycle, it would be also interesting to investigate whether escape rates, or other processes, are modulated by solar activity.

In terms of global configuration of the magnetoshpere, most observations shown here cover its dusk sector. The dawn sector was less sampled. Whether a dawn-dusk asymmetry enhances other processes at Mars could also be studied with MEX improving the coverage of the various interaction regions. This improved coverage, in both space and time, could also be preferential to investigate the configuration of the magnetosphere with magnetic anomalies at fixed local times.

Finally, a substantial progress in understanding the processes at the Martian magnetosphere can be achieved by comparing the observations of the two identical instruments, ASPERA-3 and ASPERA-4, on Mars and Venus Express, respectively. This comparison could help to evaluate the importance of the presence of crustal fields at Mars, the importance of the different ionospheric and exospheric vertical structures of the two planets, as well as the different solar wind conditions.

4 Energetic particle absorption by Saturn's icy moons: probes of magnetospheric dynamics and moon activity

Many of Saturn's moons are continuously immersed in the planet's radiation belts and are exposed to its trapped energetic particle population. The absorption of these energetic particles by the moons form evacuated regions within the magnetosphere, the lifetime of which depends on the effectiveness of particle diffusion processes (and most importantly, radial diffusion). Before radial diffusion erodes them, these absorption regions continue to drift in the magnetosphere with the properties of the pre-depletion flux tubes. What happens in reality is that the electrons or ions leading and trailing the absorption region continue to drift with zero relative velocity, giving the impression that the absorption region is drifting in the manner of the pre-depletion particles. By monitoring of the properties of the depleted flux tubes (depth, shape, magnetospheric coordinates, longitudinal separation from the absorbing moon), a lot of information can be extracted about the dynamics of the magnetosphere or even the absorber.

The absorption regions are classified in two main categories: macrosignatures and microsignatures (*Paranicas and Cheng* 1997). Macrosignatures are the permanent and azimuthally averaged decreases of the count rates in the energetic particles radial distribution. Microsignatures are count rate decreases that are strongly dependent on the longitudinal distance between the signature location and the absorbing body. Satellites, rings or dust concentrations can be the source of both macrosignatures and microsignatures.

After the first flybys at the outer planets by the Pioneer and Voyager probes, it became evident that charged particle absorption features in the radiation belts are important tracers of magnetospheric dynamical features and parameters. Many studies focused on the relation of these absorption features to energetic particle diffusion and to the validity of magnetic field models (*Thomsen et al.* 1977a,b, *Randall* 1998, *Selesnick and Stone* 1991, 1994)

Absorption regions correlated with moons and rings are even more important for characterizing the Saturnian magnetosphere, as it was briefly discussed in the Introduction (Section 1.2). The dipole axis of Saturn's intrinsic magnetic field is almost co-aligned with its rotation axis. Therefore, all charged particles pass through the orbital plane of Saturn's moon's while executing one of the fundamental motions of trapped radiation: the bounce motion along the magnetic field lines (Sections 4.2, 4.2.2). Unlike at other

planets, even equatorial particles are continuously absorbed by an extended ring system and by a number of moons with almost circular and equatorial orbits within the radiation belts. As a consequence, losses of particles to the icy moon surfaces and ring particles are expected to be higher compared to the losses in the other planetary magnetospheres.

Carbary et al. (1983) give a good summary of the Voyager 1 and 2 findings. Among the important results were the calculation of D_{LL} at the distance of Dione and the evaluation of various magnetic field models. Satellite sweeping theory and modeling approaches were developed to reconstruct single events or to consistently explain the full datasets of observations (*Paonessa and Cheng* 1985, *Fillius* 1988, *Paranicas and Cheng* 1997). *Van Allen et al.* (1980a) extracted D_{LL} values from a Mimas absorption signature and suggested that a filtering effect to radially diffusing electrons is taking place at Enceladus that results in a monoenergetic electron spectrum in the innermost Saturnian radiation belts.

However, no consistent picture could be drawn from all the pre-Cassini studies. *Paonessa and Cheng* (1986) show D_{LL} estimates from different studies extending over four orders of magnitude. A number of reasons could account for this scatter, such as dependencies on particle species and energy. Instrumental effects that could amplify differences imposed by these dependencies, can also not be ruled out. Most likely, the low statistical value of the observations did not allow any such dependencies to be resolved. The assumptions associated with the analysis might also influence the result. In several cases, "ghost" (unknown) absorbing bodies co-orbiting Saturn with the moon Mimas have been theorized to account for the observed signatures (*Simpson et al.* 1980, *Chenette and Stone* 1983, *Selesnick* 1993).

In this chapter I show several case studies of energetic particle absorption signatures in order to illustrate basic features associated with their generation and evolution in the magnetosphere. As there is a strong correlation between the evolution of these absorption signatures and the magnetospheric dynamics, the structure and dynamics of the Saturnian magnetosphere are investigated by using microsignature and macrosignature observations as a very powerful tool. All observations shown in this chapter were done with the MIMI/LEMMS sensor onboard Cassini 2.2.

4.1   The icy moons in Saturn's inner magnetosphere

Between 2.32 R_s (distance of Saturn's outer edge of the main rings) and 9 R_s from the center of Saturn ($1R_s$=60268 km), seven moons with a diameter greater than 100 km orbit the planet (Figure 4.1). Table 4.1 lists the typical characteristics of the orbits and sizes of these moons. To simplify several calculations in the following sections, it is a reasonable assumption to consider that all the orbits of the moons are equatorial. In addition, I assume that all orbits, apart from that of Mimas, Janus and Epimetheus, are circular. For these three moons their eccentricity is taken into account, since this has proven to be significant, as shown by *Van Allen et al.* (1980a).

I also consider the presence of the E-ring, which was confirmed to primarily originate at the cryovolcanic moon Enceladus (*Dougherty et al.* 2006, *Porco et al.* 2006, *Spahn et al.* 2006), and its high density regions extend mainly between 3 and 8 R_s (*Baum et al.* 1981). A more compact and slightly denser ring (G-ring) is present between the orbits of Mimas and the Janus and Epimetheus pair. All moons are assumed to be perfect absorbers
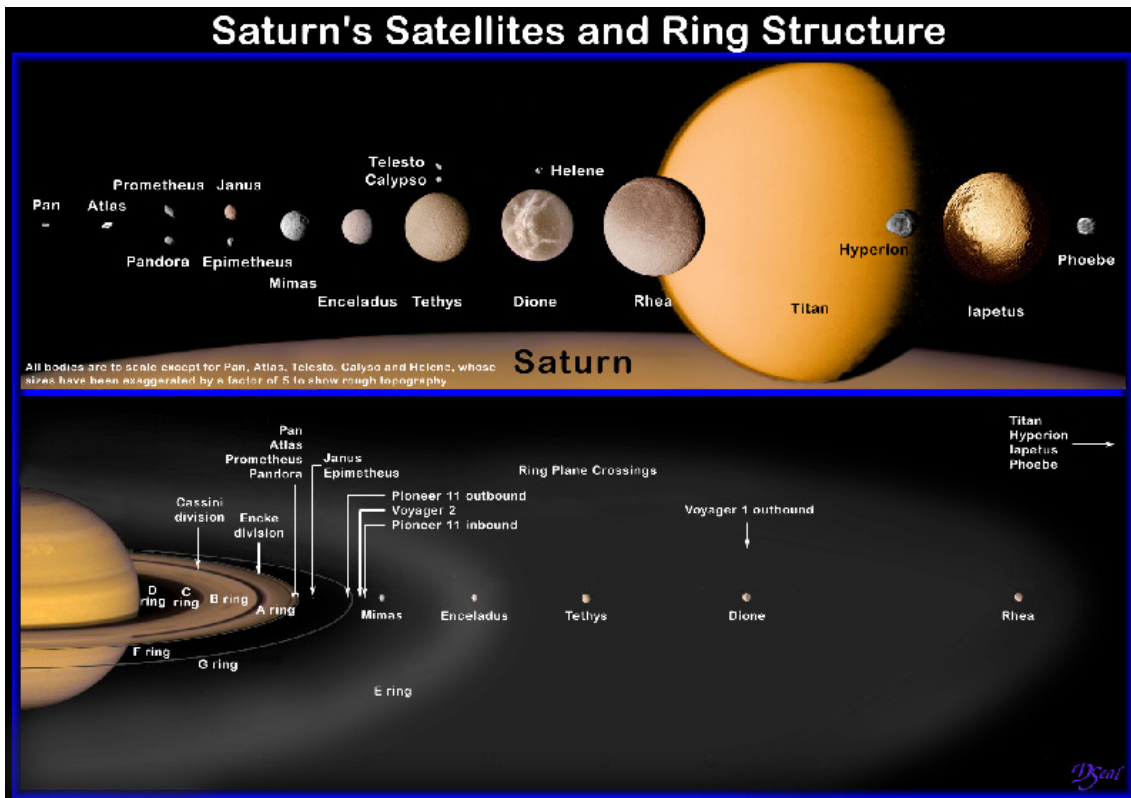
Figure 4.1: An artistic view of the moons and ring system of Saturn, as it was known before the arrival of the Cassini spacecraft in July 2004. The bottom panel shows the moons and ring system that is of interest to this study. Image credit: David Seal/ JPL

of energetic particles, except for Enceladus it was found to deviate from this behaviour, at least the sub-MeV electrons. This assumption seems to be adequate for Tethys, Dione and Rhea, based on data from several close flybys of these moons by Cassini. These assumptions are tested in Sections 4.2.1.1, 4.2.2, 4.3.1 and 4.3.2.

Two more relatively large moons (always with respect to keV/MeV electron gyroradius), Prometheus and Pandora, with diameters of 100 and 84 km, respectively, orbit in the innermost magnetosphere. However, as these two moons are inside the main ring system and close to Saturn's dense F-ring, the energetic particle environment is complex and the absorption features can be much more structured (*Cuzzi and Burns* 1988). Therefore, the study of any relevant feature from these moons will not be included in this chapter. Signatures from newly discovered kilometer sized moons or the Lagrangian co-orbitals of Tethys and Dione are shown to cause no large scale losses in the energetic particle population and are also not considered here. The effects of asteroid-sized moons in the Saturnian magnetosphere are discussed in more detail in Chapter 5.

4.2   Energetic particle motion in Saturn's radiation belts

In order to understand the origin and the evolution of the satellite absorption signatures, it is important to describe the kinematics of energetic charge particles relative to the Keplerian motion of the moons. A detailed and qualitative summary of the energetic particle

Table 4.1: List of Saturn's moons considered in this study and the typical parameters for their geometrical sizes and orbits. Data are from *Yoder* (1995). Up to date ephemeris data and constants can be found at *http://ssd.jpl.nasa.gov*. Janus and Epimetheus's orbital data vary, as this system has a special dynamical behaviour. Since Cassini crossed Janus's and Epimetheus's orbits only during SOI, the given constants refer to that period only. The f_c parameter, approximated in this study (see Section 4.2.1.1), corresponds to the plasma corotation fraction at the vicinity of each moon.

Moon	Diameter (km)	a (R_s)	e	i (deg)	f_c
Epimetheus	119	2.521	0.090	0.34	1.0
Janus	178	2.522	0.007	0.14	1.0
Mimas	397	3.075	0.020	1.53	1.0
Enceladus	498	3.985	0.004	0.02	0.85
Tethys	1060	4.890	0.000	1.09	0.85
Dione	1120	6.280	0.002	0.02	0.75
Rhea	1528	8.750	0.001	0.35	0.85

motion in Saturn's magnetosphere is given below. The mathematical description of energetic particle motion is given in *Thomsen and Van Allen* (1980). The analytical formulas from that paper are also given in *Appendix A*. All formulas are derived assuming motion in an undisturbed dipole field. In the calculations, the small northward displacement of Saturn's magnetic field source from the planet's center is not taken into account, as this produces a correction well within the error bars of the physical quantities that will be derived.
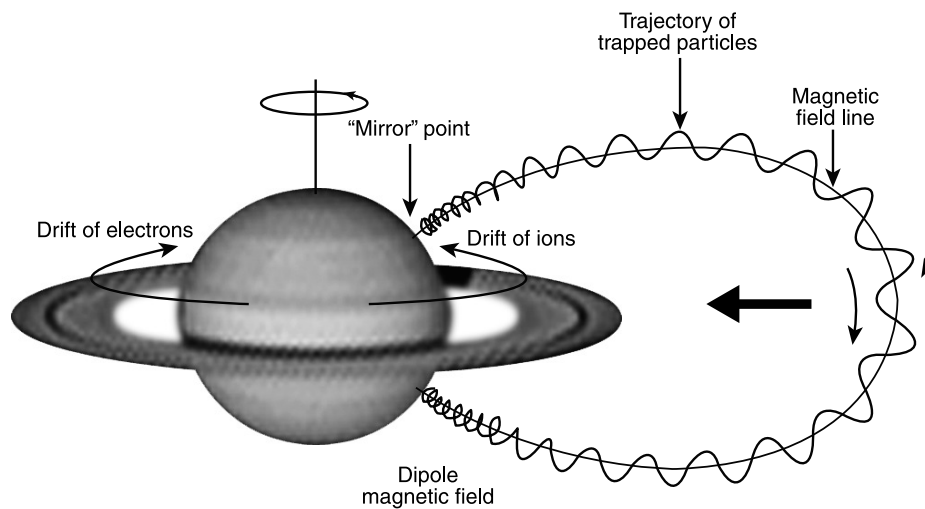
Figure 4.2: Sketch of charged particle motion in the Saturnian magnetosphere. The three fundamental motions are illustrated: gyration, bounce motion and magnetic drift in opposite directions for electrons and ions.

A sketch of the different elements of particle motion is shown in Figure 4.2. Energetic particles contain most of their energy into gyration around the magnetic field lines. Smaller contribution comes from the bounce motion along the magnetic field lines and even smaller from the drift motion around Saturn. In the following subsections, each element of the particle motion is described more extensively.

The coordinate system commonly used in this chapter has the +x-axis on the equatorial plane of Saturn, in the direction towards the Sun, +z parallel to the spin axis of Saturn and the y-axis completes the orthocanonical system. Below I also include a list with a short explanation of basic parameters or definitions that are commonly used in this chapter:

- **Dipole L-shell (or L-shell)**: The L-shell parameter describes the equatorial distance of a magnetic field line. The dipole L-shell defines this distance for an undisturbed dipole. The relation between the dipole L-shell and the radial distance (from the center of the dipole source) is $R = L\,cos^2(\lambda_{mag})$, where λ_{mag} is the magnetic latitude. The regions magnetically connected to the orbits of Saturn's moons can be given to a first approximation by the dipole L-shell. These regions are called the "moon L-shells".

- **Latitude or magnetic latitude, λ_{mag}**: The magnetic latitude is the angle measured from the magnetic equator of the dipole field until the radial position vector of the observation point, along the z-axis. It takes values from -90° to +90°. Several books make use of the magnetic co-latitude, defined as 90°-|λ_{mag}|. Due to the almost perfect alignment of the magnetic and the spin axis at Saturn, the magnetic latitude is almost identical to the kronographic latitude and can be estimated by $sin^{-1}(z/R)$.
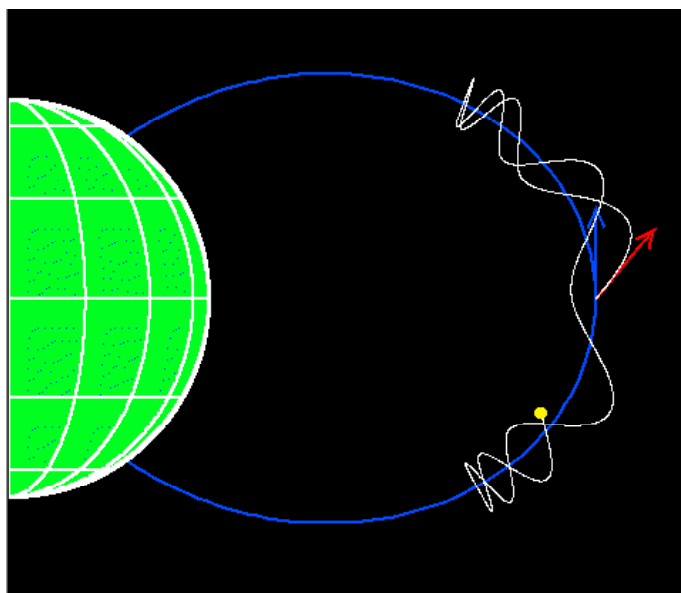
Figure 4.3: Sketch showing the pitch angle and its variation along a dipole field line. The equatorial pitch angle is the angle between the red and the blue vectors. Notice how the pitch angle changes as the particle moves to different magnetic latitudes.

- **Equatorial pitch angle,** a_{eq}: The pitch angle, a, defines the angle between the velocity vector of a particle and the direction of the magnetic field. It takes values from 0° to 180°. The two extreme values corresponding to field-aligned particles, moving parallel or anti-parallel to the field direction, respectively. The pitch angle of a trapped particle changes continuously, as the product $B \sin^2 a$ should remain constant (due to conservation of the first adiabatic invariant of motion - the magnetic moment) and the magnetic field intensity, B, changes along a filed line. Therefore the pitch angle of a particle is usually given at a reference position along a field line. That is chosen to be the magnetic equator (z=0) and the pitch angle is then called "the equatorial pitch angle" (Figure 4.3).

4.2.1 Energetic particle drift motion and applications

The drift motion of energetic particles has two important elements: an eastward drift due to the corotation electric field of Saturn (Ω) and a drift due to gradient in the magnetic field and a curvature of the field lines (ω_{gc}). The ω_{gc} drift is eastward for ions and westwards for electrons. This means that energetic electrons drift around the planet with speeds (or more correctly "bounce-averaged drift velocities") lower than those of the cold plasma corotation speed, while energetic ions drift faster.

The corotational drift occurs on curves of equal electrostatic potential. In the absence of additional electric fields, these curves coincide with the curves of equal magnetic field where gradient and curvature drift takes place and, assuming an undisturbed dipole, with the L-shells of the icy moons. Therefore, if ω_k is the Keplerian orbital angular velocity of a moon, the drift frequency of an energetic electron with respect to that moon is:

$$\omega_{rk} = f_c \Omega \pm \omega_{gc} - \omega_k \tag{4.1}$$

The dimensionless parameter $f_c(L) \equiv f_c$ corresponds to the corotation fraction at the approximate L-shell of each moon. The same equation can also give the drift frequency relative to corotation (ω_{rc}), if ω_k is set to zero. The gradient and curvature drifts depend on three parameters: the L-shell (L), the particle kinetic energy (E) and the equatorial pitch angle (a_{eq}). By analysing these simple equations, several interesting phenomena and applications can be discussed, which are different for electron and for ions.

4.2.1.1 Electrons

For electrons, and for certain combinations of L and a_{eq} an energy exists where ω_{rk} or ω_{rc} are zero. These energies are called resonant energies with respect to the Keplerian motion, and with respect to corotation (E_{rk} and E_{rc} respectively). At each L, there is a range of resonant energies, corresponding to different a_{eq}. Figure 4.4 shows the L and a_{eq} dependence of E_{rk} and E_{rc} for f_c=1.

For $E < E_{rk}$, electrons drift faster than the moons and depletions occur downstream (ahead) of a moon's orbital motion. For $E_{rk} < E < E_{rc}$, electrons counterdrift with respect to the moon and depletions occur upstream (behind) the moons' orbital motion, but electrons continue to move in the sense of corotation (westward) in an inertial coordinate system centered at Saturn. For even higher energies and at $E > E_{rc}$, gradient and curvature drifts are so strong that electrons drift opposite to the corotation direction. E_{rk}
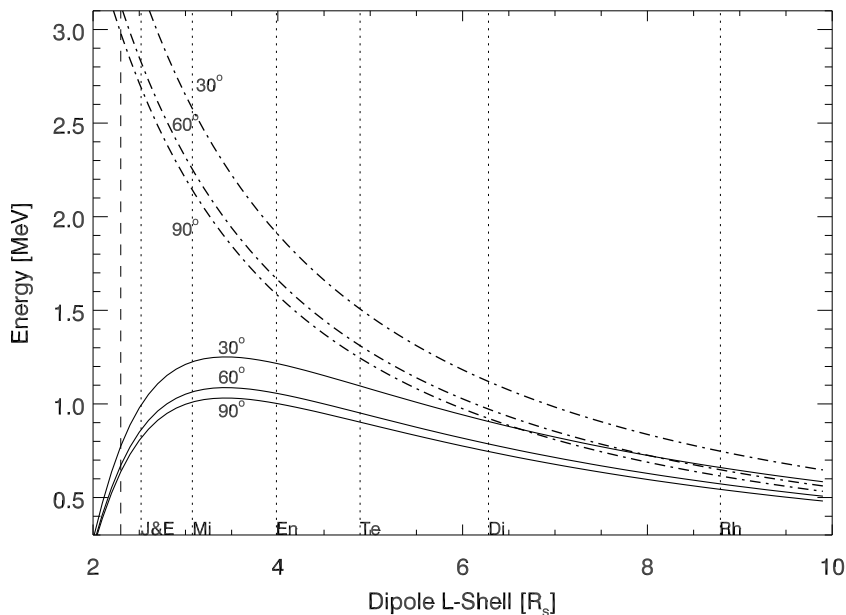
Figure 4.4: Electron resonant energy with respect to the Keplerian motion (E_{rk}) and corotation (E_{rc}), as a function of L and a_{eq}. The solid curve shows E_{rk}, while the dotted-dashed curve is for E_{rc}. The vertical dashed line denotes the approximate position of the main ring system's outer edge, while the dotted lines correspond to the icy moons' L-shells. Values are calculated assuming rigid corotation (f_c=1) all over the magnetosphere.

is fundamental for the Saturnian radiation belts. At this energy electrons have very low probability of being absorbed by the moon because they are drifting close to the moon's orbital speed and can therefore diffuse across the moon's orbit or drift along it, freely. On the other hand, E_{rc} is important since around that energy the effect of corotation vanishes. Then, any additional electric fields define the electron drift shell shape (*Cooper et al.* 1998).

The Keplerian resonant energy can be directly extracted from data of close moon flybys. An example is given below, based on data from a close Enceladus flyby. The flyby occurred on day 195 of 2005, with a closest approach 194 km upstream of the moon's surface. Therefore, electron depletions were expected above E_{rk}. Indeed, during this upstream flyby LEMMS high energy resolution data revealed a narrow energy range above which a clear moon wake appeared, where electron fluxes drop to background levels (this is explained in th section 4.2.2). The average value of this energy range corresponds to E_{rk} and its $\sim 0.85\ MeV$ (Figure 4.5).

The detection of the Keplerian resonant energy gives us a simple and practical method to calculate the plasma corotation fraction, f_c, at the orbital distance of Enceladus. Because at E_{rk}, $\omega_{rk} =0$, Equation 4.1 gives,

$$f_c = \frac{\omega_k + \omega_{gc}}{\Omega}, \tag{4.2}$$

where ω_{gc} is defined at E_{rk}. If the corotation was rigid (f_c), E_{rk} would have been around
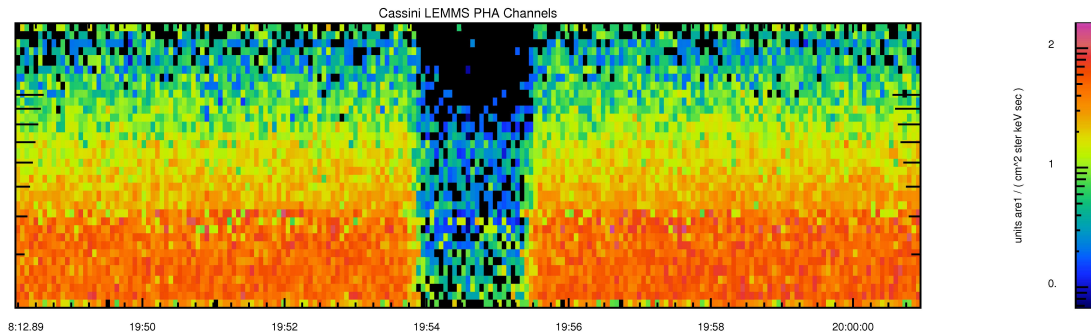
Figure 4.5: LEMMS PHA channel electron data from the close moon flyby to Enceladus on day 195 of 2005. The closest approach and the moon's wake is around 19:55, where a clear depletion of electron is seen. The actual wake is where electron fluxes go to zero (above ~ 0.85 *MeV*
. Depletions below that value correspond to a reduction of penetrating background (see text for explanation).

1 MeV. The fact that E_{rk} is lower than the expected value, in combination with Equation 4.2, suggests that plasma corotates at about 85-90% of the rigid corotation speed. The method is identical for downstream flybys, but in this case the electron depletion occurs below E_{rk}.

Combining data from all three close flybys of Enceladus that took place in 2005, it is estimated that f_c ~0.85. The upstream flyby of Dione (October 12, 2005) gave f_c =0.75 for the distance of Dione's orbit. For the close, downstream flyby of Tethys (September 24, 2005) this energy transition was obscured by MeV electron penetrating background (see next paragraphs for explanation). For the downstream flyby of Rhea at L=8.75 (November 26, 2005), this background source was absent but the fluxes of electrons above a few hundred keV, where E_{rk} was expected to be, were too low to detect this transition. For Mimas, Janus and Epimetheus, there were no close flybys. As a consequence, for these five moons f_c values were manually extracted from the study of *Saur et al.* (2004), where they modelled the radial profile for the azimuthal plasma velocity at Saturn's plasmasphere. A short summary of the f_c values used in this chapter for the distance of each moon is given in Table 4.1.

In Figure 4.5 an electron depletion can be seen even below E_{rk}. However, this should be impossible, given that these electrons have not yet being absorbed by Enceladus. What is actually seen corresponds to a background decrease: electrons around 1 MeV (that I refer to as "penetrating radiation") are so energetic that they can either penetrate the LEMMS structure directly or otherwise produce secondary radiation (Bremsstrahlung), that reaches to the various LEMMS detectors. This can be a source of a wrong signal that LEMMS cannot filter. As some energy of the penetrating radiation is deposited within the LEMMS structure, the resultant background appears at lower energies than the original penetrating particles and affects primarily the keV electron and ion channels. However, during the Enceladus flyby, this penetrating radiation was absorbed by Enceladus: its absence therefore appeared as a dropout in the low energy channels of LEMMS. This shows that at low L values, the total signal of LEMMS's low energy has notable contributions from background sources.

Using a similar method for the rest of the close moon flybys or for several flybys at intermediate distances, it is therefore possible to get an estimation of the penetrating radiation and noise in the low energy LEMMS channels, as a function of distance. The result is shown in Figure 4.6.
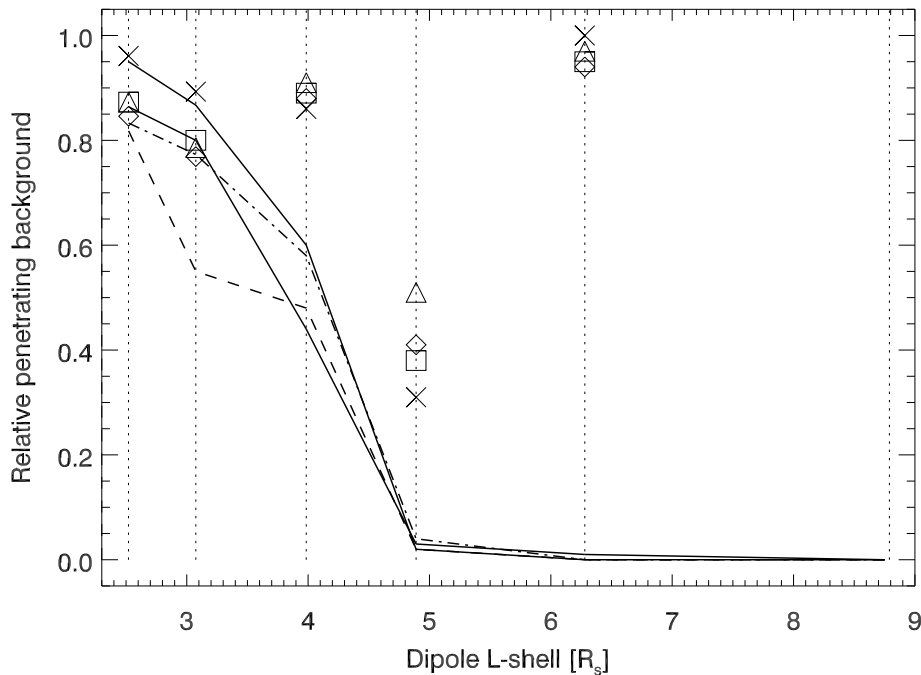
Figure 4.6: Relative contribution of penetrating radiation to the count rates of the C-channels. Continuous lines correspond to C0-C3 channels (solid: C0, long dash: C1, short dash: C2, dash-dot: C3). Unconnected points correspond to C4-C7 channels (diamonds: C4, triangles: C5, squares: C6, x: C7). As expected, penetrating radiation increases at low L. Foreground keV fluxes are sufficient to extract information through C0-C3 channels for $L > 4.5$. C4-C7 are in many cases dominated by penetrating background, although the high values at the distance of Dione could have alternative interpretations (see text for explanation). Most of this information was extracted through data from close flybys at Enceladus, Tethys, Dione and Rhea. At Mimas, Janus and Epimetheus, the estimated penetrating radiation contributions are only lower limits, as these come from observations of diffused MeV microsignatures.

Based on these estimations, it was decided to use data mainly from C0-C3 of the C-channels and from E3-E6 of the E-channels. In the analysis that follows, a percentage of the total flux is subtracted from each channel's measurements based on what it is plotted in the Figure 4.6. For E-channels it was decided to make no subtraction in this case.

A similar analysis for the ion channels showed that inside the orbit of Dione, energetic ions are almost absent and the respective measurements of LEMMS are almost purely penetrating radiation. This shows that energetic ions are filtered while diffusing radially inwards, probably by the interaction with the neutral gas torus which is produced primarily by Enceladian activity.

Results shown in Figure 4.6 should be interpreted carefully. The values of ~70% of penetrating radiation in C0-C7 at $L < 3.5$ and that of ~90% for the C4-C7 at the orbit of Dione do not suggest that LEMMS measures only background. Rather than that they imply a very low foreground signal of keV electrons at $L < 3.5$ due to a possible electron filtering effect suggested a number of studies (*Van Allen et al.* 1980a, *Chenette and Stone* 1983). This decreases significantly the signal to noise ratio for thee LEMMS detectors at these distances.

The absence of a few hundred keV electrons at Dione leads to a similar picture for C4-C7. Furthermore, subcorotation at Dione's distance results in very low values of E_{rk}. The high relative background values of channels C5 to C7 could be attributed to misinterpreting the direction of motion of the C5-C7 electrons with respect to the moon.

Such an analysis cannot reveal the full extent of penetrator contributions which relate to many parameters, such as the absolute MeV fluxes and the parameters upon which they depend (time, radial distance, latitude, and local time). Spacecraft orientation can be also important: LEMMS is better shielded if it is pointed in the direction of Cassini's own wake. These values help to construct a more realistic picture of the LEMMS measurements at low L values. Together with the calculation of the corotation fractions it is already shown how electron microsignatures can be a valuable tool for magnetospheric and even instrumental analysis.

4.2.1.2   Ions

The fundamental difference between the energetic ion and electron drift motions is the fact that ions have the direction of gradient and curvature drift along the direction of corotation. As a consequence ions drift faster than the cold plasma, whereas electrons slower, as it was demonstrated in the previous section. For this reason, ions cannot become resonant with the Keplerian motion, except for L-shells lower than 1.86 R_s (where Keplerian motion is faster than the cold plasma corotation).

The ion gradient and curvature drift velocity increases with energy. For very high energies (tens of MeV), ions can circle the planet in very short periods (a few hours or even minutes). Equally, this means that the mean encounter time between an ion and an icy moon is very short. The mean encounter time can be estimated by $t_{rk} = \frac{2\pi}{\omega_{rk}}$.

Depletion regions in the fluxes of ions with $E > 10$ MeV are not initially sharp or deep, as for energetic electrons. A large percentage of such ions can escape absorption by the icy moons due to gyroradius and bounce motion effects (see next section for more details). However, these shallow absorption regions reencounter again the moon in a short time before diffusion processes had any significant effect on them. Therefore, they progressively become deeper, until an equilibrium is reached between ion diffusion and ion depletion (steady-state situation). It is observed that for all moons this equilibrium is not reached: the ion depletion is almost 100% around the moon orbits. This means that ion absorption rates are always faster than diffusion. For this reason, no ions of $E > 10$ MeV exist along the L-shells of Janus, Epimetheus, Mimas, Enceladus, Tethys and Dione. At these locations, ions are absent in almost all magnetospheric local times and latitudes, independently of each moon's location. These regions are referred to as "ion macrosignatures". These are shown in Figure 4.7.

The data reveal clear depletion regions associated with the moons Janus, Epimetheus,
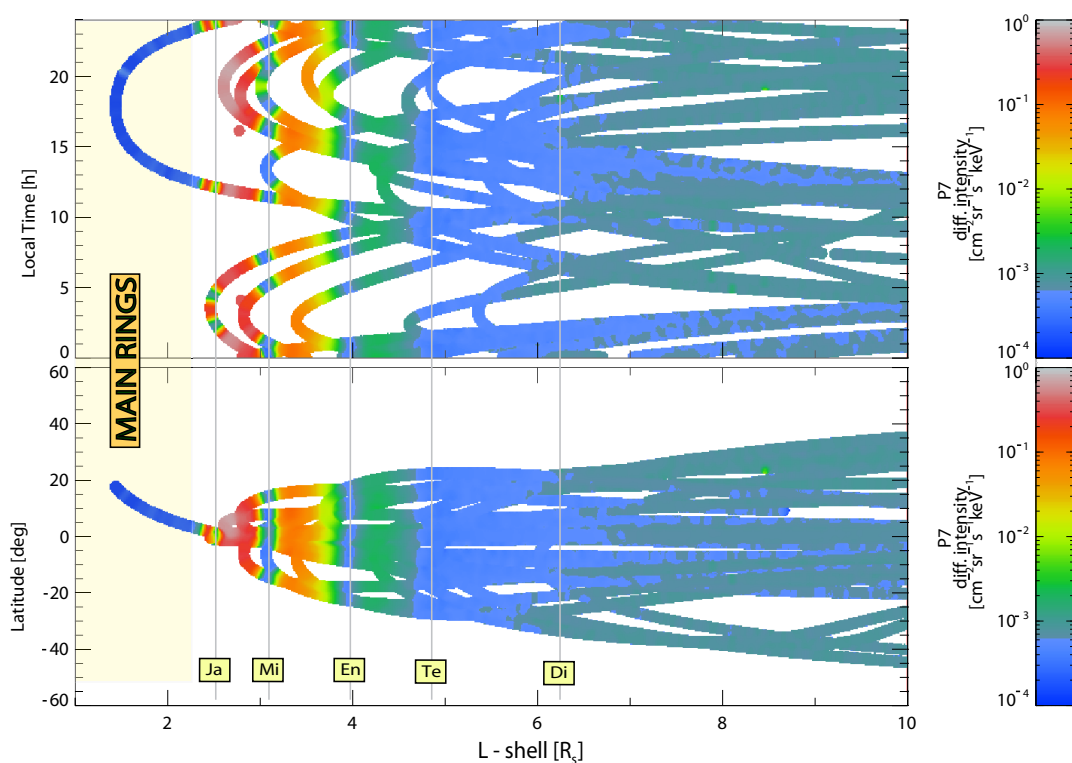
Figure 4.7: Ion macrosignatures as a function of L-Shell (x-axis) and local time (y-axis, top) and latitude (y-axis, bottom). The color denotes the ion fluxes of the LEMMS P7 channel, that detects ions with energy greater than about 10 MeV/nucleon. The macrosignature locations show an excellent correlation with the L-shells of the moons Janus, Epimetheus, Mimas and Enceladus. Data shown correspond to the period July 2004-July 2007 and are averaged every 86 s.

Mimas and Enceladus, at all local times and latitudes in the MeV ions. A more diffuse depletion region, at all local times and mainly for equatorial latitudes is also present between the orbits of Tethys and Dione, where fluxes are at background levels ($\sim 10^{-4}$ in differential intensity units). For greater L-values (L> 7) P7 measures an almost constant flux of about $\sim 10^{-3}$ cm^{-2}sr^{-1}s^{-1}keV^{-1}. A closer investigation reveals that this flux is measured at even larger distances in or out the magnetosphere, suggesting that the source is probably high energy, cosmic rays. The depletion of these cosmic ray particles between the orbits of Tethys and Dione could be due to several reasons:

- The depletion might occur at the surfaces of Dione and Tethys. The reason that the depletion appears between the orbits of these two moons could be explained by increased diffusion rates (which increases its radial extent) and the large gyroradii of the MeV, cosmic ray ions at these distances (which increases the effective region that they can be absorbed). However, depletion at the surfaces of the moons requires that these ions are initially trapped. The impact probability of an MeV ion with Dione and Tethys is very small and therefore depletion of MeV ions at all local times requires at least several hours to be completed (*Paranicas and Cheng* 1997).

However, cosmic ray particles are most likely transient from the magnetosphere since their flux is almost constant for all L> 7, even in the solar wind.

- The depletion might result from the absorption of these ions by the E-ring dust, the density of which starts to peak inside Dione's orbit. However, as cosmic ray particles are transient, they cross the E-ring plane once or only a few times. The column mass that needs to be crossed by a proton of about 10 MeV in order for a significant part of its energy to be lost is about $\sim 10^{-2}$-$\sim 10^{-1}$ g cm^{-2}. Based on the mass estimations for the E-ring (e.g. *Hill* (1982)) and assuming that most of its mass is distributed between 3 and 7 R_s, its mean column mass is less than $\sim 10^{-9}$ g cm^{-2}. This means that a 10 MeV proton would need to cross the E-ring plane millions of times in order to be absorbed. Crossing it only once will remove just a negligible fraction of its energy. An exception to this would be the case that the grain size distribution of the E-ring extends to sizes of centimeters or decimeters, with relatively low number densities of grains at these sizes. Such a population could add significant mass to the E-ring but could go unnoticed in photometric observations, from which estimates of the ring's mass can be extracted. In this case, the necessary column mass to absorb the ion energy is contained only in few grains, meaning that the number of encounters can be significantly reduced (see also Chapter 5). This is, however, contradictory to the results of detailed studies on the E-ring's grain size distribution or the propagation of dust from its main source, Enceladus (eg. *Juhász et al.* (2007)). Furthermore, it is very likely that the constant flux measured by LEMMS for very energetic ions corresponds to protons with energies in the range of 100 MeV (*Van Allen* 1983). This makes the interpretation of absorption by dust even less likely.

- A third possibility is that this extended depletion region is a "shadow region" for cosmic ray particles. The planet's volume, including that of its main rings, in combination with Saturn's magnetospheric field, can create forbidden regions within the magnetosphere for cosmic ray particles. This could explain why the constant flux of MeV ions observed in and out of Saturn's magnetosphere disappears only in several locations within L> 7. Forbidden regions for incoming cosmic rays at the Earth have been studied in great detail by tracing back cosmic ray particles on the so-called Störmer orbits. Examples are shown in the two panels of Figure 4.8. To evaluate whether this explains the flux dropout around Dione's orbit, the Störmer theory should be applied and particle trajectories should be calculated using a magnetic field model for Saturn's magnetosphere. The presence of Saturn's main ring system makes the problem of mapping the forbidden regions unique in the solar system.

Back to Figure 4.7, it can be seen that between the macrosignatures of the inner Saturnian satellites, fluxes of P7 ions are 2-3 orders of magnitude higher that in the outer regions of the magnetosphere. As the 100% ion depletion within the ion macrosignatures indicates that diffusion is slow and ions cannot cross the orbits of these moons, the source of these high fluxes cannot be radial diffusion from the outer magnetosphere.

At a given L-value, these high fluxes appear to be identical, at all local times and latitudes. This means that the angular distribution of these ions is almost isotropic, since to
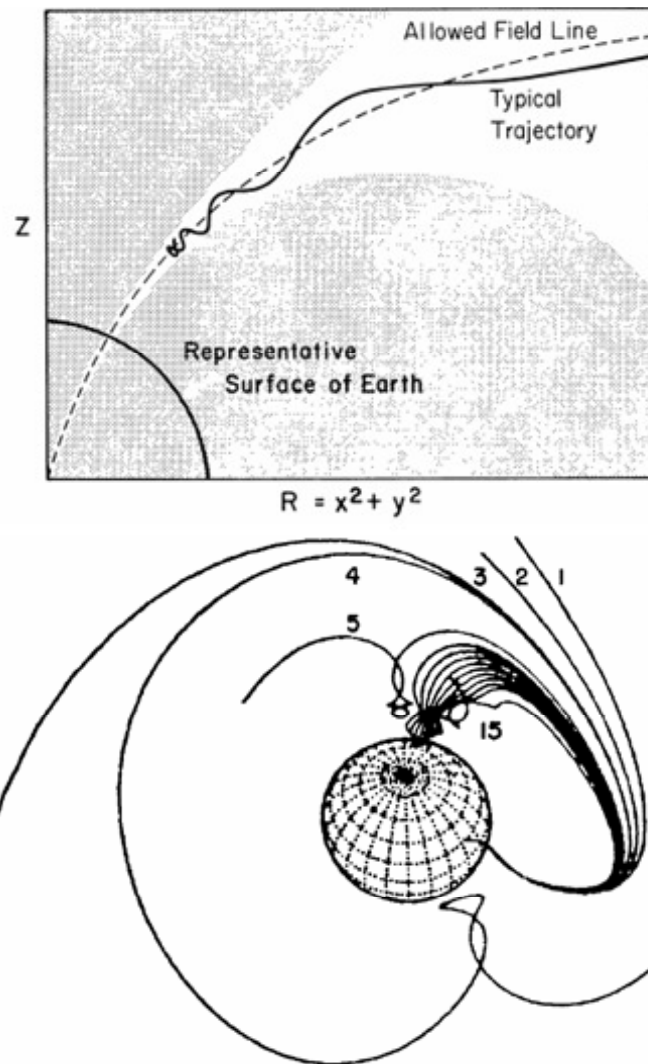
Figure 4.8: (Top) Meridian plane view of a cosmic ray particle trajectory along an allowed field line of Earth's magnetic field. The shaded regions denote areas forbidden, based on the Störmer theory. Plot extracted from *Hofmann and Sauer* (1968). (Bottom) Illustration of charged particles of different energies traced backwards from the same location on the Earth after being ejected vertically. Trajectories 1-3 corresponding to very high energy particles are allowed to reach that point of the Earth. Lower energy particles can impact the Earth, however in some cases (trajectory 15) they can escape after a series of complex loops. Figure extracted from *Smart et al.* (2000).

construct this plot no angular (or pitch angle) filter was used, and Cassini's orientation varied significantly in this region, during the various crossings from which this data was collected. This is again inconsistent with ions being transported at low L and being energized by radial diffusion, as this process tends to make pitch angle distributions more equatorial and not isotropic.

This simple application therefore shows how the observation of deep, ion macrosignatures can reveal the presence of an isotropic MeV ion source in the inner radiation belts. This source could have its origin in the CRAND process (Cosmic Ray Albedo Neutron Decay), where MeV ions are produced as beta decay products of neutrons. The neutrons could originate from cosmic ray impacts on Saturn's rings or on Saturn's atmosphere (*Randall* 1994, *Cooper et al.* 1983). To identify the exact source it is then important to map the forbidden and allowed regions for cosmic rays in Saturn's magnetosphere.
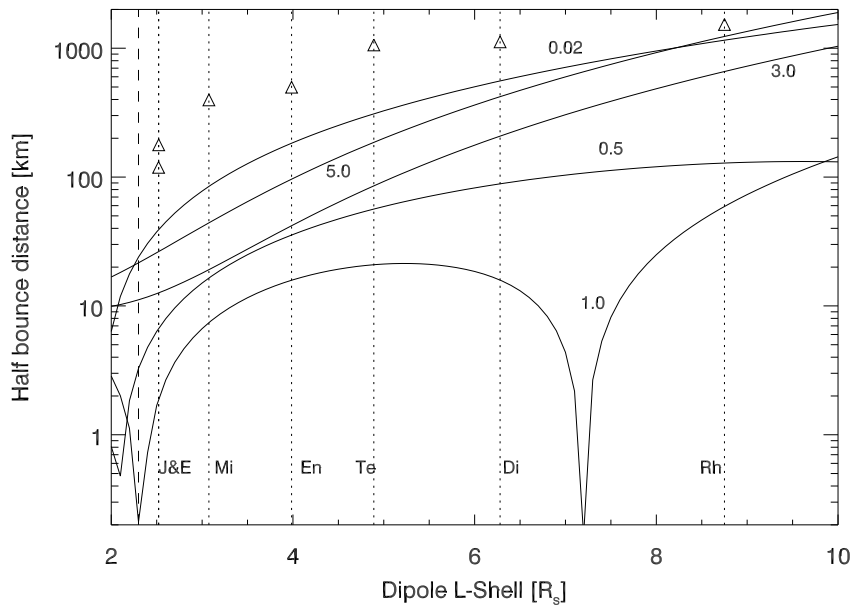
Figure 4.9: Absolute value of half bounce azimuthal distance that is transversed by electrons of 0.02, 0.5, 1.0, 3.0 and 5.0 MeV, with an equatorial pitch angle of 10°, as a function of L. The distance is given in a coordinate system that corotates with the Keplerian velocity of a circular, equatorial orbit, at each L. Triangles indicate the diameter of the seven icy moons of Table 5.1. We see that in every case the particles drift shorter distances than the moons' diameters. The peculiar shape for the 1.0 MeV curve is because electrons become resonant with the Keplerian motion at two L values. The vertical lines are the same as in Figure 4.4.

4.2.2   Particle bounce and gyration motion

For these two elements of motion, again significant differences exist for electrons and ions. Electrons within the energy range of LEMMS have much smaller gyroradii than the icy moons' radii. Therefore, if the electron's guiding center intersects the moon, the electron is practically absorbed. On the other hand, non 90° equatorial pitch angle electrons can escape absorption if the azimuthal path they traverse during half a bounce period is greater than the diameter of the absorbing moon.

Figure 4.9 shows that even for nearly field-aligned particles with high bounce periods, the path traversed (for energies between 20 keV and 5 MeV) is always smaller than the di-
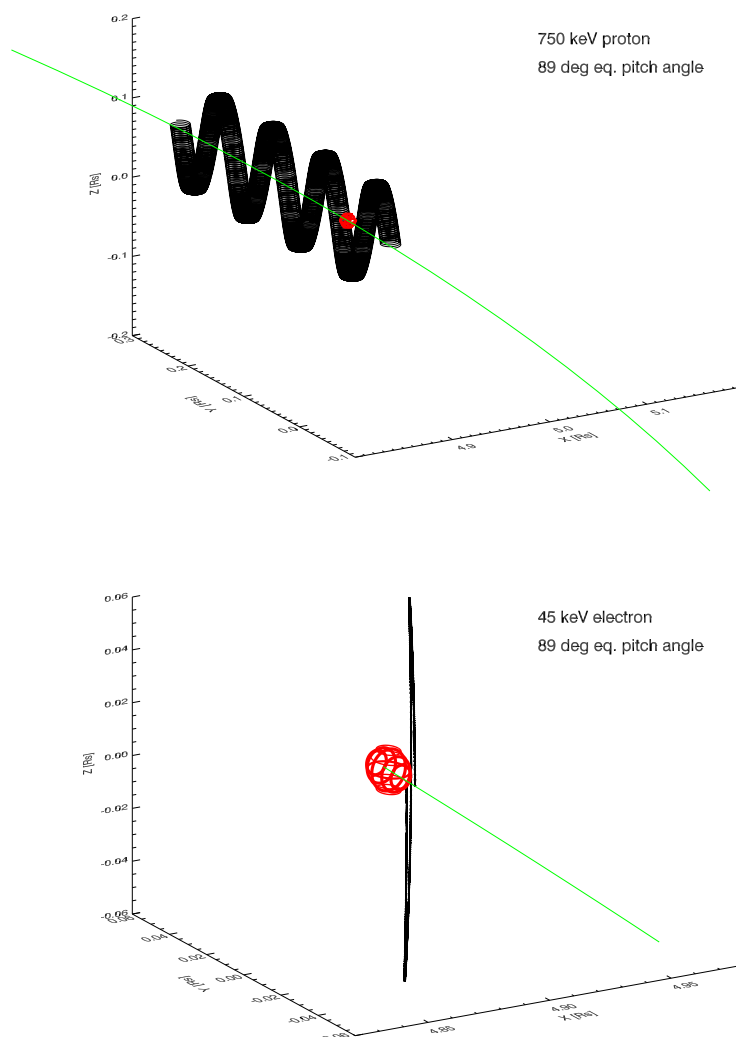
Figure 4.10: (Top) The motion of an equatorially mirroring, 470 keV proton, at the orbital distance of Tethys: Tethys is indicated by the red sphere and its orbit by the green line. The injected proton (at [4.89,0, 0] R_s) avoids absorption mainly due to the bounce motion, which for a 470 keV proton has a period of about 70 sec. The gyroradius of the proton is also comparable to the size of Tethys, a fact that can further reduce the possibility of absorption by the moon. (Bottom) Same plot for a 45 keV electron: in this case, the electron, due to its slower drift velocity compared to that of the ion, and to the rapid bounce motion (7.9 sec bounce period) cannot escape absorption by Tethys. The gyroradius of the electron (few km) cannot be resolved in the scale of this plot.

ameter of the icy moons. Therefore, it is reasonable to assume that all energetic electrons are lost when their guiding center field line passes through the moon.

On the other hand, ion gyroradii can be much larger than the icy moon radii. Furthermore, as ions drift faster than corotation the half bounce distance of energetic ions

is usually larger than the diameter of the moons and can easily escape absorption (*Fillius* 1988). As a result, energetic ion microsignatures are not expected to be observed in the LEMMS dataset. The difference between the energetic electron and ion absorption is illustrated in Figure 4.10.

4.3   Additional examples of electron microsignatures

While several examples of both micro- and macrosignatures were presented in the previous sections, data analysis in this chapter is primarily based on electron microsignatures. The primary reason is that electron microsignatures can be more easily resolved, as initially electron flux tubes are depleted completely of energetic electrons and can survive longer. On the other hand, only small fraction of energetic ions from those crossing the moon's location, are absorbed and any depletions would be shallow and hard to separate from magnetospheric fluctuations. In addition, as discussed in Sections 1.2 and 4.2.1.1, the signal to noise ratio of energetic ions inside the orbit of Dione is very low, as energetic ions are depleted due to charge-exchange reactions with Saturn's neutral gas. Energetic ions are particularly interesting for analysing macrosignatures, which are however time independent features and therefore the extraction of diffusion rates from their study is more complicated.

To illustrate some additional basic features of microsignatures in the Saturnian magnetosphere, several more examples are presented in this section. I first show several events of energetic electron microsignatures at Tethys and Enceladus.

4.3.1   Low energy electron microsignatures at Tethys

With a radius of 530 km, Tethys (Figure 4.11) is one of the largest satellites of Saturn and the source of well-defined microsignatures seen during the Voyager 2 flyby (*Carbary et al.* 1983).

Its orbit is circular and almost equatorial, at a distance of 4.89 R_s from the center of Saturn. It possesses two Lagrangian objects, Telesto and Calypso, with a radius of 12 and 10 km in the trailing and leading Lagrange points, respectively. Corotating Lagrange objects have been discussed in the past as possible sources of other moon microsignatures (*Simpson et al.* 1980, *Van Allen et al.* 1980a).

Tethys lies in a region where the deviations from the magnetic dipole field start to increase significantly: Voyager 2 detected the Tethys microsignature at L=4.80 (*Vogt et al.* 1982), where L is the dipole L-shell. Magnetospheric currents seem to contribute significantly to this deviation (*Connerney et al.* 1981, *Van Allen et al.* 1980b). *Randall* (1994) and *Maurice et al.* (1996) have also indicated the presence of a local time asymmetry in the electron intensities of the inner magnetosphere. All these are expected to be reflected in the location of the absorption features from Tethys and all the moons of the inner magnetosphere that orbit beyond ~5 R_s (e.g. Dione and Rhea).

Here several examples are shown to illustrate the characteristics of the low energy electron microsignatures in the vicinity of Tethys' L-shell. Electrons with $E < E_{rk}$ are referred to as low energy electrons in this case study. Data shown are collected from the first seven orbits of Cassini (July 2004 - April 2005).
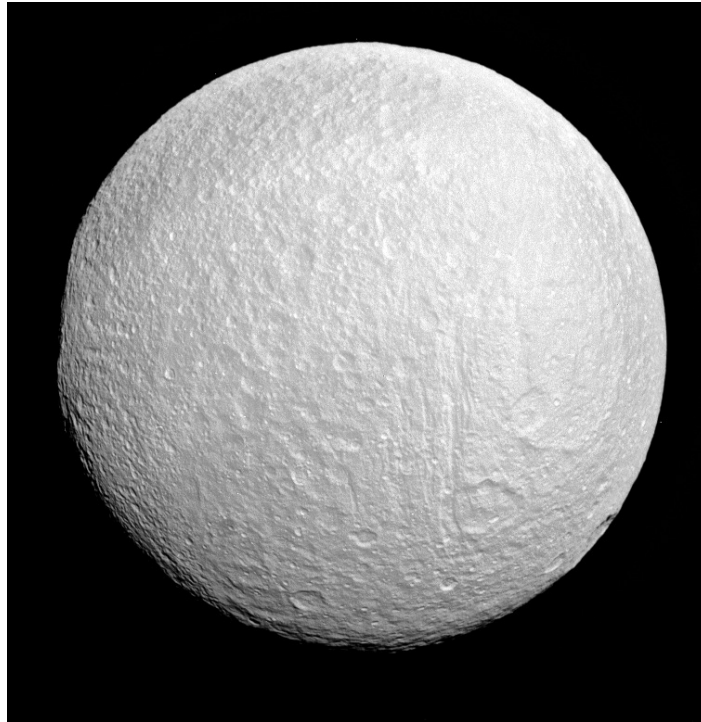
Figure 4.11: Tethys full disk image by Cassini. Image credit: NASA/JPL/Space Science Institute

During this time period, Cassini crossed Tethys's L-shell 12 times and data were available for the 11 of these. All crossings revealed single or multiple absorption features in the low energy electrons. In five cases, the microsignatures were very deep and sharp. Figure 4.12 shows some of the characteristics of most of these strong microsignatures. The feature at 3:46 is deep, sharp, with a radial extent only slightly greater than Tethys's diameter, as expected, based on the analysis presented in section 4.2.1. The results from the 11 crossings are summarized in Table 4.2.

While these characteristics were more or less expected, there are several additional remarkable observations. As can be realized from Table 4.2, microsignatures are usually displaced from the expected L-shell. In some cases, this displacement (ΔL) is more than 0.3 R_s. Also, the exact microsignature location seems to depend on the particle's energy and, in a few cases, double microsignatures appear in the same energy channel during the same crossing (Figures 4.12).

No absorption signatures were seen in channels C4-C7 and E0-E3 (>100 keV). The finding of low signal to noise ratio for C4-C7 in Section 4.2.1.1 is consistent with this observation. The absence in E0-E3 is less expected, although these channels have higher signal to noise ratio. Ion microsignatures were also absent from the data, which was expected, as discussed in the previous sections.

The three cases where double microsignatures have been detected (see Table 4.2) can be interpreted in various ways. For the event of day 16 of 2005 Cassini's periapsis was at the distance of Tethys, and for a certain period the spacecraft's path was almost parallel
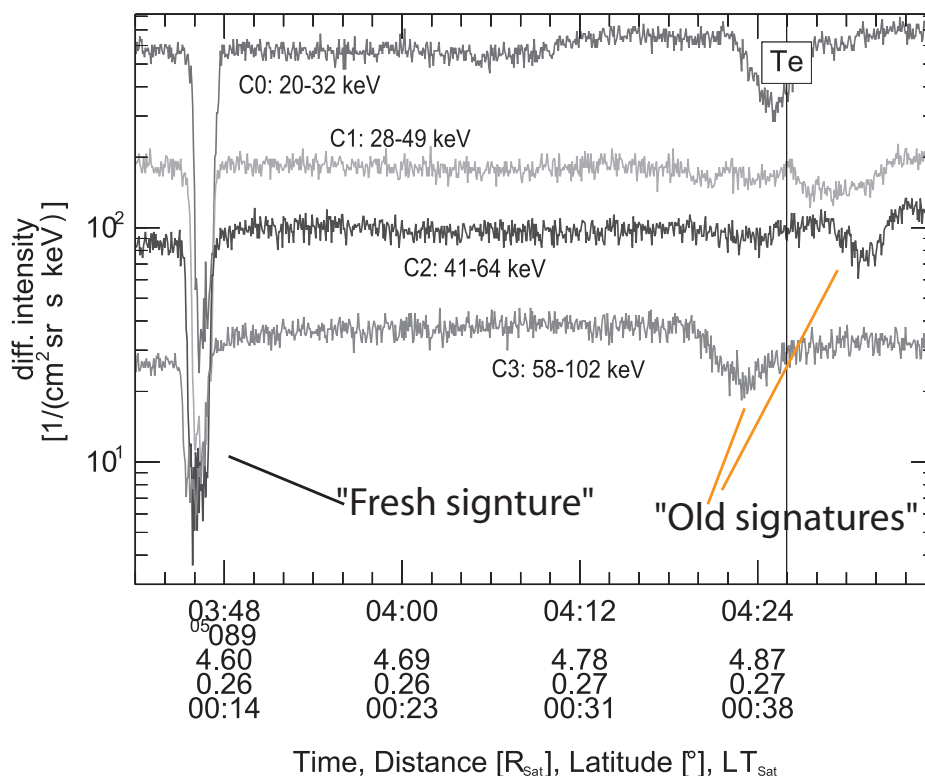
Figure 4.12: Multiple microsignatures in the C-channels during the Tethys L-shell crossing on day 89 of 2005. The sharp absorption feature at 3:46 originates Tethys and it is freshly formed. The vertical line at 4:26 indicates the expected time for Tethys' L-shell crossing. Around that time, several more aged Tethys absorption signatures are seen, with random displacements as a function of energy, around the expected L-shell crossing time. Local time values are given with respect to local noon (12:00)

to a portion of the moon's L-shell. In this case, small-scale fluctuations or temporal variations in the drift shell's shape become important: Cassini's motion almost parallel to Tethys's disturbed L-shell would lead to multiple crossings within a short time interval, and to the recording of the double microsignatures in the same channel.

The interpretation of double microsignatures should be different if the L-shell crossing geometry is not the one discussed above. That is the case for the features seen during days 47 and 89 (2005). In the former event (Figure 4.3.1), all microsignatures have similar depths and widths and therefore, probably similar ages. It can be assumed that during the formation of these absorption features, the variability of the magnetosphere was such that Tethys was "exposed" to a large range of electron drift trajectories within a short period. This caused the simultaneous formation of depletion regions, for the same species and energies, in different L-shells. Such a process could occur during a magnetospheric injection or compression event.

The double microsignature on day 89 (Figure 4.12) could not be explained in a similar way. Microsignatures do not have comparable depths and therefore have different ages. The source of the deep feature is definitely Tethys. The shallow features correspond to an old Tethys microsignature, despite the values of $\Delta\lambda$ suggesting that Cassini is in a good

Table 4.2: Summary of Tethys's L-shell crossings where microsignatures have been seen. For $\Delta\lambda$ close to 360°, Cassini is crossing the moon's wake. Negative ΔL denote inward displacements, the opposite for outward displacements. For multiple microsignatures or for microsignatures which their location shows strong energy dependence, multiple ΔL values are given. For crossings marked with a "*", almost full pitch angle coverage was available.

Expected L-shell crossing time (yyyy.dddhhmm)	$\Delta\lambda$ (Tethys-Calypso-Telesto) (deg)	Local Time (hh:mm)	ΔL (R_s)	Additional remarks
2004.1822225(*)	64-4-125	10:19	-0.1	90° pitch angle depletion also present. Variations in fluxes.
2004.1830705(*)	262-202-323	02:06	-0.3	Large flux variation.
2004.3500729	143-79-204	20:20	0.4	Deep signature. Could originate from Tethys or Dione.
2005.0160535(*)	138-74-199	18:30	0.05/0.2	Multiple microsig-. natures. 90° pitch angle depletion (*Roussos et al.* 2005)
2005.0160726(*)	132-68-194	19:45	0.08	90° pitch angle depletion (*Roussos et al.* 2005)
2005.0472008	91-27-152	15:30	0.05/0.35 -0.2	Strong energy dependence of microsignature location (Fig. 4.3.1).
2005.0480546	32-329-93	00:40	-0.15	Cassini rotating.
2005.0680651	30-326-91	15:30	0.2	Deep signature.
2005.0681628	331-267-32	00:40	-0.1	Deep signature. Cassini rotating. See also *Paranicas et al.* (2005).
2005.0881849	338-275-40	15:30	-0.05	Deep signature. Cassini rotating.
2005.0890426 microsignatures	279-216-341	00:40	-0.3/-0.05 0.05	Double microsignatures. See also Fig. 4.12.

position to record the sum effect of the drifted wake signatures from all three coorbiting moons. However, the small moons are not effective absorbers of electrons (see Chapter 5).

An estimate of $0.5\text{-}1.0 \cdot 10^{-9} R_s^2/s$ of the radial diffusion coefficient based on a single event (*Paranicas et al.* 2005), further supports what LEMMS data show: observed microsignatures do originate from Tethys and survive for more than one full orbit. The deep
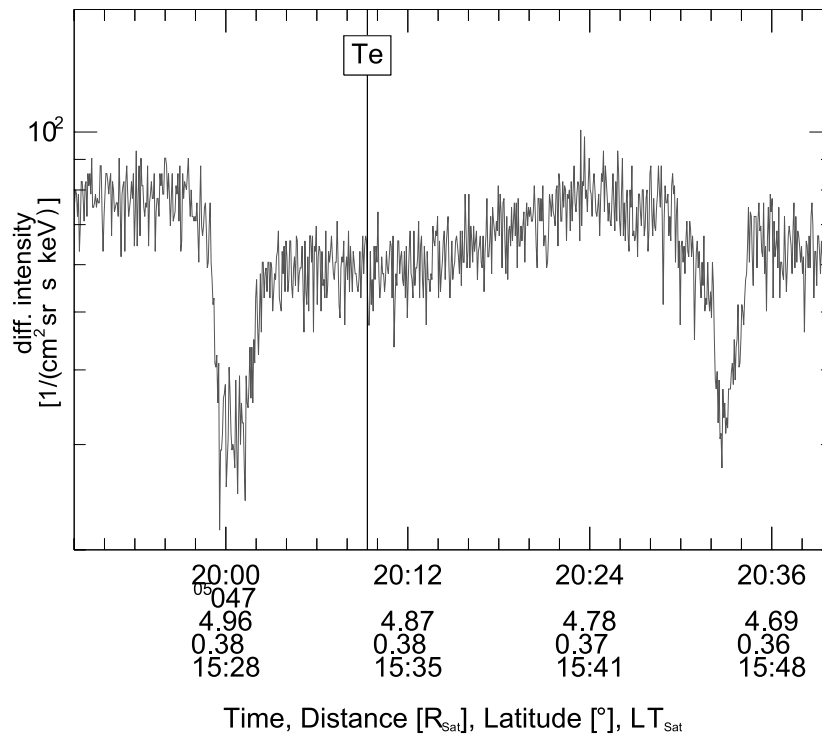
Figure 4.13: Double signature in the 28-49 keV channel (C1) seen during the L-Shell crossing of day 47 (2005). The fact that both signatures have similar geometrical characteristics suggests a possible simultaneous formation during a variable phase of the magnetosphere.

features seen ~30° upstream during the crossings of days 48 and 68 (06:51) of 2005, as well as the double signatures of day 89 prove that. Also interesting is that the microsignature during day 48 showed an inward displacement. The day 68 crossing, which had the exact same geometry with respect to Tethys, but occurred at a different local time, showed an outward displacement and, for certain energy channels, dissimilar depths compared to day's 48 feature. This is further evidence for the non-circular drift shells and for time variability of the radial diffusion rates.

In summary, through this short case study at Tethys, it has been realized that:

- Electron microsignatures from Tethys in the 20-100 keV energy range are almost always found during a crossing of the moon's L-shell

- Radial diffusion rates should be small, given the fact that Tethys' microsignatures are found in large longitudinal separations from the moon. In many cases, double microsignatures (one newly formed, and one older that has survived more than one rotation around the planet) are identified in the data.

- The location of electron microsignatures does not coincide with the predicted position, based on drifts on a purely dipole field. This means that electron drift shells are not circular.

- The displacements from the Tethys's L-shell are much larger than those predicted by magnetic field models. There are also hints for a local time dependence of the displacement direction.

- Microsignatures are rare in channels that measure electrons above 100 keV. This could be an instrumental effect, associated with the low signal to noise ratio of these channels.

4.3.2   Enceladus's keV and MeV electron microsignatures

Enceladus orbits Saturn inside the orbit of Tethys, at about 3.95 R_s. After three close flybys of the moon by Cassini in 2005 and several imaging campaigns it was realized that Enceladus is geologically active and is the primary source of dust and gas for Saturn's E-ring. More specifically, a source of dust and neutral gas was identified at the moon's south polar region (*Porco et al.* 2006, *Spahn et al.* 2006). The ionized products of this region were sufficient to create a strong interaction with the magnetosphere as it was first realized through the magnetometer data (*Dougherty et al.* 2006). Given that in the previous case study I analyzed microsignatures from an inert moon, it is interesting to investigate the complexities introduced in the microsignature structure and evolution by a large scale electromagnetic obstacle.

For this purpose, it is important to first understand the process of particle diffusion, which is considered to be the primary source of the energetic particle microsignature refilling.

The dynamics of such population differ from that of a low energy MHD fluid. The dynamical behaviour of energetic particles is to a significant extend controlled by the magnetic drifts which are negligible for the low energy plasma, as discussed in Section 1.3. Furthermore, the energy gap between the cold plasma and the energetic particles is very large (tens to hundreds of keV). A dropout in the energetic particle population cannot be "refilled" by simply energizing the more abundant, low energy particles through processes that can occur in the moon wakes (discussed in more detail in *Chapter 6*).

For instance, the plasma absorption by an icy moon (at all energies) introduces a decrease in the total plasma pressure. As a consequence, an electric field associated with a gradient in plasma pressure will drive charged particles back into the cavity and in the same time accelerate them. This acceleration, however, does not add more than several tens of eV to the total energy of the particles (see *Samir et al.* (1983) and *Chapter 6*). Such an energy gain is negligible compared to the total energy of the energetic plasma (especially electrons). This means that only "pre-existing" energetic particles refill the energetic particle cavities. The dominance of magnetic drifts will also "shadow" the effects of this electric field, meaning that wakes in low energy plasma will probably have different lifetimes than at high energies.

A series of examples shown in Section 4.3.1 show that energetic electron microsignatures have long lifetimes, probably much longer than at low energies (no relevant observations have been reported). This suggests that at long distances from the absorbing moon, these microsignatures exist as independent structures. As energetic electrons in the radiation belts of Saturn have very low densities and negligible contribution to the plasma betas (*Maurice et al.* 1996), no electromagnetic field disturbances can be found

associated with their presence. Therefore, the refilling of these cavities will occur due to a current that results from a gradient in the particle flux at the specific energy range of the absorption. This current, j, is mathematically expressed by Fick's law: $j = -\nabla f$. Fick's law can be directly transformed to the form of the diffusion equation:

$$\frac{\partial f}{\partial t} = D \, \nabla^2 \, f, \tag{4.3}$$

where D is, in this case, the local magnetospheric diffusion coefficient.

Particle diffusion is associated with the violation of one (or more) of the adiabatic invariants relevant with charged particle motion in a dipole field. Invariance is violated if perturbations act on the particle motion in time scales shorter than the period of each motion element. The invariants associated with the bounce motion and the gyration require perturbations that act in periods shorter than a few seconds or milliseconds to be violated, respectively. Such a process leads to pitch angle and/or azimuthal diffusion, and results from wave-particle interactions. Azimuthal diffusion can be neglected, according to *Simpson et al.* (1980).

What is commonly violated in planetary magnetospheres (including that of Saturn) is the third adiabatic invariant. This is associated with the drift motion around Saturn that has a period of several hours. This leads to radial diffusion of the charged particles, which is believed to be the most important process refilling the energetic electron microsignatures. As the scale of the microsignatures is of the order of $10^{-2}R_s$, it is more appropriate to say that microdiffusion refills them. Even if other diffusive processes exist, they cannot account for this refilling as they transport electrons at larger spatial scales. Therefore, whenever I mention radial diffusion in this study, unless otherwise stated, I refer to microdiffusion.

Let $t_{rk} = \frac{\Delta\theta}{\omega_{rk}}$ the time that an electron of certain energy and pitch angle needs to cover the azimuthal angular separation, $\Delta\theta$ (in radians), between the icy moon and the absorption region, with the moon/electron relative drift frequency, ω_{rk}. At $t_{rk}=0$ the absorption region should have the shape of a square well, with an extent equaling the moons diameter, that is $2R$, where R is the moon's radius. Based on the discussion above, it can be assumed that only radial diffusion primarily shapes the absorption signature profile. Then, Equation 4.3 can be reduced to one dimension, the solution of which has been found by *Van Allen et al.* (1980a):

$$f = 1 - 0.5 \left[erf(\frac{1 - x/R}{\sqrt{\tau}}) + erf(\frac{1 + x/R}{\sqrt{\tau}}) \right], \tag{4.4}$$

where $\tau = 4D_{LL}t_{rk}/R^2$. D_{LL} is the radial diffusion coefficient, and x is the radial displacement from the center of the signature. The parameter f corresponds to the normalized differential intensities or count rates of the LEMMS detector. The normalization can be carried out with respect to the maximum value just outside the microsignature, after the data are detrended and the penetrating background is removed. An illustration of Equation 4.4 profiles for different values of τ is shown in Figure 4.14.

Modelling the shape of the observed microsignatures with the profile given by Equation 4.4, radial diffusion coefficients could be determined. Furthermore, if the theoretical and the measured profiles don't agree, this would suggest additional processes and factors,
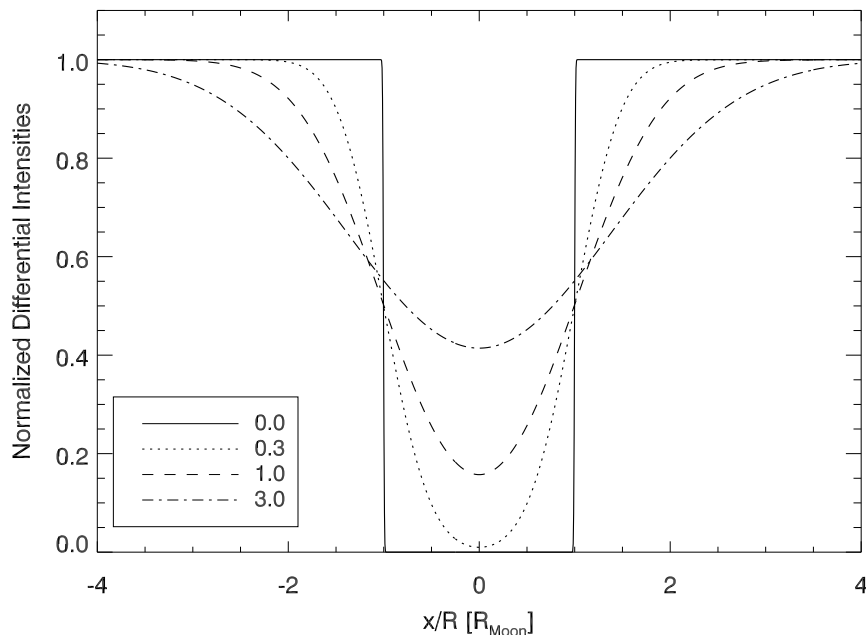
Figure 4.14: Microsignature erosion by particle diffusion according to Equation 4.4. Each linestyle corresponds to a different τ value, indicated in the plot legend.

other that radial diffusion, are eroding the microsignature signal. Enceladus's microsignatures proved to be an ideal target for such an application.

Electron microsignatures of Enceladus (in normalized counts per second, CPS) observed during Cassini's first 14 orbits around Saturn are shown in Figure 4.15. Panels (a) to (f) show 28-49 keV low-energy microsignatures downstream of Enceladus in the corotational flow. Panels (g) to (l) show upstream microsignatures, above E_{rk} with (j) to (l) showing the sharp depletions from the three close flybys. The center panel shows each event's longitudinal separation from Enceladus. Triangles denote observed microsignatures, diamonds show crossings where data gaps or spacecraft rotations preclude interpretation, and squares denote periods during which no microsignature was observed in the available data. In the latter cases, a microsignature may possibly have been present but could not be observed due to instrumental effects (e.g. increased penetrator fluxes).

Starting from the bottom panels, where upstream microsignatures are illustrated, it can be seen that MeV electron microsignatures, including those of the close flybys on days 48, 68, and 195 of 2005 (4), consistently follow the profile of Equation 4.4 (this is also realized by fitting Equation 4.4 to the measured profiles). This means that these electrons, due to their high energy, behave as if Enceladus is insulating and atmosphere free. Furthermore, the refilling of the MeV electron depleted regions is driven by radial diffusion. Electron microsignatures in the MeV range seem to survive up to 60° upstream of Enceladus. The shallow depletion plotted in panel (g), 200° upstream, is a striking exception to these observations, which could mean that it possibly does not originate from Enceladus, but from another source (e.g. dust clump, ring arc formed on the orbit of
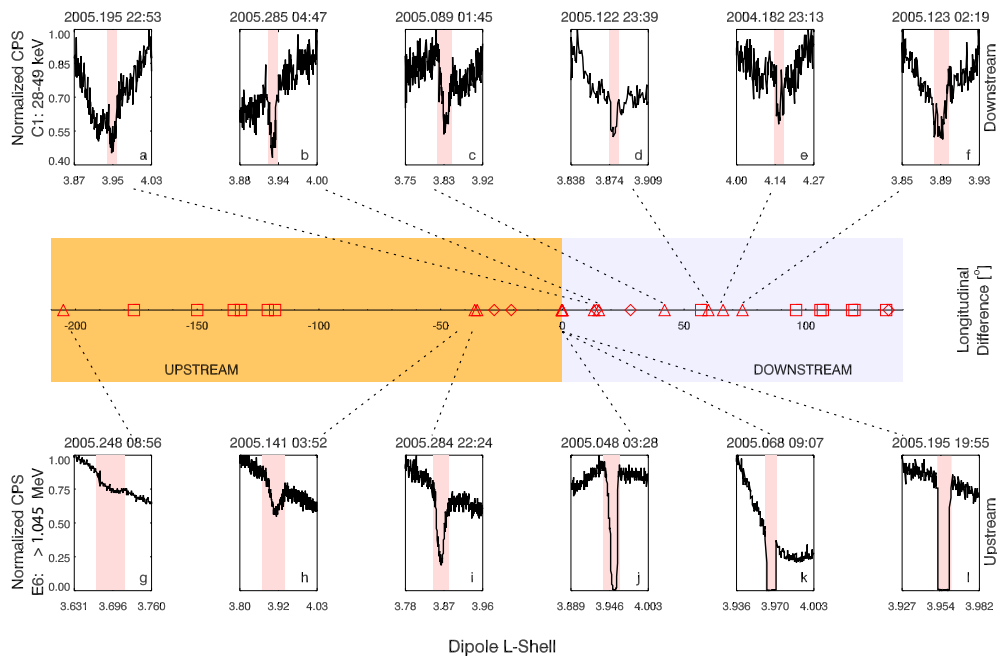
Figure 4.15: Enceladus microsignatures from the first 14 months of the Cassini mission. The top panel shows microsignatures downstream of Enceladus in the expected keV energy range, while the bottom panel shows microsignatures in the MeV energy range (above E_{rk}). See text for more detailed explanation.

an unknown moon? - See Chapter 5).

On the other hand, depths and radial extents of downstream microsignatures (top panels) are not in accord with their longitudinal separations and do not fit to the profile of Equation 4.4. Several microsignatures are flanked by a broad flux decrease: e.g. microsignature (a) which has the broadest observed width (16,000 km), was observed when Enceladus was definitely outgassing (*Dougherty et al.* 2006). Extended clouds of expelled ice particles and neutral gas would also obstruct electrons: a 1 μm ice dust particle can absorb a 20-30 keV electron with a single impact.

Furthermore, waves generated by the pickup of fresh ions originating at Enceladus and the E-ring could also increase pitch-angle diffusion rates considerably, due to wave-particle interactions. Such processes could be the source of the "mismatch" between the observed keV microsignature structure and the Equation 4.4 profiles. In this way, the electron signatures width and variable depths could signify changes on time scales of days or weeks in near Enceladian environment, the E-ring and its associated neutral gas torus. This variability is consistent with other Cassini observations (*Dougherty et al.* 2006) and ground-based E-ring observations (*Roddier et al.* 1998). Such a variability could originate from changes in Enceladus's cryovolcanic activity. A more extensive discussion can be found in *Jones et al.* (2006).

No downstream electron microsignatures have been seen at separations greater than 80°, while Tethys microsignatures persist over greater longitude ranges, as it was indicated in the previous section. Within the radiation belts, D_{LL} should increase according to the power law:

$$D_{LL} = D_o L^n, \tag{4.5}$$

where D_o is a constant and n is a positive dimensionless constant which defines the radial diffusion source (*Walt* 1994). For $n = 10$ the sources are magnetic field impulses while for $n = 6$ the drivers are electric potential fields.

This simple law tells us that at Enceladus D_{LL} should be lower than at Tethys and Enceladus's microsignatures should persist for longer time, however the opposite is seen. This is an additional indication that radial diffusion is not the sole process of refilling Enceladus's keV microsignatures. Identifying the exact source of the faster refilling would require a close, downstream flyby of Enceladus, which is planned to occur during Cassini's extended mission.

Electrons above the resonant energy are therefore lost in a predictable, steady way, whereas Enceladus's exosphere outgassing levels apparently influence lower energy electron signatures. All the close flybys to date have been upstream of Enceladus; an appraisal of the atmospheres influence on the structure of low-energy electron wakes requires future close downstream passes.

4.4   Statistical analysis of icy moon absorption signatures

With several electron microsignature examples analyzed, the next step is a statistical analysis of a collection of relevant events. The general concept of the analysis that follows is based on the described and discussed previous sections: As energetic electrons circulate in the radiation belts, they are continuously absorbed by the icy moons. The empty electron flux tubes will continue to "drift" in the radiation belts, with the properties of the pre-depletion electrons. Diffusive processes will tend to smooth out these regions. By studying the fill-in as a function of azimuthal separation from each moon (or equally, drift time), these processes can be assessed. This analysis is at the various moons at different L and electron energy in an attempt to extract the L- and energy dependence of the D_{LL}. In addition, by monitoring the L-shell of each microsignature with respect to the expected L-shell, electron drift orbits in the radiation belts could also be evaluated.

For the drift time calculation (t_{rk}) formulas given by *Thomsen and Van Allen* (1980) are used. We assume that the drift of the electrons takes place on circular orbits of $L + \Delta L/2$, where ΔL is the signature displacement from the expected location and L is the moon's L-shell (negative for inward displacements, positive for outward). Pitch angle information comes directly from the magnetometer experiment and data on the LEMMS sensor pointing. Although the observed displacement of the signatures is direct evidence that there are deviations from circular orbits (Section 4.3.1), displacements are only 3-5% of each moon's L-shell, on average. As a result, the t_{rk} calculation is not affected significantly. Equation 4.4 is appropriate to describe a monoenergetic microsignature, or, at least, a signature recorded in a detector of small energy width (C channels). The large energy width of the E channels imposes some complication that will be discussed at a later stage in this chapter.

4.4.1 Statistics and overview of observations

Up to the end 2005, Cassini performed 164 icy moon L-shell crossings and microsignatures were found in 74 of these, mainly in the keV electrons. Microsignatures detected in the E channels (MeV range) were less frequent and shallow, even for a few degrees azimuthal separation from the moons. The distribution of the L-shell crossings per icy moon and the percentage of crossings where a microsignature was detected are given in Figure 4.16.
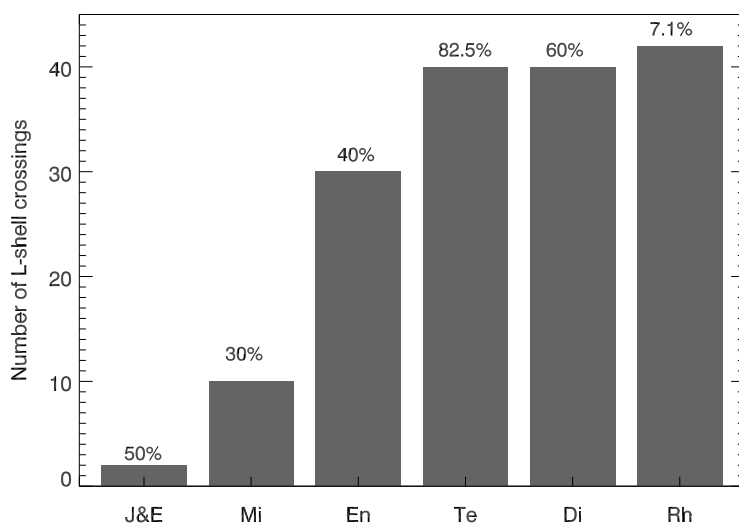
Figure 4.16: The number of L-shell crossings per icy moon. On the horizontal axis, the abbreviations for the moons are used as in most previous figures. Janus and Epimetheus L-shells were crossed only during SOI. Above each bar, the percentage of L-shell crossings per icy moon, where a microsignature was observed, is given. We note that at certain times a microsignature could have not been observed due to purely instrumental reasons, such as light contamination of LEMMS, spacecraft rotations or lack of data (LEMMS was switched off). This plot does not separate these cases (small fraction of the total), but even if those were considered, the overall picture would not change.

There is actually much more information in this plot than a simple cataloguing of L-shell crossings. Figure 4.16 shows that in almost 85% of Tethys's L-shell crossings a microsignature has been found. The percentage is probably higher, since the cases where there was no microsignature detection, spacecraft rotations, LEMMS light contamination or data gaps occurred coincidentally . This picture qualitatively agrees with the one given in Section 4.3.1 and by *Paranicas et al.* (2005): radial diffusion coefficients at the region of Tethys are very low. Double microsignatures, seem to be a common feature at Tethys. The detection percentage is lower at Dione, and even lower at Rhea. This is also consistent with the increase of D_{LL} in the radiation belts according to the power law of Equation 4.5.

The sharp decrease of the detection percentage at Rhea (compared to the decrease between Tethys and Dione) indicates fast diffusion rates at $L > 8$ and also a high n value. Inward of Tethys the detection percentage decreases, although D_{LL} values should be very

small and the microsignature lifetime should be higher. While increasing penetrating radiation levels and/or Enceladian activity could explain the absence of microsignatures in the keV electrons, this does not explain the absence of many MeV electron microsignatures. This implies that the magnetosphere inside $L = 4$ is relatively complex in structure.

Van Allen et al. (1980a) and *Chenette and Stone* (1983) have shown evidence for an electron spectrum filtered from keV electrons and with a peak at about 1 MeV, in the inner magnetosphere. The presence of the filtered spectrum is also hinted from the analysis of the penetrating radiation in Section 4.2.1.1. In addition, LEMMS measurements in the vicinity of Mimas suggest that the spectral characteristics of this region are indeed peculiar.
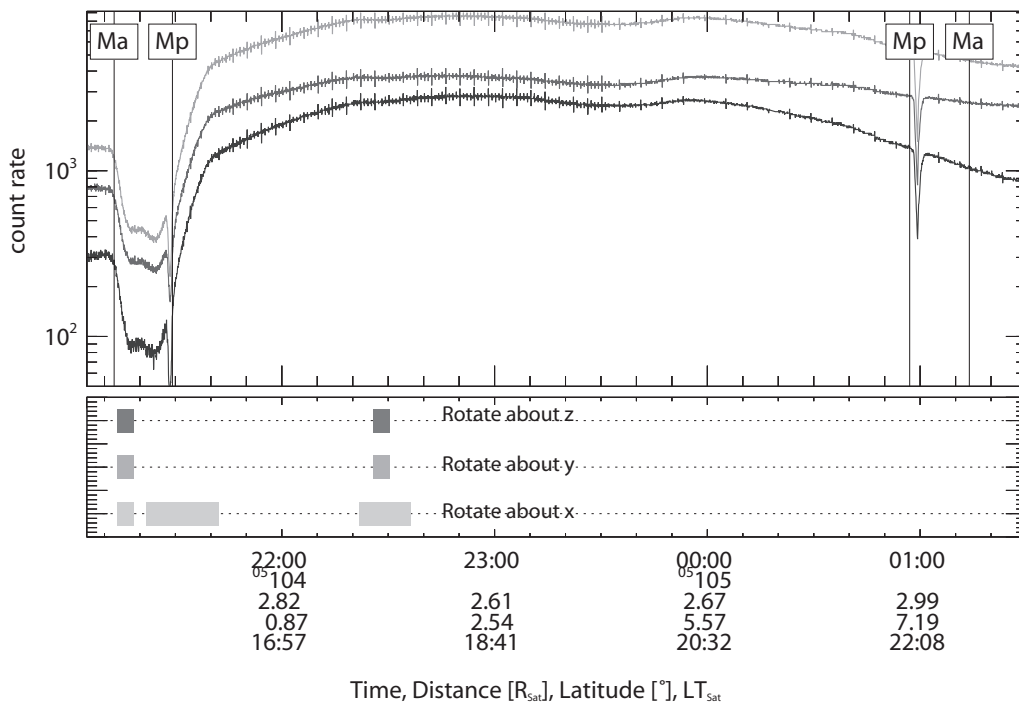
Figure 4.17: Two Mimas microsignatures seen during the consecutive inbound and outbound crossings of Mimas's L-shell range, on day 104 of 2005. The plotted values from top to bottom show the E4, E5 and E6 count rates. The vertical lines on the top panel, denoted as "Ma" and "Mp" correspond to the L-shell of Mimas's apoapsis and periapsis, respectively. We point out that these microsignatures helped us evaluate the contribution of penetrators in the C-channels, at the distance of Mimas. The bottom panel shows Cassini's attitude. Several spacecraft rotations are correlated to changes in the measured count rates, as LEMMS points to different pitch angles of a region with a non-isotropic pitch angle distribution. The observed periodic spikes in the data are instrumental and not magnetospheric features. We also note that the use of the count rate as a unit for the E-channel recordings is done with respect to the uncertainties in their geometrical factors and passbands, as discussed in Section 2.2.1.

Figure 4.17 shows two events recorded on day 104 and 105 of 2005, during the periapsis of the seventh Cassini orbit. The absorption features appeared simultaneously in almost all LEMMS channels (even in the ion detectors), implying that the real decrease

was in the energy range of the penetrating radiation, that is a few MeV. All signatures have been detected on the L-shells that correspond to the periapsis or apoapsis of Mimas's orbit: physically this is explained by the large contact time of Mimas with the L-shell in these regions, due to its almost zero radial orbital velocity (see *Selesnick* (1993), Figure 3).

Taking Mimas's eccentricity into account, the time the signature needs to drift from Mimas to the spacecraft can be evaluated (see *Van Allen et al.* (1980a)): Assuming a circular orbit for the electron signature, the time that Mimas was previously at the same L-shell is estimated. It is found that the inbound microsignature was created 0.83 or 23.5 hours earlier, while the outbound 4.3 or 26.9 hours earlier. The multiple solutions correspond to the two most recent periapsis passages of Mimas. Each drift time can provide up to two solutions for the electron energy: one for an eastward drift ($E < E_{rc}$) and one for the westward drift ($E > E_{rc}$). The results are summarized in Table 4.3. Due to the relatively low fluxes at energies greater than 5 MeV (*Chenette and Stone* 1983), I did not consider the 8.0 and 9.1 MeV solutions.

Table 4.3: Analysis of Mimas's microsignatures. The notations "W" and "E" refer to the westward and eastward solutions, respectively (see text for explanation).

Drift time (hours)	Energy (MeV)	Comment
0.83	8.0	Inbound (W)
23.5	1.6	Inbound (E)
23.5	2.9	Inbound (W)
4.3	1.8	Outbound (E)
4.3	9.1	Outbound (W)
26.9	2.4	Outbound (E)
26.9	3.5	Outbound (W)

If the energy ranges of the E0-E6 channels and the solutions in Table 4.3 are taken into account, it is most likely that the 1.6 and 2.9 MeV solutions for the inbound trajectory are actually the ones that are recorded in the E0-E6 channels and the decreases in lower energy C channels (not shown) are of the penetrating background.

For the outbound crossing three solutions between 1.8 and 3.5 MeV are found, approximately in the same range as for the inbound signatures. The fact that the inbound and outbound features have comparable geometrical characteristics, might also suggest similar drift times, which makes the 2.4 and 3.5 MeV solutions more probable than the 1.8 MeV one.

A possible absorption feature from Mimas has been found during day 248 of 2005 (10:22). The microsignature is very shallow and located close to Mimas's periapsis (but not exactly on the periapsis, $L \sim 3.03$). Eight solutions for the energy are possible, if it is assumed that this microsignature was formed in one of the two earliest Mimas periapsis passages. These solutions suggest a formation between 1.7 and 3.3 MeV with drift times that range from ~19 to ~45 hours.

The shallowness of the signature could imply a large microsignature lifetime. Alternatively, the dispersion in position effect is applicable in this case (*Van Allen et al.* 1980a) and could account for the microsignature depletion. Then the question is why these data reveal only one microsignature. Solutions actually suggest the detection of many more structures in the energy range of 1-5 MeV, where the electron spectrum is thought to be continuous and the electron fluxes considerable (*Chenette and Stone* 1983).

A microsignature in the MeV energy range also appeared between L =2.535 and L =2.540 during the inbound SOI trajectory (day 183 of 2004, 00:52). Orbital considerations and the assumption for circular drift shells suggest that this microsignature comes from Epimetheus and not Janus. As in the case of Mimas, it is observed at the L-shell of Epimetheus's apoapsis and it has probably been formed at 3.4±0.1 MeV.

The lack of microsignatures in 8 out of the 11 crossings of Mimas's, Janus's and Epimetheus's L-shells can only be the result of a peaked or not continuous spectrum, the eccentric orbits of those moons and the approximate circular drift shells for $L < 3.5$. This combination leads to electron holes being quantized features rather than continuous structures at each L, that can only be detected if Cassini is in the right position, at the right time.

A lot of different observations also suggest that a filtering of radially diffusing electrons is taking place, allowing mainly electrons of a few MeV to be present in the vicinity of Mimas and inward. Where and why does this filtering take place are questions that still need to be answered. Are there physical mechanisms that can help electrons "escape" this filtering process and populate the inner magnetosphere? Results in the following section could shed some light on this matter.

4.4.2   Electron radial microdiffusion

The estimation of D_{LL} at the L-shells of the icy moons is based on the fit of the solution described by Equation 4.4 to the microsignature profiles. A representative example of such a fit is shown in Figure 4.18. The event occurred close to the L-shell of Tethys on day 104 of 2005, in the inbound segment of Cassini's orbit.

The analytical profile describes well the overall shape and depth of the microsignature. In general, fits were satisfactory for microsignatures that were not very fresh or not very diffuse. Shallow (diffuse) absorption signatures were especially difficult to fit, as the depth of the microsignature was sometimes comparable with the amplitude of fluctuations in the data. Sharp (fresh) microsignatures do not reveal the effects of diffusion in their shape, which makes difficult to extract the actual D_{LL}.

In the following plots, included are only D_{LL} values from where the fit was termed satisfactory. The standard deviation was used as a primary criterion for the goodness of the fit. Visual inspection of the fitted curve was always necessary in order to evaluate cases where the standard deviation criterion could have been misleading (diffuse or fresh signatures), or to fine-tune some pre-defined parameters for the fitting (e.g the center of the microsignature).

Beforehand, it was investigated whether there are trends in D_{LL} that need to be removed. In several cases a slight increase of D_{LL} towards the equatorial pitch angles could be observed. An example is shown in Figure 4.19. As this variation was comparable to the uncertainty of the derived D_{LL} values, no correction was applied.
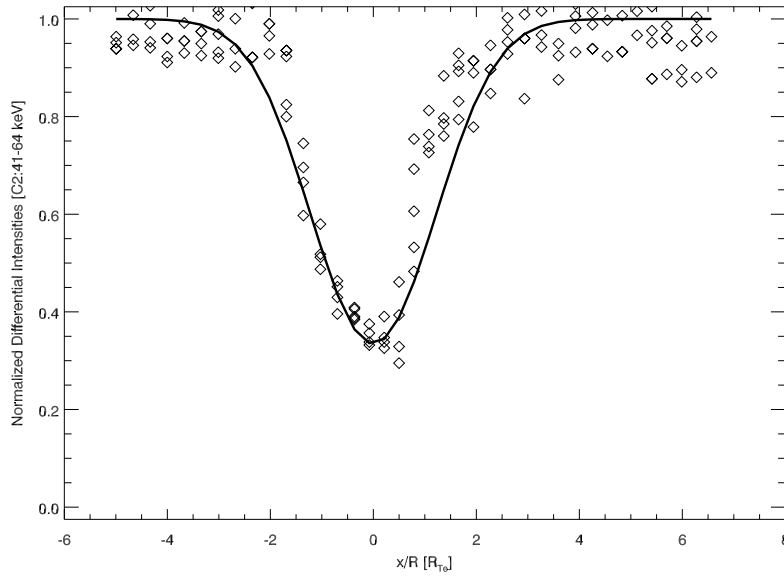
Figure 4.18: Fit of the Equation 4.4 (solid curve) to a Tethys microsignature profile (points), detected on day 104 of 2005 (17:47, channel C2). The fit gave a $D_{LL} = 4.7 \cdot 10^{-10} R_s^2/s$.
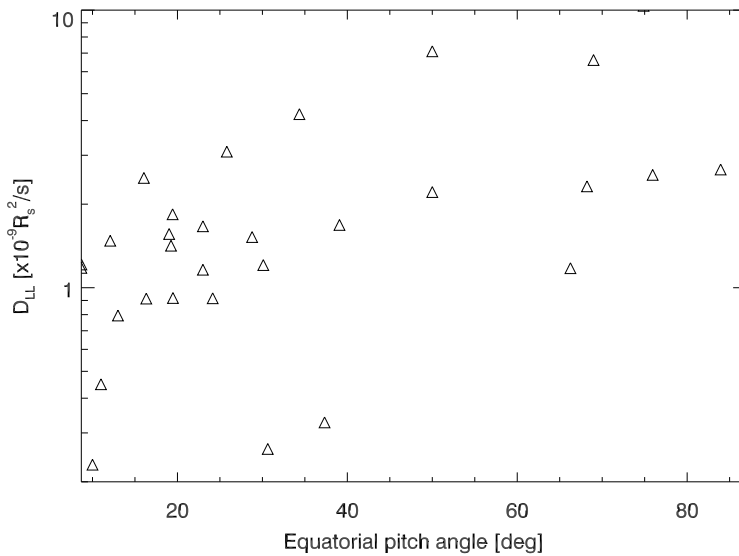
Figure 4.19: Variation of D_{LL} at Tethys, as a function of equatorial pitch angle (a_{eq}) for electrons of 41-64 keV. An increase of D_{LL} towards equatorial pitch angles is expected theoretically when radial diffusion is driven by magnetic field impulses.

Starting with the microsignatures seen in the C channels, D_{LL} is plotted as a function of $L + \Delta L/2$ (Figure 4.20). Results are shown only for Tethys, Dione and Rhea. No microsignature in the keV range has been found for Mimas, Janus or Epimetheus. At Enceladus, radial diffusion alone cannot explain the microsignature fill-in, as it was dis-

cussed in previous sections. No calculation of the additional refilling components was done, meaning that the estimation of D_{LL} at Enceladus with the discussed method gives only upper limits. By removing the penetrating background, the upper limit for D_{LL} at Enceladus was reduced to $4 \cdot 10^{-9} R_s^2/s$, which is a factor of two less than what is given by *Jones et al.* (2006).
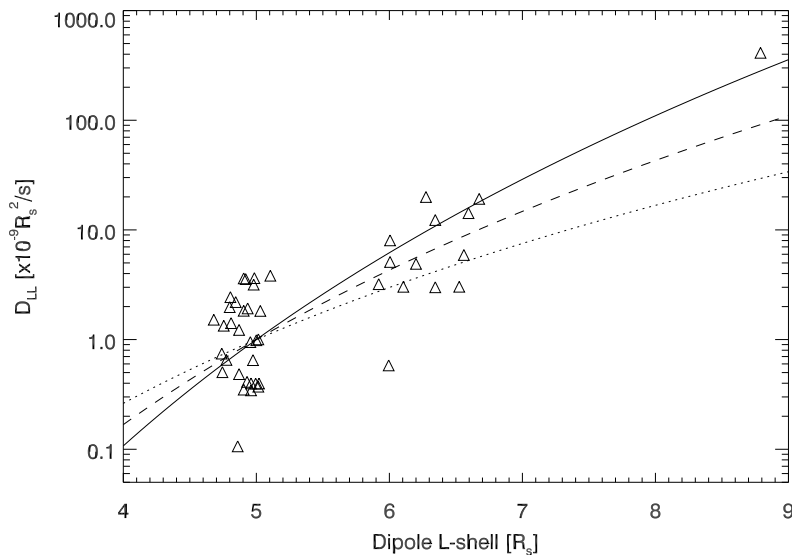
Figure 4.20: L-dependence of the D_{LL} for the C1 energies (28-49 keV). Three reference curves are shown that correspond to Equation 4.5, for n =6,8 and 10 (dotted, dashed and solid curve, respectively).

Figure 4.20 shows the results for the L-dependence of D_{LL} for the 28-49 keV electrons. A significant scattering is seen for D_{LL} at Tethys and Dione, which could be attributed to a number of reasons, such as temporal and spatial variations of D_{LL} or the quality of the signal for the different events that were fitted.

The D_{LL} at Dione and Tethys are below the lower limits set by *Paonessa and Cheng* (1985). This qualitatively agrees with the observed long lifetime of the microsignatures (see Section 4.2.1.1). If we only consider Dione's and Tethys's extracted D_{LL} values, Equation 4.5 can fit equally well for all n ranging from 6 to 10. The single microsignature event at Rhea, however, suggests that D_{LL} should vary as $\sim L^{10}$. More Rhea events could have revealed a similar scattering as at Dione and Tethys. *Krimigis et al.* (1981) estimated a D_{LL} at Rhea almost one order of magnitude less than is estimated here. In combination with the present results, this would give an n value between 8 and 10. The difference of one order of magnitude is within the limits of the D_{LL} accuracy at Rhea, due to the known deviations from simple dipole magnetic field drifts (*Birmingham* 1982).

The L-dependence gives similar results for C0, C2 and C3 channels, where n ranges between 8 and 10.5. The results on the L-dependence of D_{LL} are consistent with a refilling of the energetic electron microsignatures by radial microdiffusion generated by field impulses. A pitch angle dependence of D_{LL}, with the profile seen in Figure 4.19, is theoretically expected (*Walt* (1994), Figure 8.3). In addition, these results agree with those

by *Cooper et al.* (1983), where he found an $\sim L^9 D_{LL}$ dependence by assuming a Cosmic Ray Albedo Neutron Decay (CRAND) process at Saturn's rings, in order to explain the high energy proton fluxes measured by Pioneer 11.

Maybe one of the most important results are the very low D_{LL} at Tethys and Dione. Given that there is a gradient in the electron phase space density (*Randall* 1994), we can relate directly the value of D_{LL} with the time, t, that a particle needs to diffuse from L_2 to L_1 according to *Mogro-Campero and Fillius* (1976):

$$t \sim \frac{(L_2 - L_1)^2}{4D_{LL}} \tag{4.6}$$

Our D_{LL} estimations therefore show that 20-100 keV electrons need approximately the same time to diffuse across Dione's orbit, as the mean encounter time between Dione and these particles ($T_{rk} = 2\pi/\omega_{rk}$). At Tethys this diffusion time can be greater than T_{rk}. This means that a radially diffusing electron will encounter Tethys and Dione at least once, if its azimuthal drift path is circular.
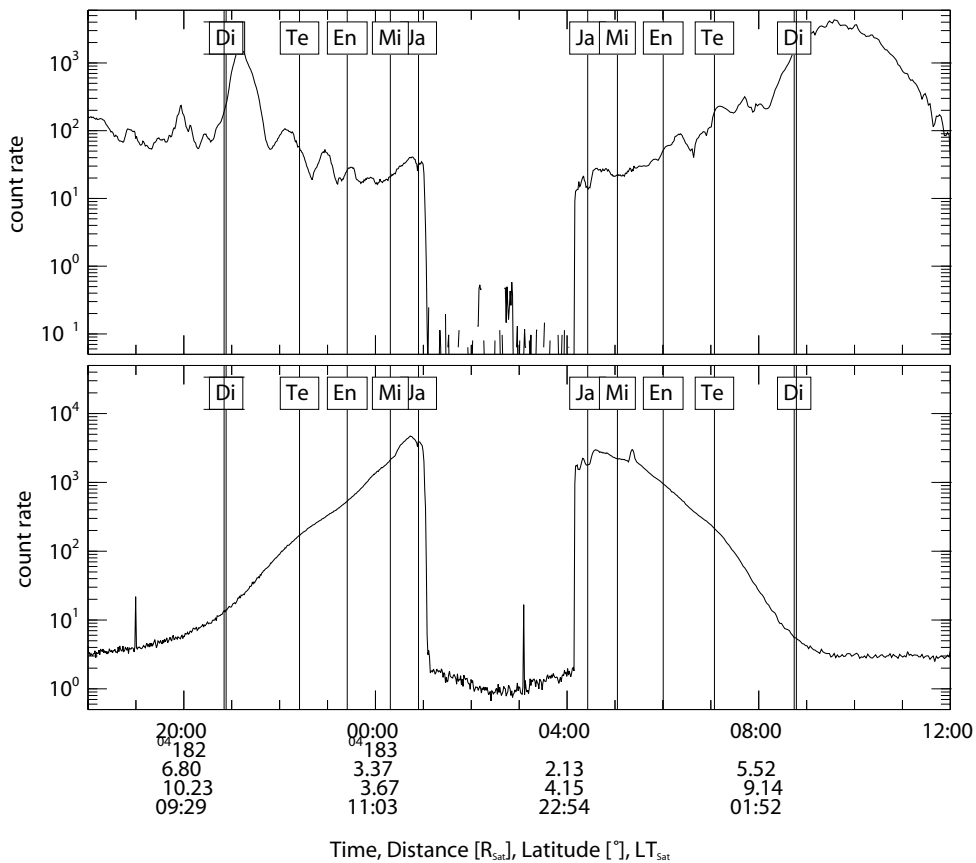
Figure 4.21: 86 s averaged electron count rates of the C2 (top) and E5 (bottom) channels, during SOI. Vertical lines denote the icy moon L-shells. Electron count rate drops start near the L-shell of Dione, for the C2 electrons. On the other hand, MeV electron count rates continuously increase towards lower L values. Notice also how the C2 electron intensity profile matches the one of the E5, inside the L-shell of Mimas, indicating that the C2 signal is dominated by MeV penetrating background.

98

Therefore, we should expect that a large amount of diffusing electrons are removed, starting from the orbit of Dione. A filtering effect should take place, as electrons of $E \sim E_{rk}$ should have the largest probability to diffuse across the orbits of any icy satellite inside the orbit of Dione.

LEMMS observations agree partly with this picture. Figure 4.21 shows sector averaged count rates of C2 and E5 channels measured during SOI. Electron count rates of the C2 channel drop one or two orders of magnitude around the L-shells of Dione and Tethys (more clearly visible in the outbound sector). On the other hand, E5 fluxes increase steadily. The E5 channel measures MeV electrons that have much higher T_{rk} than keV electrons. This typical picture of many of Cassini's orbits, is also expressed in phase space density profiles, as in *Randall* (1994) and in *Rymer et al.* (2007). Still, if filtering from the moons is the source of this dropout, one would primarily expect to happen exactly on Dione's or Tethys's L-shell. An alternative explanation is that this large scale dropout occurs due to electron collisions with the E-ring dust or neutrals from the associated neutral cloud (*Randall* 1994).

A number of effects have not been discussed so far: pitch angle diffusion, asymmetric inward and outward radial diffusion and the integrated signal of an energy dispersed signature (due to the finite energy width of each channel) . Pitch angle diffusion has probably more significant effects at the orbit of Enceladus. Asymmetries in inward and outward radial diffusion cannot be evaluated currently, but they did not seem to affect the quality of the fits significantly, as it is seen in Figure 4.18.

Energy dispersion, however, can be important. As most energy channels record electrons between values of E_1 and E_2 ($E_1 < E_2$), the signal of E_1 has drifted for less time than that of E_2, for $E_i < E_{rk}$ (and the opposite for $E_i > E_{rk}$). Therefore, the total signal of the detector is the integral of absorption regions with different lifetimes. This effect should add to the erosion of the microsignatures.

The E channels have large passbands and their lowest energy close to the E_{rk} of each icy moon (Table 2.1). The drift time of a signature created in E_1 is much greater than that of E_2. So a microsignature in the E-channels can be the sum effect of an absorption region that has probably vanished due to a long lifetime ($E = E_1 \sim E_{rk}$), absorption regions that have only short lifetimes and account for the measured depletion ($E_1 < E < E_2$), and regions with low contribution to the total signal ($E \sim E_2$), due to a typical power law shape of the energy spectrum. This effect could contribute to the erosion of microsignatures in the E-detectors, if the energy spectrum at MeV energies is continuous and the spectral index value is small.

This is examined by assuming a simple power law for the energy spectrum, $f = f_o E^{-\gamma}$, where γ is the spectral index. The energy spectrum of a few MeV is divided in many finite energy steps, and for each energy step the respective profile of a hypothetical microsignature described by Equation 4.4 is estimated. Assuming circular drift shells, the absorption signature has contribution from electrons of all energies that the detector covers. A sum is done over all energies to construct the equivalent signal that a detector of passband ΔE would measure. D_{LL} was assumed to be constant over this ΔE.

Examples are shown in Figures 4.22 and 4.23. When $\gamma > 3$ and E_1 is close to a Keplerian resonant energy E_{rk}, the resultant microsignature profile is defined by the energies around $E_1 + E'$, where E' is around 0.2-0.3 MeV. The microsignature can be well described by Equation 4.4 with an equivalent D_{LL} slightly lower than the normal. The
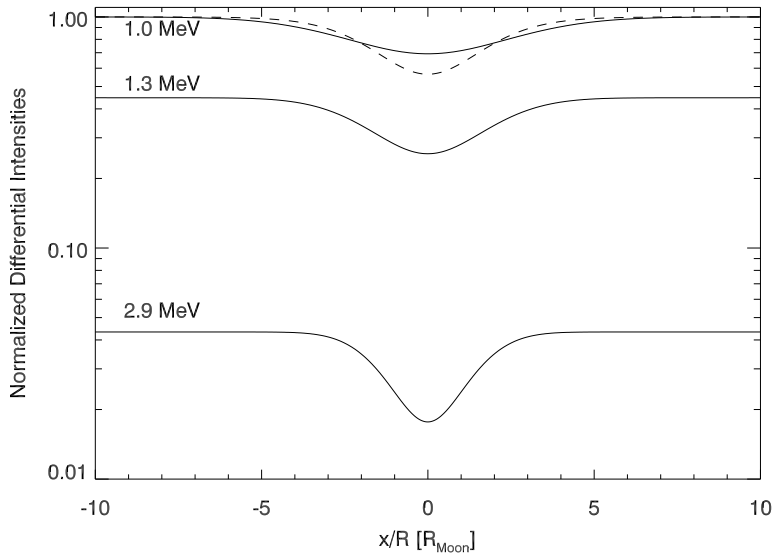
Figure 4.22: Simulated 90° pitch angle electron microsignature from Tethys recorded by a detector of with an energy range, ΔE, of 2 MeV and an energy threshold, E_1, of 1 MeV. D_{LL} is assumed to be $5.0 \cdot 10^{-8} R_s^2/s$, the spectral index $\gamma=3$ and the flyby 40° upstream of Tethys. Note that E_1 is close to Tethys's Keplerian resonant energy. The dashed curve resembles the integrated over all energies microsignature profile, normalized towards the total intensity, while sample microsignature profiles are given for certain energies (normalized towards the maximum intensity at $E = E_1$).
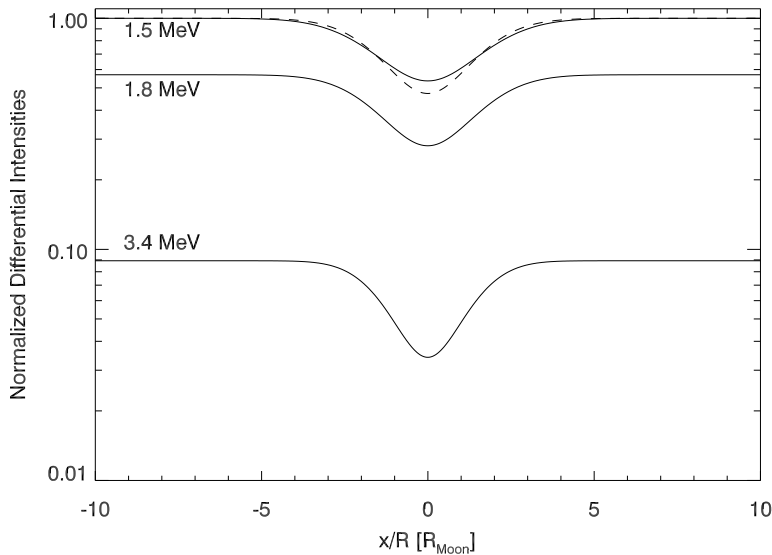
Figure 4.23: As in Figure 4.22, for E_1=1.5 MeV and ΔE=2 MeV.

overall microsignature is narrower than the absorption region of an electron with energy E_1.

Overall, the finite ΔE of the detectors tends to increase the depth and reduce the width of the microsignature signal, for electrons above E_{rk}, and the opposite for electrons below E_{rk}, as long as the spectrum has a power law dependence (or a similar description). However, these effects are small if E_1 and E_{rk} are not close and $\gamma > 3$. Then E_1 defines the overall shape of the microsignature and the profile matches exactly the one given by Equation 4.4, for $E \sim E_1$. For the 10-20 keV passbands and the low energies of the C0-C3 channels these effects are negligible.

Based on this analysis, Equation 4.4 is fit to E-channel microsignatures. As the electron spectral index varies between 6 and 11 for $3 < L < 8$ for electrons between 600 keV and 2 MeV (*Maurice et al.* (1996), *Randall* (1994)), fits were excellent to many MeV microsignatures of Mimas, Enceladus and Tethys (Figure 4.24). E-channel absorption signatures from Dione were also fitted with good results. The microsignature from Epimetheus consisted of few data points due to the very high inbound velocity of Cassini during SOI, and the fit was not successful.
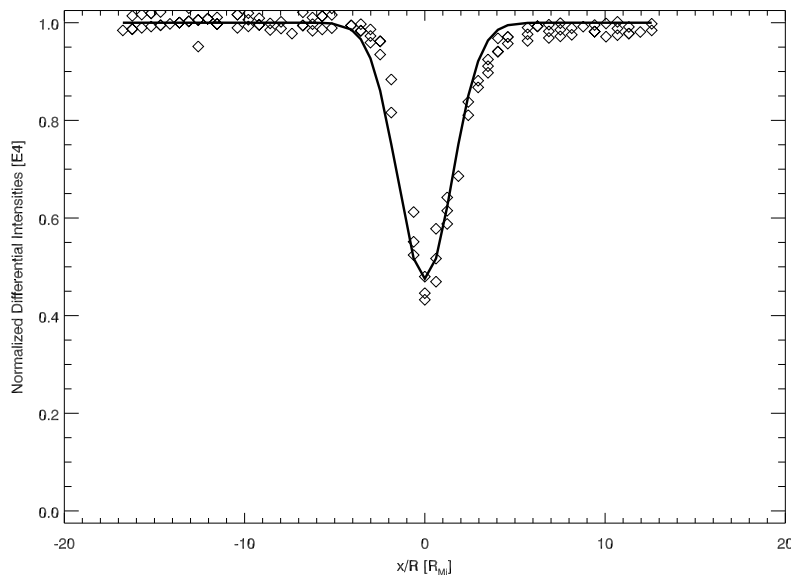
Figure 4.24: Fit of the Equation 4.4 (solid curve) to a Mimas microsignature profile (points), detected on day 105 of 2005 (00:55, channel E4). The fit gave a $D_{LL} = 1.4 \cdot 10^{-10} R_s^2/s$. This is almost identical to the value given by *Van Allen et al.* (1980a).

Only in the cases of Mimas's microsignatures it was possible to extract directly the drift time and calculate a D_{LL} of approximately $(1 \pm 0.3)\, 10^{-10} R_s^2/s$, a value which differs less than one order of magnitude from those estimated by *Van Allen et al.* (1980a) and *Cooper et al.* (1983). For Enceladus, Tethys and Dione, the drift time depends on the energy at which we assume the microsignature signal is dominated.

According to the previous analysis, it was assumed that the dominant electron energy shaping the E4, E5 and E6 microsignatures is ~0.2-0.3 MeV above the E_{rk} at a given L-shell. Again, the D_{LL} varies as $\sim L^{10}$ (Figure 4.25). If D_{LL} values at Mimas are neglected (as they correspond to energies different than the assumed energy for the other moon microsignatures), D_{LL} varies as $\sim L^8$.
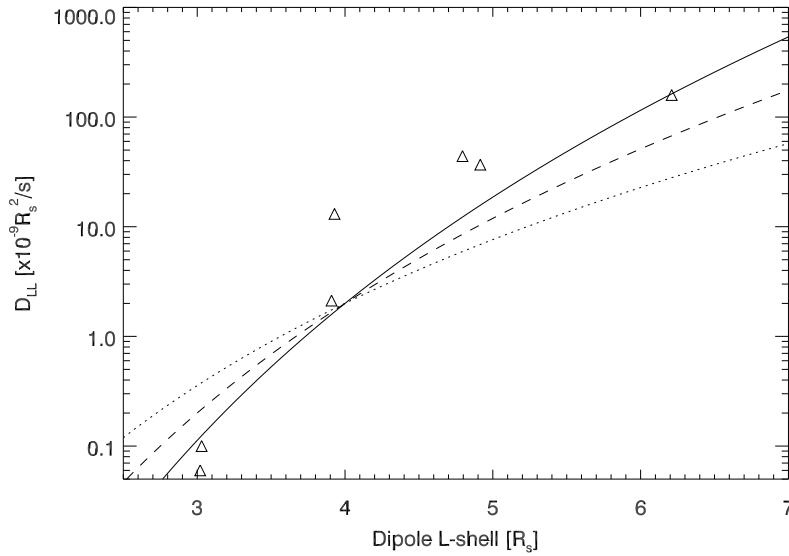
Figure 4.25: Same as in Figure 4.20, for fits of microsignatures seen in E6 channel. Here the solid reference curve corresponds to $n = 10.5$. One of the fits at Enceladus gave a much higher value than could be derived by the power law dependence of D_{LL}. The rest of the fits agree with the an $\sim L^{10.5}$ law. The D_{LL} values are higher compared to those for keV electrons, which explains the small number of detected microsignatures at MeV energies.

It is therefore found that through this simple approach data should be interpreted as a sharp increase of D_{LL} towards MeV energies. Energy dependence of D_{LL} is theoretically permitted when the sources of radial diffusion are field impulses. This analysis suggests that this is not a finite passband effect.

Despite this approach being simple and straightforward, there are a number of factors not taken into account that could change the picture. These are discussed in the following section where it is actually shown that the faster depletion of the MeV microsignature signal can result from a series of other physical mechanisms.

4.5   Discussion

Using LEMMS microsignature observations, electron microdiffusion in the Saturnian radiation belts has been studied. For the first time statistically significant number of D_{LL} values from five different moons at various distances and energy ranges have been extracted. This allowed to study the D_{LL} dependencies with L, energy and pitch angle. In the following subsections the main results of this study and possible interpretations are presented.

4.5.1   The radial microdiffusion source

The increase of D_{LL} with L, at all energies, is consistent with the expected power law dependence described in Equation 4.5. The extracted value for n ranged between 8 and 10.5. The high n value shows that electron microdiffusion is probably driven by magnetic field impulses. This result is also supported by an observed weak equatorial pitch angle dependence of D_{LL}. The L-dependence agrees well with previous studies (*Cooper et al.* 1983), where an $\sim L^9 D_{LL}$ dependence was found for high energy protons, but disagrees with others, such as the analysis by *Randall* (1994), where an $\sim L^3$ dependence was used in fits to energetic electron phase space densities.

Magnetic field impulses are sudden changes in the magnetic field followed by a slow decay towards the original field configuration. These changes violate the conservation of the third invariant and lead to the radial diffusion of the particles. In the Saturnian magnetosphere, magnetic field impulses can be imposed by magnetospheric compression due to energetic solar wind events, or by plasma injections, between 6 and 20 R_s (*Burch et al.* 2005, *Hill et al.* 2005). These impulses usually have an amplitude of a few nT, which explains why they cannot be effective in diffusing plasma at low L, where the background magnetic field is of the order of $10^2 - 10^4$ nT.

Physically, an observed D_{LL} scattering could reveal its temporal variations. Such variations could be a response to changing solar wind conditions, to hot plasma injections or even the mass loading activity from Enceladus. A highly variable (in both intensity and time) diffusion source is implied due to the over an order of magnitude D_{LL} variability at the L-shells of Dione and Tethys. At 5-6 R_s, such a source is more probably linked to plasma injections rather than to the changing solar wind conditions. On the other hand, as it will be shown in Section 4.5.3, there are indications that the solar wind interaction is possibly affecting to the shape of the electron drift shells at low L, meaning that solar wind effects can access the inner magnetosphere.

A variability in the corotation fractions, f_c, with time is also likely. If we imply rigid corotation at all L, then D_{LL} increases by a factor of 1.5 to 3.0, depending on the event. Even in this case, the value of n does not fall below $n = 8$. The reduction of penetrating background helped mainly in achieving better quality fits to the microsignature profiles.

The diffusion source can be magnetic impulses, also if $n = 8$. A more general expression than Equation 4.5 for the L-dependence of D_{LL} in the case of field impulses can be found in *Walt* (1994):

$$D_{LL} \sim L^{6+2k}\mu^{2-k} \tag{4.7}$$

Here, k corresponds to the ν^{-k} dependence of the power spectral density of the field variation (P), where ν is the drift frequency. The particle energy in this relation is included through the first adiabatic invariant, μ.

Using the median D_{LL} values estimated at energies of C0-C3 channels, the dependence of D_{LL} upon energy was also examined. An R^2 correlation of 0.98 at Tethys and 0.7 at Dione was found for a linear dependence. Due to the large amount of penetrating radiation influencing the C4-C7 channels, it was not possible to extract D_{LL} information for the corresponding energy ranges. The linear increase of D_{LL} with E implies a P variation as a function of ν^{-1} and $n = 8$. An evaluation of this power spectral density index could be used as an additional test for this theory. Alternative interpretations are presented in the

following sections.

4.5.2 Keplerian motion resonance and energy dependence of D_{LL}

The observed increase of D_{LL} with energy could also be explained as a filtering effect imposed by the icy moons and the E-ring dust and neutral gas. The complete radial diffusion equation balances sources, losses, and D_{LL}. In the solution of the local diffusion equation (*Van Allen et al.* 1980a) that I use, no loss or source terms are included, apart from the depletion at $t = 0$, and radial diffusion, respectively.

Other local losses and/or sources can therefore influence the value of D_{LL} obtained, so all three quantities must always be considered in its interpretation. For example, if a particle gets absorbed during this process, it would give the sense that it takes an infinite time to diffuse. Therefore, for a collection of similar particles, the effective D_{LL} (that is measured) would be lower than the real one.

A characteristic example occurs at Saturn's main ring system. The environment within the L-range of Saturn's main rings is almost empty of plasma, as this plasma is absorbed while it diffuses inward. If the presence of the rings is neglected, then the result would have been $D_{LL} \sim 0$, which, of course, is not true.

In a similar manner an icy moon is equivalent to a dense ring for a charged particle. The lower the mean encounter time of this moon with the particle, the more this picture is valid. Electrons at keV energies have relatively short mean encounter times with the icy moons, which means that many diffusing electrons are removed, microsignatures refill more slowly resulting in an effective D_{LL} lower than the real one.

For MeV energies and close to the Keplerian resonant energy, E_{rk}, the mean encounter time is close to infinity. Therefore these electrons diffuse freely and the measured D_{LL} is higher than for keV energies. Such a mechanism would produce an increase of D_{LL} with energy, even if $P \sim v^{-2}$.

If this mechanism dominates, Equation 4.6 is not completely valid: the diffusion time, t, is not estimated by the actual radial diffusion coefficient, but by an effective one. This could provide a partial explanation to the paradox that was encountered: how can keV electrons diffuse across Dione and Tethys with such low diffusion speed implied by the estimated D_{LL}? The answer is that the actual D_{LL} is probably higher.

However, this mechanism probably does not dominate and the measured and actual D_{LL} are not very different. The E-ring is not effective in absorbing electrons at non-equatorial pitch angles, except maybe at its core. In addition, the equivalence of an icy moon with a dense ring would have been very important if electron drift shells were circular and identical with the moon L-shells. Then the moon directly obscures electrons that refill the microsignature. This is contradictory to the observations of non-circular drift shells (Section 4.2.1.1), at least outward of Tethys.

4.5.3 Non-axisymmetric drift shells

To further investigate the microsignature displacement observations, the L-displacement of Tethys's and Dione's keV electron microsignatures is plotted as a function of local time. Figures 4.26 and 4.27 clearly show a preference in the displacement direction:

inward in the midnight region and outward in the noon to dusk sector. Furthermore, the displacement is greater on average at Dione compared to that at Tethys.
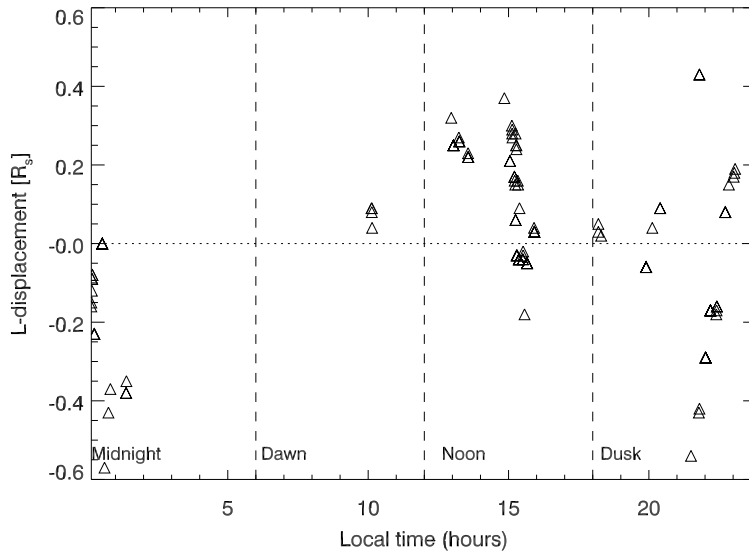
Figure 4.26: Displacement of Tethys C-channel microsignatures from the expected dipole L-shell, as a function of local time. Positive displacements are away from Saturn, while negative displacements are towards Saturn. We note that most of these displacements are observed at low latitudes.
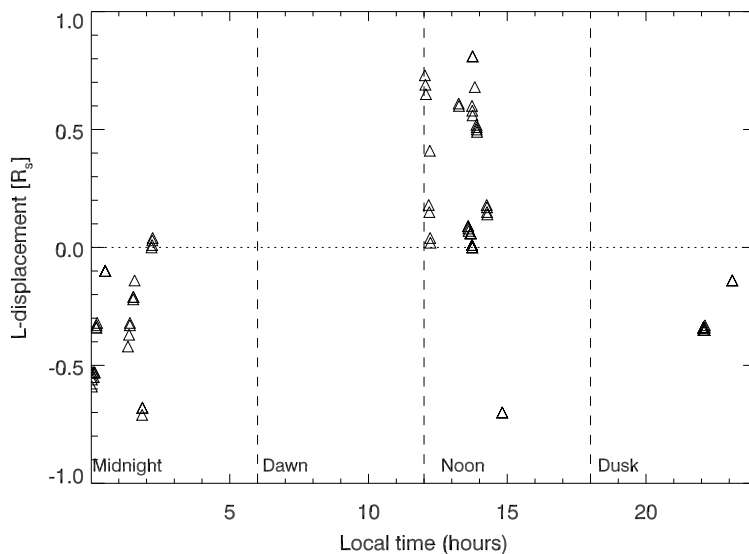
Figure 4.27: Same as in Figure 4.26, but for Dione's microsignatures.

Therefore the non-circular drift shells are a steady situation and the observed displacements are not temporal events. Such drift orbits could provide the means of transporting keV electrons past the orbits of Dione and Tethys.

Electrons drifting on these shells have a significant radial velocity that is physically different from their L-velocity due to radial diffusion. Electrons only intersect the moon orbits at two locations at which absorption is possible. If the electron does not meet the moons at these locations during the time it needs to diffuse away from their region of influence, it is transported to the inner magnetosphere by radial diffusion. That, in addition to other mechanisms, such as hot plasma injections, could explain how electrons avoid being absorbed by Tethys and Dione while diffusing inward, despite the very low D_{LL}.

In summary, while a notable contribution to large scale keV electron drop-outs (Figure 4.21) could originate from the partial depletion of inward diffusing electron flux on the moon surfaces, due to low radial diffusion speeds, the non-circular drift shells can explain why these drop-outs do not coincide exactly with Tethys's or Dione's L-shells and why a sufficient foreground signal can be measured inside those moons' L-shells. So far electron-neutral and dust collisions were assumed to be the only mechanism to account for these large scale depletions. However, electron flux gradients seem too high at 6-8 R_s for the relatively low densities of the E-ring there.

4.5.4   Non-axisymmetric drift shells and energy dependence of D_{LL}

The existence of non-circular drift shell adds even more complication in the study of the energy dependence of microsignatures, but could be used to explain the shallowness of the MeV microsignatures. This is shown in Figure 4.28.

In this simplified sketch, a moon absorbs electrons (e.g. for $E < E_{rk}$) at the position A. The absorption signature propagates away from the moon's L-shell (due to the non-axisymmetric drift shells), on the drift shell AA'. The absorption region has a width comparable to the moon's diameter and a length S, which is proportional to the energy passband $\Delta E = E_2 - E_1$ of a LEMMS detector.

Cassini crosses this absorption region with a certain angle and samples only a few energies from this box. Assume now that some time earlier, the moon absorbed electrons at B, that move on the drift shell BB'$\neq$AA'. As Cassini crosses the absorption region at B', it samples different energies than at A'.

This means that non-axisymmetric drift shells could act as an energy spectrometer for microsignatures, in the same way that Mimas's eccentricity acts in the inner magnetosphere. Under certain conditions, observed microsignatures would be monoenergetic structures and the assumption that the signal has contributions from electrons of all energies that a detector covers is not adequate. The depth of a microsignature would decrease with increasing detector passband and D_{LL} would seem high.

These conditions have not been quantified, but qualitatively it can be inferred that the angles u_A, u_B and the length of the absorption region, $S \propto \Delta E$ have to be large (E-channels). If the drift shells were coinciding with that of the moon, or the angles u_A, u_B were small, then all "boxes" would overlap with the result being that the observed microsignatures cover all energies of the detector range.

For small ΔE (C-channels), S is small and even if u_A, u_B are large, the "boxes" overlap. In Figure 4.29 for example, the L-displacement difference between microsignatures of C0-C2 (noted as DL_A, DL_B in Figure 4.28) is smaller than the microsignature width (case of overlapping boxes). To determine which scenario is more applicable for the
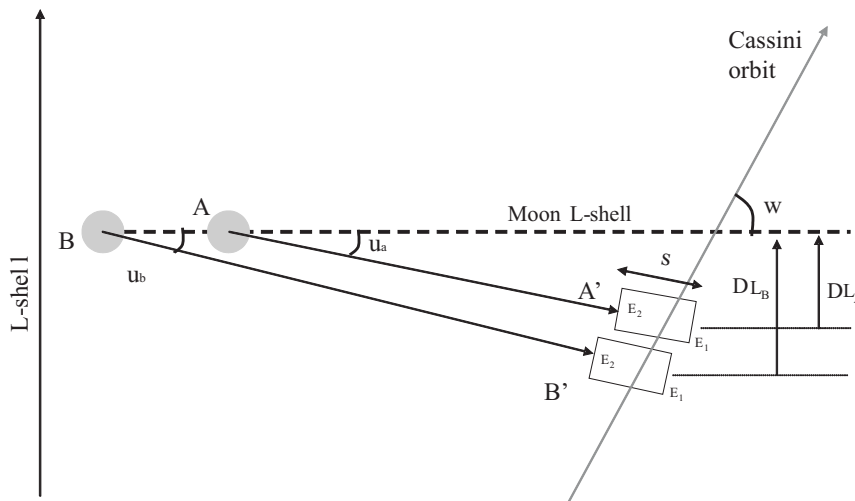
Figure 4.28: The geometry of a microsignature detection for non-axisymmetric drift shells (see text for explanation). In this simplified sketch drift shells are drawn as straight lines. All parameters are time dependent, as the absorption region crosses different local times. Furthermore, in this sketch its assumed that drift shells are independent of the electron energy. If the source of non-axisymmetric drift shells is an electric field, the picture becomes more complex as electrons of different energy will follow different paths, even if they start from the same point.

E-channels (monoenergetic versus non-monoenergetic microsignatures), magnetospheric field models should be used.

Practically, the theoretical treatment of the signal structure in large passband detectors can be avoided by looking at the high energy resolution LEMMS PHA channels. These were used only qualitatively to assess the results for the high D_{LL} values at these energies. MeV electron microsignatures appeared very shallow also in this case. This observation is in favour of faster radial diffusion for MeV electrons, at least up to the energies of 2 MeV that PHA channels cover.

4.5.5 Additional implications

The existence of non-circular drift shells have even more implications: a series of modeling approaches in the past estimated plasma loss rates to the icy moon surfaces (*Paranicas and Cheng* 1997, *Paonessa and Cheng* 1985). Drift shells were considered circular, and absorption escape mechanisms were related, amongst others, to the small, but non-zero orbital eccentricities of the icy moons. Results in this chapter show that L-displacements due to magnetospheric processes are orders of magnitude higher than the icy moon L-shell variability due to the non-zero eccentricities and inclinations.

A filtered electron spectrum at low L-values, inferred from Voyager and Pioneer 11 studies, appeared through this analysis in many ways: (i) Very low foreground signal for electrons of tens or hundreds of keV, (ii) Mimas's and Epimetheus's microsignatures appeared only in the MeV energy range and (iii) the detection percentage of microsignatures from Mimas, Janus and Epimetheus at the MeV range, where the foreground is sufficient, was small, despite the low D_{LL} values. The results shown here are consistent with the
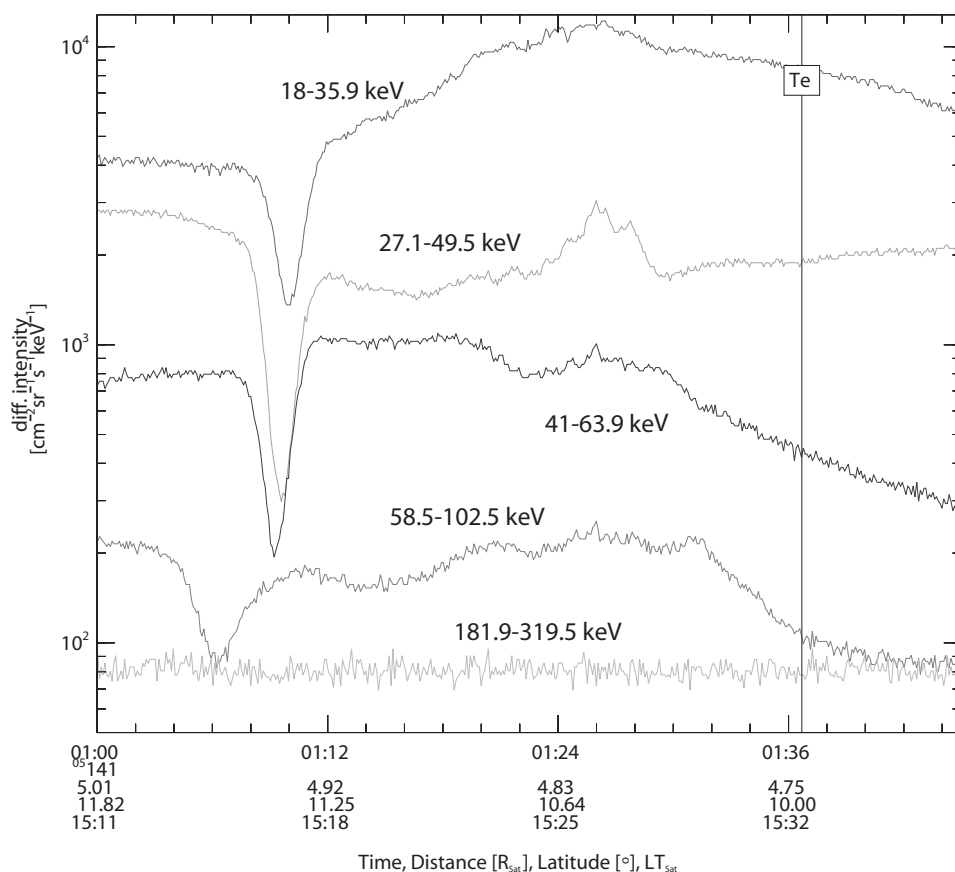
Figure 4.29: A characteristic example of a microsignature in the LEMMS dataset: fluxes of different electron channels are plotted against time. The absorption region produced by Tethys is clearly seen between 1:00 and 1:12. The vertical bar around 1:37 indicates the position of Tethys's L-shell, according to a simple centered, dipole magnetic field source. Note also that no signature is seen for the 181.9-319.5 keV electrons (C5), which is most likely the result of significant penetrating radiation contribution to the signal of this detector. In the horizontal axis, the radial distance, the local time and the latitude of Cassini are given.

theory that satellite sweeping of inwardly diffusing electrons has a significant contribution to this filtering. Electron collisions with neutrals and dust grains are probably also contributing.

Deviations from circular drift shells are very low but still present at Enceladus. Therefore a filtering of inwardly diffusing electrons cannot be as effective at Enceladus as expected before (*Van Allen et al.* 1980a), which implies that the core of the E-ring should also contribute to this process. E-ring dust clumps (e.g. at the Lagrange points) could also add to this filtering (*Jones et al.* 2006).

The non-axisymmetric drift shells at Enceladus's orbit can maybe explain why the energy spectrum inside $L = 4$ is not highly monoenergetic with a sharp peak around 1.5 MeV (*Van Allen et al.* 1980a). These drift shells could be a source of absorption escape mechanism for non-resonant electrons, as in the case of Tethys and Dione.

A large and dense clump was recently detected within the G-ring though optical and

electron absorption data (see Chapter 5). Mimas and this feature could also add to the electron filtering for $L < 3$ and further complicate the picture. The absence of at least three expected microsignatures from Janus and Epimetheus could be related to this complexity. If the main source of a few MeV electrons at Janus and Epimetheus is inward radial diffusion, then the electron spectrum inward of the G-ring would also depend on how stable the physical characteristics (density, size) of this feature are.

4.6   Open questions and outlook

Through this study, a number of questions arise, such as which is the source of the non-axisymmetric drift shells. The answer seems not to be straightforward. A simple calculation (eg. *Roederer* (1970)) can reveal that a solar wind induced dusk to dawn electric field, as suggested by *Cooper et al.* (1998), should have a strength of more than 0.1 mV/m to account for the observed displacements. This is over an order of magnitude from the expected value within the magnetosphere of Saturn, assuming that the solar wind electric field penetrates in the inner magnetosphere with a 10% efficiency.

It could be argued that this efficiency and the solar wind induced electric field vary significantly, in a way that such values can be achieved. Even in that case dusk to dawn electric field would lead to maximum inward or outward displacements at dawn and dusk, respectively (*Cooper et al.* 1998). The maxima, however, are closer to noon and midnight, but still the coverage of the dawn and dusk sectors is poor. In a similar way, a dawn to dusk electric field due to tailward mass injections (*Barbosa and Kivelson* 1983) is inconsistent with the direction of displacements.

The displacement direction also has a similarity to the shape of the curves of equal magnetic field due to the magnetopause current disturbance. This has a form of $B_{MP} \sim L\cos\theta$ at the equatorial plane, where θ is measured counterclockwise from midnight. Still, one should then assume that the magnetopause current can introduce disturbances as high as 20-30 nT at Tethys and at Dione in some cases, which is almost 30% of the dipole field value minus an average of 10 nT ring current disturbance. This topic should be further investigated using magnetic field models, but gives a more reasonable explanation on the origin of the non-circular drift shell.

In addition, LEMMS observations of Mimas microsignatures seem to add to the mystery regarding the explanation of their detailed structure. Although the purpose of the study here is not to solve the Mimas problem (*Chenette and Stone* 1983), it should be stressed that microsignatures are small scale phenomena, and therefore a detailed study of their structure will depend highly on the assumptions made.

For example, in the case of Mimas circular drift shells were assumed, in addition to a simple centered and spin-aligned dipole field and an equatorial orbit for the moon. Similar assumptions were made in past studies. These are adequate to explain and analyze the observed microsignatures, as shown here, but not to predict the detailed structure and the existence of all Mimas's microsignatures.

From Table 4.1 we see that Mimas has an inclination of 1.53°. Furthermore, a possible tilt of 0.1° to 0.3° of the dipole field and a northward displacement of 0.04 R_s of its source from the center would mean that at certain regions of Mimas's orbit, 85° to 95° equatorial pitch angle particles could escape absorption as they mirror below Mimas's latitude.

As Mimas is at very low L, conservation of the second adiabatic invariant means that pitch angle distributions are more equatorial, and therefore a large percentage of electron flux would escape absorption. Such a mechanism could explain, for example, the absence of some of the expected Mimas microsignatures. As there have not been any close flybys of Mimas to date, possible unique interaction characteristics at this moon (due to an unexpectedly dense exosphere) cannot be assessed. If present, they could further complicate the picture, as in the case of Enceladus.

Furthermore, as the filtering of the electron spectrum at Enceladus could be modulated by the state of the neutral gas and dust cloud at and the shape of the electron drift shells there (which both could be variable), the resulting electron spectrum at Mimas might be also variable and cannot be standardized. In this case, it would be interesting to investigate if the electron spectrum shape at Mimas could be used as an index of the magnetospheric state or even Enceladian activity.

Finally, the good agreement of the extracted D_{LL} values and L-dependence with those given by (*Cooper et al.* 1983) for high energy protons is consistent with no dependence of these parameters by particle species. This could be further investigated with the more statistically significant proton measurements by LEMMS.

Without any doubt icy moon absorption signatures are an extremely valuable tool which can be used to effectively probe a series of dynamical processes in the Saturnian magnetosphere.

5 Detection and physical characterization of rings and dust structures of the Saturnian system

In the previous chapter the detection and the evolution of energetic particle microsignatures and macrosignatures has been primarily linked to magnetospheric processes at Saturn, such as the estimation of electron diffusion rates and the factors that determine the shape of the charged particle drift shells. Similar observations, however, can reveal the interaction with undetected moons or dusty obstacles. The identification of particle depletions with the energetic electron and ion detectors of Pioneer 10 and 11 probes, have helped to identify the Gossamer rings of Jupiter (*Selesnick* (1993) and references therein), Epimetheus (moon of Saturn), as well as the F and G rings of Saturn (*Van Allen et al.* 1980b, *Van Allen* 1982, 1983, 1987). Several other authors, based on the same datasets, inferred the presence of possible dust clouds sharing the same orbit with Mimas (*Chenette and Stone* 1983, *Selesnick* 1993) or the presence of a moonlet belt along Saturn's F-ring (*Cuzzi and Burns* 1988).

All the aforementioned studies were not only limited to identifying unknown particle absorbers: the understanding of the charged particle motion in the magnetosphere and of the propagation of plasma through inert matter can be used to infer the physical properties of the absorbers. Similar studies have also been performed with particles and fields data collected from the environment of the terrestrial planets and the heliosphere. For instance, *Dubinin* (1993) and (*Saur et al.* 1993) studied several magnetic field and plasma disturbances seen along the orbits of the martian moons Phobos and Deimos. The authors investigated a possible correlation of these disturbances with the presence of a neutral gas or dust torus at the orbits these two moons. *Jones et al.* (2003) detected a series of interplanetary magnetic flux enhancements (IFEs) in the magnetic field data of the Ulysses spacecraft, possibly associated with charged dust in cometary or asteroidal trails.

In this chapter I present new observations from the Cassini MIMI/LEMMS instrument that reveal the presence of optically undetected rings and dust clouds in orbit around Saturn. The importance of energetic electron microsignatures as tracers of unknown moons, rings or dust clump structures is highlighted, especially for low optical depth structures that are not easily detectable by remote sensors.

As charged particle depletions from unknown obstacles could originate either from a small, asteroid-sized moon, or from a dust cloud, it is important to identify some criteria according the nature of absorber can be classified to one of these two categories. For this purpose, several absorption effects (microsignatures) from two known, small Saturnian

moons, Telesto and Helene (both less than 30 km in diameter), are discussed. No microsignatures from such small moons have been previously reported. The detection and the understanding of such microsignatures show that the observed electron absorptions at the orbit of another small moon, Methone, cannot be attributed to Methone itself, but to an obstacle that comprises large dust grains. Through a similar analysis and by using additional information in images provided by the Cassini's ISS camera, the physical characterization of a ring arc in Saturn's G-ring is performed.

Table 5.1: List of several physical and orbital parameters for Telesto, Helene and Methone. The given diameter values correspond to the average diameters, as these bodies have irregular shapes. Up to date ephemeris data and constants can be found at *http://ssd.jpl.nasa.gov*

Moon	Diameter (km)	Semimajor axis (R_s)	Inclination (deg)	Eccentricity
Methone	3	3.23	0.007	0.0001
Telesto	24	4.89	1.19	0.001
Helene	32	6.26	0.199	0.0022

5.1   Energetic electron absorption by asteroid-sized moons

The basic orbital and physical parameters of Telesto, Helene and Methone are presented in Table 5.1. Viewing these bodies as energetic electron absorbers, their efficiency is small compared to that of physically larger moons, such as Tethys, Mimas, or even Prometheus and Pandora. As explained in the previous chapter, this efficiency is a function of energy and pitch angle, or equivalently of electron gyroradius, bounce period and drift velocity. Fig 5.1 illustrates how absorption is determined by some of these parameters.

For energies less than a few hundreds of keV the electron gyroradius is smaller than or comparable to the sizes of all three moons. This means that electrons avoid absorption mainly as a result of the large azimuthal distances that these electrons cover during half a bounce period (usually on the order of 10^2 km). At energies of the order of a few MeV, the gyroradius is still comparable to the moons' sizes. Around 1 MeV which is close to E_{rk} the relative electron-moon velocity is almost zero. For even higher energies, gyroradii and relative azimuthal velocities become large. Therefore, the electron absorption efficiency for these small moons should reach a maximum for energies around E_{rk}.

For a relatively close flyby to any of these moons, before diffusive processes broaden the microsignature, it should have a radial extent of approximately $(2R + 2r_g)$, where R is the moon's radius and r_g the gyroradius at the energy where the absorption occurred. This also can be referred to as the "effective absorption region".
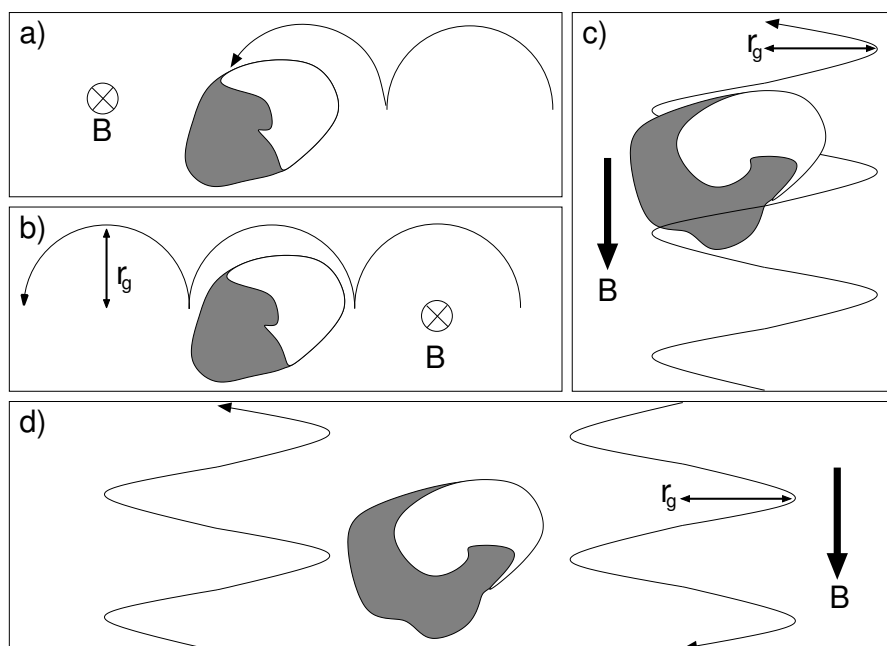
Figure 5.1: Absorption escape possibilities when the gyroradius of electrons is comparable to the moon sizes: (a) and (b) outline the case of a particle with a 90° equatorial pitch angle, where absorption is a direct function of the particle gyrophase. In case (a), the particle impacts the satellite, whereas in (b), the particle escapes absorption despite having a gyroradius r_g of a scale comparable to the moon itself. Cases (c) and (d) emphasize the contribution of the bounce motion for non-90° equatorial pitch angle particles. Despite their guiding center of motion passing through the moon, a particle of the correct gyrophase can avoid absorption (c). Even when the gyrophase is appropriate for absorption, electrons can bounce above or below the obstacle while they convect across its equatorial position and avoid impact - a process termed leapfrogging. Leapfrogging can result even in sub-keV electrons escaping absorption from large moons.

5.2 Electron absorption by Telesto and Helene

The main purpose of studying Helene's and Telesto's microsignatures is to demonstrate the theory of energetic electron absorption by inert, asteroid-sized bodies in the Saturnian radiation belts, and to increase our confidence that this theory is sufficiently understood and that it can be used to interpret microsignatures in the vicinity of other small bodies (in this case, Methone).

While this theory is based on simple and fundamental principles, direct observations could reveal the action of unexpected effects that alter the predicted microsignature structure. For example, observations of double absorption signatures and of very low diffusion rates at the orbit of Tethys have left open a small window for the possibility of successive absorptions by coorbiting satellites. Although such a possibility extremely small, it would also be interesting to demonstrate it through observations, rather than just by theory.

In the two panels of Figure 5.2, E_{rk} and the expected effective absorption region at the distances of the three moons is plotted. The lower limits for E_{rk} at Telesto and Helene
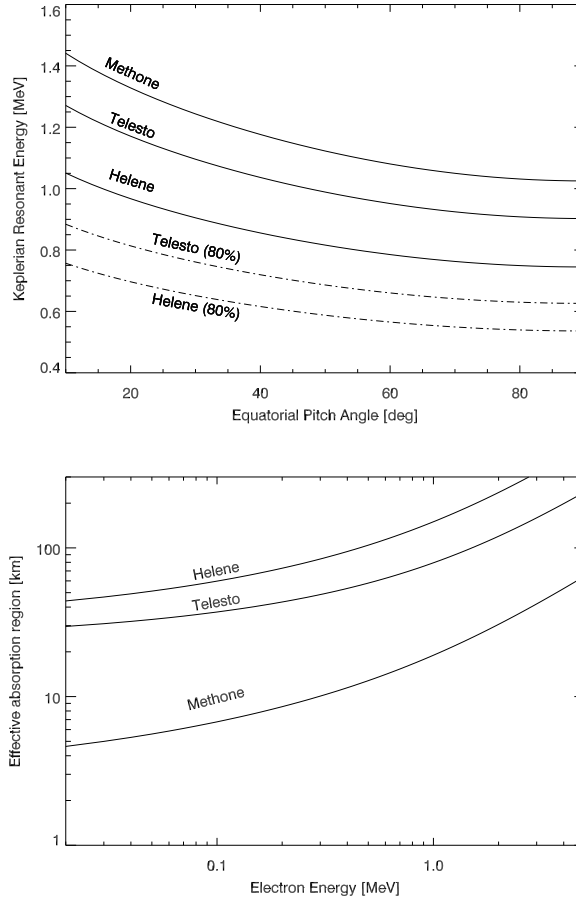
Figure 5.2: The Keplerian resonant energy (E_{rk}) as a function of equatorial pitch angle (left panel) and the effective absorption regions for electrons with energies between 0.02 and 5 MeV (right panel), for the distances of the three moons under study. In the left panel, I provide E_{rk} values from $0° − 90°$. Solid lines assume the plasma is rigidly corotating, while the dashed lines are for 80% subcorotation. The E_{rk} curves are symmetric with respect to the 90° values, for the $90° − 180°$ pitch angle range. For Methone's distance, no deviations are expected from rigid corotation (*Saur et al.* 2004).

come from the assumption that the corotation could be as low as $75 − 80\%$ of rigid motion at these distances (*Richardson* 1986).

5.2.1   The Telesto microsignature

Telesto resides around Tethys's leading Lagrangian point (L4), approximately 4.89 R_s from the center of Saturn. Cassini performed its closest approach to this body on day 284 of 2005 (October 11), reaching a minimum distance of 9524 km (Fig. 5.3). This corresponds to about 1° separation in longitude from the moon. The flyby was upstream of Telesto and therefore a microsignature was expected above E_{rk}. As the equatorial pitch angle of the observed electrons was around 162°, E_{rk} could lie between 0.82 and 1.18

MeV.

2005 day 284 (October 11)
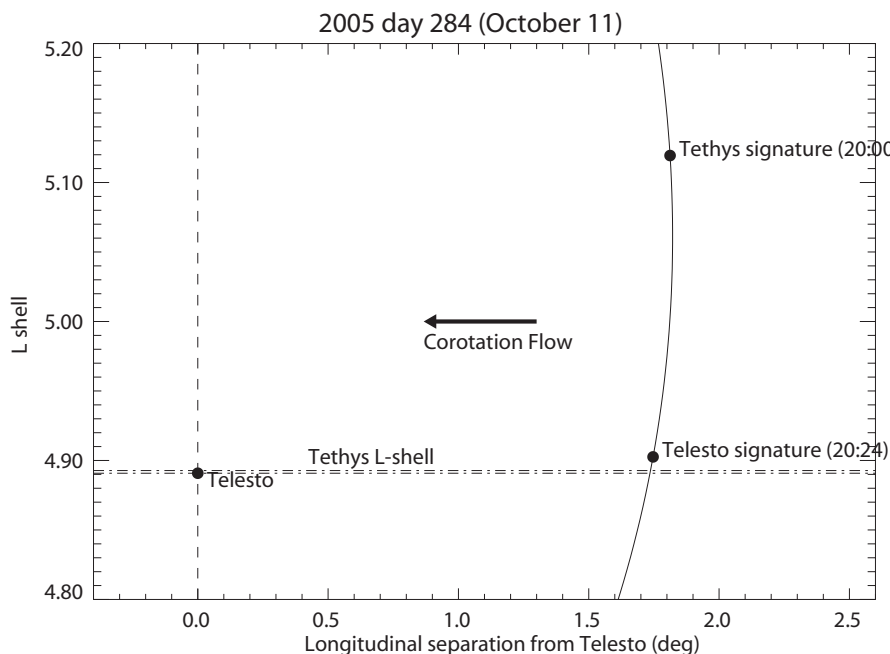
Figure 5.3: The geometry of Cassini's encounter with respect to Telesto. The flyby was upstream of Telesto, as indicated by the corotation flow direction. During that crossing, Cassini, was $\sim 60°$ downstream of Tethys and LEMMS also detected a clear Tethys microsignature in the 20-100 keV electrons at 20:00UT. Telesto shares almost the same L-shell as Tethys (dotted-dashed lines). The microsignature from Telesto was seen almost exactly at the expected position. The small displacement can be either due to magnetospheric processes (this is definitely the case for the Tethys signature - see Section 4.3.1), or due to the fact that the small inclination and eccentricity of Telesto is not taken into account here. The L-shell calculation includes the small northward displacement of the dipole field (*Dougherty et al.* 2004b)

Assuming a simple dipole, the expected time of observation of the signature was around 20:24 UT. Fig. 5.4 shows the electron count rates recorded in the E-channels that monitor electrons of energies greater that 95 keV. A small absorption feature is seen clearly at 20:24 UT in channels E3 and E4 (top panel). E0 is featureless (bottom panel) as it covers primarily electrons of $E < E_{rk}$, while it is maybe affected by background noise. Channels E1, E2 (bottom panel) are also dominated by $E < E_{rk}$ electrons (assuming an inverse power law, energy dependent flux), but have higher contributions from MeV electrons compared to E0. Together with E6 (bottom panel), they show possible absorption features, which, however, cannot be easily distinguished from small fluctuations (noise) seen in the data.

As the signal seems more clear in E3-E5 (665 keV lower threshold) and absorption should be more effective around E_{rk}, it is expected that the magnetosphere is not corotating rigidly, otherwise the microsignature should have been more pronounced in E6 (lower threshold of 1.045 MeV). This is in accordance to the estimated corotation fractions in the previous chapter.
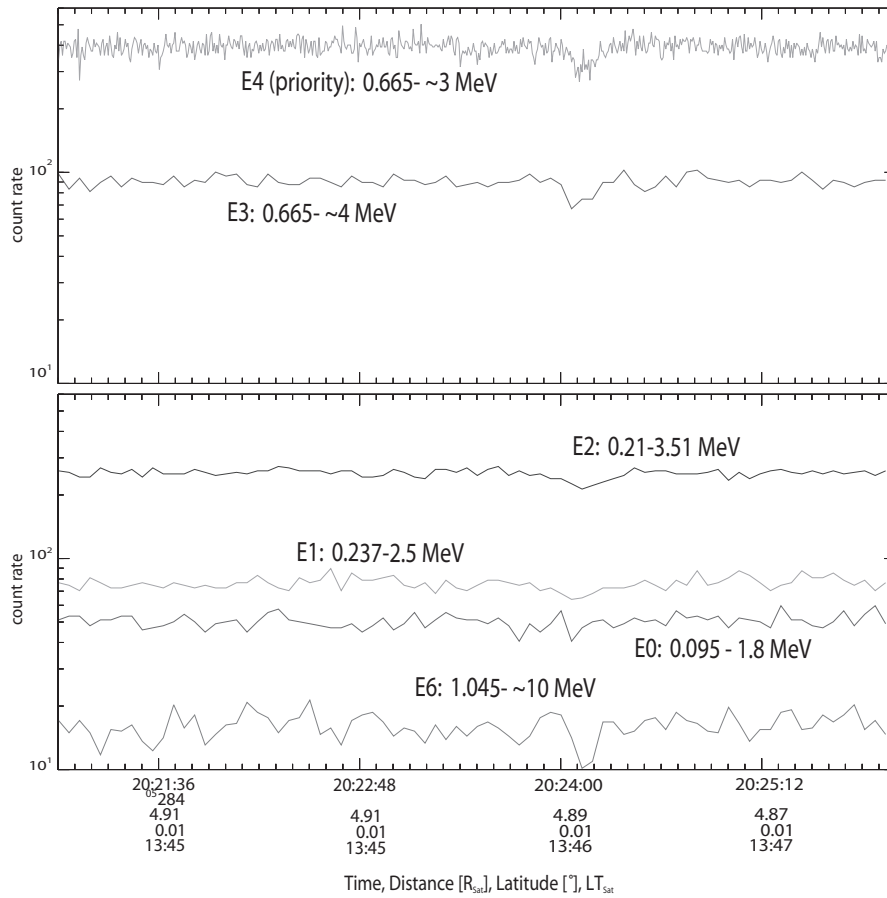
Figure 5.4: The microsignature of Telesto. The two panels show the count rates of several LEMMS E-channels with respect to time. Channels shown in the top panel are E3 and E4. E5 count rates are identical to those of E4 and are hence not plotted. E4 is a priority channel and has eight times better time resolution. In the bottom panel, E0, E1, E2 and E6 count rates are shown. The Telesto microsignature (20:24:12 UT) is more obvious in the E3-E5 channels. We point out that the recordings of the E-channels are given in count rates (counts s^{-1}) due to some uncertainties in these channels' energy widths and geometric factors.

Using the high time resolution measurements of the priority channel E4, it is found that the microsignature has a radial extent of about 100 ± 10 km. Subtracting Telesto's diameter, it is estimated that electrons with energy between E_{rk} and up to 2 MeV contribute to this microsignature signal. These observations agree with the microsignature formation principles described in Section 5.1.

5.2.2 The Helene microsignature

Helene is co-orbital with Dione and is located at its leading Lagrangian point (L4). A close flyby to the moon occurred in day 229 of 2006 (August 17) around 03:58 UT. The flyby was 2 degrees downstream of Helene and about 60 degrees downstream of its "parent" body, Dione (Fig. 5.5). Therefore a microsignature was expected by both

moins in the keV electron population ($E < E_{rk}$).
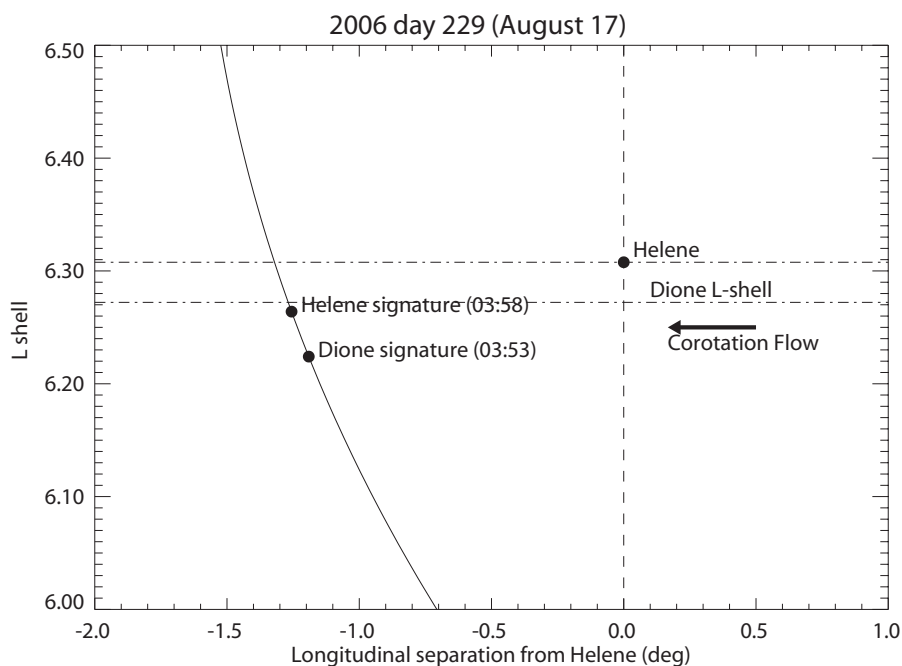
Figure 5.5: Same as in Fig. 5.3, but for the Helene flyby. Here the flyby is downstream of Helene. The Helene and Dione average L-shells differ slightly, due to small differences in the orbital elements of these two bodies. Helene's inclination and the fact that the Cassini was at a latitude of about $7°$, where the dipole approximation at that distance from Saturn has measurable errors, could explain the observed displacement. Dione's orbit has very small inclination and eccentricity and the observed displacement can be explained primarily by magnetospheric processes.

Fig. 5.6 shows the features from Dione and Helene in the C0-C3 channels of LEMMS (20-100 keV). Radial displacements of the microsignatures by magnetospheric processes, which are described in Chapter 4, help to distinguish the tiny Helene feature, which could have been hidden under certain circumstances, in the larger scale electron depletion by Dione.

This extremely fortuitous event shows that the contribution of the small moons to the total plasma losses, when compared to that of the large moon, is negligible. This contradicts any possibility that the long microsignature lifetime at these distances is due to their reinforcement by successive satellite absorptions. Furthermore, this example further supports the theory of microsignature formation from tiny moons: with increasing energy (or as we move closer to E_{rk}) the microsignature depth increases. The radial width of the microsignature projected at the equator is around 70 ± 10 km, which is only slightly larger than the expected size of the effective absorption region (~ 50km), probably due to the effect of radial diffusion or due to a reduced magnetic field magnitude under the action of the magnetospheric ring current (which could increase the electron gyroradius).

In total, the observed absorption effects of Telesto and Helene are in agreement with expectations about small body effects in the Saturnian magnetosphere, and could be used
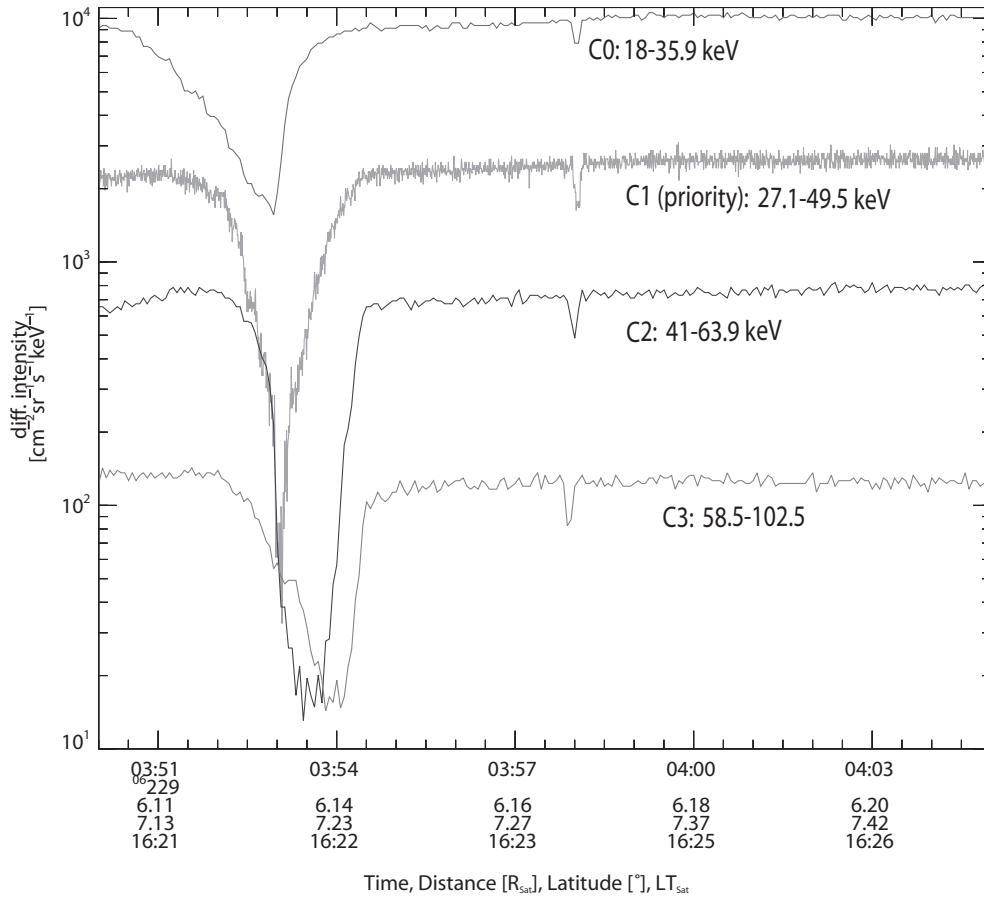
Figure 5.6: The microsignatures of Helene (03:58 UT) and Dione (03:51-03:55) in the C0-C3 channels of LEMMS. Energy ranges are indicated on the plot. Starting from C0, the decreases in electron intensities at Helene's microsignature are approximately 20%, 24%, 32% and 36% indicating that as we are closer to E_{rk} electron absorption is more effective (see Section 5.1).

as a reference to predict or explain candidate signatures from other small moons of Saturn. A summary of these observations is given in Table 5.2, including the events at Methone's distance that will be discussed in the following sections.

It is noted that analogous absorption escape effects explain why microsignatures in energetic ions are so rare, even from the large icy moons. The relation between the size of the large icy moons, and the ion gyroradii, velocity and bounce period, is qualitatively similar to that of the electrons with the "asteroid-sized" moons.

5.3 Electron depletions at Methone's distance

Methone, discovered in images from the ISS camera of the Cassini spacecraft, is a ~3 km-wide moon whose orbit lies between those of Mimas and Enceladus, at approximately 3.23 R_s (*Spitale et al.* 2006). The satellite's motion is visibly affected by gravitational perturbations of Mimas, but these effects are insignificant for the purposes of analyzing

Table 5.2: Summary of the observed microsignatures. Times are given in UT. The microsignature width is calculated, along the radial direction, after it is projected on the equatorial plane. The third column gives the equatorial pitch angle of the observed microsignature. Equatorial pitch angles are calculated using information on Cassini's magnetic latitude and the value of the measured local pitch angle of the particles (*Roederer* 1970).

Event date (yyyy.dddhhmm)	Microsignature width (km)	Equatorial pitch angle (deg)	Additional remarks
2005.2842024	100 ± 10	162	1° upstream of Telesto seen in E3-E5, microsignature from Tethys, observed at 20:00 UT
2006.2290358	70 ± 10	45	1.5° downstream of Helene seen in C0-C3, microsignature from Dione observed at 03:53 UT
2006.2521707	2400	55	17° upstream of Methone, seen in E0-E6, also appears in lower energy ion and electron LEMMS channels (penetrating radiation decrease) (*Paranicas et al.* 2005)
2006.2521909	1500	50	5° upstream of Methone seen in E0-E6, Mimas microsignature seen in E2 at ~19:00UT

the microsignatures that will be described here.

Methone is an order of magnitude smaller that Telesto and Helene. However, the gyroradius of electrons is smaller than at those moons due to the much higher magnetic field magnitude at Methone's distance. Therefore, Methone can theoretically produce similar effects to those seen by Telesto and Helene, scaled to the size of Methone's effective absorption region (see Fig. 5.2). An important constraint in detectability is that Cassini's radial velocity should be sufficiently small so that a depletion with an expected width of 10-30 km can be sampled by LEMMS.

This situation occurred on September 9 of 2006 (day 252) when Cassini crossed Methone's orbit, inbound and outbound, with a relatively small radial velocity of 2.2 and 4.7 km s^{-1}, respectively. During the outbound pass, Cassini made its closest approach to the moon to date, ~12000 km from its surface. The geometry of Cassini's periapsis, with respect to Methone, is shown in Fig. 5.7. The flyby, both inbound and outbound, was upstream and any absorption effects were expected above E_{rk} (~ 1.15 MeV). Surprisingly, LEMMS measured two wide depletions in energetic electrons count rates with a width on the order of 10^3 km. Fig. 5.8 shows the electron count rates of channels E4, E5 and E6 as a function of the dipole L-shell.

The inbound signature occurred approximately at 17:07 UT, while Cassini was at a
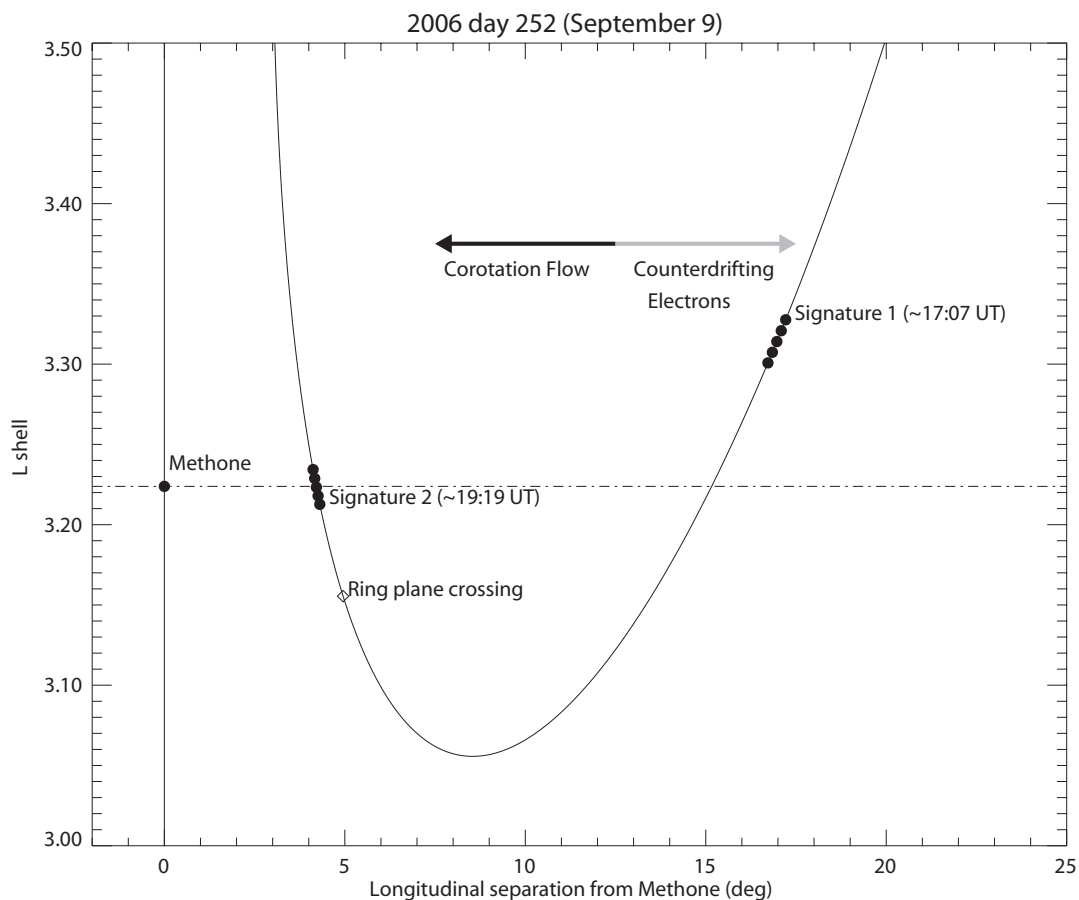
Figure 5.7: The Methone flyby geometry. Both inbound and outbound Cassini was upstream of the moon. The large black points indicate microsignature detections. The location of the ascending ring plane crossing is also shown.

latitude of 17°, with LEMMS pointing at a local pitch angle of 95°. This corresponds to an equatorial pitch angle of 55°. The signal was strong enough for it to appear in many LEMMS electron and ion channels, as the decrease of energetic electrons in this region translates into a reduction of penetrating radiation for the lower energy ion and electron channels. It had a radial extent of about 2400 km at the equator and was centered at $L = 3.3$. The longitudinal separation from Methone was about 17°.

The outbound microsignature was observed at 19:19 UT when Cassini was close to the equatorial plane. The event occurred closer to Methone than inbound (angular separation of ~5°). The local pitch angle of observation at that time was about 50°, almost identical to the equatorial pitch angle. The depletion region spans a width of 1500 km and occurs exactly on Methone's L-shell.

In both cases, Cassini's orientation was not changing so that instrumental effects as a cause of the count rate decreases can be ruled out. 14 earlier Cassini crossings of this region, with the closest to Methone being during SOI (Saturn Orbit Insertion - day 183 of 2005) and day 248 of 2005, did not reveal anything similar in LEMMS measurements. It is however interesting that both of these L-shell crossings had almost similar geometry
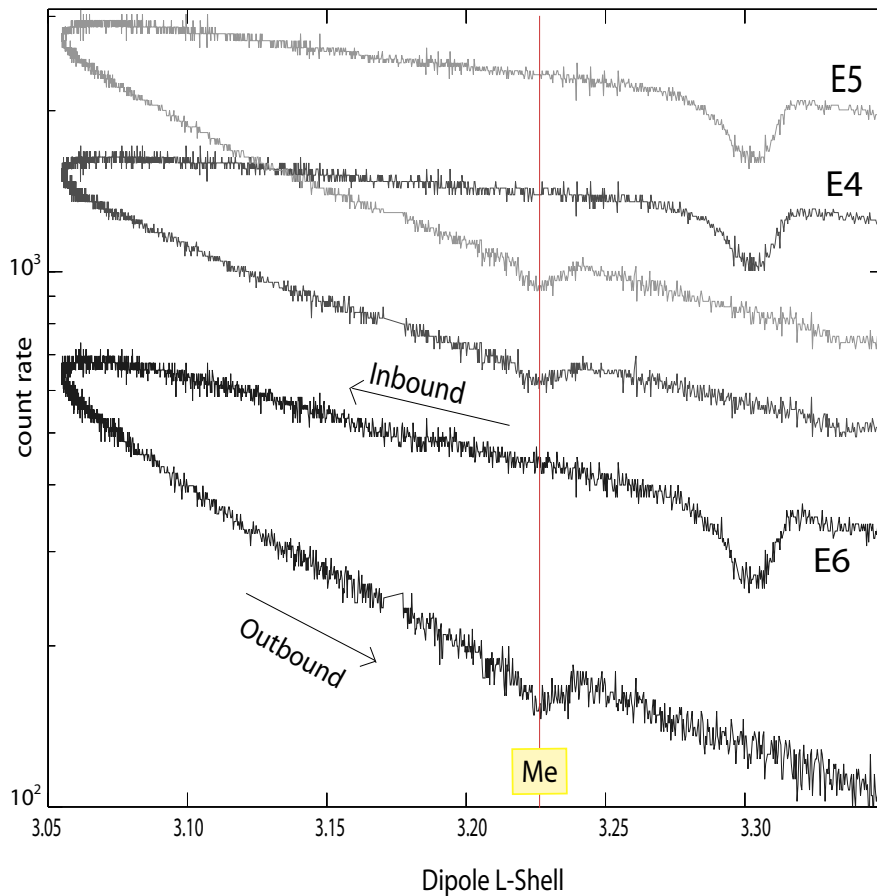
Figure 5.8: Depletions around Methone's orbit in LEMMS channels E4-E6 as a function of dipole L-shell. E0-E3 (not shown) show a similar microsignature signal, with that of E0-E2 being slightly weaker. The outbound microsignature occurs exactly on Methone's L-shell.

with respect to Methone as the inbound crossing of Fig. 5.8 (~ 18° and ~ 13° upstream of the moon, respectively).

The Cassini magnetometer (*Dougherty et al.* 2004a) data acquired during that period have also been reviewed *(K. Khurana, personal communication)*, but no peculiar magnetic field signature associated with these events was identified. It is worth noting, however, that the inference about the presence of a dust torus at the orbits of the Martian moon Phobos, is based on magnetic field perturbations recorded by the magnetometer of the Phobos-2 spacecraft. *Saur et al.* (1993) identified such disturbances as phase-standing waves resulting from the solar wind interaction with charged dust.

The proximity of the two microsignatures to Methone's L-shell, as well as the fact that they coincided with the closest approach to this moon to date, makes it logical to examine the possibility that Methone is the direct source. However, the theory and observations presented earlier discount this possibility.

It is very unlikely that a 3 km sized inert moon can produce depletions with a width of the order of a thousand kilometers. Even if radial diffusion is considered as the source of the microsignature broadening, it can only expand the signal not more than ~100 km wide.

121

Furthermore, such an explanation would require fast diffusion rates, which contradicts up to date observations (*Paranicas et al.* (2005), *Van Allen et al.* (1980a) and Section 4.3.1). In addition, the inbound microsignature is substantially deeper than the outbound, despite Cassini being closer to Methone on the outbound segment of its periapsis.

There are more problems with considering Methone as the direct source of the inbound microsignature: The radial displacement of that microsignature from Methone's L-shell cannot be easily explained. While radial shifts in microsignature positions commonly occur for $L > 4$ due to magnetospheric processes (*Paranicas et al.* (2005), *Jones et al.* (2006) and Chapter 4), at the distance of Methone such displacements are less likely, as the dipole magnetic field dominates drifts by other electromagnetic processes. This displacement ($\sim 0.07 R_s$) is higher than the average displacement of Enceladian microsignatures ($\sim 0.05 R_s$), during close encounters to that moon (*Jones et al.* 2006), while the opposite would have been expected.

One possible, but highly unlikely explanation, that could support a direct formation of the microsignatures at Methone, is that Methone is not inert but possesses a tiny magnetic field that in turn makes the effective obstacle larger. A magnetized asteroid has been observed in the past by Galileo (*Kivelson et al.* 1993). However, the composition of the rings and moons of Saturn is not supportive of the possibility that Methone can be composed by magnetic carrier materials. Even if Methone is magnetized, it would still be hard to explain why its effects in the magnetosphere would appear as electron absorption.

It is therefore established that the observed electron depletions have most likely not originated directly at Methone. Here I examine the case for a dust arc (or arcs) at Methone's distance as the possible absorber, and I discuss different possibilities about its structure, origin and location.

5.3.1   The structure of the arc

Independent of the arc's source, rough estimations about its optical depth will be made first. It is considered that the absorbing body has a similar structure to an arc-like feature close to the orbit of Enceladus, observed by *Roddier et al.* (1998). It is therefore assumed that it has a longitudinal extent of $l = 15°$ (or 8.1×10^3 cm at Methone's distance), that it is composed of water ice particles of $\rho_o = 1 g\,cm^{-3}$ and that it moves on an equatorial orbit. Most of the above values and assumptions are arbitrary, but in the absence of relevant observations such approximations are unavoidable. Following *Cuzzi and Burns* (1988), the normal optical depth, τ of the arc can be approximated from Equation. 5.1.

$$\tau = \frac{3}{8} \frac{(pK)\,V_d T_b \cos a}{l \rho_o r} \tag{5.1}$$

$K(g\,cm^{-2})$ is a measure of the absorption efficiency of water ice called the range, defined as the column density required to reduce the flux of electrons by a factor of e^2. The distance required to produce the observed flux decrease is pK. In this case, $p=0.2$. For the range, experimental values are retrieved from the National Institute of Standards and Technology (NIST) website *(http://physics.nist.gov/PhysRefData/)*. A typical value of K for 1 MeV electrons is $0.43 g\,cm^{-2}$. The parameters V_d (cm s^{-1}), T_b (s), a (deg) and r (cm) are the electron drift velocity, the bounce period, the equatorial pitch angle

and the particle size (radius of spherical particle), respectively. In Equation. 5.1, the arc longitudinal length, l, is expressed in units of length (cm).

The optical depth values estimated using Equation. 5.1 are shown in Fig. 5.9 for the absorption of 0.8-1.65 MeV electrons. The results shown in this figure indicate two different scenarios for the structure of the arc that caused the absorption.

First it is assumed that the dominant population in the particle size distribution is that of the $\sim 1 - 10^3$ μm grains with optical depth values between 10^{-4} and 1 . That is orders of magnitude higher that the mean optical depths of the G-ring and the E-ring ($\sim 10^{-6}$). A reasonable upper limit for the optical depth is $\tau \sim 10^{-3}$. The selection of this upper limit comes from the estimated maximum τ value of F-ring clumps by *Cuzzi and Burns* (1988). That is a rather generous upper limit, given that the F-ring clumps accrete in a material richer environment ($0.1 < \tau < 1.0$) than the inner edge of the E-ring. Values greater than 10^{-3} anyway seem unrealistic, as this would mean that this arc would have comparable or similar efficiency in scattering or reflecting light as part of Saturn's main rings, which have τ that range from ~0.05 to 2.5 (*Nicholson* 2000).

This upper limit for τ translates into a lower limit of $r \sim 100\mu$m for the particle sizes. In any case, τ estimations support the previous statement, that an obstacle comprised by small grains has to be dense and that simply a presence of a faint ring is not sufficient for MeV electron absorption. Such an object would be sufficiently optically thick to be detected by remote sensing instruments.
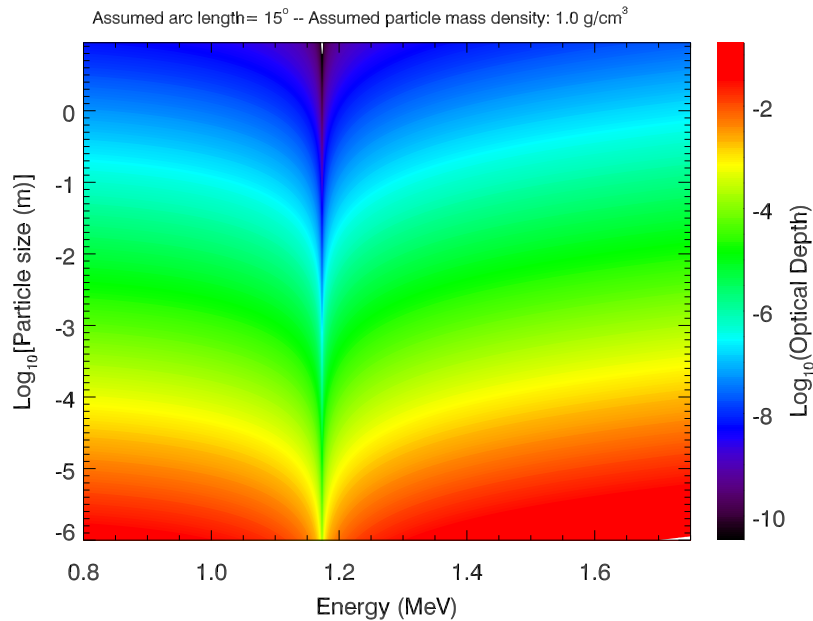
Figure 5.9: Estimation of the arc's optical depth using Equation. 1 as a function of electron energy and particle size. We point out that Equation. 5.1 is fairly accurate only if the particle size distribution in the arc is very narrow. The estimated optical depth values will be higher or lower, if we assume a more longitudinally compact object or a more extended ring structure, respectively.

A second possible scenario is that the arc comprises larger than mm-sized particles.

Its optical depth can then be even lower than that of the E and G rings, and this might make its remote detection difficult. The reason is that the amount of mass needed to stop electrons in such a case can be contained in only a few large grains which are not numerous enough to scatter or reflect significant fraction of the incoming radiation from the Sun.

For both scenarios an interesting case exists and it is indicated by the optical depth "dropout" region around 1.17 MeV. This is the value of E_{rk} at which electrons have almost zero velocity with respect to the arc material and interact continuously with it. In that case, electron absorption is very effective even if the arc material is optically thin. If the observed absorption took place primarily at E_{rk}, then the lower limit for the particle size goes down to $r \sim 10\mu$m. Unfortunately, the exact energy (or energies) of the observed absorptions cannot be distinguished.

For the plotted energy range in Fig 5.9 the values of τ are almost symmetric with respect to the E_{rk} region, which means that the most important parameter in this calculation is the energy dependent relative velocity towards the arc, rather than the increase of the range, K, with energy. For much higher or much lower energies the variation of K with energy becomes the most important factor.

5.3.2   The origin of the arc

Analysis of Galileo spacecraft and ground based observations showed that Jupiter's Gossamer rings are associated with the small moons Amalthea and Thebe (*Burns et al.* 1999). Recently, a ring, or partial ring, has been detected by Cassini at the orbital distance of the 4 km sized Pallene, that orbits Saturn slightly outside Methone, at 3.54 R_s (*R/2006 S1; IAU Circular 8759*). It is therefore reasonable to infer that a similar ring or arc could exist at Methone's orbit.

To date, the MIMI/LEMMS instrument has detected no clear signature in the LEMMS data around Pallene's orbit. No microsignature is routinely detected in electrons associated with Saturn's G-ring. This means that electron depletions cannot be established solely by the presence of a weak ring, as it was also stated previously. The ring has to be relatively dense or otherwise contain arcs within its structure. As the optical depth estimations suggest, the optical thickness of such an arc will strongly depend on the size of the particles that constitute it.

An arc of dust particles appears to be a conceivable way of producing such broad signatures. Examples of such features can be found in the Neptune ring system, where they are caused by resonances between the ring material and the planet's moons (*de Pater et al.* (2005) and references therein).

Micrometeoroid impacts on Methone can easily release material from its surface, thus producing a narrow and weak ring, on top of which an arc could develop. The release of material due the to action of interplanetary impactors on small moons at Jupiter is found to be very effective, primarily because of the low escape velocities (*Burns et al.* 1999). The situation might not be too different at Saturn. The arc could later develop under the influence of resonances and gravitational perturbations from Saturn's larger moons (for Methone's orbit, that could be for example the 15:14 mean longitude resonance with Mimas). The formation and evolution of F-ring transient objects or clumps, for example, seems to be associated with such mechanisms (*Spitale et al.* 2006, *Murray and Dermott*

2001). An additional source of material for a possible arc at Methone's distance can simply be E-ring particles which are continuously present down to 3 R_s (*Baum et al.* 1981). Gravitational perturbations by Methone could focus some of this material in regions near the satellite, in the same way that Prometheus attracts material from Saturn's F-ring (*Giuliatti et al.* 2000) (see also Figure 5.10).
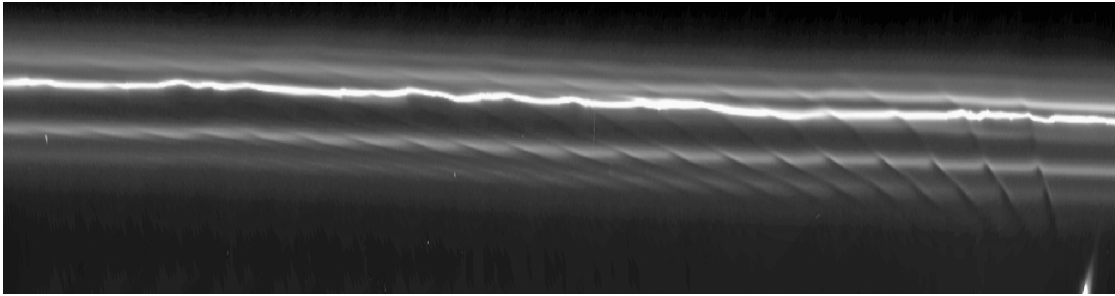

Figure 5.10: This mosaic of 15 Cassini images of Saturn's F ring shows how the moon Prometheus disturbs the ring once every 14.7 hours, as it moves on its eccentric orbit. The straightened image of the ring shows a region ~60°) of longitude around the ring. Prometheus is the overexposed feature at the bottom right of the image. Image credit: NASA/JPL/Space Science Institute

Alternatively, dust emitted at the south pole of Enceladus can drift inward by e.g. Poynting-Robertson drag (*Roddier et al.* 1998) and be a different source of the electron absorption, independent of Methone's presence. The latter seems a rather complicated process, but there are some observations that could support it. Inward spiralling of dust cloud under the Poynting-Robertson drag has been employed to explain the evolution of Jupiter's gossamer ring material (*Burns et al.* 1999).

In Figure 4.15 a microsignature is shown 200° upstream of Enceladus (panel "g"). This signature could attributed to Enceladus. However, its relatively large inward radial displacement from Enceladus's orbit (almost 0.2 R_s), and the fact that the rest of the upstream microsignatures from that moon suggested that they are depleted less than 100° away, leaves room for different interpretations. In the context of the observed signatures at Methone and the observations of *Roddier et al.* (1998), the possibility that this microsignature was produced by an inwardly spiralling dust cloud that was formed by Enceladian activity, is a reasonable proposition to consider.

It is unlikely that any of these mechanisms could result to the formation of a dust clump or arc with an optical depth greater than $\sim 10^{-3}$. The amount of material available from the E-ring ($\tau \sim 10^{-6}$), Enceladian activity or the micrometeoroid impact products at Methone's surface are probably not sufficient for the accretion of very dense structures. Considering these as the only possible sources for a dust arc at Methone, that the suggested upper and lower limits for the optical depth and the particle sizes, respectively, seem reasonable.

5.3.3   The location and the evolution of the arc

The different assumptions about the arc's structure give rise to a series of possibilities for its location with respect to Cassini and Methone at the time of the observation. For

example, if the arc was a very compact object (less than 1° extent in longitude), it would mean that the microsignature formed rapidly, as the passage of electrons through it would last just a few seconds. The microsignature would have then evolved only under the influence of magnetospheric effects (e.g radial diffusion and energy dispersion), which would progressively diminish its depth as it was drifting away from its creation point. Therefore, given that the inbound microsignature was deeper than the outbound (and assuming that these were formed by the same object), Cassini should have been downstream (ahead) of the arc and therefore the arc would have been at least 17° behind Methone in its orbit.

On the other hand, if the arc extended for many degrees in longitude and if the radial diffusion rate is weaker that the electron loss rate, the microsignature would build up progressively, and the deeper microsignature would be the one that "spent" the most time within the arc. In that case, the deeper inbound microsignature would be older than that outbound, implying that the arc extends mainly upstream (ahead) of Cassini, in a location that could even include Methone. If on the other hand the diffusion rate is higher, the arc should be downstream. Therefore, a much more extensive analysis and additional observations by other Cassini instruments (e.g. flux and size distribution of dust particles by the CDA and RPWS experiments) are necessary to select which of the cases is more plausible.

The fact that no electron absorption was found during earlier crossings of this region, has multiple interpretations. One possibility is that the putative dust arc is new; such temporary structuring within the E-ring has been previously reported (*Roddier et al.* 1998) and Methone's L-shell had not been traversed by Cassini for almost one year prior to the discussed event. *de Pater et al.* (2005) report that Neptune's ring arc structuring shows time variability, so this scenario is not unlikely for Saturn's case.

On the other hand, a continuous presence of an arc does not necessarily mean that microsignatures should be observed at every L-shell crossing of that region. The observed microsignatures show only a ~30% reduction of electron counts. Such shallow depletions can be quickly erased by diffusion, and thus may be observable close to the obstacle that created them.

A different case arises from the possibility that the inbound and outbound microsignatures were formed by the same obstacle. This would mean that the obstacle is moving on an eccentric orbit. Electron absorption from obstacles with eccentric orbits at distances less than 4 R_s (e.g. Mimas), seem to be difficult to predict, primarily due to the peculiarity of the electron energy spectrum (*Van Allen et al.* 1980a, *Chenette and Stone* 1983, *Selesnick* 1993). Indeed, Mimas's "ghost" or absent microsignatures, discussed in these three studies might be quite relevant to the LEMMS observations at Methone's orbit.

The possibility of an eccentric ring or ring arc seems however unlikely. While this chapter was written, the discovery of Saturn's 60th moon was announced by Cassini's ISS camera *(IAU Circular S/ 2007 S 4* - see Figure 5.11). The moon, now called Anthe, orbits Saturn between Pallene and Methone, at about 3.28-3.29 R_s, at the location where the inbound microsignature was seen. It is much more likely that this small moon, only 2 km wide, releases dust forming ring arcs or dust clumps around its orbit, that absorb MeV electrons. A similar assumption could be also used to explain the energetic electron depletion, at 3.68 R_s upstream of Enceladus (Figure 4.15, panel "g"): a small, unknown moon could orbit at this location, releasing material that can eventually form this depletion region.
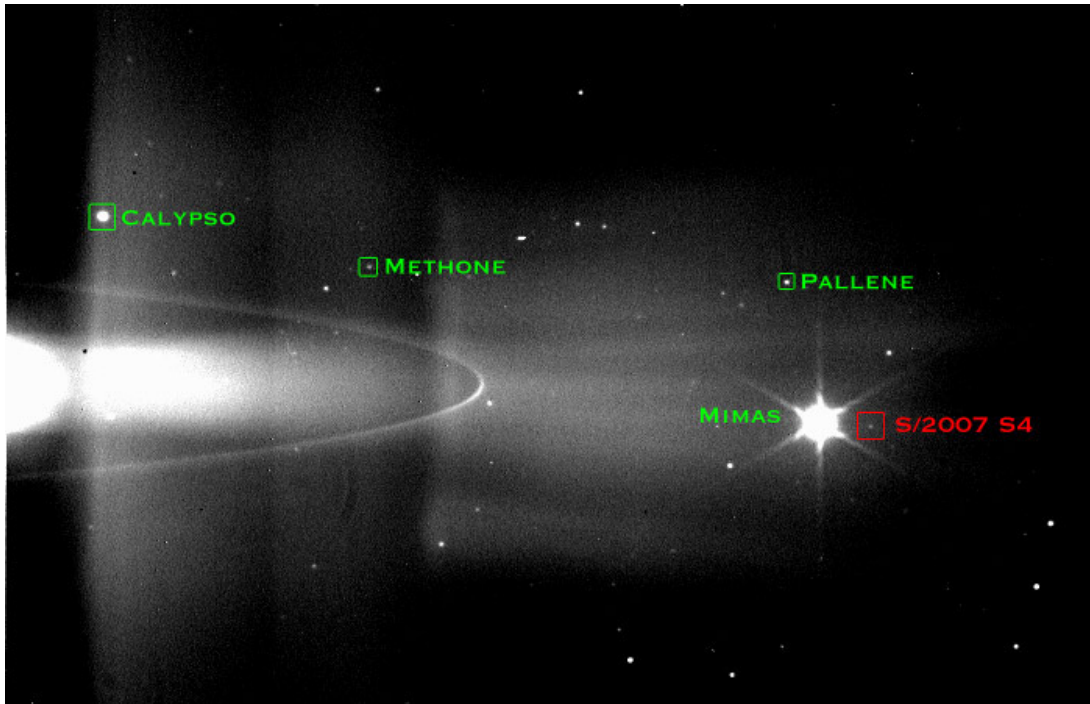
Figure 5.11: Saturn's 60th discovered moon, Anthe (S/ 2007 S 4), in one of the discovery images by Cassini's ISS camera.

5.4   The discovery of an arc in Saturn's G-ring

In the previous section, the existence of large particle populations or dust clumps was inferred at the orbit of Methone, at the orbit of the newly discovered moon of Saturn, Anthe, and at a distance of 3.68 R_s (location of undetected moon?), based on observations of MeV electron depletions. A large range of possibilities were also discussed as alternative explanations of these findings, mainly because LEMMS observations were not complemented by an optical detection of such features or because no there datasets were other.

A multi-instrument approach can be very useful in such studies, as even negative results from an instrument can impose important constraints on the interpretation of the data from another one. Such a possibility occurred when LEMMS detected an unexpected MeV electron depletion during the crossing of Saturn's G-ring L-shell. Around the same time, a dust arc was found in the images of the ring, superimposed on the G-ring. By combining these observations, it was possible to evaluate the source region of Saturn's G-ring, as it is shown in the following sections.

5.4.1   The G-ring

Saturn's G-ring was originally detected by the identification of its ion macrosignature from the Pioneer 11 energetic particle detectors. This macrosignature was attributed to losses on the "main body" of the G-ring or to undetected moonlets (that confine the G-ring's dust gravitationally), each lower than 2-3 km in diameter (*Van Allen* 1983, 1987).

This macrosignature is commonly detected from the LEMMS MeV ion detectors (Figure 5.12).
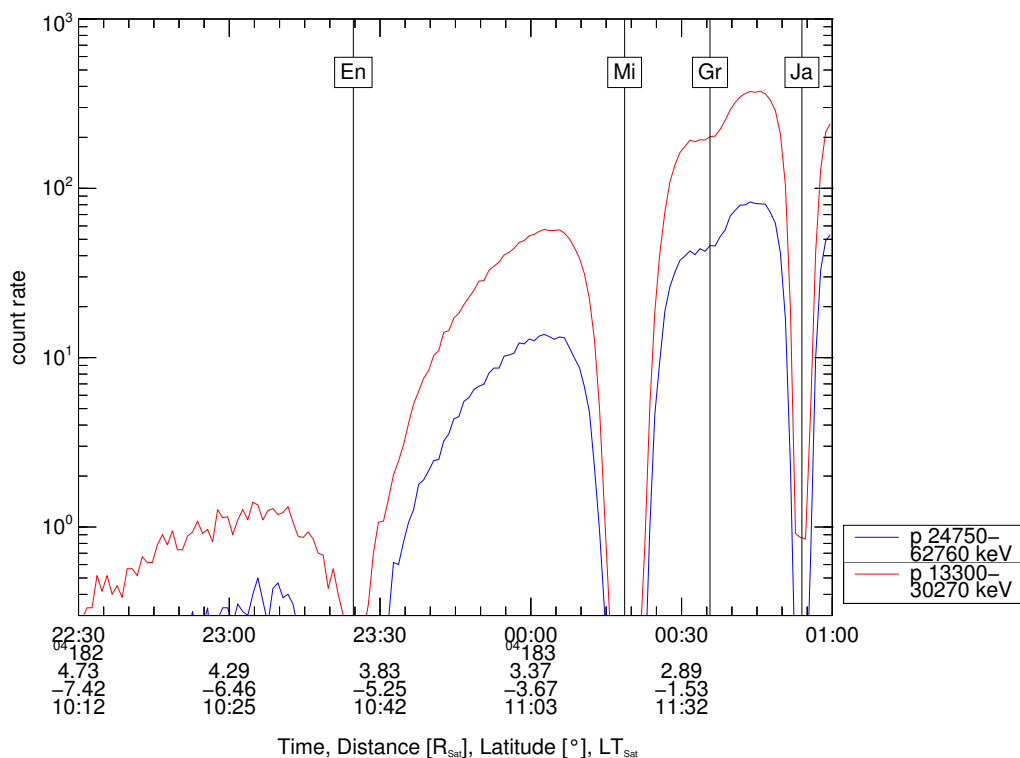
Figure 5.12: 86 second averaged countrates of the P7 and P8 LEMMS channels (MeV ions) from Saturn Orbit Insertion, during the inbound leg of the orbit. Seen are the macrosignatures from the moons Enceladus, Mimas, and the Janus and Epimetheus pair. The G-ring macrosignature is located at the L-shell of the G-ring, marked with the label "Gr".

G-ring is located at a distance of about 2.82 R_s from Saturn, it has a width of a few thousand kilometers. Its presence was considered a mystery, as there seemed to be no source that confines the dust in such a formation (e.g. as Prometheus and Pandora confine the dust in Saturn's F-ring), while there was also no source to replenish the dust lost due to sputtering of G-ring grains from magnetospheric ions, such as Enceladus replenishes the E-ring (Figure 5.13).

5.4.2   The G-ring arc

Cassini crossed regions magnetically connected to the G-ring during three orbits (until the end of 2006), with six total passes inbound and outbound. Apart from the expected MeV ion macrosignature, no other depletion was detected in electrons or lower energy ions in LEMMS data, with the exception of the September 5, 2005 crossing, when at ~12:13 UT an unexpected, localized and sharp 50% decrease in MeV electron count rates was seen.

Around that date, Cassini's ISS camera team announced the discovery of a distinct arc on the G-ring. After several observing runs, the arc's orbit was determined (*Hedman*
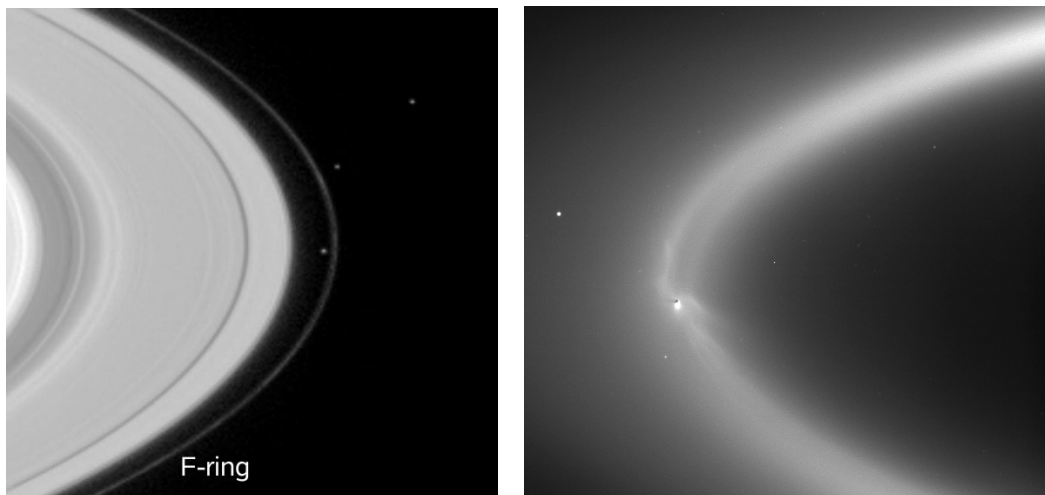
Figure 5.13: (Left): An image of Saturn's F-ring by Cassini's ISS camera. Prometheus and Pandora are seen on each side of the ring. (Right) Long exposure image of Saturn's E-ring and Enceladus. Enceladus south polar cryovolcanos are seen errupting and adding mass to the E-ring. Image credits: NASA/JPL/Space Science Institute

et al. 2007) and it was realized that when LEMMS observed the electron microsignature, Cassini had a close encounter with the arc, and actually crossed field lines directly connecting to this structure. Images of the arc are shown in Figure 5.14. The fact that LEMMS did not observe any other electron microsignature during previous G-ring crossings, made clear that the observed depletion did not originate from the main body of the G-ring, but from the newly discovered arc.
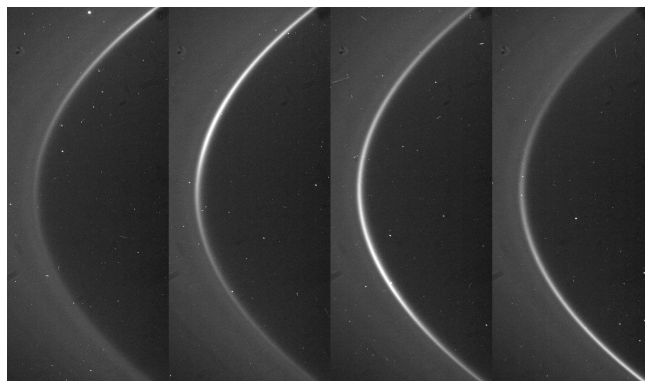
Figure 5.14: A sequence of G-ring images showing the arc moving on its orbit, on top of the G-ring. Image credit: NASA/JPL/Space Science Institute

Most images of the arc were taken at high phase angle: that is the angle between the lines connecting Cassini and the arc, with the Sun. Under such geometry the ISS camera measured forward scattering light, which revealed the effects of the micron-sized dust of the structure (*Hedman et al.* 2007). A measurement of the arc's normal optical depth profile in the micron-size grains was then possible. The profile is shown in Figure 5.15,

along with the MeV electron depletion and its projected location on the G-ring plane. The radial displacement of the microsignature's location, with respect to the location of the arc is peculiar and could imply the presence of a localized, electromagnetic interaction between the arc and the magnetospheric plasma. The displacement cannot result from an eccentric or inclined orbit of the arc, as the arc orbit was constrained to be circular and equatorial, based on ISS camera images (*Hedman et al.* 2007).
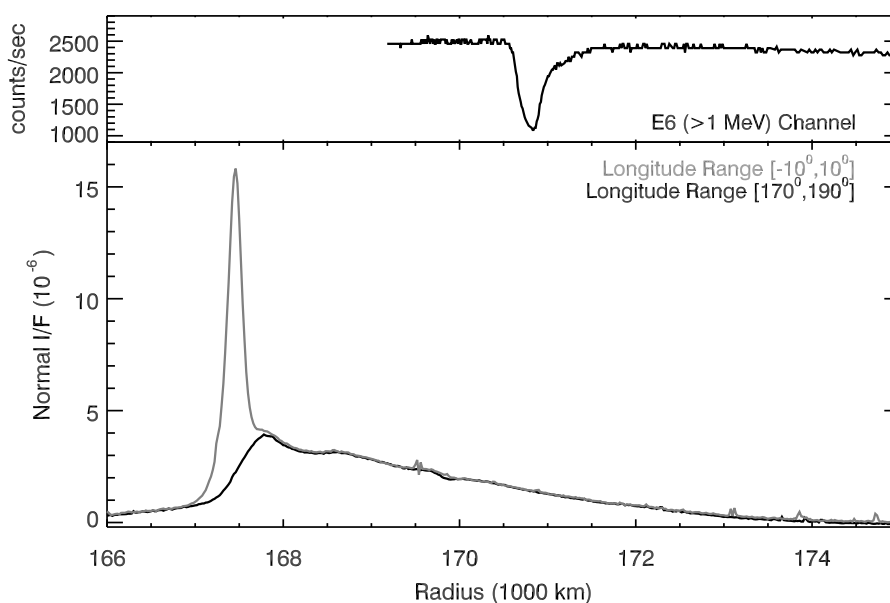
Figure 5.15: The G-ring arc normal optical depth profile in the micron-sized grains is shown (grey line, bottom panel), as a function of distance from Saturn. For reference, the optical depth profile of the "main body" of the G-ring is also shown (black curve). The top panel shows the drop-out seen in the E6 electron count rate during a close passage of Cassini from the magnetic field lines that map to the G-ring arc.

As it can be seen from Figure 5.15, the peak optical depth of the arc in the micron sized particles (the particles that constitute the visible arc), is about $1.5\ 10^{-5}$. Using similar methods for optical depth calculation as it was done for the electron absorptions close to Methone's orbit (Section 5.3.1), it can be easily found that micron sized particles could have only absorbed the MeV electrons if the optical depth of their population would have been around 10^{-3}. Larger particles or boulders, in the size of centimeters or even meters are needed to deplete the MeV electrons. This is further supported by the fact that the depletion appeared also in channel E7 of LEMMS, which is sensitive to electrons of ~10 MeV. An unfortunate event, provided additional hints about the presence of large particles in the arc: during the close approach to the arc, the dust detector of Cassini (CDA - Cassini Dust Analyzer) was damaged by a hit from a large dust grain, the size of which is estimated to be larger than $100\ \mu m$.

Such a population of large grains could have an optical depth of $10^{-8} - 10^{-7}$, a limit

that cannot be accessed by the remote cameras of Cassini. These "invisible" bodies are important to understand why the G-ring exists: sputtering of the large grains by energetic particles and intercollisions of the arc's boulders produces large smaller particles, that can disperse along the arc's orbit, forming the G-ring. Non-gravitational forces (such as ion drag) and sputtering account for the expansion of the smaller grains radially outward, as it is seen in the optical depth profile in Figure 5.15. The large particles of the arc are not affected by non-gravitational forces and are trapped in a restricted region of the ring due to a 7:6 mean longitude resonance with the moon Mimas (*Hedman et al.* 2007).

5.5   Outlook

In this chapter, energetic electron depletions were considered as tracers of new moons, rings, ring arcs or dust clumps. Despite Cassini having a powerful camera system, and despite the advancements in Earth-based telescopic observations (with ground based observatories or the Hubble Space Telescope), LEMMS data show that there are many ring or dust structures still not accessible to optical instruments. Such low optical depth structures can be detected by LEMMS if they comprise large grains or dust clumps. The condition for energetic electron absorption by dust is satisfied if the dusty obstacle contains sufficient column mass and not necessarily if it is optically thick.

On the other hand, it is not possible to derive all properties of the absorber by considering only LEMMS data. The observation of a single absorption signature by an unknown absorber can be explained in many different ways. What can be best approximated is whether the grain size distribution of the dusty obstacle extends to sizes of centimeters or even higher. Multi-instrument studies can impose further constraints and help to achieve a more complete explanation of the data from LEMMS and other instruments. The example of the multi-instrument approach in order to explain different observations of the G-ring arc has shown the importance of combining different datasets.

Overall, results in this chapter show the first steps to analyze several LEMMS observations of signatures from unknown absorbers, which to some extent were unexpected. An attempt to get more information out of these observations would require first of all a better calibration of the MeV electron channels of LEMMS. As it has been shown in Section 4.4.2, the spectral shape and the exact passband of a detector could influence the shape of a microsignature (see Figures 4.22 and 4.23), especially if the passband of the detector is large. This is the case of the LEMMS E-channels, where most of the uncorrelated microsignatures have been detected.

It is also important to establish better the structure of the space environment in the inner magnetosphere and evaluate the presence of possible mechanisms which could erode a microsignature signal. For instance, microsignatures from most of the large icy moons outside $L = 4 R_s$ survive for many hours and are commonly detected in almost all periapsis crossings of Cassini. The microsignatures from the inferred structures around Methone's distance or the microsignature of the G-ring arc have been detected only once. That is peculiar, since radial diffusion coefficients in that region of the magnetosphere are very low (Section 4.4.2).

However, a similar behaviour has been observed for the microsignatures by Mimas, Janus and Epimetheus, many of which were "missing", contrary to expectations (Section

4.4.1). This further confirms that the innermost magnetosphere has a peculiar structure in energetic electrons, either because radially diffusing electrons are filtered by the E-ring, Enceladus and the outer moons or because a source of energetic electrons acts in this region (e.g. CRAND) (*Cooper et al.* 1983). Establishing the exact reason, can help quantify better the exact depletion depths and lifetimes of the observed microsignatures by dusty obstacles and provide valuable input to better infer the physical properties of the absorber, and even its location.

Finally, it is important to establish the limits where the approach used for determining the absorber's optical depth. For instance, Equation 5.1 (or variations of it) can be derived practically by integrating the path length of an electron through an absorber with a given spatial profile of the dust number density. In this first-order approach, the electron's path length is practically the path of its guiding center under the assumption that for energetic electrons the gyration scales are comparable to the mean distance of dust grains in a low optical depth cloud. In this case the dust medium can be considered as continuous.

A more accurate description would be to consider the electron path as the real spiral trajectory of a particle in the radiation belts. In this case the path length through the medium (much larger than the guiding center path) should be multiplied by an impact probability, which should normally be much lower than unity, and a function of energy and pitch angle. The calculation of this impact probability could be done with the use of test particle codes. This would give more accurate results regarding the energy loss of electron (or ions) through a dust cloud.

6 Hybrid simulations of Saturn's moon Rhea interaction with the magnetospheric plasma

Since the Saturn Orbit Insertion (SOI) of the Cassini/Huygens spacecraft (July 2004), moon-magnetosphere studies have been focused on two saturnian moons, Titan and Enceladus. Titan possesses a substantial ionosphere which forms a Venus or Mars-like interaction within a submagnetosonic flow. On the other hand, Enceladus's south polar source of dust and heavy gas molecules forms a large scale electromagnetic obstacle compared to the moon's size and results in an interaction which resembles that of a comet with the solar wind (*Dougherty et al.* 2006). Both moons are considered important plasma sources and potential drivers of the global dynamics of Saturn's magnetosphere.

As also discussed in the two previous chapters, a large number of satellites orbits Saturn within the region occupied by its magnetosphere. Most of these moons, which sizes range from that of an asteroid (e.g. Telesto, Calypso) to that of a large moon (e.g. Mimas, Tethys, Rhea), probably have weak exospheres produced from sputtering of their surfaces by energetic particles. Such exospheres are not sufficient to slow down the incoming plasma flow or to cause a significant pile-up of the upstream magnetic field. To a good approximation, these moons are considered to be inert and are expected to have an "absorbing body" type or "lunar type" interaction with Saturn's plasma. While this has been clearly demonstrated with energetic electron data, the assumption still holds for low energy (cold) plasma. On the other hand, the wake dynamics at the sub-keV energy are most likely not driven by radial diffusion.

In this chapter, wake dynamics in the low energy plasma through a hybrid simulation code are studied and the macroscopic wake structures in the plasma and the electromagnetic fields are identified. The Saturnian moon chosen for this case study is Rhea. A brief comparison of the simulation results will be done with data from the magnetometer experiment of Cassini, collected during the first close Rhea flyby by Cassini..

6.1 Lunar type interactions at Saturn

Saturn's magnetosphere is an ideal environment for the study of lunar type interactions. Since Saturn's spin and magnetic axes are aligned and almost colocated, the plasma bulk velocity vector is continuously almost perpendicular to the magnetic field in the equatorial plane, where most moons orbit the planet. As a result, the bulk velocity vector, $\mathbf{u}$, the magnetic field $\mathbf{B}$ and the resulting corotational (or motional) electric field, $\mathbf{E} = -\mathbf{u} \times \mathbf{B}$

always define an orthocanonical system upstream of a moon. In addition, since many of Saturn's inert moons orbit within the plasmasphere of the planet, the upstream plasma moments can be considered quasi-stable for large time scales compared to the duration of a Cassini flyby or a simulation run. Such a configuration eliminates many complications which can otherwise mask important physical processes associated with the dynamics of a lunar wake. Moreover it makes the set up of a realistic simulation of the interaction more feasible.

For example, the solar wind impinging on the Earth's Moon can experience notable short term variations of its properties, e.g. in the interplanetary magnetic field (IMF) magnitude or orientation. Besides that, the angle between **u** and **B** is in most cases oblique. Furthermore, the macroscopic parameters of the Moon's space environment can vary substantially, as this can be located in the solar wind, in the Earth's magnetosheath, the current sheet or the tail lobes. The Jovian moons experience a similar variability as they can be positioned in or out of the plasma disk (since the axis of the Jupiter's dipole moment is tilted by 9.8° with respect to the spin axis). In this case, the sampling of the interaction during only several flybys (as it is possible with most planetary missions) cannot be termed as representative and the comparison with simulations can be difficult. Such complications are less pronounced for Saturn's moons.

6.2   Saturn's moon Rhea

Rhea is the second largest satellite of Saturn and most likely, a geologically inactive moon (Figure 6.1). It has a radius of R_{Rh}=764 km and orbits Saturn in a circular and equatorial orbit, with a semimajor axis of 8.75 Saturnian radii, R_s (1 R_s=60268 km). Based on the value of the moon's mean volume density and the modeling of its gravitational field, it is believed that Rhea is composed by a mixture of ice and rock and therefore it should have the physical behaviour of an insulator (*Anderson and Schubert* 2007). The magnetic field signature from the first close Rhea flyby by Cassini to date (November 26, 2005) is consistent with a plasma absorbing type of interaction with Saturn's magnetospheric plasma (*Khurana et al.* 2007). Equally, this means that plasma loss at Rhea's surface dominates any electromagnetic effect imposed by a sputtering-produced exosphere that probably surrounds the moon. This makes Rhea an appropriate choice for the purposes of the simulation attempts.

As mentioned earlier, Saturn's inert moons are numerous. However, selecting Rhea as the target body of the simulation instead of another inert moon is not an arbitrary choice. There are both physical and practical reasons behind this selection.

Rhea orbits Saturn at the edge the planet's E-ring (*Baum et al.* 1981), a location which can be seen as a "transition region" within the magnetosphere: there the magnetic field holds its dipolar configuration to a large extent but the magnetic field magnitude drops to values around 30 nT, while the plasma pressure is almost peaked (*Sergis et al.* 2007). This leads to plasma beta values around unity, which means that both the magnetic field and plasma dynamics can be important in the interaction.

Another important element for Rhea's interaction is the magnetospheric variability at its distance (see Table 6.1). Although the values of the plasma and fields parameters are quasi-stable for relatively large time scales (e.g hours), the variance around the average
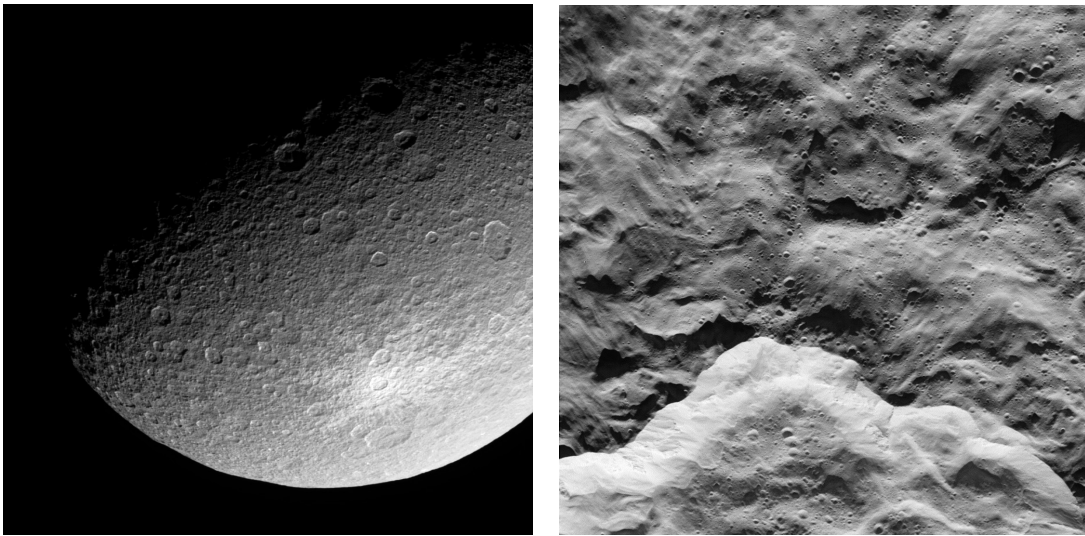
Figure 6.1: (Left): Global view of Rhea from the Cassini ISS Camera. The surface is heavily cratered, while a large, ray-crater, signifies the presence of a large impact in the early history of the moon. (Right) A close up of Rhea's surface from Cassini's ISS camera, during the close flyby to the moon, on November 2005. Image credits: NASA/JPL/Space Science Institute

values can be quite large. For instance, *Sergis et al.* (2007) have found that the plasma beta, β_i, can vary about two orders of magnitude at the distance of Rhea, based on the abundance of energetic water group ions in the plasma. The plasma density values vary by a factor of 2-3, while the bulk plasma velocity can be between 80 and 90% of the rigid corotation.

On average, the plasma flow with respect to Rhea is subalfvenic ($M_A < 1$), supersonic ($M_S > 1$) and submagnetosonic ($M_{MS} < 1$). Such a combination of Mach numbers is similar to that found in the vicinity of the Galilean moons of Jupiter.

What is interesting is that the Alfvenic Mach number, M_A is close to 1, and given the range of values that the plasma parameters can take, extreme configurations of Rhea's space environment (e.g. high plasma density, low dipole magnetic field magnitude due to strong ring current, high plasma bulk velocity) could lead to M_A and $M_{MS} \sim 1$. Then the conditions for a shock formation are satisfied and the presence of Rhea's exosphere cannot be neglected. It is not known, however, if such configurations are possible.

Magnetospheric variability is probably also significant for other inert moons, like for example Tethys and Mimas, that orbit Saturn at 4.89 R_s and 3.11 R_s, respectively. However, as these moons orbit Saturn in regions of strong magnetic field and low plasma velocity, plasma betas are always small and the interaction is always submagnetosonic. On that respect, the different configurations that the space environment can take, make its interaction with the magnetospheric plasma unique.

Adding to all the aforementioned unique characteristics of Rhea's interaction is the fact that the gyroradius of the water group ions is comparable to size of Rhea and to the width of the moon's wake, which means that ion kinetic effects can be important, especially if a weak exosphere is modelled around the moon. Again, due to the strong

magnetic field and the low plasma velocity at Tethys and Mimas, the ion gyration scales are much smaller and possible relevant effects (if any) would be very hard to illustrate. This makes Rhea a better choice for the application of a hybrid code.

Finally, as the plasma velocity relative to Rhea ($\sim$60 km s^{-1}) is higher than at Tethys and Mimas ($\sim$34 and $\sim$16 km s^{-1} respectively), the plasma convection time through an equal sized simulation box can be at least 2-3 times lower for a Rhea simulation than it is required for the two other moons. The same conclusion can be reached if we consider that in lunar type interactions, the sound speed is the characteristic velocity with which disturbances propagate (*Samir et al.* 1983).

One complication factor could come from the fact that Rhea might possess an extended dusty exosphere. This was hinted by data from the MIMI/LEMMS and CAPS instruments of Cassini which detected a weak, but quite unusual interaction region, with a scale equal to that of the moon's Hill sphere ($\sim$ 15 R_{Rh} diameter) - the region where Rhea's gravity dominates that of Saturn's (*Jones et al.* 2008). While no "dust component" is included in the simulations shown, the results can be used to show indeed that such a large interaction region cannot be reproduced by a hybrid code, if Rhea is simply modelled as an inert obstacle and with no mass deposited around it (in any form).

Parameter	Values	Additional comments	References
Magnetic field, B	25-35 nT	$\mathbf{B} \perp \mathbf{u}$ continuously	(Dougherty et al. 2004b, Khurana et al. 2007)
Plasma density, n	3-9 cm^{-3}		Richardson (1986), Maurice et al. (1996), Persoon et al. (2005), Sittler et al. (2006)
Relative plasma velocity, u	55-65 km s^{-1}		Richardson (1986), Saur et al. (2004), Mauk et al. (2005), Sittler et al. (2006)
Ion composition	Protons, Water group ions	$< m > = 17$ amu	Richardson (1986), Sittler et al. (2006)
Electron temperature, T_e	30-50 eV		Maurice et al. (1996), Sittler et al. (2006)
Ion Temperature, T_i	100-200 eV		Richardson (1986), Sittler et al. (2006)
Electron beta, β_e	0.03-0.3		Maurice et al. (1996), Calculated
Ion beta, β_i	0.05-1		Richardson (1986), Sergis et al. (2007)
Proton gyroradius, $r_{g,p+}$	17-24 km (0.02-$0.03\ R_{Rh}$)	Single charged	Calculated
Water group ion gyroradius, $r_{g,w+}$	290-400 km (0.38-$0.52\ R_{Rh}$)	Mass assumed: 17 amu, single charged	Calculated
Alfvenic Mach number, M_A	0.43-1.5		Calculated
Sonic Mach number, M_S	1.2-1.5		Calculated
Magnetosonic Mach number, M_{MS}	0.4-1.0		Calculated
Neutral exospheric surface number density, n_{exo}	$< 10^8$ cm^{-3}		Saur and Strobel (2005)

Table 6.1: Values and ranges of the various parameters describing Rhea's space environment. We note that the value range of plasma moments could partly be attributed to the moment calculation method.

6.3 The simulation code

For the simulation of Rhea's interaction I make use of a hybrid code, where ions are treated as individual particles and electrons as a massless, charge neutralizing fluid. The code has been originally developed for the modeling the interaction of weak comets with the solar wind (*Bagdonat and Motschmann* 2002), but has also been successfully applied for the simulation of the interaction of Mars and magnetized asteroids with the solar wind and of Titan with Saturn's magnetospheric plasma (*Bößwetter et al.* 2004, *Simon et al.* 2007a,b).

For the current simulation runs a slightly modified version of the code is used, compared to the one applied in the aforementioned references. The main modification is the inclusion of a resistivity term in the equations, which is necessary for a more physically correct description of the propagation of the magnetic field through the interior of Rhea. In the following subsections a short summary of the code's basic features is included for the completeness of the chapter. A more detailed description of the code's main aspects is included in the earlier studies, mentioned before.

6.3.1 Basic equations

The equations of the hybrid code are the following:

- Equation of motion for the individual ions (single particle motion) with charge q and mass m:

$$\frac{d\mathbf{x}}{dt} = \mathbf{v} \ , \tag{6.1}$$

and

$$\frac{d\mathbf{v}}{dt} = \frac{q}{m} \left(\mathbf{E} + \mathbf{v} \times \mathbf{B}\right) \ , \tag{6.2}$$

where $\mathbf{x}$ and $\mathbf{v}$ correspond to the vector position and velocity of each individual ion, respectively. The $\mathbf{E}$ and $\mathbf{B}$ vectors are the electric and magnetic field vectors.

- Fluid, of massless, charge-neutralizing electrons (momentum equation)

$$0 = -q\,n\,(\mathbf{E} + \mathbf{u_e} \times \mathbf{B}) - \nabla P_e + \left\{\frac{\eta}{\mu_o}\nabla \times \mathbf{B}\right\} \ , \tag{6.3}$$

where $\mathbf{u_e}$ describes the mean velocity of the electrons, n is the electron number density (equal to the ion number density, due to the assumption of charge neutrality) and P_e is the electron pressure of the magnetospheric plasma.

- Electromagnetic fields equations:

  For the electric field equation we have:

$$\mathbf{E} = -\mathbf{u_i} \times \mathbf{B} + \frac{(\nabla \times \mathbf{B}) \times \mathbf{B}}{\mu_o qn} - \frac{\nabla P_e}{qn} + \left\{ \frac{\eta}{\mu_o} \nabla \times \mathbf{B} \right\}, \tag{6.4}$$

while the equation for the temporal evolution of the magnetic field is:

$$\frac{\partial \mathbf{B}}{\partial t} = \nabla \times (\mathbf{u_i} \times \mathbf{B}) - \nabla \times \left[\frac{(\nabla \times \mathbf{B}) \times \mathbf{B}}{\mu_o qn} \right] - \left\{ \nabla \times (\frac{\eta}{\mu_o} \nabla \times \mathbf{B}) \right\}. \tag{6.5}$$

The last three equations include an additional term compared to the previous applications of the code. The term highlighted in brackets has been introduced for the propagation of electromagnetic fields through a medium of finite resistivity, η. The inclusion of this terms is important for a self-consistent calculation of the electromagnetic field properties in the interior of Rhea. This is briefly described in Section 6.3.2.

- Electron population description, using an adiabatic scaling for the electron pressure:

$$P_e \propto \beta_e \left(\frac{n}{n_o} \right)^k , \tag{6.6}$$

where k=2 (*Bößwetter et al.* 2004), n_o is the initial number density of the plasma and β_e is the electron beta. Using Equations 6.3 and 6.6, electron temperature effects can be described with this model. Because of the adiabatic description of the electron pressure, no relevant pressure term appears in Equation 6.5 (*Simon et al.* 2007a).

Parameter	Values	Comments
Mag. field magnitude, B	26 nT	Ideal case ($\mathbf{B} \perp \mathbf{u}$):
		$\left[B_x, B_y, B_z \right]$ = [0, 0, −26] nT
		For comparison with Cassini data:
		$\left[B_x, B_y, B_z \right]$ = [0.2, 1.5, −26] nT
Plasma density, n	4 cm^{-3}	
Relative plasma velocity, u	57 km s^{-1}	$\left[v_x, v_y, v_z \right]$ = [57, 0, 0] km s^{-1}
Ion composition	< m >=17 amu	—
Electron beta, β_e	0.09	$T_e = 40 eV$
Ion beta, β_i	0.24	$T_i = 100 eV$
M_A	0.83	—
M_S	1.44	—
M_{MS}	0.73	—

Table 6.2: List of parameters used for the two simulation runs.

6.3.2 Modeling the solid body of Rhea

Like in various geophysical applications studying induction effects within the Earth (eg. *Martinec* (1999)), the solid body of Rhea is modelled as an Ohmic conductor. The last terms in Equations 6.4 and 6.5 emerge from the assumption of an Ohmic law for Rhea's interior, where the scalar resistivity profile η has to be specified for each simulation. As stated above, Rhea can approximately be described as an insulating solid medium. For this reason a high homogenous resistivity is applied which can be expressed by its reciprocal value, the conductivity $\sigma_{Rhea} = 5 \cdot 10^{-7} S/m$. This value has been chosen because a similar conductivity is estimated for the terrestrial Moon (*Lipatov* 2002). Everywhere in the plasma the resistivity is assumed to be zero. In order to accommodate the solid nature of Rhea every particle impinging on its surface is removed from the simulation.

To selfconsistently integrate the insulating body of Rhea into the plasma environment, Equations 6.4 and 6.5 are solved within the entire computational domain. Whether the moon's exterior or interior is modelled is exclusively controlled by means of the coefficients u_i, n and η . This is implemented by using the resistivity profile defined above and setting the velocity u_i and the reciprocal density $1/n$ to zero within the obstacle.

6.3.3 Simulation parameters

The simulation is carried out within a 3D-box of 8×8×8 Rhea radii (R_{Rh}). A high spatial resolution is achieved using a cartesian grid with 120 cells along each box side. The coordinate system of the simulation is defined as follows: the positive x-axis is along the plasma velocity direction, the positive z-axis points is antiparallel to the magnetic field orientation and the positive y-axis points toward Saturn, opposite to the direction of the corotational (or motional) electric field, $\mathbf{E} = -\mathbf{u} \times \mathbf{B}$.

The center of the box is at $[x, y, z] = [0, 0, 0]$, while Rhea is offset by about 1 R_{Rh} towards the left side of the box ($x < 0$). In this way the simulation area allocated for the wake is sufficiently large. Larger offsets can increase this area even more, but that was not done in order to avoid possible interactions of the weakly conductive Rhea with the left side of the simulation box. Compared to simulations of the Earth's Moon wake, the simulation box is sufficiently wider along the magnetic field direction (z-axis), as at Rhea the velocity parallel to the magnetic field ($\mathbf{v}_\parallel$) is comparable to the perpendicular velocity ($\mathbf{v}_\perp$) and this could result in a north-south extension of the wake.

The upstream plasma and fields parameters are chosen to have average values from those given in Table 6.1. The selected values are given in Table 6.2. Results are shown from two, almost identical simulations. In the first ("ideal case") the magnetic field vector is perpendicular to the plasma bulk velocity vector. The second case is set up with non-zero B_x and B_y components, where $|B_x|, |B_y| \ll |B_z|$. This is mainly done for a better the comparison with the magnetic field data from the first Cassini flyby of Rhea.

In summary, the upstream plasma velocity relative to Rhea is set to about 85% of the rigid corotation. For the ion composition description I use single ion species assuming that the plasma is dominated by water group ions (< m >=17 amu). The selected electron and ion temperatures correspond to β_e of 0.09 and β_i of 0.24. The magnetic field magnitude is set to ~26 nT and the ion/electron density to 4 cm^{-3}. Therefore the interaction is subalfvenic, supersonic and submagnetosonic.
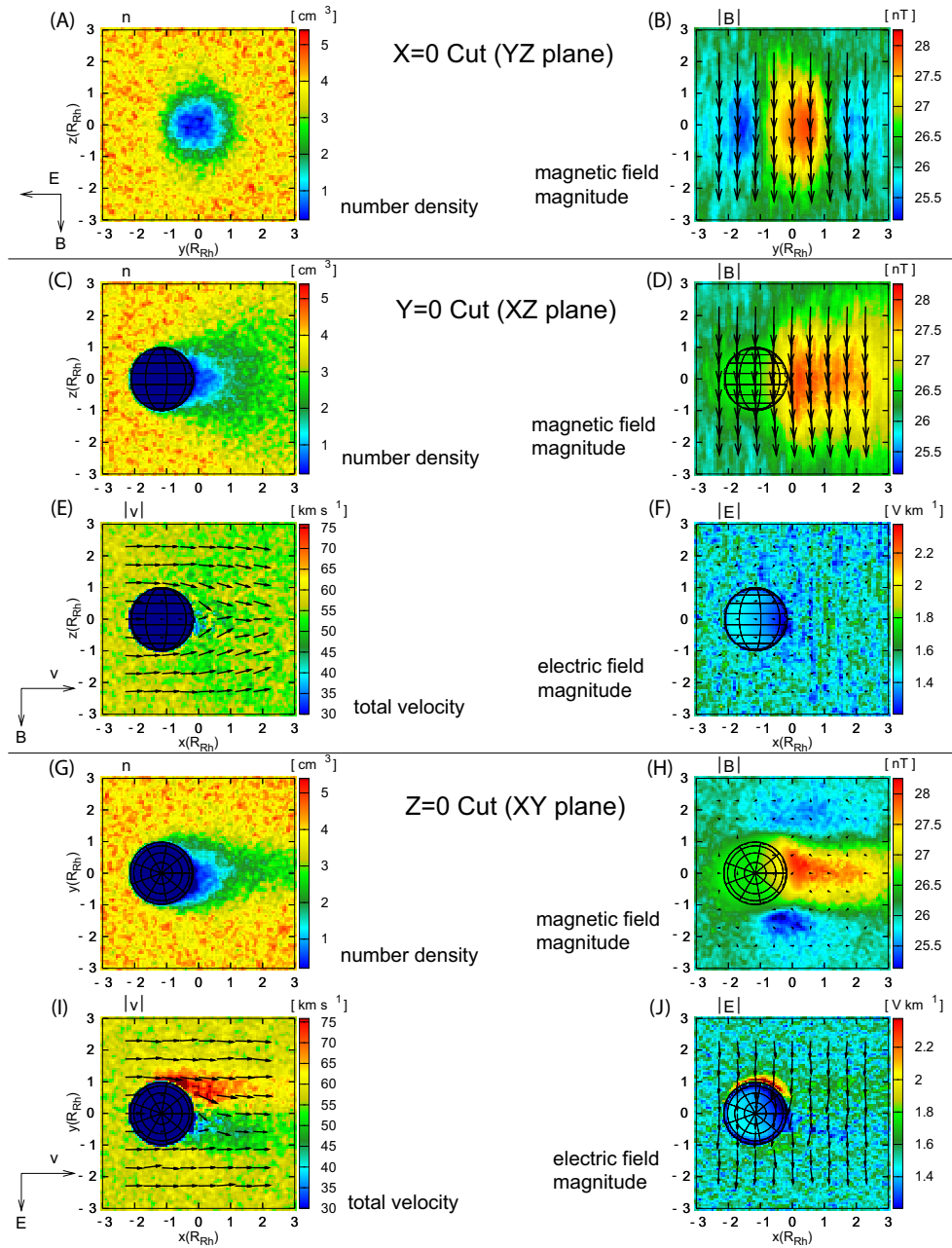
Figure 6.2: Overview of results for the "ideal case" run. Different parameters are plotted, at three different cuts through the simulation box. The top panel (x=0 cut / letters A,B) contains the plasma density and magnetic field just behind Rhea. The second panel (y=0 cut / letters C to F) shows the north-south configuration of the plasma density, velocity and electromagnetic fields, while the last panel of plots (z=0 cut /letters G to J) includes the same parameters, projected on Rhea's equatorial plane. In all panels, a small part of the simulation box is not shown, as it contains uninteresting regions (e.g. far upstream of Rhea). We also note that all vector parameters are plotted in the rest frame of Rhea. Additional plots in the plasma rest frame or with the background magnetic field subtracted are shown in Section 6.4.

For the interior of Rhea the chosen resistivity value ensures a diffusion time of the magnetic field through the solid body which is similar to the plasma convection time across Rhea's diameter. The simulation time step ($3 \; 10^{-3} m_i/qB$) satisfies the Courant condition. Normally, the simulation reaches steady state after ~2500-3000 time steps.

6.4 Results

In this section, results from the simulation runs are shown. I mainly focus on the "ideal case" scenario ($\mathbf{B} \perp \mathbf{u}$). The results from the run where $B_x, B_y \neq 0$ are almost identical and I only refer to those for the comparison with the magnetic field measurements by Cassini (Section 6.4.4).

The results from the simulation are summarized in Figure 6.2. We will now discuss the structures observed in each individual parameter.

6.4.1 Plasma density

In all density plots (plots A, C, G) the most easily recognizable feature is Rhea's wake, identified as a dropout in the plasma density. The central region of the wake is formed due to the shadowing of the plasma flow from Rhea's volume.

Starting from the plot in panel A (yz plane, just behind Rhea), the wake of Rhea is seen as an almost circular cross section with a diameter approximately equal to that of the moon. The central depletion region is slightly narrower than Rhea and densities are in most bins are above 0.5 cm^{-3}. This reveals that the plasma expands relatively fast into the vacuum.

Moving on to panel C (xz plane), the structure of the wake is revealed along the magnetic field direction. As particles can easily be moved along the magnetic field lines, this plot can reveal the plasma temperature effects. The "umbral cone" of the wake becomes progressively narrower and disappears after less than 1 R_{Rh} downstream of the moon. In the same time the plasma depletion region expands north and south of Rhea's geometrical wake.

This expansion can be explained in two different ways. The first explanation is purely geometrical and is proposed by *Khurana et al.* (2007). Within the radiation belts of Saturn, the ratio $\mathbf{v}_\perp/\mathbf{v}_\parallel$ can be close to unity or much smaller, due to the rapid bounce motion of the charged particles along the magnetic field lines and the low plasma bulk velocity. This means that in the xz-plane the impact trajectory of the charged particles on Rhea can have a large angle with respect to the wake axis (x-axis) and this would result in a extended, north-south depletion region. For the same reason, particles within a certain energy range can even avoid absorption (e.g. sub-keV electrons), while for other populations (e.g. keV electrons, $\mathbf{v}_\perp/\mathbf{v}_\parallel \ll 1$) the flux tube convecting past Rhea can empty completely (see Chapter 4) .

The bounce motion results from the latitudinal variation of |B| along a dipole field line, which cannot be described in such a simulation. Still, the effects of the bounce motion can be reproduced through the non-zero plasma temperature. This can be realized through a one-dimensional treatment of the plasma expansion into a vacuum, applied so far in many relevant studies.
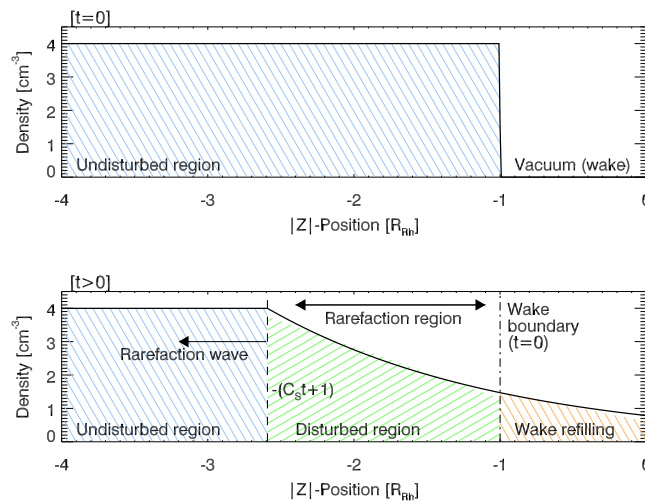
Figure 6.3: Illustration of Equations 6.7. The position up to which the rarefaction wave has propagated is given by $-(C_s t + 1)$. The dependence of the solution from the sound speed, tells us that the wake structure in the xz plane is determined by the plasma temperature. It is noted that in most previous studies the wake boundary is set at $z=0$ and the limb location at $x_{limb}=0$, which results in a slightly different form of Equations 6.7. To be in compliance with the simulation coordinate system, this slight modification in the equations has been introduced.

The momentum and continuity equations, assuming charge neutrality and a Maxwellian distribution for the ions (as in the simulation), can be solved analytically with boundary conditions that describe a vacuum: $\left(t = 0, \; z \leq -1 \rightarrow n_o = 4 \; \text{cm}^{-3}\right)$ and $(-1 < z \leq 0,$ $t = 0 \rightarrow n_o = 0)$. These boundary and initial conditions define along the z-axis (perpendicular to the flow) a 100% plasma depletion inside $z = -1 \; R_{Rh}$ at $t = 0$, where t is the convection time past Rhea's limb. The convection time can be approximated as $t = (x - x_{limb})/u$, where u is the plasma velocity, x_{limb} is the location of the limb along the x-axis and $x > x_{limb}$. These conditions are symmetrical for $z > 0$, with the depletion occurring inside $z = 1 \; R_{Rh}$. The solution for the density is given by the following expressions (*Samir et al.* 1983):

$$n(x, z) = n_o \; exp\left[-\left(\frac{(z + 1)\,u}{(x - x_{limb})\,C_s} + 1\right)\right], \tag{6.7}$$

for $(z + 1)/t > -C_s$. For $(z + 1)/t \leq -C_s$ the solution is simply $n(x, z) = n_o$. As mentioned earlier, the time t is expressed as:

$$t = (x - x_{limb})/u \; . \tag{6.8}$$

In Equations 6.7 and 6.8, the ion sound speed, C_s, is approximately 40 km s^{-1}. That solution defines that for a given vertical cut through the wake, at a distance $x - x_{limb}$ downstream of Rhea's limb, the plasma density increases exponentially into the wake $(z > -1)$. For for $z \leq -1$ the density drops exponentially from its initial value (n_o). This density drop propagates outwards $(z < -1)$ as a rarefaction wave with the ion sound
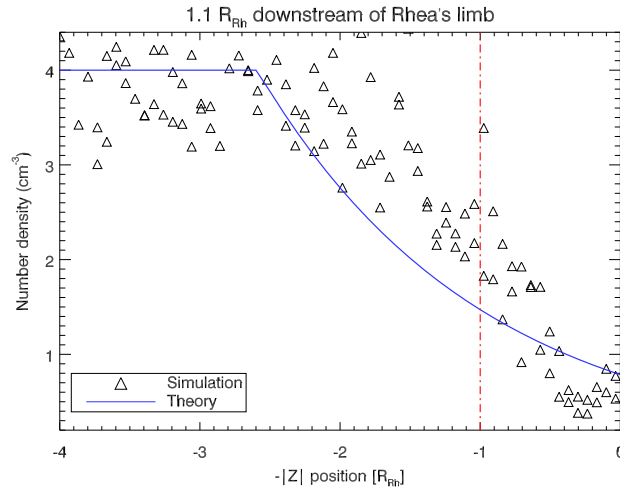
Figure 6.4: Comparison of Equation 6.7 solutions with the simulated data, for a distance of 1.1 R_{Rh} downstream of Rhea's limb.

speed. This exponential behaviour is valid for $(z - 1) \geq -C_s t$, up to the distance that the rarefaction wave has expanded. The solutions are illustrated in Figure 6.3. It is noted that in this treatment, electromagnetic fields are not described in the equations, while the boundary conditions do not restrict the plasma density values (as it is done in the edges of the simulation box).

As it can be seen in Equation 6.7, the ratio of the plasma velocity to that of the sound speed, or equally the sonic Mach number, M_s, will define how fast the wake will expand along the z-axis. For small M_s this expansion will be rapid and will occur very close to the moon (as seen in the simulation results), while for large M_s this expansion will occur at very large distances downstream of the absorbing body (e.g. as seen at the Earth's Moon). This description gives similar results with the geometrical approach introduced by *Khurana et al.* (2007).

The simulation results can be directly compared with this simple model. A comparison is shown in Figure 6.4. As it can be seen, the trend of the analytical solution is in good agreement with the simulation results. The main difference is that the density depletion in the rarefaction region is slightly slower compared to what the analytical solution predicts. This probably results from the simplicity of the one-dimensional approach, and the lack of consideration of the electromagnetic fields in the equations, as well as from the different boundary conditions used in the two approaches.

What is well predicted is the distance up to which the rarefaction wave has propagated. This good agreement is found at almost all distances downstream of Rhea, up to $x \sim 3 R_{Rh}$, where the expansion extends beyond the limits of the simulation box. An alternative way to investigate the expansion width is by comparing the opening angle of the rarefaction region with that of a Mach cone, at the given sound speed, C_s, in the simulation. The opening angle of a Mach cone, ϑ is given by the expression (e.g. *Zhdanov et al.* (2004)):

$$\vartheta = tan^{-1}\left[\sqrt{\frac{C_s^2}{u^2 - C_s^2}}\right] \qquad (6.9)$$

The same equation can be expressed as a function of the sonic Mach number, M_s, if one divides the nominator and the denominator by C_s^2. From Equation 6.9 it is found that ϑ should be $\sim 43°$. The opening angle of the rarefaction region in the simulation (plot C, Figure 6.2) is about 45°, almost in excellent agreement with the expected value. All these results show that the sonic Mach number is important for lunar-type interactions and that the one dimensional approach of the plasma expansion into vacuum is fundamentally valid, at least for the wake evolution in the plane that contains the bulk plasma velocity and the magnetic field (xz-plane in the simulation).

According to Equations 6.7, the wake expansion will continue until the density gradient across the z-direction will be zero. This theoretically happens at infinity, but with simple calculations it is estimated that very small gradients are achieved around 7-8 R_{Rh} downstream of Rhea's limb. At these distances, the resulting plasma density is equal to $\sim$40% of the initial ambient plasma density, n_o. This is of course unrealistic, otherwise charge particles would be depleted all over Saturn's magnetosphere. Practically, additional mechanisms will tend to bring the density values up to n_o (e.g. magnetospheric diffusion, electromagnetic field perturbations, instabilities, three -dimensional nature of the interaction), which is actually what is seen in the simulation. Given that, and considering also the variability of the space environment at Rhea's distance, it is expected that the plasma wake can extend to a maximum distance not much more than 10 R_{Rh} downstream of the moon. It is interesting to note here that the picture is different in energetic electrons as the wake refilling is only driven by magnetospheric diffusion, which is a relatively slow process, even at Rhea. Energetic electron wakes have been observed even 60 R_{Rh} downstream of Rhea (Section 4.4.2).

Moving now to the density profile in the equatorial plane (xy-plane, Figure 6.2, plot G), a much different wake configuration is seen compared to that in the xz-plane. The plasma depletion does not expand much more beyond Rhea's geometrical shadow. It progressively becomes narrower and one can easily infer from the plot that it would not extend much more than 6 R_{Rh} downstream. No similar temperature effects to those in the xz-plane can be seen in this projection.

This can be easily explained considering the single particle motion: from the maxwellian distribution of ions, an ion with energy greater or lower than the energy due to its bulk motion is selected. The velocity vector for this ion is $\mathbf{v_i} = \mathbf{v} + \mathbf{v_{th}}$, where $\mathbf{v}$ is the bulk velocity along the x-axis and $\mathbf{v_{th}}$ an additional, random velocity vector with components $v_{th,x}$, $v_{th,y}$ and $v_{th,z}$. These additional components will give to the particle a non-zero velocity with respect to the convecting magnetic field lines. With the magnetic field oriented along the negative z-axis, the solution of the equation of motion tells us that the ion will move "freely" on the north-south direction, with a constant velocity $v_{th,z}$. The perpendicular thermal velocity components $v_{th,x}$ and $v_{th,y}$ (or simply $v_{th,\perp} = \sqrt{v_{th,x}^2 + v_{th,y}^2}$) will cause the ions to gyrate around the magnetic field lines.

This means that ion motion along the xy-plane is restricted by the magnetic field, while along the z-axis it is not. Therefore, following the geometrical approach by *Khurana et al.* (2007) it is clear why the plasma wake can only expand north-south and not east or
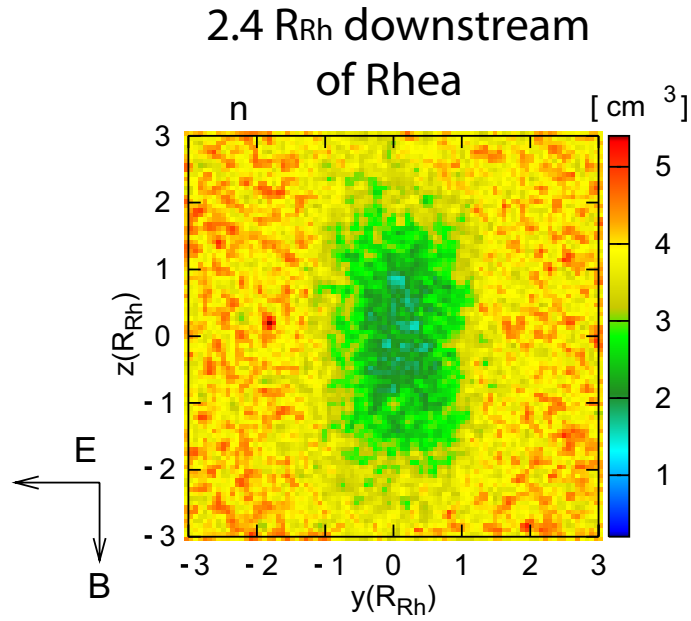
Figure 6.5: The asymmetric shape of Rhea's wake parallel and perpendicular to the magnetic field lines. The cut is at   2.4 R_{Rh} downstream of Rhea (or at x=1.3 R_{Rh}).

west of Rhea. Particle cross-field motion is only possible in the presence of an electric field (as for example the corotating electric field which is responsible for the plasma bulk motion perpendicular to the magnetic field lines). The one dimensional approach that was used previously is therefore not appropriate for the description of the wake structure in the xy-plane, as the constraints in the particle motion due to the magnetic field are not included in the equations.

The difference between the density wake structure along the magnetic field lines and perpendicular to it is better illustrated in a yz-cut through the simulation box, 2.4 R_{Rh} downstream of Rhea's limb (Figure 6.5). The wake has an almost rectangular shape and is at least four times wider along the z-axis. At the Earth's Moon this difference is much less pronounced in ions (due to the high sonic Mach number). It is more clear in electrons, which have a much higher thermal velocity than the ions (*Bale* 1997).

Jones et al. (2008) show that during the flyby of Rhea on November 2005, an extended energetic electron depletion was seen ($\sim$ 15 R_{Rh} wide) along a trajectory which is practically parallel to the y-axis. Figure 6.5 shows that such extended depletions cannot occur along the y-axis, unless additional absorbing material is present. If they can occur without the necessity of absorbing material around Rhea, that would require processes that cannot be described by such a hybrid simulation set-up.

Due to the gyration motion discussed previously, ions can impact Rhea even if their guiding center of motion does not intersect the moon. Given the ion temperature in the simulation, a maximum gyration radius for the upstream plasma of about 300 km, or $0.4R_{Rh}$ ($\sim$ 6 simulation cells) is estimated. Still, upstream ions with such large gyroradii comprise only small part of the total ion distribution and have small contribution to the total density. Therefore, any depletion region upstream of the moon, or any widening of the wake due to gyroradius effects, is rather small and has insignificant effects in the

simulation outcome.

Finally, the observation of the wake narrowing downstream of Rhea in the xy-plane can be explained by two possible mechanisms: diffusion or plasma convection due to field disturbances. The first explanation is not very likely to be the answer, since diffusion alone tends to make the depletion region shallower and broader. The second possibility seems more appropriate, given the various structures seen in the electric field in the xy-projection. These are discussed in more detail in Section 6.4.3.

6.4.2   Magnetic field

The magnetic field plots in the overview Figure 6.2 are shown in plots B, D and H (x=0, y=0 and z=0 cuts, respectively). As in the previous section, I begin first with the description of the field configuration in the yz-plane, just behind Rhea.

Here two main features are seen: a central region where the magnetic field magnitude increases by about 10% of the upstream value, and two almost similar field dropout regions, at the side of the magnetic field enhancement. The central enhancement region develops as a consequence of the requirement for total pressure balance. Since plasma pressure is lost on Rhea's surface, a field compression balances this loss in the wake. Because of $\nabla\mathbf{B}$ =0 a field decompression (or rarefaction) occurs on each side of Rhea's cavity.

Several interesting features are visible: the central enhancement follows the trend of the density depletion and extends north and south of Rhea's cavity. Along the y-direction it is confined within the moon's diameter. The rarefaction regions are also extended north-south. In the y-direction their spatial extent reaches up to the edge of the simulation box. What is also interesting is that the magnetic field decrease is asymmetric with respect to the pointing of the corotational electric field, $\mathbf{E}$. More specifically, it is stronger in the direction that $\mathbf{E}$ is pointing (y <0). In the same time, the peak of the magnetic field enhancement is slightly shifted in the opposite direction (y >0).

As magnetic field disturbances are only ~10% of the upstream value, changes in the field orientation can be realized more easily if the background field is subtracted. This is shown in Figure 6.6. The two main regions are also easily identified in this plot and the asymmetry along the y-direction is also clear. At the equator (z=0), opposite field perturbations in the y-direction cancel each other out, leaving only a perturbation in B_z.

The magnetic field residual vectors form closed loops, indicating the presence of a current towards the wake for y >0 ($\mathbf{J_{in}}$) and a current that points away from the wake for y <0 ($\mathbf{J_{out}}$). This is consistent with the idea that diamagnetic currents that circulate around Rhea maintain the magnetic field configuration in and around the wake. The dipolarized pattern of the residual field indicates that the electric current density is distributed in a circular configuration.

Switching to the xz-plane (Figure 6.2, plot D), the magnetic field enhancement seen correlates well to the spatial configuration of the plasma density depletion (Figure 6.2, plot C). This is a direct consequence of the fact that pressure balance has to be achieved everywhere.

Subtracting the background field, as before, perturbations in B_x and B_z can be seen clearly (Figure 6.7). The magnetic field lines are drawn into the wake by the plasma expanding into the cavity. The magnetic field perturbations are usually expected in B_y
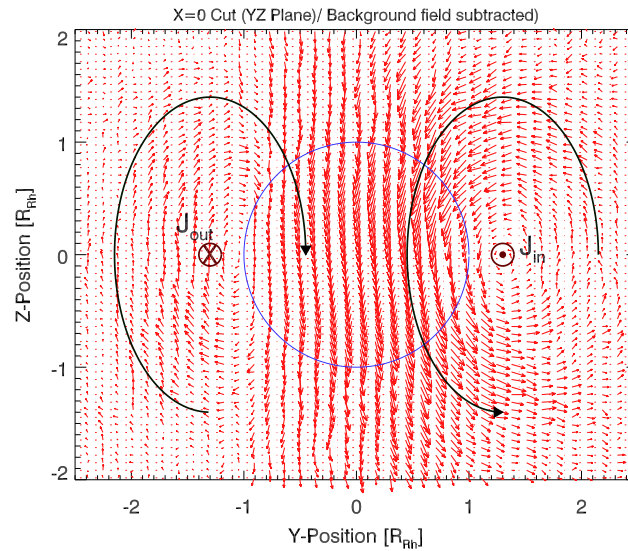
Figure 6.6: Magnetic field perturbations in a the yz-plane, just behind Rhea. The direction of the plasma flow (and the wake) points out of the page. Here the background field has been subtracted to enhance visibility of the compression and decompression regions of the magnetic field. The blue circle indicates the location of Rhea's geometrical shadow. The length of the arrows (arbitrary units) is indicative of the perturbation amplitude. The peak amplitude of the residual B_y in this simulation is about 1.5 nT. The closed magnetic field loops and the inferred current flow vectors are also sketched.

and B_z, but not in B_x (*Khurana et al.* 2007). However, in this case the perturbation of B_x is rather significant.

Three dimensional plasma expansion could explain the faster wake refilling observed, compared to what a one dimensional model predicts (Section 6.4.1). At Rhea, plasma betas are close to unity and the flow is relatively slow, even a weak acceleration of the plasma e.g. along the $-x$ direction can lead to notable changes in B_x. For the Earth's moon for instance, where the sonic Mach number is greater than 10, the peak disturbance in the B_x was only $\sim 2\%$ of its upstream value, as it was found by *Kallio* (2005).

The last magnetic field plot shows $|\mathbf{B}|$ projected on the equatorial plane (z=0 cut, Figure 6.2, plot H). As in the equatorial plane, B_x and B_y positive and negative perturbations cancel out, what is actually seen is the change in the B_z component. The $|B_z|$ reaches a peak value of about 28.5 nT, just behind Rhea, a value that drops further downstream. The rarefaction regions, and the asymmetry in the amplitude of the magnetic field dropout along the y-axis are also well illustrated in this plot.

A peculiar feature is the weak magnetic field pile-up upstream of Rhea (seen also in plot D, Figure 6.2). This magnetic field enhancement is created due to an induction process, which is in detail discussed by *Sonett and Colburn* (1968). It can be summarized as follows. Within the interior of a resistive body which is surrounded by a constant plasma flow, an electric field arises which is equal to the motional electrical field $\mathbf{E} = -\mathbf{u} \times \mathbf{B}$ (see plot F and J, Figure 6.2). As a consequence of the Ohmic law, currents flow inside Rhea's solid body whose density is $\mathbf{j} = -\sigma_{\text{Rhea}}\mathbf{u} \times \mathbf{B}$. The current path is closed at neighbouring plasma regions and a magnetic field is induced, which is toroidal with respect to
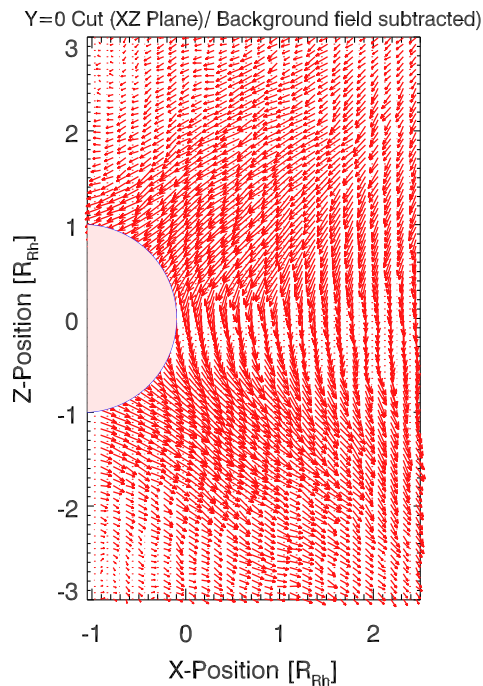
148

Figure 6.7: Magnetic field perturbations in a the xz-plane. The background field has been subtracted to enhance visibility of weak field disturbances. The peak amplitude of the residual B_x is about 2 nT. Also here, positive and negative B_x residuals cancel out on the equator, leaving only a disturbed B_z.

the motional electric field. At the dayside of Rhea this toroidal induction mode amplifies the external magnetic field as both fields are parallel and a pile-up in the total magnetic field results. To counteract this effect, higher resistivity values can be chosen to diminish the current and hence the induced toroidal magnetic field, but this translates into longer simulation runtime. As this weak field pile-up does not change the big picture derived from the simulation results, no higher resistivity was used.

6.4.3 Velocity and electric field

In the overview Figure 6.2, plasma velocity and electric field are only shown for the xz- and xy-planes (plots E,F, I and G). A plot of the velocity on a yz-projection is shown in Figure 6.8.

It is found that just behind Rhea the plasma expands towards the center of the cavity. The spatial extent of the acceleration region is not much greater than Rhea's cross section. Further downstream the region becomes broader along the z-axis. The non-zero v_z can be easily explained by motion of plasma along the field lines, but the observed non-zero v_y requires an electric field perturbation in the xy-plane. This perturbation should be associated to the presence of diamagnetic currents, inferred from the analysis in Section 6.4.2 (see also Figure 6.6).

The velocity plot in the xz-plane (Figure 6.2, plot E) shows clearly a symmetric north-south expansion of the plasma into the cavity. Northward and southward expanding
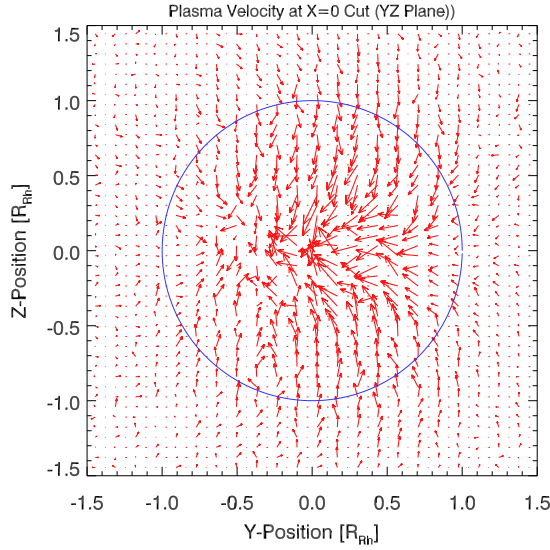
Figure 6.8: Perturbations of v_y and v_z in an yz-cut just behind Rhea. The expansion of the plasma velocity inside the cavity is clearly seen. The peak amplitude of the v_y or v_z components is about 30 km s^{-1}.

plasma streams should normally form counterstreaming populations and set up a two stream instability, that could enhance the refilling of the plasma void. This has been observed in the lunar wake, in both data and simulations (e.g. *Ogilvie* (1996), *Farrell et al.* (1997)).

Transforming the same data in the plasma rest frame (Figure 6.9), it is found that this expansion actually takes place along the disturbed field lines (compare this figure with Figure 6.7). The expanding plasma does not seem to enter the wake in the form of accelerated beams (as has been identified at Earth's Moon). Rather than that expansion takes place all over the flux tube connected to Rhea and Rhea's wake.

The plot for the E_x and E_z components is almost featureless but in plot F of Figure 6.2 a slight reduction of the electric field magnitude superimposed on the extended north-south plasma depletion region is barely seen. This probably results from the slight reduction of v_x (in the reference frame of Rhea) in this cutting plane, which introduces a perturbation in E_y.

As along the $y = 0$ cut electric field disturbances are insignificant and the wake refilling is driven by the expansion of the along the magnetic field lines, the one dimensional, analytical approach that was applied in Section 6.4.1 for the plasma density, can be also tested for the velocity. Here, the resulting solution for v_z is:

$$v_z = \frac{(z+1)\,u}{(x - x_{limb})} + C_s,$$
(6.10)

for $(z+1)/t > -C_s$.

This equation practically tells us that v_z should increase linearly into the wake, but as *Samir et al.* (1983) point out, the predicted extreme velocity values for regions of very low density are not physically valid.

Simulation results do show the linear increase of the v_z component into the wake,

150
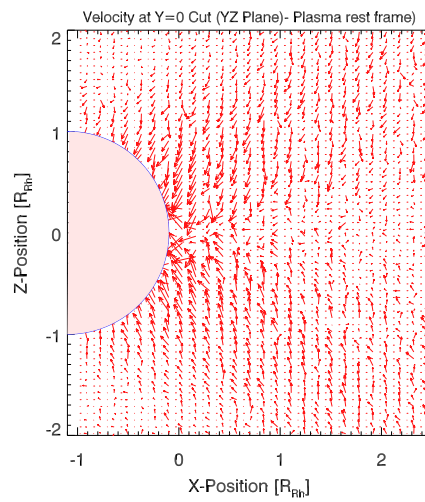
Figure 6.9: Perturbations of v_x and v_z in an yz-cut just behind Rhea, in the plasma rest frame. Plasma expands along the magnetic field lines, symmetrically with respect to the z=0 line.

Figure 6.10: Comparison of Equation 6.10 solution (blue line) with the simulated data, for a distance of 1.2 R_{Rh} downstream of Rhea's limb. Triangles show the variation of v_z from the simulation results, while diamonds show the velocity variation when the residual v_x is considered.

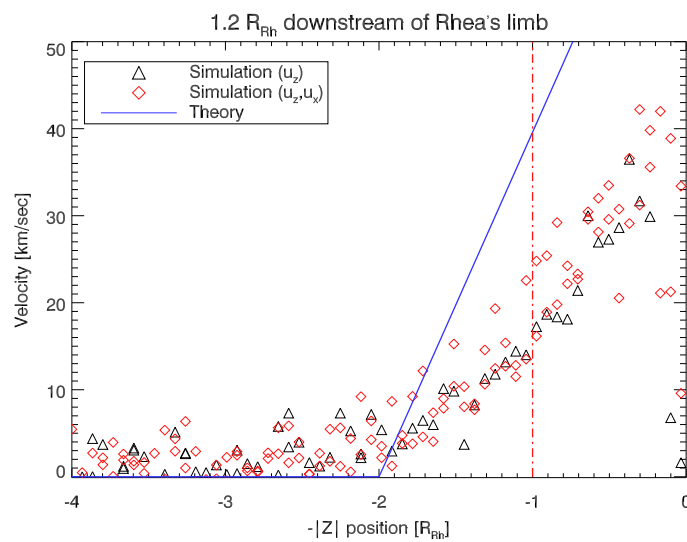however the slope of this increase is much different than the slope defined from the simulated points (Figure 6.10). Since the expansion occurs along the disturbed magnetic field lines, that have also a non-zero B_x component, $v' = \sqrt{v_x^{2'} + v_z^2}$ was also considered as the characteristic expansion velocity (diamond points / v_x' is the x-velocity in the plasma rest frame). However, this introduces only minor corrections. Again, what is well predicted is the location up to which acceleration into the void occurs, which shows undoubtly that disturbances propagate with the ion sound speed.

The differences observed between the one dimensional approach and the simulation outline once more the importance of electromagnetic fields in the plasma expansion and the complexities introduced by the three-dimensional approach. As mentioned earlier, electrostatic instabilities can also be important.

For instance, *Halekas et al.* (2006) found that if kappa functions are used to describe the distribution of electrons and ions, the analytical expressions for the density, the velocity and the potential drop deviate from the isothermal solutions of *Samir et al.* (1983). Several studies also discuss and emphasize the importance of the magnetic field (or the plasma betas) for the plasma expansion in a magnetized medium (*Huba et al.* 1992, *Gisler and Onsager* 1992, *Gisler and Lemons* 1992).

The most interesting structures in the velocity and the electric field are seen in the equatorial projections (Figure 6.2, plots I, J). The plots show that on the one side of Rhea's limb, an increase of the electric field magnitude (plot J) and rather weak perturbations on the other side. This increase is much stronger for $y > 0$. Further downstream the electric field increase is seen only for $y > 0$, while for $y < 0$ a dropout of $|\mathbf{E}|$ is found.

This hemispheric asymmetry is more clear in the velocity plot, where for $y > 0$ plasma is accelerated and for $y < 0$ the total velocity decreases. This probably explains the electric field enhancement for $y > 0$ and the dropout for $y < 0$. Several test runs were carried out with lower or even zero electron temperature to investigate whether this electric field enhancement is due to the electron pressure term in Equation 6.4, but the overall picture did not change. This suggests that the observed effect results from the $\mathbf{j} \times \mathbf{B}$ force on the ions. This better explains why this electric field enhancement is seen only in the equatorial plane. A similar asymmetry has been reported in the three-dimensional lunar wake simulations by *Kallio* (2005).

Replotting these parameters in the plasma rest frame (Figure 6.11), it is found that close to Rhea the $\mathbf{j} \times \mathbf{B}$ forces drive the plasma directly towards the cavity center. Further downstream, the asymmetric velocity structures seen in the rest frame of Rhea appear as a plasma circulation pattern in the plasma rest frame, where two sectors of oppositely moving plasma are visible (Figure 6.11, top panel). These structures are consistent with the diamagnetic current pattern inferred from Figure 6.6. The associated electric field disturbances are not easily seen in this representation, except for regions close to Rhea (bottom panel).

There is an interesting analogy in the simulation results with experimental and simulation results presented by *Hurtig et al.* (2003), where they studied structures developing after injecting plasma beams in a curved magnetic field. The authors report the formation of a similar diamagnetic current system (e.g see Figure 6 from that paper), as well as asymmetric current structures in the "transition region" of their experiment (region where the field becomes curved). These results are partly attributed to the induced electric field that arises when the injected plasma (in Rhea's case plasma refilling the wake)
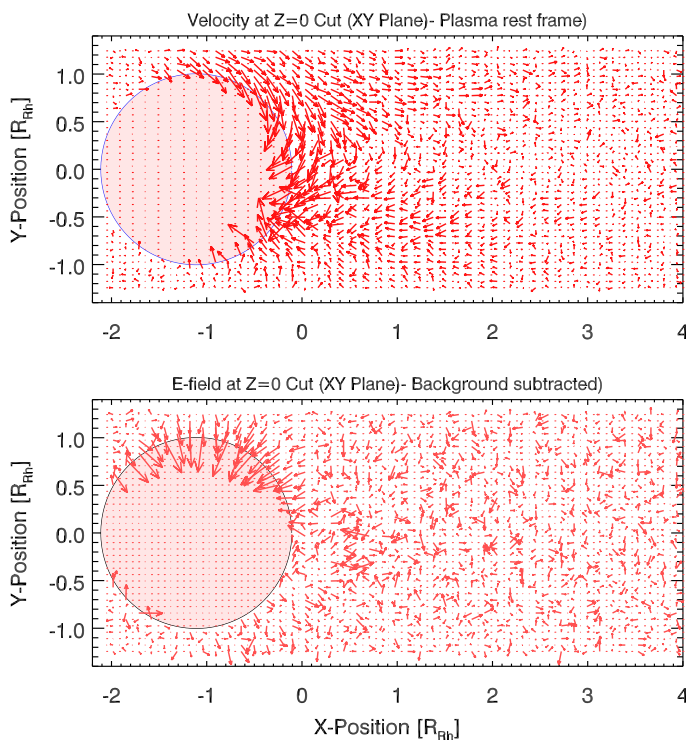
Figure 6.11: Velocity and electric field in the plasma rest frame, projected on the equatorial plane (top and bottom panel respectively).

experiences a time-changing magnetic field in the "transition region" (in Rhea's case the magnetic field change in the wake). The authors also highlight the importance of the $\mathbf{j} \times \mathbf{B}$ forces in this interaction, which probably explains the effects seen in the equatorial plane of the simulation box.

Finally, it is also interesting to note in Figure 6.2 (plots F,G) that the electric field magnitude in the interior of Rhea is self-consistently calculated approximately equal to the external electric field, as expected (*Sonett and Colburn* 1968). While predefining the electric field vector in the moon's interior is a reasonable approximation (e.g. *Kallio* (2005)), equaling it with the upstream corotational electric field might not be completely accurate, given the structures in the electric field that arise in the region of the obstacle.

6.4.4   Comparison with the magnetic field data

The Cassini spacecraft made its first close flyby of Rhea to date on November 2005, where a magnetic field signature, typical for a plasma absorbing body, was observed by the spacecraft's magnetometer (*Dougherty et al.* 2004a). Cassini's flyby trajectory was almost perpendicular to the plasma wake of Rhea (parallel to the y-axis and about 0.65 R_{Rh} downstream of Rhea) and slightly south of Rhea's equatorial plane ($z \sim -0.3 R_{Rh}$). A more detailed description of the flyby and the observations can be found in *Khurana et al.* (2007).

Before the encounter the magnetometer measured small values in B_x and B_y, and therefore for a more direct comparison with the results, a simulation was set up with non-
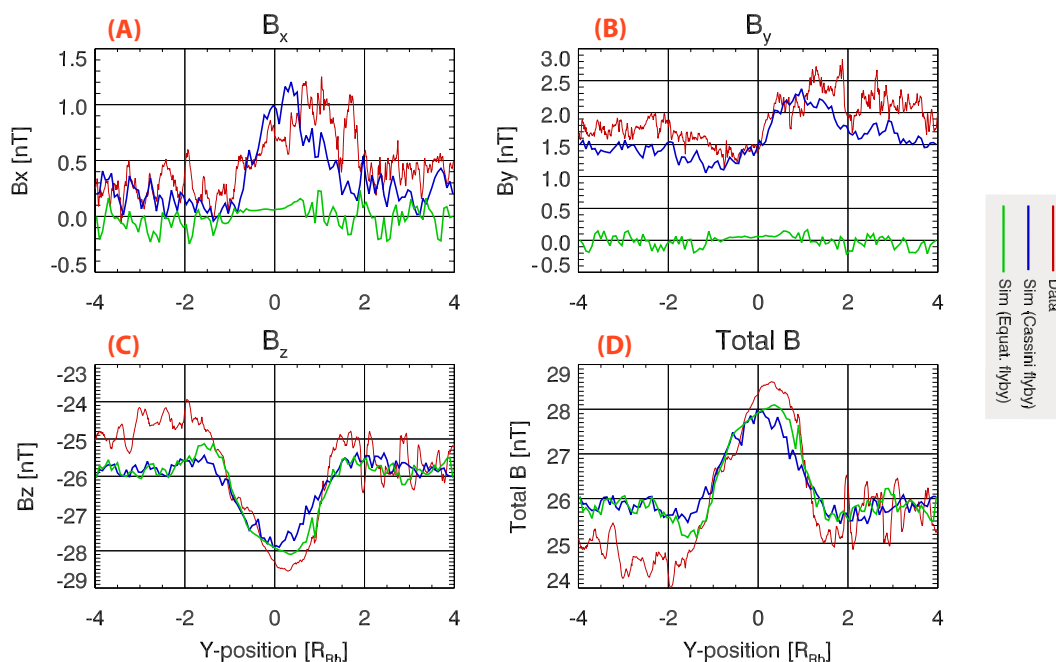
Figure 6.12: Comparison of the simulation results with the magnetometer data from the Cassini flyby. In green color I also show the magnetic field signature on an equatorial trajectory in the wake along the y-axis, from the "ideal case" run.

zero B_x and B_y components, as it is also described in Section 6.3.3. The overall results from that simulation do not differ from those presented for the "ideal case" scenario, since B_x and B_y are still much smaller than B_z.

The comparison is shown in Figure 6.12. As it can be seen there is a very good agreement in all three components of the magnetic field. Both the amplitude of the per-turbations as well as the spatial extent of the perturbed regions are reproduced, which means that the main features of the interaction can be described by the simulation code. The agreement in the asymmetric amplitude of the B_y perturbation for $y > 0$ and $y < 0$ is especially interesting (panel B), meaning that asymmetries along the y-direction seen in the simulation can be realistic.

Although the exact agreement of the data and the simulation is beyond the scope of the study in this chapter, it is interesting to discuss the origin of several differences seen, such as in the exact increase of $|\mathbf{B}|$ in the wake (panel D). The measured peak increase in $|\mathbf{B}|$ is about ~30% higher to what is found see in the simulation results. There are two main sources of this discrepancy.

Probably the most important one is the choice of the plasma betas, which at Rhea can vary significantly. The plasma betas practically define how much plasma pressure is lost on Rhea's surface. For example, during several test runs with the plasma temperature set to 200 eV, the peak in $|\mathbf{B}|$ was above 29 nT in the wake, which is in much better agreement with the observations. The same can be achieved by varying the plasma density.

A less important source of the discrepancy is the choice of a finite conductivity for Rhea's interior. This leads to a small magnetic field pile-up upstream of Rhea which opposes to the energy loss due to plasma absorption. Therefore the required compression

of |**B**| in the wake will not be as strong as when this pile-up is not present.

Another difference seen is that the measured |**B**| and |B_z| (panels C, D) tend to increase from $y = -4\ R_{Rh}$ to $y = 4\ R_{Rh}$. This is simply because Cassini moves close to Saturn where the dipole field strengthens.

Data shows that within the range of the simulation box, the measured |**B**| increases about 1-1.5 nT (or about 4% of the background value). It is not clear whether this variation induces any additional effect in the interaction. An additional relevant effect is that of the gradient drift, which in the Saturnian magnetosphere accelerates ions and decelerates electrons. Furthermore, the corotation velocity also varies slightly along the y-axis. All these could maybe enhance the observed asymmetries along the y-direction, but any such enhancement will probably be insignificant, given that the simulated area is rather small.

In Figure 6.12 I also plot the simulated magnetic field components from a trajectory through the wake, but along Rhea's equatorial plane (z =0) (green line). The data are retrieved from the "ideal case " run, where B_x and B_y are initially zero. What is highlighted in this case that with such a trajectory no variation in B_x and B_y is seen and the only indication about the nature of the interaction is in B_z. While in most cases the increase in B_z is sufficient to reveal that plasma absorption dominates, B_z can also be enhanced within the current system region of an ionosphere. Therefore for very low altitude, equatorial flybys, the signature of B_z alone could be misleading. For non-equatorial, downstream flybys, the shape of the B_y variation can reveal the type of the interaction (*Khurana et al.* 2007). On the other hand, it is interesting to note that in the simulation run where B_x and B_y were non-zero, it was not possible to find a realistic flyby trajectory where B_x and B_y where undisturbed, as in the case of the "ideal-case" run.

6.4.5   Kinetic effects and phase-space diagrams

In this chapter I did not present simulations where a weak exosphere is modelled around Rhea, and therefore kinetic effects cannot be easily realized in the results. On the other hand, these results show that the code can give a valid description of the wake of an absorbing body, and its use can be extended to more complex scenarios.

For illustration purposes only, Figure 6.13 shows the escape of heavy ions from a test run where a weak exosphere was included. No differences were found in the resulting wake structure or the configuration of the electromagnetic fields, compared to what was presented in the previous sections. The magnetospheric plasma did not "notice" the presence of the low density exospheric ions. The corotational electric field penetrated down to the surface, accelerating the ions in spiral escape trajectories. The characteristics of these trajectories (spiral width and height) are in agreement with the analytical description given by *Simon et al.* (2007a). The initial acceleration of the exospheric ions along the electric field direction is also seen.

Apart from the exospheric ion escape, particle phase-space plots were constructed with detailed information about the particle distributions in each region. Several examples from the "ideal case" simulation run are shown here, where a particle phase-space plot was converted to an ion spectrogram, equivalent to the one that Cassini's CAPS/IMS instrument should have observed along the Rhea flyby trajectory.

What stands out from this spectrogram is the peculiar shape of the ion wake. Given that the mean energy at each position defines the particle velocity, the shape of the ion
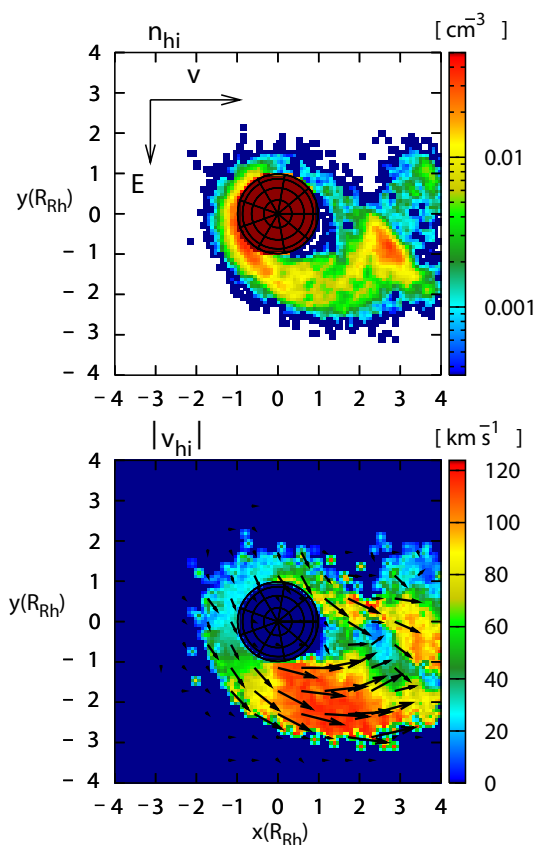
Figure 6.13: Illustration of the density (top) and velocity (bottom) of escaping heavy ions from a weak exosphere of Rhea. The plots shown are cuts through the equatorial plane of Rhea (xy-plane). The direction of the upstream plasma velocity and corotational electric field are shown on the top panel. Note that for this test run, Rhea was at the center of the simulation box. Here the heavy ion mass was chosen to be 17 amu and the exospheric scale height was set to 100 km.

wake is due to the fact that for positive and negative y, the ions are accelerated and decelerated, respectively. Similar wake structures in ion spectrograms have been observed at the moon *Ogilvie* (1996), and have been reproduced at various lunar-wake simulations (*Kallio* 2005, *Birch and Chapman* 2001, *Travnicek et al.* 2005).

The width of the ion distribution represents the ion temperature at each point. In the near wake region, distributions become narrower, suggesting a drop in ion temperature. In the central wake, the distribution is broad, consistent with an increase in temperature. At larger distances downstream, the distribution retains again its Maxwellian form and ion temperature drops. It is noted that the treatment by *Samir et al.* (1983) (Equations 6.7, 6.10) is based on an isothermal plasma expansion in the cavity.

Several additional interesting features can be found through the phase space diagrams: the top panel of Figure 6.15 shows velocity phase-space plots of v_z along a hypothetical trajectory that is parallel to the x-axis and crosses Rhea through its center. We can clearly detect that downstream, two distinct populations exist, with non-zero v_z, while populations with $v_z \sim 0$ are filtered by Rhea.
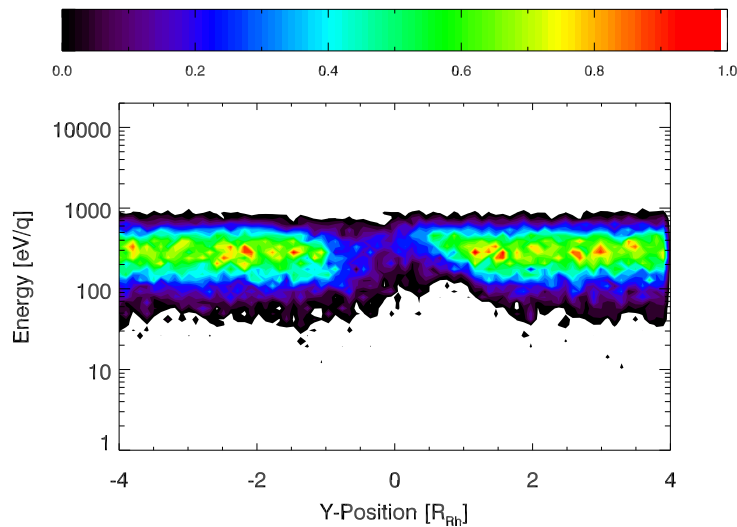
Figure 6.14: Synthetic ion spectrogram along the Rhea flyby trajectory. The color represents the ion flux, normalized towards the maximum.

Initially, one maxwellian with v_z =0 could describe the distribution, but downstream, two maxwellians are required with v_z = ±30 km s^{-1}. As Rhea orbits in a dipolar region, these accelerated ions will become trapped populations mirroring at low magnetic latitudes and will continue drifting around Saturn, which means that plasma absorbing moons tend to make angular (or pitch angle) distributions in the magnetosphere more field-aligned. The presence of such populations is further enhanced by the electron and ion interaction with Saturn's E-ring dust and the associated neutral gas cloud.

An ion spectrometer with a 4π angular coverage should therefore detect two ion populations along the magnetic field lines, during an equatorial wake crossing. Similar observations in the lunar wake have been reported by *Ogilvie* (1996).

What is also interesting is that particles with high v_z are the ones that first appear downstream of Rhea. This is consistent with the geometrical concept for explaining the phase-space distribution in the wake, introduced by (*Khurana et al.* 2007), as an alternative to the analytical treatment of the problem by *Samir et al.* (1983). A simple illustration of this approach is shown in the bottom panel of Figure 6.15. Particles with high v_z that just avoid impacting on Rhea appear first in the wake due to the large angle of their trajectory with respect to the x-axis.

6.5   Summary and outlook

In the present chapter the magnetospheric interaction of Saturn's moon Rhea using a three dimensional, hybrid plasma simulation code has been studied. The space environment of Rhea (low bulk velocity, high thermal velocity) is ideal to emphasize the relative importance of plasma parameters and to understand basic physical process that occur when plasma expands into a vacuum. The main results of this case study are summarized below:
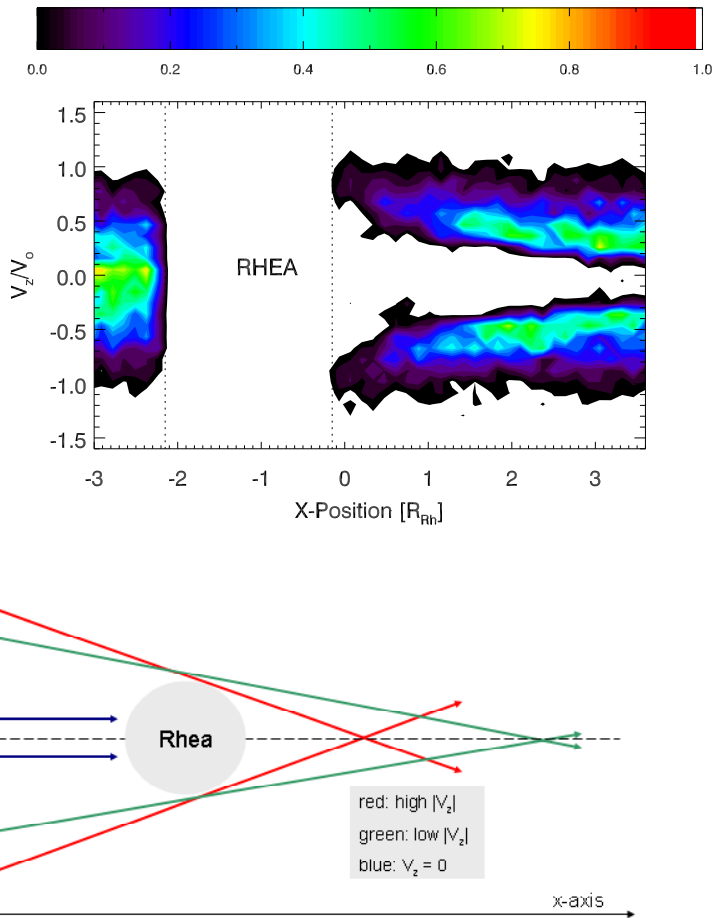
Figure 6.15: (Top) Phase-space plot of V_z along a hypothetical trajectory which is parallel to the x-axis and crosses Rhea through its center. The white region in the plot denotes the space occupied by Rhea's volume. (Bottom) Sketch that explains the phase-space plot in the top panel. The dashed line shows the hypothetical trajectory along which the diagram of the top panel has been drawn.

- The plasma wake of Rhea probably does not extend much more than 10 R_{Rh} down-stream of the moon. The extension of the wake depends on the ion sonic Mach number. The length of this extension can be approximated by requiring that the density gradient along the x-axis (calculated from Equation 6.7) is close to zero, given the good agreement of this analytic description by *Samir et al.* (1983) with the simulation results.

- Disturbances in Rhea's wake propagate with the ion sound speed, C_s, as described by *Samir et al.* (1983).

- Due to the high thermal velocity with respect to the plasma bulk velocity, the depletion region behind Rhea extends along the magnetic field. The magnetic field magnitude increases in all this region to maintain the total pressure. The extension of the depletion region and the response by the magnetic field has been seen during

the flyby of Saturn's moon Tethys by Cassini, below that moon's equatorial plane (*Khurana et al.* 2007). In the equatorial plane the density wake is restricted by the magnetic field within Rhea's geometrical shadow.

- Although several studies consider that B_x in the wake should remain undisturbed, the magnetic field downstream of Rhea varies in all three components. This is also verified by the comparison with the Cassini magnetometer data. The B_x perturbation in the wake probably reflects the difference between supersonic and subsonic lunar-type interactions.

- Positive and negative perturbations in B_x and B_y cancel out on Rhea's equatorial plane ($z=0$), leaving only a perturbation in B_z.

- A decompression (rarefaction) of the magnetic field occurs on the side of Rhea's geometrical wake. The amplitude of the magnetic field dropout is asymmetric with respect to the direction of the electric field. This asymmetry is also seen in the magnetometer data (e.g. the B_y component, Figure 6.12, plot B).

- On the xz-plane the wake refilling occurs by plasma expansion along the field lines, while on the equatorial plane plasma is accelerated into the vacuum under the action of $\mathbf{j} \times \mathbf{B}$ forces.

- A diamagnetic current system is developed in the equatorial regions in the wake. The presence of this current system is revealed by the plasma residual velocity distribution on the equatorial plane (Figure 6.11) and by the residual magnetic field projected on the yz-plane (Figure 6.6).

- The asymmetric structures seen in the equatorial plane probably result from the action of the $\mathbf{j} \times \mathbf{B}$ forces on the ions.

- The interaction of a mass absorbing moon within a planetary magnetosphere tends to enhance the field aligned component of the particle angular (or pitch angle) distributions.

- The assumption of a finite resistivity for the interior of Rhea can adequately and self-consistently describe the behaviour of the electromagnetic fields in this region.

Besides these results, there are still many more issues that could be interesting to investigate in future studies. For instance, the structure of Rhea's wake under the different plasma environments, or any effects that result from the presence of a weak exosphere when the fast Magnetosonic Mach number is greater than one, would be worth investigating. It would also be interesting to model how the system responds if there is a change in the upstream plasma configuration (e.g. during a plasma injection (*Hill et al.* 2005)).

The latter scenario is theoretically very interesting: during an injection the flux of energetic ions ($> 50keV$) increases significantly, and these ions carry more than 70% of the total plasma pressure (*Sergis et al.* 2007). In the same most of these ions can escape absorption from Rhea due to their large gyroradii ($>> 1 \ R_{Rh}$), their large bulk velocities and long bounce periods. In this case, the pressure drop in the wake will be small and

therefore the low energy plasma wake could be sustained for large distances downstream, even greater than the 10 R_{Rh} predicted through the present simulations.

Through a fully kinetic approach, such as the one by *Birch and Chapman* (2001), high frequency or small scale phenomena (down to the Debye length, ~20-30 m for Rhea) could also be studied. In particular, effects resulting from the fast expansion of electrons into the wake and the deviation from charge neutrality could play a significant role in the plasma dynamics downstream of Rhea. Such effects cannot be described in a hybrid code, due to the unavoidable assumption of charge neutrality. For a non-neutral plasma distribution in Rhea's wake, an additional term in the current will be added. In total, the current in this region will be given approximately by the expression:

$$j_{tot} = q \ [(n_e - n_i) \ \mathbf{u_e} - n_i \ (\mathbf{u_e} - \mathbf{u_i})] \qquad (6.11)$$

In a hybrid code, the first term on the right hand side is zero, as $n_e = n_i$ and cannot be described. If the second term, which can be calculated from the simulation code, is more important then the assumption of charge neutrality will not affect significantly the overall results.

On the other hand, if this term is greater than the second term, then close to Rhea ion acceleration into the cavity from all sides will dominate and will form additional structures in the ion and electron velocity fields compared to what the simulation code used here predicts. These additional structures will also be related to an ambipolar electric field resulting from a non-zero $(n_e - n_i)$ term. *Kallio* (2005) described this field analytically in his lunar-wake hybrid simulations and realized only small differences in the results compared to the case where this electric field was neglected. Still, *Birch and Chapman* (2001) have shown that a self-consistent calculation of the charge separation effects results in much more complex structures in the wake that the analytical description of *Kallio* (2005) probably cannot reproduce.

Finally, increasing the resolution to the scales of the Debye length would also be interesting for the investigation of surface currents and charging processes (*Farrell et al.* 2007). Surface charging at Rhea could reach extreme values as Rhea orbits in the ring current region of Saturn and it is therefore continuously exposed to energetic particles (see for instance *Halekas et al.* (2006)). What makes such a region unique for investigation is also the fact that Rhea's dayside (where surface photoemission currents are generated) does not coincide with the hemisphere where Saturn's plasma is impinging, unless Rhea is situated on the dusk sector of the magnetosphere. For example, during the flyby of Rhea by Cassini, Rhea was at a local time of ~12:00 and therefore photoemission currents were also created in the plasma wake, a case impossible for the Earth's moon.

7 Concluding remarks

Using data from two different particle instruments at two different environments in the solar system and a hybrid simulation code, a series of results where obtained on the interaction of weakly magnetized or unmagnetized bodies (WUBs) with their surrounding space environment. The work performed for this thesis has highlighted many of the interesting and important aspects of studying WUBs and many novel results have been obtained, important for different scientific groups and topics. Among the primary results of the thesis work, are the ones listed below for each of the different solar system object research topics:

- Plasma moment maps where constructed for the first time for the Martian plasma environment. Such maps could be the first step for constructing a reference model for the interaction of Mars with the solar wind. Such a reference model could be used for a series of important applications, such as for the calculation of charge-exchange rates or impact ionization profiles, and their dependence on solar wind and UV radiation properties.

- Using a 3-year dataset of ASPERA-3 electron data it was possible to identify the presence of energetic electron events in the martian magnetotail and establish that their origin requires combined configurations of the planet's crustal fields with the pointing of the solar wind's convective electric field to occur. This is the first time that a global magnetospheric feature is found to be associated with the combination of two different processes, and one of the first indications that the martian crustal fields can be a source of global asymmetries in the magnetosphere.

- By studying the evolution, the topology and the structure of satellite absorption signatures in the Saturnian radiation belts it was for the first time possible to derive and study the L-shell and energy dependence of radial diffusion coefficients in the planet's plasmasphere, to provide evidence of non-circular but disturbed energetic electron drift shells and the presence of a possible high energy ion source in the innermost magnetosphere. Most results indicate a dynamic and variable magnetosphere, with radiation belts being supplied with energetic electrons primarily through particle injections. These results can find interesting applications in the future: the profiles of satellite absorption signatures could be used to extract fundamental properties about injections and their frequency, while the disturbed electron trajectories could "hide" important information in their properties, such as the magnetopause distance.

- Two new rings (or partial rings) have been discovered along the orbits of two

asteroid-sized moons of Saturn: Methone and Anthe, suggesting that at Saturn similar processes are ongoing as at Jupiter, where dust from the small moons is forming the gossamer and halo rings of the planet. Furthermore, it found that these rings comprise large particle populations or a series of dust clumps. The physical characterization of a ring arc in Saturn's G-ring made possible to solve the mystery of its origin and its sustainment.

- For the first time the physics of submagnetosonic plasma absorption has been studied with a three dimensional, hybrid plasma simulation code, with Saturn's moon Rhea selected for the case study. Many interesting analogies with supersonic, lunar-type interactions have been found. The outcome of the simulation clearly illustrates the differences between a supermagnetosonic and a submagnetosonic interaction and reproduces well the magnetic field data collected from Cassini during a close flyby to this moon. These simulations can be further advanced by adding more components in the interactions, such as a component for the charged E-ring dust, a profile of a sputtering produced exosphere and function to describe the moon's surface charging.

One of the biggest challenges during this thesis was the attempt to adjust the methods and results to the continuously increasing datasets that were retrieved from Mars Express and Cassini, to respond fast to surprising or unexpected observations and to be in compliance, as much as this was possible, to newly published results by other research groups. Cassini and Mars Express still continue to operate successfully (and hopefully will continue to do for many more years), while a lot of data has been retrieved the last few months during which this thesis was being written. It is very likely that some of these new observations could help to answer some of the open questions derived from this thesis results, or even modify to some extend some other findings. In any case, I believe that many of the results presented here contribute to the progress in each respective research field, and even more importantly, highlight the significance of studying the interactions of weakly magnetized or unmagnetized bodies, not just for plasma physics, but for a much broader range of scientific applications.

A   Motion of trapped particles in Saturn's magnetosphere

Here, a series of constants and formulas that are used to calculate parameters of energetic electron and ion motion in the Saturnian magnetosphere, is provided. The formulas have been applied in the data analysis methods presented in Chapters 4 and 5. This short chapter is basically a reproduction of *Thomsen and Van Allen* (1980), with small modifications and additions where it was termed necessary.

The motion of trapped particles has three main elements: the gyration around a magnetic field line, the latitudinal bounce along a field line, and a longitudinal drift perpendicular to a field line that results from the corotational electric field, a gradient in the magnetic field and a curvature of the magnetic field lines.

Each of the motion elements has a dependence from the particle's kinetic energy, E, the magnetic L-shell parameter (equatorial distance of a field line), L, the equatorial pitch angle, a_{eq}, the particle's charge and mass, q and m, and the dipole moment of Saturn, M. Unless otherwise stated, formulas and constants are provided in CGS units. Energies are expressed in MeV and angular velocities in $\mathrm{rad\,s^{-1}}$. All formulas are extracted assuming motion in a pure dipole magnetic field.

A.1   Symbols and constants

Below, a list of symbols and constants that are used in the formulas that will follow, are provided:

c: speed of light $c = 2.997925 \times 10^{10} \mathrm{cm\,s^{-1}}$;

mc^2: rest energy of a particle (0.511 MeV for electrons and $Z \times$ 938.3 MeV for ions with atomic number Z);

E: kinetic energy of a particle. For trapped particles considered in this study, this energy is attributed to the gyration energy rather than the bulk velocity of the particle;

u: speed (bulk velocity) of the particle;

β: $\beta = u/c$;

γ: $\gamma = \left(1 - \beta^2\right)^{1/2}$;

q: charge of particle (4.80325×10^{-10} esu per unit charge);

R_s: equatorial radius of Saturn; $1\,R_s=6.0268 \times 10^9$ cm. Note that *Thomsen and Van Allen* (1980) use $R_s=6.0 \times 10^9$ cm;

B_o: equatorial surface magnetic field for Saturn ($B_o = 0.21$ Gauss). Note that *Thomsen and Van Allen* (1980) use $B_o = 0.20$ Gauss;

r: radial distance from the center of the planet;

a_{eq}, a_l: equatorial and local pitch angle of a particle, respectively. The equatorial pitch angle is defined as the angle between the magnetic field and the particle's velocity vector at the magnetic equator. Similarly, the local pitch angle is defined at the local point of measurement;

L: equatorial distance of a magnetic field line (or dipole L-shell) in units of R_s; For a pure dipole field $r = L\cos^2\lambda$ where λ is the magnetic latitude;

λ: the magnetic latitude;

λ_m: magnetic latitude of a particles mirror point;

$B(\lambda), B(\lambda_m)$: magnetic field strength at λ, λ_m;

GM_s: Saturn's gravitational constant ($GM_s = 3.79311 \times 10^{22}$ cm^3 s^{-2});

J_2: second zonal harmonic of Saturn's gravitational potential (1667×10^{-5});

a: the semimajor axis of a moon's orbit;

A.2   Useful expressions

The following expressions are extracted from *Roederer* (1970). In a pure dipole field, the relation between the local and the equatorial pitch angle is given by the following expression:

$$sin^2 a_l = sin^2 a_{eq} \frac{(4 - 3cos^2\lambda)^{1/2}}{cos^6\lambda} \tag{A.1}$$

In a similar way, the expression for the relation between the magnetic field strength at the equator and at a magnetic latitude λ (for the same field line), is given by Equation A.2:

$$B(\lambda) = B_{eq} \frac{(1 + 3sin^2\lambda)^{1/2}}{cos^6\lambda} \tag{A.2}$$

The determination of the mirror points ($\pm\lambda_m$) can be found by solving numerically the equation:

$$\frac{cos^6\lambda_m}{(4 - 3cos^2\lambda_m)^{1/2}} = sin^2 a_{eq} \tag{A.3}$$

A.3   Longitudinal drifts

Longitudinal drifts in dipole fields have been studied by *Hamlin et al.* (1961) and *Lew* (1961). The bounce averaged angular velocity of the guiding center of a particle is given by:

$$\omega_{gc} = \frac{3mc^3\beta^2\gamma L}{2qB_oR_s^2}\frac{F(\lambda_m)}{G(\lambda_m)} = \pm 1.965 \times 10^{-5}LE\left(\frac{E+2mc^2}{E+mc^2}\right)\left(\frac{F}{G}\right) \tag{A.4}$$

By adopting a convention that the longitudinal velocity is positive for eastward drifts and negative for westward drifts (in a reference frame corotating with the planet), the positive sign is for positively charged ions, while the negative sign is for electrons. The parameter (F/G) is an integral that is carried out over a latitudinal bounce period and can be approximated by:

$$(F/G)^{-1} = \left(1.04675 + 0.45333\sin^2\lambda_m - 0.04675\,e^{-6.34568\sin^2\lambda_m}\right) \tag{A.5}$$

The total angular velocity, ω, of the particle in an inertial frame is given by adding the eastward drift, Ω, due to the corotating electric field, $E = \frac{1}{c}(\Omega \times r) \times B$. Therefore:

$$\omega = f_c\Omega + \omega_{gc} \tag{A.6}$$

For Ω we adopt the Voyager derived value of $1.637\ 10^{-4}$rad s^{-1}. Our calculations are not sensitive to the uncertainty or possible variability of this value. The dimensionless parameter $f_c(L) \equiv f_c$ corresponds to the corotation fraction at the approximate L-shell of each moon (usually between 0.7 and 1.0).

A.4   Keplerian motion and relative motion to charged particles

The inclusion of formulas for the Keplerian motion in the calculations is important in order to determine the relative plasma velocity as a function of L, a_{eq} and E with respect to the motion of the icy moons and rings.

The mean angular velocity of a neutral body in gravitational orbit around Saturn is:

$$\omega_k = \left(\frac{GM_s}{a^3}\right)^{1/2}\left(1 - \frac{3J_2R^2}{2a^2}\right)^{-1/2} \tag{A.7}$$

Using the given constants and with a in units of R_s, Equation A.7 becomes:

$$\omega_k = \frac{4.1626 \times 10^{-4}}{a^{3/2}}\left(1 + \frac{1.25 \times 10^{-2}}{a^2}\right) \tag{A.8}$$

Most of the icy moons and ring structures at Saturn move on the same longitudinal drift paths with the charged particles, due to the alignment of the magnetic moment and rotational axis at Saturn. Therefore, the relative angular velocity between charged particles and gravitationally bounded neutral bodies is given by

$$\omega_{rk} = (f_c\Omega + \omega_{gc}) - \omega_k \tag{A.9}$$

165

The angular velocity with respect to corotation is found by setting $\omega_k = 0$.

The interval between two consecutive encounters of a charged particle and a satellite is

$$T_{rk} = 2\pi/(|(\Omega + \omega_{gc}) - \omega_k|) \tag{A.10}$$

For a zero energy charged particle that moves only due to the corotating electric field's action ($\omega_{gc} = 0$), a synchronous orbit ($\Omega = \omega_k$) is achieved at $a = 1.867R_s$. This distance is on top of Saturn's main ring system. For $a < 1.867R_s$, $\Omega < \omega_k$ while for $a > 1.867R_s$, $\Omega > \omega_k$, assuming rigid corotation ($f_c = 1$). This means that for the distances in the Saturnian magnetosphere considered in this study (2.5-9 R_s), the cold plasma always moves faster than the icy moons and ring particulates. This is valid even for subcorotation as low as $\sim 70\%$ of the rigid.

For energetic plasma ($E \gtrsim 5\,keV$) where gradient and curvature drifts start to become important, relative velocities with respect to gravitationally bound objects is strongly dependent from E and a_{eq}.

Positively charged energetic ions always have ω_{gc} in the direction of Ω and therefore move faster than the cold plasma corotation speed. Therefore for ions outside 1.867 R_s, $\omega_{rk} > \Omega - \omega_k$ always.

On the other hand, electrons have ω_{gc} opposite to the direction of Ω. Then, ω_{rk} can be positive (eastward drift with respect to the Keplerian motion and $\omega_{rk} < \Omega - \omega_k$), zero (Keplerian resonant motion), or negative (westward drift with respect to the Keplerian motion).

The value of the Keplerian resonant energy, E_{rk}, can be found by setting $\omega_{rk}=0$ in Equation A.9. This gives:

$$E_{rk} = 0.5\left[E' - 1.022 + (E'^2 + 1.0444)^{1/2}\right], \tag{A.11}$$

where the parameter E' is expressed by:

$$E' = 5.089 \times 10^4 (f_c\Omega - \omega_k)/(LF/G) \tag{A.12}$$

The resonant energy with respect to corotation, E_{rs}, can be found by Equations A.11 and A.12 if ω_k is set to zero. Resonant ions can only occur within the zero energy corotation distance of 1.867 R_s.

A.5   Bounce motion

The most important parameters to describe the latitudinal bounce motion are the bounce period, T_b, and the latitude of the mirror points, λ_m. The latter can be estimated by solving Equation A.3. The bounce period is estimated by solving the integral

$$T_b = \oint \frac{ds}{u_\parallel}, \tag{A.13}$$

which is carried out over the magnetic field line arc length s, for a round trip between the mirror points. For a dipole field this integral can be reduced to

$$T_b = 0.80413\frac{L}{\beta}H(a_{eq}) = 0.80413\frac{L(E + mc^2)}{[E(E + 2mc^2)]^{1/2}}H(a_{eq}) \tag{A.14}$$

The parameter $H(a_{eq})$ is an integral that has been found by *Lenchek et al.* (1961) to be approximately

$$H(a_{eq}) = 1.38 - 0.32(sina_{eq} + sin^{1/2}a_{eq}) \tag{A.15}$$

A.6   Gyration motion

In the equatorial plane, where $B = B_o L^{-3}$, the relativistically corrected angular gyrofrequency of a charged particle is given by

$$\omega_g = \frac{qBc}{E + mc^2} = \frac{1.888 \times 10^6}{L^3(E + mc^2)}, \tag{A.16}$$

while the equatorial gyroperiod equals to $2\pi/\omega_g$. Finally, the equatorial gyroradius (radius of the cylindrical surface on which the particle's helical radius lies) can be calculated by

$$r_g = \frac{\beta c\, sina_{eq}}{\omega_g} = 1.588 \times 10^4\, sina_{eq}\, L^3[E(E + 2mc^2)]^{1/2} \tag{A.17}$$

Using these formulas, plots with values for the bounce-averaged drift velocity, the gyroradius and the bounce period for electrons and ions of various energies are shown in Figure A.1 as a function of L-shell.

A.7   Applicability of formulas

The given formulas are applicable for a pure dipole field, and therefore deviations are expected to increase with increasing L. *Birmingham* (1982) found that for $L \gtrsim 7$ deviations start to become notable and that they peak between 8.5 and 15 R_s. Therefore formulas are sufficient to study the interaction with moons and rings, most of which lie between 2.5 and 6.3 R_s. At Rhea's distance (8.75 R_s) these formulas should be carefully treated.
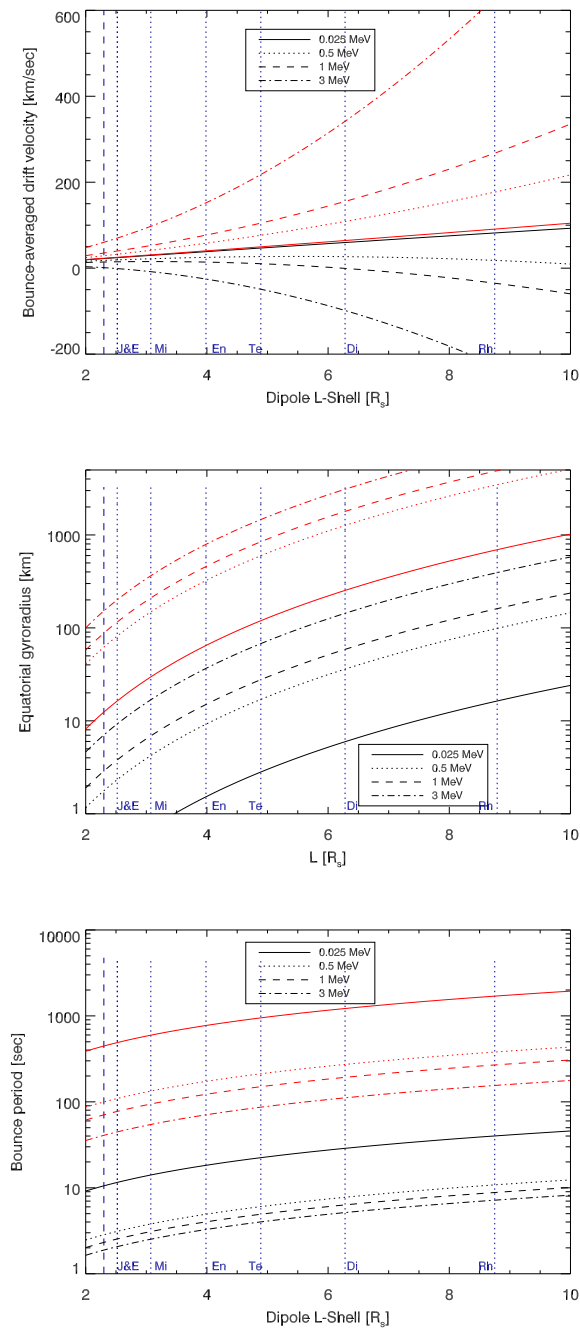
Figure A.1: (Top): Bounce averaged drift velocity at Saturn as a function of energy (see legend) and L-shell. Black curves denote are for electrons and red curves for ions. All values are for equatorial particles (90° pitch angle) and assuming rigid corotation, in an inertial, Saturn-centered coordinate system. (Bottom left): Same plot for the gyroradius of equatorial electrons and ions. (Bottom right) Bounce period of electrons and ions with a pitch angle of 45°. In all panels, the location of the various icy moon L-shells are indicated with blue, dotted lines. The blue dashed line indicates the L-shell of the main rings outer edge.

Bibliography

Acuña, M. H., et al., 1998. Magnetic field and plasma observations at Mars: initial results of the Mars Global Surveyor mission, *Science*, 279, 1676 - 1680, doi:10.1126/science.279.5357.1676

Anderson, J.D., Schubert, G., 2007. Saturn's satellite Rhea is a homogeneous mix of rock and ice, *Geophys. Res. Lett.*, 34, L02202, doi: 10.129/2006GL028100.

Bagdonat, T., Motschmann, U., 2002. From a Weak to a Strong Comet - 3d Global Hybrid Simulation Studies, *Earth, Moon, and Planets*, 90, 305-321.

Bale, S.D., 1981. Shadowed particle distributions near the Moon, *J. Geophys. Res*, 102, 19773-19778

Barabash, S. et al., 2007a. The analyzer of space plasmas and energetic atoms (ASPERA-3) for the Mars Express Mission, *Space Sci. Rev*, doi: 10.1007/s11214-006-9124-8

Barabash, S., Fedorov, A., Lundin, R., Sauvaud, J.-A., 2007b. Martian atmospheric erosion rates, *Science*, 315, 501-503, doi: 10.1126/science.1134358

Barbosa D.D. and M.G. Kivelson, 1983. Dawn-dusk electric field asymmetry of the Io plasma torus, *J. Geophys. Res.*, 10, 210-213

Baum, W.A, Kreidl, T., Westphal, J. A., Danielson, G.E., Seidelmann, P.K., Pascu, D. and Currie, D.G.,1981. Saturn's E ring I. CCD observations of March 1980, *Icarus*, 47, 84-96

Bertaux, J.-L., Leblanc, F., Witasse, O., Quemerais, E., Lilensten, J., Stern, S. A., Sandel, B.; Korablev, O., 2005. Discovery of an aurora on Mars, *Nature*, 435,790-794, doi: 10.1038/nature03603
Bertaux, J.-L., Leblanc, F., Witasse, O., Quemerais, E., Lilensten, J., Stern, S. A., Sandel, B.; Korablev, O.

Birch, P.C, Chapman, S.C., 2001. Detailed structure and dynamics in particle in-cell simulations of the lunar wake, *Physics of Plasmas*, 8, 4551-4559, doi: 10.1063/1.1398570

Birmingham, T. J., 1982. Charged particle motions in the distended magnetospheres of Jupiter and Saturn, *J. Geophys. Res.*, 87(A9), 7421-7430.

Blanc, M. et al. 2002. Magnetospheric and plasma science with Cassini-Huygens, *Space Sci. Rev.*, 104, 253-346, doi: 10.1023/A:1023605110711

Bößwetter, A. et al., 2007. Comparison of plasma data from ASPERA-3/Mars-Express with a 3-D hybrid simulation, *Ann. Geophys.*, 25, 1851-1864.

Bößwetter, A., Bagdonat, T., Motschmann, U., Sauer, K., 2004. Plasma boundaries at Mars: A 3D simulation study, *Ann. Geophys.*, 22, 4363-4379.

Bockelée-Morvan, D., Crovisier, J., Mumma, M. J. and Weaver, H. A., 2004. The composition of cometary volatiles, in *Comets II*, University of Arizona Press, edited by M.C. Festou, H.U. Keller, and H.A. Weaver, pp. 391-423, Tucson, Arizona, USA.

Brain, D.A., 2006a. Mars Global Surveyor measurements of the martian solar wind interaction, *Space Sci. Rev.*, 126, 77-112, doi: 10.1007/11214-006-9122-x

Brain, D.A., Halekas, J.S., Peticolas, L.M., Lin, R.P., Luhmann, J.G., Mitchell, D.L., Delory, G.T., Bougher, S.W., Acuña, M. H.; Rème, H., 2006b. On the origin of aurorae on Mars, *Geophys. Res. Let.*, 33, L01201, doi:10.1029/2005GL024782.

Brain, D.A., Halekas, J.S., Lillis, R., Mitchell, D.L., Lin R.P., Crider, D.H., 2005. Variability of the altitude of the Martian sheath, *Geophys. Res. Let.*, 32, L18203, doi: 10.1029/2005GL023126

Brice, N.M., 1967. Bulk motion in the magnetosphere, *J. Geophys. Res*, 72, 5193-5211

Bridge et al., 1982. Plasma observations near Saturn: Initial results from Voyager 2 *Science*, 215, 563-570

Bridge et al., 1981. Plasma observations near Saturn: Initial results from Voyager 1 *Science*, 212, 217-224

Burch, J.L., J. Goldstein, T. W. Hill, D.T. Young, F.J. Crary, A.J. Coates, N. André, W.S. Kurth, and E.C. Sittler Jr., 2005. Properties of local plasma injections in SaturnâĂŹs magnetosphere, *Geophys. Res. Lett.*, 32, L14S02,doi:10.1029/2005GL022611.

Burns et al., 1999. The formation of Jupiter's faint rings, *Science*, 284, 1146-1149

Carbary J.F., S.M. Krimigis and W.-H. Ip, 1983. Energetic particle microsignatures of Saturn's satellites, *J. Geophys. Res.*, 88, 8947-8958

Chenette, D.L. and Stone, E.C., 1983. The Mimas ghost revisited: An analysis of the electron flux and electron microsignatures observed in the vicinity of Mimas at Saturn, *J. Geophys. Res.*, 88, 8755-8764

Cohen, C. M. S., T.L. Garrard, E.C. Stone, J.F. Cooper, N. Murphy, N. Gehrels, 2000. Io encounters past and present: A heavy ion comparison, *J. Geophys. Res.*, 105 ,7775-7782

Connerney, J.E.P., Acuña, M. H., Wasilewski, P.J., Kletetschka, G., Ness, N.F., Réme, H., Lin, R.P. and Mitchell, D.L., 2001. The global magnetic field of Mars and implications for crustal evolution, *Geophys. Res. Lett.*, 28, 4015-4018, doi: 10.1029/2001GL013619.

Connerney J.E.P., M.H. Acuña and N.F. Ness, 1981. Saturn's ring current and inner magnetosphere, *Nature*, 292, 724-726.

Cooper J.F., E.C. Sittler Jr., S. Maurice, B.H. Mauk and R.S. Selesnick, 1998. Local time asymmetry of drift shells for energetic electrons in the middle magnetosphere of Saturn, *Adv. Space Res.*, 21, 1479-1482.

Cooper J.F., 1983. Nuclear cascades in Saturn's rings: cosmic ray albedo neutron decay and the origins of trapped protons in the inner magnetosphere, *J. Geophys. Res*, 88, 3945-3954.

Crider, D.H. et al., 2002. Observations of the latitude dependence of the location of the martian magnetic pileup boundary, *Geophys. Res. Lett.*, 29, 11-1, doi: 10.1029/2001GL013860

Cruikshank, D.P., 2005. Triton, Pluto, Centaurs, and Trans-Neptunian Bodies, *Space Sci. Rev.*, 116, 421-439, doi: 10.1007/s11214-005-1964-0

Cuzzi, J.N. and Burns, J.A., 1988. Charged particle depletion surrounding Saturn's F ring: Evidence for a moonlet belt?, *Icarus*, 74, 284-324.

de Pater, I., Gibbard, S.G., Chiang, E., Hammel, H.B., Macintosh, B., Marchis, F., Martin, S.C., Roe, H.G. and Showalter, M., 2005. The dynamic neptunian ring arcs: evidence for a gradual disappearance of Liberté and resonant jump of courage, *Icarus*, 164, 263-285

de Pater, I., Lissauer, J.J., 2001. Introduction, *in Planetary Sciences*, edited by de Pater, I. and Lissauer, J.J., Cambridge University Press, 1st ed., pp. 1-18, Cambridge, UK.

Dougherty M.K., K.K. Khurana, F.M. Neubauer, C.T. Russell, J. Saur, J.S. Leisner and M.E. Burton, (2006), Identification of a dynamic atmosphere at Enceladus with the Cassini magnetometer, *Science*, 311, 1406-1409.

Dougherty M.K. et al., 2004a. The Cassini Magnetic Field Investigation, *Space Science Reviews*, 114, 331-383.

Dougherty M.K. et al., 2004b. Cassini magnetometer observation during Saturn Orbit Insertion, *Science*, 307, 1266-1269.

Dubinin, E., Chanteur, G., Fränz, M., Modolo, R., Woch, J., Roussos, E., Barabash, S., Lundin, R., 2007. Asymmetry of plasma fluxes at Mars. ASPERA-3 observations and hybrid simulations, *submitted to Plan. Space Sci.*

Dubinin, E. et al., 2006a. Plasma morphology at Mars. ASPERA-3 observations, *Space Sci. Rev*, doi: 10.1007/s11214-006-9039-4

Dubinin, E., Fraenz, M., Woch, J., Barabash, S., Lundin, R., Yamauchi, M., 2006b. Hydrogen exosphere at Mars: Pickup protons and their acceleration at the bow shock, *Geophys. Res. Lett.*, 33, L22103, doi: 10.1029/2006GL027799

Dubinin, E. et al., 2005. Solar wind plasma protrusion in the martian magnetosphere: ASPERA-3 observations, *Icarus*, 182, 343-349, doi: 10.1016/j.icarus.2005.08.023

Dubinin, E., Sauer, K., Lundin, R., Baumgärtel, K., and Bogdanov, A., 1996. Structuring of the transition region (plasma mantle) of the Martian magnetosphere, *Geophys. Res. Let.*, 23, 785-788, doi: 10.1029/96GL00701

Dubinin, E., 1993. The Phobos and Deimos effects, *Adv. in Space Res.*, 13, 271-290, doi:10.1016/0273-1177(93)90079-Q

Elphic, R.C., Russell, C.T., Slavin, J.A., and Brace, L.H., 1980. Observations of the dayside ionopause and ionosphere at Venus, *J. Geophys. Res.*, 85, 7679

Espley, J. R., Cloutier, P. A., Brain, D. A., Crider, D. H., Acuña, M. H, 2004. Observations of low-frequency magnetic oscillations in the Martian magnetosheath, magnetic pileup region, and tail, *J. Geophys. Res.*, 109(A7), A07213, doi: 10.1029/2003JA010193

Farrell, W.M., Stubbs, T. J., Vondrak, R.R., Delory, G.T., Halekas, J. S., 2007. Complex electric fields near the lunar terminator: The near-surface wake and accelerated dust, *Geophys. Res. Let.*, 34, L14201, doi: 10.1029/2007GL029312

Farrell, W.M., Kaiser, M.L., Steinberg, J.T., 1997. Electrostatic instability in the central lunar wake: A process for replenishing the plasma void?, *Geophys. Res. Let.*, 24, 1135-1138.

Fedorov, A. et al., 2005. Structure of the Martian wake, *Icarus*, 182, 329-336, doi: 10.1016/j.icarus.2005.09.021

Fillius W., 1988. Toward a comprehensive theory for the sweeping of trapped radiation by inert orbiting matter, *J. Geophys. Res*, 93, 14284-14294.

Frahm, R.A. et al., 2006. Locations of atmospheric photoelectron energy peaks within the Mars environment, *Space Sci. Rev.*, 126, 389-402, doi: 10.1007/s11214-006-9119-5

Fränz, M. et al., 2007. Plasma moments in the environment of Mars: Mars Express ASPERA-3 observations, *Space Sci. Rev*, doi: 10.1007/s11214-006-9115-9

Fränz, M. et al., 2005. Plasma intrusion above Mars crustal fields - Mars Express ASPERA-3 observations *Icarus*, 182, 406-412, doi: 10.1016/j.icarus.2005.11.016

Gisler, G.R., Lemon, D.S., 1992. Dynamics of a plasma expanding into a uniform magnetic field, *J. Geophys. Res.*, 94, 10145-10149.

Gisler, G.R., Onsager, T.G., 1992. On the thermodynamics of diamagnetic plasma expansions, *J. Geophys. Res.*, 97, 4265-4173.

Giuliatti, W., Murray, C.D., Gordon, M., 2000. Perturbations to Saturn's F-ring strands at their closest approach to Prometheus, *Planetary and Space Science*, 48, 817-827.

Halekas, J.S., Bale, S.D., Mitchell, D.L., Lin, R.P., 2005. Electrons and magnetic fields in the lunar plasma wake, *J. Geophys. Res.*, 110, A07222, doi:10.1029/2004JA010991.

Halekas, J.S. et al., 2007. Extreme lunar surface charging during solar energetic particle events, *Geophys. Res. Let.*, 34, L02111, doi:10.1029/2006GL028517.

Hamlin, D. A., Karplus, R., Vik, R. C., Watson, K. M, 1961. Mirror and azimuthal drift frequencies for geomagnetically trapped particles, *J. Geophys. Res.*, 66, 1

Harnett, E.M. and Winglee R.M., 2005. Three dimensional fluid simulations of plasma asymmetries in the Martian magnetotail caused by the magnetic anomalies *J. Geophys. Res*, 110, A07226, doi: 10.1029/2003JA010315

Hedman, M.M., Burns, J.A., Tiscareno, M.S., Porco, C.C., Jones, G.H., Roussos, E., Krupp, N., Paranicas, C., Kempf, S., 2007. The Source of Saturn's G Ring, *Science*, 317, 653-656, doi: 10.1126/science.1143964

Hide, R. and Palmer, T.N., 1982. Generalization of Cowling's theorem, *Geophys. Astrophys. Fluid Dyn.*, 19, 301-309.

Hill, T.W., A. M. Rymer, J. L. Burch, F. J. Crary, D. T. Young, M. F. Thomsen, D. Delapp, N. André, A. J. Coates, and G.R. Lewis, 2005. Evidence for rotationally driven plasma transport in Saturn's magnetosphere, *Geophys. Res. Lett.*, 32, L14S10, doi:10.1029/2005GL022620.

Hill, T.W., 1982. Saturn's E-ring, *Adv. Space Res.*, 4, 149-157, doi:10.1016/0273-1177(84)90020-6

Horne, R.B., 2005. Wave acceleration of electrons in the Van Allen radiation belts, *Nature*, , 437, 227-230, doi: 10.1038/nature03939.

Hofmann, D.J. and Sauer, H.H. 2000. Magnetospheric cosmic-ray cutoffs and their variations, *Space Sci. Rev.*, 8, 750-803.

Huba, J.D., Bernhardt, P.A., Lyon, J.G., 1992. Preliminary study of the CRRES magnetospheric barium releases, *J. Geophys. Res*, 97, 11-24

Hurtig, T., Brenning, N., Raadu, M.A. 2003. Three dimensional, particle-in-cell simulation with open boundaries applied to a plasma beam entering a curved magnetic field, *Physics of Plasmas*, 10, 4291-4305, doi:10.1063/1.1619381

Interational Astronomical Union, 2006. "Definition of a Planet in the Solar System" AND "Pluto", *http://www.iau.org/fileadmin/content/pdfs/Resolution_GA26-5-6.pdf*, XXVIth IAU General Assembly, Prague.

Jones, G.H. et al., 2008. The Dust Halo of Saturn's largest icy moon, Rhea, *Science*, doi:10.1126/science.1151524, 2008.

Jones, G.H., Roussos, E., Krupp, N., Paranicas, C., Woch, J., Lagg, A., Mitchell, D.G., Krimigis, S.M. and Dougherty, M.K. 2006. Enceladus' Varying Imprint on the Magnetosphere of Saturn, *Science*, 311, 1412-1415.

Jones, G.H., Balogh, A., McComas, D. J. and MacDowall, R. J., 2006. Strong interplanetary field enhancements at Ulysses-evidence of dust trails' interaction with the solar wind?, *Icarus*, 166, 297-310, doi: 10.1016/S0019-1035(03)00288-4

Juhász, A., Horányi, M. and Morfill, G.E., 2007. Signatures of Enceladus in Saturn's E ring, *Geophys. Res. Lett.*, Volume 34, L09104, doi: 10.1029/2006GL029120

Kallio, E., 2005. Formation of the lunar wake in a quasi-neutral hybrid model, 2005. *Geophys. Res. Let.*, 32, L06107, doi:10.1029/2004GL021989

Khurana, K. K., Russell, C.T. and Dougherty, M.K., 2007. Magnetic portraits of Tethys and Rhea, *accepted for publication in Icarus*

Khurana K.K. and Schwarzl, H.K., 2005. Global structure of Jupiter's magnetospheric current sheet, *J. Geophys. Res.*, 110, A07227, doi: 10.1029/2004JA010757

Khurana, K. K., Kivelson, G.K., and Russell, C.T., 2001. Searching for liquid water in Europa by using surface observatories, *Astrobiology*, 2, 93, 103.

Kivelson, M., Bargatze, L.F., Khurana, K.K., Southwood, D.J., Walker, R.J. and Colemann Jr., P.J., 1993. Magnetic field signatures during Galileo's closest approach to Gaspra, *Science*, 261, 331-334.

Krimigis, S.M., Sergis, N., Mitchell, D.G., Hamilton, D.C. and Krupp, N., 2007. Imaging and Properties of SaturnâĂŹs Ring Current, *accepted for publication in Nature*

Krimigis, S.M., et al., 2004. Magnetosphere Imaging Instrument (MIMI) on the Cassini Mission to Saturn/Titan, *Space Science Reviews*, 114, 223-329.

Krimigis, S.M., 1992. Voyager energetic particle observations at interplanetary shocks and upstream of planetary bow shocks - 1977-1990, *Space Science Reviews*, 59, 167-201.

Krimigis S.M., T.P. Armstrong, W.I Axford, C.O. Bostrom, G. Gloecker, E.P. Keath, L.J. Lanzerotti, J.F. Carbary, D.C. Hamilton, and E. C. Roelof (1981), Low-energy charged particles in Saturn's magnetosphere: Results from Voyager 1, *Science*, 212, 225-230.

Lagg A., N. Krupp, J. Woch and D.J. Williams, 2003. In-situ observations of a neutral gas torus at Europa, *Geophys. Res. Lett.*, 30(11), 1556, doi:10.1029/2003GL017214.

Lenchek, A.M., Singer, S. F., Wentworth, R. C., 1961. Geomagnetically Trapped Electrons from Cosmic-Ray Albedo Neutrons, *J. Geophys. Res.*, 66, 4027

Lew, J.S., 1961. Drift rate in a dipole field, *J. Geophys. Res.*, 66, 2681.

Lipatov, A.S., 2002. The Hybrid Multiscale Simulation Technology, *Springer*.

Lundin, R. et al., 2006. Auroral plasma acceleration above Martian magnetic anomalies, *Space Sci. Rev.*, doi: 10.1007/s11214-006-9086-x

Lundin, R. et al., 2005. Ionospheric plasma acceleration at Mars: ASPERA-3 results, *Icarus*, 182, 308-319, doi: 10.1016/j.icarus.2005.10.035

Lundin, R. and Barabash, S., 2004a. The wakes and magnetotails of Mars and Venus, *Adv. Space Res.*, 33, 1945-1955, doi: 10.1016/j.asr.2003.07.054

Lundin, R. and Barabash, S., 2004b. Evolution of the Martian atmosphere and hydrosphere: Solar wind erosion studied by ASPERA-3 on Mars Express, *Planetary and Space Science*, 52, 1059-1071, doi:10.1016/j.pss.2004.07.020.

Martinec, Z., 1999. Spectral-finite element approach to three-dimensional electromagnetic induction in a spherical earth, *Geophysical Journal International*, 136, 229-250.

Maurice, S., E. C. Sittler, Jr., J. F. Cooper, B. H. Mauk, M. Blanc, and R. S. Selesnick (1996), Comprehensive analysis of electron observations at Saturn: Voyager 1 and 2, *J. Geophys. Res.*, 101, 1556, 15211-15232.

Mogro-Campero, A. and R.W. Fillius, 1976. The absorption of trapped particles by the inner satellites of Jupiter and the radial diffusion coefficient of particle transport, *J. Geophys. Res.*, 81, 1289-1295.

Mauk et al., 2005. Energetic particle injections in Saturn's magnetosphere, *Geophys. Res. Let.*, 32, L14S05, doi: 10.1029/2005GL022485

Maurice and Engle, 1995. Idealized Saturn magnetosphere and field, *J. Geophys. Res.*, 100, 17143-17151.

Murray, C.D. and Dermott, S.F., 2001. Solar System Dynamics, 2nd ed., pp. 474-525, Cambridge University Press, Cambridge.

Müller, J., 2007. Entwicklung eines numerischen Modells zur Untersuchung der Wechselwirkung leitfähiger Objekte mit dem Sonnenwind, Institut für Theoritische Physik der Technishen Universität Braunschweig, Germany (in German).

Nagy, E. et al., 2004. The plasma environment of Mars, *Space Sci. Rev.*, 11, 33-114

Nicholson, P.D., French, R.G., Tollestrup, E., Cuzzi, J.N., Harrington, J., Matthews, K., Perkovic, O.; Stover, R.J., 2000. Saturn's rings I. Optical depth profiles from the 28 Sgr occultation, *Icarus*,145, 474-501

Ogilvie, K.W., Steinberg, J.T., Fitzenreiter, R.J., Owen, C.J., Lazarus, A.J. Farell, W.M., Torbert, R.B., Observations of the lunar plasma wake from the WIND spacecraft on December 27 1994, 1986. *Geophys. Res. Let.*, 23, 1255-1258.

Orlowski, D. S., Russell, C. T., Krauss-Varban, D., Omidi, N., 1995. Properties of ultra low frequency upstream waves at Venus and Saturn: A comparison. *Adv. Space Res.*, 16, (4)143-(4)148.

Patharea, A.V. and Paigeb, D.A., 2005. The effects of martian orbital variations upon the sublimation and relaxation of north polar troughs and scarps. *Icarus*, Volume 174, 419-443, doi: 10.1016/j.icarus.2004.10.030

Paonessa, M. and A.F. Cheng, 1986. Limits on ion radial diffusion coefficients in Saturn's inner magnetosphere, *J. Geophys. Res.*, 91, 1391-1396.

Paonessa, M. and A.F. Cheng, 1985. A theory for satellite sweeping, *J. Geophys. Res.*, 90, 3428-3434.

Paranicas, C., Mitchell, D.G., Livi, S., Krimigis, S.M., Roussos, E., Krupp, N., Woch, J., Lagg, A., Saur, J., and Turner, F.S. (2005), Evidence of Enceladus and Tethys microsignatures, *Geophys. Res. Lett.*, 32, doi:10.1029/2005GL024072.

Paranicas, C., B. H. Mauk, R. W. McEntire, and T. P. Armstrong, 2003. The radiation environment near Io, *Geophys. Res. Lett.*, 32, 30(18), 1919, doi:10.1029/2003GL017682

Paranicas C. and C.F. Cheng, 1997. A model for satellite microsignatures for Saturn, *Icarus*, 125, 380-396.

Persoon, A. M., Gurnett, D. A., Kurth, W.S., Hospodarsky, G.B., Groene, J.B., Canu, P., Dougherty, M.K., 2005. Equatorial electron density measurements in Saturn's inner magnetosphere, *Geophys. Res. Let.*, 32, L23105, doi: 10.1029/2005GL024294

Porco et al., 2006. Cassini observes the active south pole of Enceladus, *Science*, 311, 1393-1401

Porco et al., 2004. Cassini Imaging Science: Instrument characteristics and anticipated scientific investigations at Saturn, *Space Science Reviews*, 115, 363-497

Randall B.A., 1998. An improved magnetic field model for Jupiter's inner magnetosphere using a microsignature of Amalthea, *J. Geophys. Res.*, 103, 17535.

Randall B.A., 1994. Energetic electrons in the magnetosphere of Saturn, *J. Geophys. Res.*, 99, 8771-8785.

Richardson J., Thermal ions at Saturn: Plasma parameters and implications, 1986. *J. Geophys. Res.*, 91, 1381-1389.

Roddier, C., Roddier, F., Graves, J.E. and M.J. Northcott, 1998. Discovery of an arc of particles near Enceladus' orbit: a possible key to the origin of the E-ring, *Icarus*, 136, 50-59.

Roederer J.G., 1970. Dynamics of geomagnetically trapped radiation, 1st ed., Springer, Heidelberg

Roussos E. et al., 2005. Low energy electron microsignatures at the orbit of Tethys: Cassini MIMI/LEMMS observations, *Geophys. Res. Lett.*, 32, L24107, doi:10.1029/2005GL024084.

Rymer et al., 2007. Electron sources in Saturn's magnetosphere, *J. Geophys. Res.*, 112, A02201, doi:10.1029/2006JA012017

Samir, U., Wright, K.H., Stone, N.H., 1983. The expansion of plasma into a vacuum: basic phenomena and processes and applications to space plasma physics, *J. Geophys. Res.*, 21, 1631-1646

Saur J., Strobel, 2005. Atmospheres and Plasma Interactions at Saturn's Largest Inner Icy Satellites, *The Astrophysical Journal*, 620, L115-L118, doi:10.1086/428665

Saur J., B.H. Mauk, A. Kaßner and F.M. Neubauer, 2004. A model for the azimuthal plasma velocity in Saturn's magnetosphere, *J. Geophys. Res.*, 109, A05217, doi:10.1029/2003JA010207

Saur K., Baumgärtel, K., and Motschmann, U., 1993. Phobos events as precursors of solar wind-dust interaction, *Geophys. Res. Lett.*, 20, 165-168

Selesnick, R.S and E.C. Stone. 1994. Radial diffusion of relativistic electrons in Neptune's magnetosphere, *Geophys. Res. Lett.*, 21, 1579-1582.

Selesnick R.S, 1993. Micro- and macro- signatures of energetic charged particles in planetary magnetospheres, *Adv. Space Res.*, 13, (10)221-(10)230.

Selesnick R.S and E.C. Stone, 1991. Energetic electrons at Uranus: Bimodal diffusion in a satellite limited radiation belt, *J. Geophys. Res.*, 96, 5651-5665.

Sergis, N., Krimigis, S. M., Mitchell, D. G., Hamilton, D. C., Krupp, N., Mauk, B. M., Roelof, E. C., Dougherty, M., 2007. Ring current at Saturn: Energetic particle pressure in Saturn's equatorial magnetosphere measured with Cassini/MIMI *Geophys. Res. Let.*, 34, L09102, doi:10.1029/2006GL029223.

Simon, S., Bößwetter, A., Bagdonat, T., Motschmann, U., 2007. Physics of the Ion Composition Boundary: a comparative 3-D hybrid simulation study of Mars and Titan, 2007. *Ann. Geophys.*, 25, 99-115

Simon, S., Bößwetter, A., Bagdonat, T., Motschmann, U., 2007. Three dimensional multispecies hybrid simulation of Titan's highly variable plasma environment, 2007. *Ann. Geophys.*, 25, 117-144

Simpson J.A., T.S. Vastian, D.L. Chenette, R. B. McKibben and K.R. Pyle, 1980. The trapped radiations of Saturn and their absorption by satellites and rings, *J. Geophys. Res.*, 85, 5731-5762

Sittler et al., 2006. Cassini observations of Saturn's inner plasmasphere: Saturn orbit insertion results, *Planetary and Space Science*, 54, 1197-1210, doi:10.1016/j.pss.2006.05.038

Smart, D.F., Shea, M.A. and Flückiger, E.O., 2000. Magnetospheric models and trajectory computations, *Space Sci. Rev.*, 93, 305-333.

Spahn et al., 2006. Cassini dust measurements at Enceladus and implications for the origin of the E ring, *Science*, 311, 1416-1418

Spitale, J.N., Jacobson, R.A., Porco, C.C. and Owen Jr., W.M., 2006. The orbits of Saturn's small satellites derived from combined historic and Cassini imaging observations, *Astron. J.*, 132, 692-710, doi: 10.1086/505206

Sonett, C.P. and Colburn, D.S., 1968. The Principle of Solar Wind Induced Planetary Dynamos, *Physics of the Earth and Planetary Interiors*, 1, 326-346

Soobiah, Y. et al., 2005. Observations of magnetic anomaly signatures in Mars Express ASPERA-3 ELS data, *Icarus*, 182, 396-405 doi: 10.1016/j.icarus.2005.10.034

Szego, K., Sagdeev, R.Z., Shapiro, V.D. and Shevchenko, V.I., 1992. On the dayside mantle region around those nonmagnetic solar system bodies which have ionosphere, *Adv. Space Res.*, 12, 291-298

Thomsen, M.F. and Van Allen, J.A., 1980. Motion of trapped electrons and protons in Saturn's inner magnetosphere, *J. Geophys. Res.*, 85, 5831-5834.

Thomsen M.F. C.K Goertz and J.A. Van Allen, 1977a. On determining magnetospheric diffusion coefficients from the observed effects of Jupiter's Satellite Io, *J. Geophys. Res.*, 82, 5541-5550.

Thomsen M.F. C.K Goertz and J.A. Van Allen, 1977b. A determination of the L dependence of the radial diffusion coefficient for protons in Jupiter's magnetosphere, *J. Geophys. Res.*, 82, 3655-3658.

Tokar et al., 2006. The interaction of the atmosphere of Enceladus with Saturn's plasma, *Science*, 311, 1409-1412.

Travnicek, P., Hellinger, P., Schriver, D., Bale, S.D., 2005. Structure of the lunar wake: two dimensional global hybrid simulations. *Geophys. Res. Let.*, 32, L06102, doi: 10.1029/2004GL022243.

Trotignon et al., 1993. Position and shape of the martian bow shock: The Phobos 2 plasma wave system observations *Planet. Space Sci.*, 41, 189-198

Van Allen, J.A., 1987. An upper limit on the sizes of shepherding satellites at Saturn's ring G, *J. Geophys. Res.*, 92, 1153-1159.

Van Allen J.A., 1984. Energetic particles in the inner magnetosphere of Saturn, in *Saturn*, edited by J.A. Gehrels T. and Mattheus M.S., The University of Arizona Press, 1st ed., pp. 281-317,Tuscon, Arizona

Van Allen, J.A., 1983. Absorption of energetic protons by Saturn's Ring G, *J. Geophys. Res.*, 88, 6911-6918.

Van Allen, J.A., 1982. Findings on rings and inner satellites of Saturn by Pioneer 11, *Icarus*, 51, 509-527, doi:10.1016/0019-1035(82)90143-9

Van Allen, J.A., Thomsen, M.F. and Randall, B.A., 1980a. The energetic charged particle absorption signature of Mimas, *J. Geophys. Res.*, 85, 5709-5718.

Van Allen J.A., M.F. Thomsen, B.A. Randall, R.L. Rairden and C.L. Grosskreutz, 1980b. Saturn magnetosphere, rings and inner satellites, *Science*, 207, 415-421.

Verigin, M.I. et al., 2001. Evidence of the influence of equatorial martian crustal magnetization on the position of the planetary magnetotail boundary by Phobos 2 data, *Adv. Space Res.*, 28, 885-889, doi:10.1016/S0273-1177(01)00510-5

Vignes, D., Mazelle, C., Reme, H., Acuña, M. H., Connerney, J.E.P., Lin, R.P., Mitchell, D.L., Cloutier, P., Crider, D.H., Ness, N.F., 2000. The solar wind interaction with of Mars: Locations and shapes of the bow shock and the magnetic pile-up boundary from the observations of the MAG/ER experiment onboard Mars Global Surveyor, *Geophys. Res. Let.*, 27, 49-52

Vignes, D., Acuña, M. H., Connerney, J.E.P., Crider, D.H., Reme, H., Mazelle, C., 2000. Factors controlling the location of the Bow Shock at Mars, *Geophys. Res. Let.*, 29, 42-1, doi: 10.1029/2001GL014513

Vogt R.E., D.L. Chennete, A.C. Cummings, T.L. Garrard and E.C. Stone, 1982. Energetic charged particles in Saturn's magnetosphere: Voyager 2 Results, *Science*, 215, 577-582.

Walt M., 1994. Diffusion in L coordinate or radial diffusion, in *Introduction to geomagnetically trapped radiation*, edited by Dessler A.J., Houghton J.T. and Rycroft M.J., Cambridge University Press, 1st ed., pp. 132-146, Cambridge, Great Britain.

Watt, C.E.J and Rankin, R., 2006. Electron acceleration due to inertial Alfvén waves in a non-Maxwellian plasma, *J. Geophys. Res*, 112, A04214, doi:10.1029/2006JA011907

Whang, Y.C., Ness, N.F., 1970. Observations and interpretation of the Lunar Mach Cone, *J. Geophys. Res*, 75, 6002-6009

Winningham, J.D. et al., 2005. Electron oscillations in the induced martian magnetosphere, *Icarus*, 182, 360-370 doi: 10.1016/j.icarus.2005.10.033

Wood, B.E., 2006. The solar wind and the Sun in the past, *Space Sci. Rev.*, 126, 3-14 doi: 10.1007/s11214-006-9006-0

Yoder C.F, 1995. Astrometric and geodetic properties of Earth and the Solar System,in *Global Earth Physics, A Handbook of Physical Constants*, AGU Reference Shelf 1, American Geophysical Union.

Zhdanov, S.K., Morfill, G.E., Samsonov, D., Zuzic, M., Havnes, O., 2004. Origin of the curved nature of Mach cone wings in complex plasmas, 2004. *Physical Review*, E69, doi:10.1103/PhysRevE.69.026407

Publications

Teilergebnisse aus dieser Arbeit wirden mit Genehmigung der Fakultät fur Elektrotechnik, Informationstechnik, Physik, vertreten durch den Mentor oder den Betreuer der Arbeit, in folgenden Beiträgen vorab veröffentlich:

Refereed publications:

E. Roussos, M. Fränz, E. Dubinin, C. Martinecz, J. Woch, U. Motschmann, D. J. Winningham, R. Frahm, S. Barabash, and R. Lundin, Energetic electron asymmetries in the Martian magnetosphere: ASPERA-3 observations, *Planet. and Space Sci.*, in press, 2008.

E. Roussos, J. Müller, S. Simon, A. Bößwetter, U. Motschmann, M. Fränz, N. Krupp, J. Woch, K. Khurana, and M.K. Dougherty, Plasma and fields in the wake of Rhea: 3D hybrid simulation and comparison with Cassini data, *An. Geophys.*, in press, 2008.

E. Roussos, G. H. Jones, N. Krupp, C. Paranicas, D.G. Mitchell, S. M. Krimigis, J. Woch, A. Lagg, K. Khurana, Energetic electron signatures of Saturn's smaller moons: evidence of an arc of material at Methone, *Icarus*, 193/2, 455-464, doi: 10.1016/j.icarus. 2007.03.034, 2008.

E. Roussos, G. H. Jones, N. Krupp, C. Paranicas, D. G. Mitchell, A. Lagg, J. Woch, U. Motschmann, S. M. Krimigis, and M. K. Dougherty, Electron microdiffusion in the Saturnian radiation belts: Cassini MIMI/LEMMS observations of energetic electron absorption by the icy moons, *J. Geophys. Res.*, 112, A06214, doi:10.1029/2006JA012027, 2007.

E. Roussos, N. Krupp, J. Woch, A. Lagg, G. H. Jones, C. Paranicas, D. G. Mitchell, S. Livi, S. M. Krimigis, M. K. Dougherty, T. Armstrong, W.-H. Ip, and U. Motschmann, Low energy electron microsignatures at the orbit of Tethys: Cassini MIMI/ LEMMS observations, *Geophys. Res. Lett.*, 32, L24107, doi:10.1029/2005GL024084, 2005.

C. Paranicas, D. G. Mitchell, S. M. Krimigis, D. C. Hamilton, **E. Roussos**, N. Krupp, G. H. Jones, R. E. Johnson, J. F. Cooper, and T. P. Armstrong, Sources and losses of energetic protons in SaturnâĂŹs magnetosphere, *Icarus*, submitted 2008.

C. Martinecz, M. Fränz, J. Woch, N. Krupp,**E. Roussos**, E. Dubinin, U. Motschmann, S. Barabash, R. Lundin, M. Holmström, et al., Venus bow shock and ion composition boundary located by Venus Express ASPERA-4, *Planetary and Space Science*, in press 2007.

E. Dubinin, G. Chanteur, R. Modolo, M. Fränz, J. Woch, **E. Roussos**, S. Barabash, R. Lundin, Asmmetry of plasma fluxes at Mars: ASPERA-3 observations and hybrid simulations, *Planetary and Space Science*, in press 2007.

G.H. Jones, **E. Roussos**, N. Krupp, U. Beckmann, A.J. Coates, F. Crary, I. Dandouras, V. Dikarev, M.K. Dougherty, P. Garnier, C.J. Hansen, A.R. Hendrix, G.B. Hospodarsky, R.E. Johnson, S. Kempf, K.K. Khurana, S.M. Krimigis, H. Krüger, W. S. Kurth, A. Lagg, H.J. McAndrews, D.G. Mitchell, C. Paranicas, F. Postberg, C.T. Russell, J. Saur, F. Spahn, R. Srama, D. F. Strobel, R. Tokar and J.-E. Wahlund, The Dust Halo of Saturn's largest icy moon, Rhea, *Science*, doi:10.1126/science.1151524, 2008.

A. Bößwetter, S. Simon, T. Bagdonat, U. Motschmann, M. Fränz, **E. Roussos**, J. Woch, J. Schüle, S. Barabash and R. Lundin. Comparison of plasma data from ASPERA-3/Mars-Express with a 3-D hybrid simulation, *Ann. Geophys.*, 25, 1851-1864, 2007.

E. Dubinin, M. Fränz, J. Woch, **E. Roussos**, S. Barabash, R. Lundin, J. D. Winningham, R. A. Frahm, and M. Acuña, Plasma Morphology at Mars. Aspera-3 Observations, *Space Sci. Rev.*, 126, 209-238, doi:10.1007/s11214-006-9039-4, 2006.

M. Fränz, E. Dubinin, **E. Roussos**, J. Woch, J. D. Winningham, R. Frahm, A. J. Coates, A. Fedorov, S. Barabash, and R. Lundin, Plasma Moments in the Environment of Mars, *Space Sci. Rev.*, 126, 165-207, doi:10.1007/s11214-006-9115-9, 2006.

M. Fränz, J. D. Winningham, E. Dubinin, **E. Roussos**, J. Woch, S. Barabash, R. Lundin, M. Holmström, H. Andersson, M. Yamauchi, A. Grigoriev, R. A. Frahm, J. R. Sharber, J. R. Scherrer, A. J. Coates, Y. Soobiah, D. R. Linder, D. O. Kataria, E. Kallio, T. Säles, P. Riihelä, W. Schmidt, H. E. J. Koskinen, J. Kozyra, J. Luhmann, E. Roelof, D. Williams, S. Livi, C. C. Curtis, K. C. Hsieh, B. R. Sandel, M. Grande, M. Carter, J.-A. Sauvaud, A. Fedorov, J.-J. Thocaven, S. McKenna-Lawler, S. Orsini, R. Cerulli-Irelli, M. Maggi, P. Wurz, P. Bochsler, N. Krupp, K. Asamura, and C. Dierker, Plasma intrusion above Mars crustal fields/Mars Express ASPERA-3 observations, *Icarus*, 182, 406-412, doi:10.1016/j.icarus.2005.11.016, 2006.

M. M. Hedman, J. A. Burns, M. S. Tiscareno, C. C. Porco, G. H. Jones, **E. Roussos**, N. Krupp, C. Paranicas, and S. Kempf, The Source of Saturn's G Ring, *Science*, 317, 653-656, doi:10.1126/science.1143964, 2007.

G. H. Jones, N. Krupp, H. Krüger, **E. Roussos**, W.-H. Ip, D. G. Mitchell, S. M. Krimigis, J. Woch, A. Lagg, M. Fränz, M. K. Dougherty, C. S. Arridge, and H.

J. McAndrews, Formation of Saturns ring spokes by lightning-induced electron beams, *Geophys. Res. Lett.*, 33, L21202, doi:10.1029/2006GL028146, 2006.

G. H. Jones, **E. Roussos**, N. Krupp, C. Paranicas, J. Woch, A. Lagg, D. G. Mitchell, S. M. Krimigis, and M. K. Dougherty, Enceladus' varying imprint on the magnetosphere of Saturn, *Science*, 311, 1412-1415, doi:10.1126/science.1121011, 2006.

H. Nilsson, E. Carlsson, H. Gunell, Y. Futaana, S. Barabash, R. Lundin, A. Fedorov, Y. Soobiah, A. Coates, M. Fränz, and **E. Roussos**, Investigation of the Influence of Magnetic Anomalies on Ion Distributions at Mars, *Space Sci. Rev.*, 126, 355-372, doi:10.1007/s11214-006-9030-0, 2006.

C. Paranicas, B. H. Mauk, K. Khurana, I. Jun, H. Garrett, N. Krupp, and **E. Roussos**, Europa's near-surface radiation environment, *Geophys. Res. Lett.*, L15103, doi:10.1029/2007GL030834, 2007.

C. Paranicas, D. G. Mitchell, S. Livi, S. M. Krimigis, **E. Roussos**, N. Krupp, J. Woch, A. Lagg, J. Saur, and F. S. Turner, Evidence of Enceladus and Tethys microsignatures, *Geophys. Res. Lett.*, 32, L20101, doi:10.1029/2005GL024072, 2005.

J. Saur, B. H. Mauk, D. G. Mitchell, N. Krupp, K. K. Khurana, S. Livi, S. M. Krimigis, P. T. Newell, D. J. Williams, P. C. Brandt, A. Lagg, **E. Roussos**, and M. K. Dougherty, Anti-planetward auroral electron beams at Saturn, *Nature*, 439, 699-702, doi:10.1038/nature04401, 2006.

Conference proceedings:

N. Sergis, K. Dialynas, **E. Roussos**, and X. Moussas, Magnetospheric Electron Flows In The Martian Ionosphere. Detection And Implications, in: Recent Advances in Astronomy and Astrophysics: 7th International Conference of the Hellenic Astronomical Society. *AIP Conference Proceedings*, vol. 848, pp. 263-272, 2006, doi:10.1063/1.2347990.

N. Sergis, K. Dialynas, **E. Roussos**, and X. Moussas, Mars: Determination of the most appropriate electron energy for the bow shock identification, using MGS data, in: Recent Advances in Astronomy and Astrophysics: 7th International Conference of the Hellenic Astronomical Society. *AIP Conference Proceedings*, vol. 848, pp. 163-167, 2006, doi:10.1063/1.2347973.

Posters and Presentations:

E. Roussos, J. Müller, S. Simon, A. Bößwetter, U. Motschmann, N. Krupp, M. Fränz, J. Woch, K.K. Khurana, and M.K. Dougherty, Fields and plasma in the wakes of the Saturnian inert moons: global hybrid simulation results, American

Geophysical Union, Fall Meeting 2007, San Francisco, December 2007 (Oral - invited).

E. Roussos, G. H. Jones, N. Krupp, C. Paranicas, D. G. Mitchell, M. M. Hedman, J. A. Burns, and U. Motschmann, Detection and physical characterization of dust structures at Saturn, through energetic charged particle data: new results from Cassini, European Planetary Science Congress 2007, Potsdam, August 19-24, 2007. (Oral).

E. Roussos, J. Müller, S. Simon, A. Bößwetter, U. Motschmann, M. Fränz, and N. Krupp, The magnetic and plasma wake of Rhea: results from hybrid plasma simulations, European Planetary Science Congress 2007, Potsdam, August 19-24, 2007. (Oral).

E. Roussos, N. Krupp, G. H. Jones, C. Paranicas, D. G. Mitchell, S. M. Krimigis, U. Motschmann, A. Lagg, and J. Woch, Energetic charged particle absorption by Saturn's icy moons: future studies and new applications, European Planetary Science Congress 2007, Potsdam, August 19-24, 2007. (Invited - Oral).

E. Roussos, M. Fränz, E. Dubinin, C. Martinecz, U. Motschmann, S. Barabash, J. Woch, R. Lundin, R. Frahm, and J. D. Winningham, Energetic electron asymmetries at Mars: Mars Express ASPERA-3 observations, European Planetary Science Congress 2007, Potsdam, August 19-24, 2007. (Oral and poster).

E. Roussos, N. Krupp, G. H. Jones, C. Paranicas, D. G. Mitchell, and S. M. Krimigis, Determining the Timing of Injections at Saturn: Prospects from Energetic Electron Absorption by the Icy Moons, Magnetospheres of the Outer Planets (MOP) Meeting, San Antonio, Texas, USA, June 25-29, 2007. (Poster).

E. Roussos, J. Müller, S. Simon, A. Bößwetter, U. Motschmann, N. Krupp, M. Fränz, and J. Woch, Rhea's interaction with Saturn's magnetospheric plasma: a combined data-simulation approach, Planetary seminar, University of Braunschweig, June 28, 2007 (Oral).

E. Roussos, The origin of Saturn's G-ring, Solar System Seminar, Max Planck Institute for Solar System Research, June 27, 2007. (Oral).

E. Roussos, Saturn's rings through magnetospheric measurements, Space physics lectures, University of Athens, June 12, 2007. (Oral).

E. Roussos, N. Krupp, G. H. Jones, C. Paranicas, A. Lagg, J. Woch, D. G. Mitchell, S. M. Krimigis, and M. K. Dougherty, Icy moon absorption signatures reveal non-axisymmetric drift shells in the Saturnian radiation belts: implications for a magnetospheric electric field?, European Planetary Science Congress 2006, Berlin, Sept 18-22, 2006. (Oral).

E. Roussos, Interaction of weakly or non-magnetized bodies with their surrounding plasma environment: observations at Mars with Mars Express/ASPERA-3 and at the moons of Saturn with Cassini/MIMI-LEMMS experiments, Space physics

course - seminar talk, University of Athens, Physics Department, December 20, 2006. (Oral).

E. Roussos, S. Simon, A. Bößwetter, U. Motschmann, M. Fränz, N. Krupp, J. Woch, and G. H. Jones, Interaction Scenarios Between Rhea and Saturn's Magnetospheric Plasma: a Hybrid Simulation Approach, AGU Fall Meeting, San Francisco, USA, Dec 11-14, 2006. (Poster).

E. Roussos, N. Krupp, G. H. Jones, C. Paranicas, D. G. Mitchell, S. M. Krimigis, U. Motschmann, M. K. Dougherty, A. Lagg, and J. Woch, Icy moon absorption signatures: Probes of Saturnian magnetospheric dynamics and moon activity, AGU Fall Meeting, San Francisco, USA, Dec 11-14, 2006. (Invited - Oral).

E. Roussos, The plasma environment of Mars: Mars Express ASPERA-3 observations, Solar System Seminar, Max Planck Institute for Solar System Research, May 31, 2006. (Oral).

E. Roussos, N. Krupp, G. H. Jones, C. Paranicas, D. G. Mitchell, A. Lagg, J. Woch, and S. M. Krimigis, The inner Saturnian magnetosphere as revealed by Cassini/LEMMS moon absorption signature observations, General Assembly of the European Geosciences Union, Vienna, Austria, April 2-7, 2006. (Oral).

E. Roussos, N. Krupp, G. H. Jones, A. Lagg, J. Woch, C. Paranicas, D. G. Mitchell, S. M. Krimigis, M. K. Dougherty, W. H. Ip, and T. P. Armstrong, Electron microsignatures from the Saturnian satellites: Cassini MIMI/LEMMS observations, AGU Fall Meeting, San Francisco, USA, December 5-9, 2005. (Poster).

E. Roussos, Moon-magnetosphere interactions at Saturn: Cassini MIMI/LEMMS observations, Solar System Seminar, Max Planck Institute for Solar System Research, November 23, 2005. (Oral).

Acknowledgements

Trying to acknowledge in just a couple of pages all the people who have helped and supported me for the successfull completion of this thesis is even more challenging than writing the thesis! I do hope that the short text written below can reveal how grateful I am to all of them.

First of all I want to thank my four supervisors: Dr. Norbert Krupp, Dr. Markus Fränz and Dr. Joachim Woch at MPS and Prof. Dr. Uwe Motschmann at the University of Braunschweig. I want to thank all of them for allowing me to work on such a challenging project involving data analysis from two different missions and the application of an advanced simulation code! For giving me the freedom, along their general guidelines of course, to try my own ideas on so many diverse and interesting subjects. This is definitely one of the reasons that I was never bored with my work and why I am really motivated to continue working in the same field. Undertaking such a complicated project was definitely a risk, but I am glad they trusted me. I hope the results of this thesis and this 3year collaboration satisfy everyone.

More specifically, I want to thank Dr. Norbert Krupp for accepting me in the LEMMS team, for suggesting me to work on a series of very interesting projects and for his help to promote my work within the Cassini community and in (really many) international conferences. I am very grateful to Dr. Markus Fränz for his continuous support to my Mars Express work, for his critical comments to my results, and for making my life easy thanks to the excellent analysis software he has developed. I am thankful to Dr. Joachim Woch for his ideas and guidelines throughout the duration of the thesis work, as well as for his suggestions on how the work on so many different subjects should be handled. I want to thank Prof. Dr. Uwe Motschmann for many valuable discussions, for his guidance and for insisting that I should perform simulations as part of my thesis work. Thanks to him I learned a lot by working on a field I always thought it was not appropriate for me.

Apart from my supervisors, many more people from the MPS and IMPRS community supported me during the last three years. I want to thank Dr. Andreas Lagg for useful discussions, for providing me with an excellent analysis software for my Cassini work and for solving many of my problems with IDL. I want to thank Dr. Edward Dubinin for many useful, constructive and really critical discussions on plasma physics and on my thesis results. I am very grateful to Dr. Geraint Jones for working with him on many science topics, for always bringing forward exciting and interesting interpretations of the Cassini data and for his tireless efforts to improve the quality of English in my texts. I am sure our work on Rhea's rings will be finally accepted! I want to acknowledge the great help I got from the "simulation group" of the Braunschweig University (Dr. Sven Simon, Joachim Müller and Alexander Bößwetter). Without their efforts and dedication my simulation work would have been almost impossible. I appreciate a lot the efforts

Curriculum Vitae

Persönliche Daten

Name: Elias Roussos

Geburtsdatum: 13 April, 1979

Geburtsort: Athens, Greece

Staatsangehörigkeit: Greek

Schulausbildung

1984-1997:   Doukas School, Athens, Greece

Studium

1998-1999:   University of Patras, Greece, Physics Department (1st year)

1999-2003:   Diploma in Physics, University of Athens, Greece

2003-2004:   M.Sc. Space Studies, International Space University, Strasbourg, France

2005-2008:   PhD, Max Planck Institut für Sonnensystemforschung and the University of Braunschweig, Germany